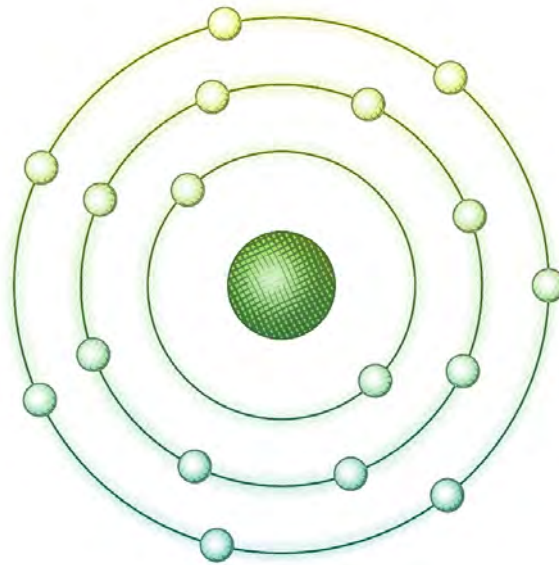# Hydrothermal Activity at Slow-Spreading Mid-Ocean Ridges: Evidence from Chlorine in Basalt

Dissertation
zur Erlangung des Doktorgrades
der Mathematisch-Naturwissenschaftlichen Fakultät
der Christian-Albrechts-Universität zu Kiel

vorgelegt von
Froukje Marieke van der Zwan

Kiel, 2014

Referent:………………………………………………………………..Prof. Dr. Colin W. Devey

Koreferent: ……………………………………………………………. PD Dr. Thor H. Hansteen

Tag der mündlichen Prüfung:……………………………………….............………16. Mai, 2014

Zum Druck genehmigt:………………………………..………..………………..16. Mai, 2014

Der Dekan

I

Hiermit erkläre ich, dass ich die vorliegende Doktorarbeit selbständig und ohne Zuhilfenahme unerlaubter Hilfsmittel erstellt habe. Sie stellt, abgesehen von der Beratung durch meinen Betreuer, nach Inhalt und Form meine eigene Arbeit dar.

Weder diese, noch eine ähnliche Arbeit wurde an einer anderen Abteilung oder Hochschule im Rahmen eines Prüfungsverfahrens vorgelegt, veröffentlicht oder zur Veröffentlichung vorgelegt.

Ferner versichere ich, dass die Arbeit unter Einhaltung der Regeln guter wissenschaftlicher Praxis der Deutschen Forschungsgemeinschaft entstanden ist.

Kiel, den 20. März, 2014

Froukje Marieke van der Zwan

Abstract

Hydrothermal circulation is an active process along the entire mid-ocean ridge system, which profoundly alters the composition of the oceanic crust, but also generates seafloor massive sulphide deposits and provides habitats for chemosynthetic living communities at e.g. black smoker vent fields. However, the exploration of these vent fields, particularly those that are presently inactive, is difficult. Also the depth extent of hydrothermal circulation is uncertain, which is important for mass and energy balances (e.g. the cooling) of newly formed oceanic crust. Hydrothermal activity can be traced by the chemistry of erupted mid-ocean ridge basalts, for which chlorine (Cl) is a key-element in tracing water-rock interactions. High-temperature alteration of the oceanic crust significantly increases its Cl content. Assimilation of these rocks by rising magma can increase the Cl in the magma, making Cl in basalts a potentially sensitive tool for tracing hydrothermal activity. Chemical thermobarometry of the same magmas can further give information on the depth extent of seawater penetration into the crust.

Assimilation of hydrothermally altered crust has been shown to occur at fast-spreading ridges (evidenced by Cl concentrations up to 1200 ppm), but the intrinsically lower Cl concentrations in basalts from slow-spreading ridges (~50-200 ppm), so far made the tracing of hydrothermal activity more arduous there, especially if Cl is measured by conventional methods. This thesis study aimed to examine the basaltic Cl concentrations and the processes of assimilation of hydrothermally altered crust at slow-spreading ridges by developing and applying an improved high-precision method for Cl measurements. A particular focus lies on the depth extent of hydrothermal circulation, if Cl can be used as an exploration tool for hydrothermalism, and what the differences in Cl contents are between various (ultra-) slow-spreading ridges.

To obtain high-precision Cl data, a new method was developed to measure chlorine in basaltic glasses by electron microprobe. This method applies mapping techniques and calibrates the raw data by standard-sample bracketing. Calibration of the method was performed by the use of minerals with fixed chlorine contents (0 and 16.6 wt.%) and compared to informational values of international standard reference materials, resulting in improved Cl concentration values for these standards. Special care was taken for an appropriate preparation and measurement procedure to avoid Cl contamination from the environmental background, including the mounting medium. This procedure involves cleaning by Milli-Q water, dry storage and a minimum sample thickness of 1 mm for the measurements. The new method can measure Cl at very low detection limits (<10 ppm) and with a long-term precision of 1-2 ppm standard deviation.

The high-precision Cl measurements were performed on basaltic glasses and melt inclusions from three slow-spreading ridges: the Southern Mid-Atlantic Ridge (SMAR) at 7-10 °S (spreading rate ~3 cm/yr), the Red Sea Rift at 16.5-26.5 °N (max. 1.6 cm/yr) and the Gakkel Ridge at 6 °W - 85 °E (max. 1.5 cm/yr). Chlorine contents of the basaltic glasses vary from 40 up to 400, 700 and 1300 ppm respectively, whereas SMAR melt inclusions range between 20 and 460 ppm. These Cl contents are generally higher than observed at other slow-spreading ridges. Moreover, small variations can be resolved by the new measurement technique and show that Cl concentrations in >75% of the samples are elevated relative to elements with similar mantle incompatibility (e.g. K, Nb). High Cl/Nb ratios are not the result of magmatic or seafloor Cl addition as is indicated by the homogeneous within-sample Cl concentrations, high Cl/K in melt inclusions, decoupling of Cl/Nb from other trace elements and the independence of Cl/Nb to the presence of highly saline seafloor brines at the site of eruption. Instead, Cl/Nb ratios that are higher than the mantle ratio of <26 (Red Sea, up to 420; SMAR, up to 62; Gakkel Ridge, up to 36) are interpreted to be the result of assimilation of hydrothermal fluids or hydrothermally altered crust. Assimilation of ocean crust is further supported by phenocryst disequilibrium textures and the abundant occurrence of xenocrysts and gabbroic fragments in the samples.

At all three ridges, hydrothermal vents sites or features associated with hydrothermal venting, are found to lie within 10 km of basaltic samples with high Cl/Nb meaning that basaltic Cl/Nb can probably be used as a tracer for the exploration of present or ancient hydrothermal vent fields. Based on this relation and Cl/Nb in basalts, sites of particular interest for future hydrothermal research in the Red Sea are the Thetis-Hadarba-Hatiba Deeps (specially their large axial domes), the northern Port Sudan Deep and the dome volcano in Mabahiss Deep. An important target for a now inactive hydrothermal vent field is an axial high on the SMAR A2 segment.

Earlier Cl studies strongly suggested a restricted depth for hydrothermal circulation, because slow-spreading ridge basalts with calculated crystallization depths of mostly >300 MPa apparently lacked any Cl addition. In contrast, pressures calculated here based on melt composition of basalts with high Cl/Nb display the full range of calculated crystallization pressures (15-750 MPa). The present thesis demonstrates that the glasses are typically not in equilibrium with all phenocrysts and that crustal assimilation, which may increase Cl, can further modify the major element composition of the magma leading to erroneous calculated pressures. Therefore, pressure calculations based on glass compositions alone are highly unreliable and cannot be used to determine the depth of Cl addition. Pressure calculations based on equilibrium Cpx-melt pairs give more robust pressures that indicate lower crustal crystallization (300-400 MPa). The Cpx-melt crystallization pressures together with petrographic and geochemical indications (e.g. melt inclusions with high Cl/K) for crustal assimilation in magma chambers combined with earlier petrologic and thermodynamic evidence for lower crustal melt-rock reactions and crystallization indicate assimilation of hydrothermally altered rocks in the lower crust to a depth of at least 10 km. Such assimilation depths imply that hydrothermal fluids circulate down to the lower crust at slow-spreading ridges, probably aided by extensive faulting there. Deep hydrothermal circulation removes one of the objections to the sheeted sill model for the formation of the lower oceanic crust at slow-spreading ridges - namely that these sills should be difficult to cool.

Although all three ridges display high Cl/Nb ratios in basalts, there is a variation in the degree of hydrothermal Cl addition between the ridges. The highest elevated Cl/Nb signals are found in samples in the proximity of evaporite outcrops (in the Red Sea) and/or bathymetric signs of volcanism on the seafloor. Trace-element-enriched magmas (with a higher primordial Cl) are less sensitive to Cl addition due to assimilation and have less elevated Cl/Nb. The spreading rate and the intensity of seafloor fracturing do not seem to play a role between slow-spreading ridges, but there is a difference to fast-spreading ridges. Cl/Nb at slow-spreading ridges is lower compared to fast-spreading ridges, likely due to the lack of large shallow magma chambers and a more localized and less intensive action of assimilation and hydrothermal circulation processes at depth.

Zusammenfassung

Hydrothermale Zirkulation, ein weit verbreiteter Prozess entlang der mittelozeanischen Rücken (MOR), verändert tiefgreifend die chemische Zusammensetzung der ozeanischen Kruste, bildet Massivsulfidlagerstätten und bietet Lebensräume für chemosynthetische Lebewesen z.B. an den 'Schwarze Raucher' genannten Hydrothermalquellen. Die Suche nach diesen submarinen Hydrothermalfeldern, besonders nach den gegenwärtig inaktiven, gestaltet sich jedoch meist als schwierig. Des weiteren ist die Tiefe der hydrothermalen Zirkulation in die Ozeankruste weitgehend unbekannt und verbirgt somit wichtige Informationen über mögliche Stoff- und Energiebilanz junger ozeanischer Kruste (z.B. deren Kühlung). Hydrothermale Zirkulation kann indirekt über die chemische Zusammensetzung von MOR Basalten nachgewiesen werden, wobei dem Element Chlor (Cl) eine Schlüsselfunktion zukommt, da Wasser-Gesteins Reaktionen und Hochtemperaturalteration den Cl Gehalt der ozeanischen Kruste deutlich erhöhen. Die Assimilation der so alterierten Krustengesteine durch aufsteigendes Magma erhöht dann auch die Cl-Konzentration des assimilierenden Magmas, was wiederum die Cl-Konzentration in eruptierten Basalten zu einem möglicherweise guten Anzeiger für die vorangegangene hydrothermale Aktivität macht. Methoden der chemischen Thermobarometrie können weitere Informationen über die tatsächliche Tiefe der Seewasserpenetration und hydrothermalen Zirkulation in der ozeanischen Kruste liefern.

Die Assimilation hydrothermal alterierter Kruste wurde für schnell spreizende Rücken bereits nachgewiesen (durch Cl-Konzentrationen von bis zu 1200 ppm) allerdings sind die Cl-Gehalte in Basalten von langsam spreizenden Rücken um ein Vielfaches geringer (~50-200 ppm), was bis jetzt den Nachweis hydrothermaler Aktivität an langsam spreizenden MOR anhand von Cl-Gehalten mit konventionellen Mitteln sehr erschwert. Die vorliegende Studie untersucht Cl-Konzentrationen in Basalten und Prozesse der magmatischen Assimilation hydrothermal alterierter Kruste an langsam spreizenden MOR. Dazu wurde eine neue Methode zur präzisen Messung von Cl entwickelt und angewandt. Der Fokus dieser Untersuchungen liegt im Wesentlichen in der Ermittlung der Tiefe hydrothermaler Zirkulation in ozeanischer Kruste, der Validierung der Möglichkeit basaltisches Cl als Explorationswerkzeug für Hydrothermalismus an langsam spreizenden Rücken zu nutzen, sowie der Untersuchung der Unterschiede von Cl-Konzentrationen in Basalten verschiedener (sehr) langsam spreizender MOR.

 Um hochpräzise Messungen von Cl-Konzentrationen zu erhalten wurde eine neue Methode zur Messung von Chlor in basaltischen Gläsern mittels der Elektronenmikrosonde entwickelt. Diese Messmethode basiert auf dem Prinzip der Elementkartierung und Proben wurde mittels der Standard-Probe-Standard Methode kalibriert. Die Kalibrierung dieser Methode wird mit Mineralien mit festen Chlor-Gehalten (0 Gew% und 16.6 Gew%) im Vergleich zu internationalen Standardreferenzmaterialien durchgeführt, was zu einer genaueren Bestimmung der Cl-Konzentrationen in diesen Standardmaterialien führte. Besondere Aufmerksamkeit galt der Entwicklung einer geeigneten Präparationstechnik um jegliche Kontamination des Probenmaterials durch Umgebungschlor und Chlor im Präparationsmedium weitestgehend auszuschließen. Die Prozedur schließt dabei u.a. gründliches Reinigen mit miliQ Wasser, trockene Lagerung sowie eine Minimumdicke der Probe von 1 mm für die Analyse ein. Diese neue Mikrosondenmethode ermöglicht Messungen von Cl bei sehr geringen Konzentrationen (<10ppm) mit einer dauerhaften Präzision von nur 1-2 ppm Standardabweichung.

Präzisionsmessungen von Cl wurden an basaltischen Gläsern und Schmelzeinschlüssen von drei langsam spreizenden MOR durchgeführt: dem Südlichen Mittelatlantischen Rücken (SMAR) bei 7-10°S (Spreizungsrate ~3 cm/yr), dem Roten Meer Rift zwischen 16.5-26.5°N (max. 1.6 cm/yr) und dem Gakkel Rücken zwischen 6°W-85°E (max. 1.5 cm/yr). Die Chlorgehalte in basaltischen Gläsern variieren jeweils zwischen 40 bis zu 400, 700 und 1300 ppm, während SMAR-Schmelzeinschüsse Cl-Konzentrationen von 20-460 ppm zeigen. Diese Cl-Konzentrationen sind generell höher als bislang für langsam spreizende Rücken berichtet. Darüber hinaus können mit der neuen Messmethode kleinere Variationen der Cl-Konzentrationen aufgelöst werden. Die Daten zeigen, dass Cl in >75% der Proben, im Vergleich zu Elementen mit vergleichbarer Mantelinkompatibilität (wie z.B. K, Nb),

angereichert ist. Die gemessenen, hohen Cl/Nb Verhältnisse sind aus folgenden Gründen nicht das Resultat von Cl-Zuführung durch magmatische Prozesse oder Ozeanbodenalteration: (I) wegen der homogenen Verteilung in den Proben, (II) der hohen Cl/K Werte in Schmelzeinschlüssen, (III) der Entkoppelung von Cl/Nb von anderen Spurenelementen und (IV) aufgrund der Unabhängigkeit von Cl/Nb von der Anwesenheit hochsalinarer Brines am Meeresboden. Stattdessen sind Cl/Nb Verhältnisse von >26 höher als die des Erdmantels (Rotes Meer bis zu 420, SMAR bis 62 und Gakkel Rücken bis 36) und das Resultat der magmatischen Assimilation von hydrothermalen Fluiden und/oder hydrothermal alterierter ozeanischer Kruste. Assimilation ozeanischer Kruste wird unterstützt durch die Präsenz von Phänokristallen mit Ungleichgewichtstexturen sowie dem reichlichen Vorkommen von Xenokristallen und gabbroischen Fragmenten in den untersuchten Proben.

An allen drei MOR wurden basaltische Proben mit hohen Cl/Nb innerhalb eines 10 km Radius um hydrothermale Felder oder in Bereichen mit Anzeichen hydrothermaler Aktivität gefunden, was darauf hinweist, dass das Cl/Nb Verhältnis möglicherweise als Anzeiger für rezente oder vergangene hydrothermale Aktivität dienen kann. Darauf basierend konnten als interessante Gebiete für die Suche nach Hydrothermalquellen im Roten Meer identifiziert werden: die Thetis-Hadarba-Hatiba Tiefs (besonders große axiale Domvulkane), das nördliche Port Sudan Tief und der Domvulkan im Mabahiss Tief. Ein sehr interessantes Explorationsziel für inaktive Hydrothermalfelder wäre demnach eine axiale Aufwölbung am SMAR Segment A2.

Frühere Cl-Studien wiesen eindringlich darauf hin, dass die Tiefe der hydrothermalen Zirkulation an langsam spreizenden MOR limitiert sei, da Basalte mit berechneten Kristallisationstiefen von >300 MPa keine Zunahme von Chlor zeigten. Im Gegensatz dazu zeigen die hier, auf Basis der Schmelzzusammensetzung, berechneten Drücke von Basalten mit hohen Cl/Nb Verhältnissen eine sehr hohe Bandbreite von Kristallisationsdrücken (15-750 MPa). Diese Arbeit zeigt, dass basaltische Gläser normalerweise nicht im Gleichgewicht mit allen Phänokristallen sind und dass magmatische Krustenassimilation, die möglicherweise auch Cl-Konzentrationen erhöht, die Hauptelementzusammensetzung so modifiziert, dass etwaige Druckberechnungen zu fehlerhaften Ergebnissen führen. Daher sind Druckberechnungen, die allein auf der Zusammensetzung basaltischer Gläser basieren, sehr unzuverlässig und für die Ermittlung der Tiefe der Cl-Zuführung ungeeignet. Druckberechnungen auf der Basis von Klinopyroxen-Schmelze-Gleichgewichten ergeben dagegen stabilere Ergebnisse und deuten auf Kristallisationstiefen in der unteren ozeanischen Kruste (300-400 MPa). Die Kristallisationstiefen, basierend auf Klinopyroxen und Befunde für magmatische Krustenassimilation (z.B. Schmelzeinschlüsse mit hohen Cl/Nb Verhältnissen) indizieren - in Kombination mit früheren petrologisch-thermodynamischen Indikationen für tiefe Schmelze-Gesteins Interaktion und Kristallisation – die magmatische Assimilation von hydrothermal alterierten Gesteinen in der unteren ozeanischen Kruste bis in Tiefen von mindestens 10 km. Diese Assimilationstiefen deuten darauf hin, dass hydrothermale Fluide an langsam spreizenden Rücken bis in die untere Kruste zirkulieren können - möglicherweise begünstigt durch komplexe und tief reichende Störungen. Die Möglichkeit solch tiefer hydrothermaler Zirkulation beseitigt auch eine Schwäche des sog. „Sheeted Sill" Models für die Bildung ozeanischer Kruste, namentlich dass die Sills schwerlich zu kühlen sind.

Auch wenn alle drei untersuchten MOR Basalte mit hohen Cl/Nb Verhältnisse zeigen, gibt es doch Variationen im Grad der Cl-Anreicherung zwischen den MOR. Die höchsten Cl/Nb Anreicherungen wurden in Proben in unmittelbarer Nähe zu submarinen Evaporiten (im Roten Meer) bzw. bathymetrischen Indikatoren für ausgeprägten Vulkanismus am Meeresboden gefunden. Magmas mit Spurenelementanreicherungen (mit höheren ursprünglichen Cl Konzentrationen) reagieren weniger sensibel auf Cl-Anreicherung und zeigen dementsprechend geringere Zunahme in Cl/Nb. Spreizungsraten und der Grad der Tektonik scheinen bei langsam spreizenden MOR keine wesentliche Rolle zu spielen. Dennoch gibt es Unterschiede zu schnell spreizenden MOR. Im Vergleich zu schnell spreizenden Rücken sind die Cl/Nb Werte von langsam spreizenden MOR wesentlich geringer, was wahrscheinlich am Fehlen großer, flacher Magmenkammern und einer eher lokalen, weniger intensiven hydrothermalen Zirkulation und magmatischer Assimilation in größeren Tiefen liegt.

Contents

x

Preface

This thesis consists of three independent but thematically related chapters that comprise one published paper and two finished manuscripts, bracketed by introduction and conclusion chapters.

The introduction describes the framework and the objectives of the thesis. Chapters 2 to 4 represent the respective manuscripts and therefore each has an own introduction and conclusions. Each chapter also has its own figure, table and section numbers. A reference list for all chapters is followed at the end. Chapter 2 describes the development of a new method to measure chlorine, including the preparation and calibration of this method. This paper was published in *Journal of Analytical Atomic Spectrometry* (van der Zwan et al., 2012) and has its own page numbers and reference list. Chapter 3 covers chlorine measurements together with other compositional data measured on basalts of the Red Sea Rift and discusses the process of assimilation of hydrothermally altered crust and how chlorine can be used as a tracer for hydrothermal activity. This manuscript is currently under review in *Geochimica et Cosmochimica Acta*. Chapter 4 compares chlorine and other chemical data on basalts from the Southern Mid-Atlantic Ridge and the Gakkel Ridge to data from the Red Sea, and examines the depth of hydrothermal circulation and the factors influencing chlorine concentrations. This manuscript is in preparation to be submitted to *Contributions to Mineralogy and Petrology*. Chapter 5 concludes with the most important findings and implications from this thesis.

This thesis study was performed within the framework of the Jeddah Transect Project between the King Abdulaziz University and GEOMAR Helmholtz-Center for Ocean Research.

Chapter 1:

Introduction

1 Hydrothermal circulation at slow-spreading ridges

Hydrothermal circulation of seawater driven by the magmatic heat of the young oceanic lithosphere is an important process at all mid-ocean ridges. At the seafloor, hydrothermal activity is expressed as diffuse (low temperature) or focused (high temperature) venting of fluids that can create (black) smoker fields, which may form habitats for chemosynthetic communities. Interaction of seawater with hot magma and rocks of the new oceanic crust leads to a metal enrichment in the fluids that upon cooling can build economically interesting seafloor massive sulphide deposits.

Hydrothermal vent fields are found at all mid-ocean ridges, but the abundance of high-temperature hydrothermalism appears to increase with spreading rate (e.g. Baker and German, 2004; Hannington et al., 2011). The largest hydrothermal ore deposits are, however, found at slow-spreading ridges (e.g. Fouquet, 1997) that are thus most attractive from an economic point of view. At present, active high-temperature fields are mostly found by the detection of their emanations in the overlying water column. However, the search for hydrothermal fields is a difficult and time-consuming process, particularly due to the scarcity of detailed maps of the ocean floor. The discovery of extinct hydrothermal fields, which are economically most interesting for potential mining as they do not host fragile marine life, is at best extremely challenging.

Apart from its economical and biological relevance, hydrothermal circulation and the depth to which this is active, is important for the cooling of the oceanic crust (e.g. Maclennan et al., 2005; Hasenclever et al., 2014). Convective cooling by fluid circulation enhances crystallisation and can, therefore, aid in particularly the formation of the lower crust. Two endmember models were developed, mostly for fast-spreading ridges (>5.5 cm/yr), regarding the formation of the lower crust based on different assumptions on the depth of hydrothermal circulation (Maclennan et al., 2005; VanTongeren et al., 2008). The gabbro glacier model assumes mainly shallow hydrothermal activity (Nicolas et al., 1988; Henstock et al., 1993; Morgan and Chen, 1993; Quick and Denlinger, 1993; Chen, 2001; Coogan et al., 2002b), while the sheeted sill model, requires deep cooling by hydrothermal circulation (Kelemen et al., 1997; Korenaga and Kelemen, 1997; Kelemen and Aharonov, 1998; Lissenberg et al., 2004).

Studies of ophiolites and oceanic drill sections at fast-spreading ridges show high temperature alteration of the lower crust by hydrothermal fluids (Gregory and Taylor, 1981; McCulloch et al., 1981; Stakes and Vanko, 1986; Nehlig and Juteau, 1988; Nehlig et al., 1994; Lecuyer and Reynard, 1996; Kawahata et al., 2001; Coogan, 2003; Nicolas et al., 2003; Bosch et al., 2004; Koepke et al., 2011), consistent with constant calculated cooling rates as a function of depth, indicating deep hydrothermal cooling (e.g. VanTongeren et al., 2008). Deep hydrothermal circulation next to magma chambers is further suggested by seismic evidence (Dunn et al., 2000), thermodynamic models (Cherkaoui et al., 2003; Maclennan et al., 2005; Hasenclever et al., 2014) and models of microfracturing that allow fluids to penetrate into hotter ductile crustal areas (above ~700°C up to 1000°C (Lister, 1974; Manning et al., 2000; Nicolas et al., 2003; Koepke et al., 2005)).

Information on the depth of hydrothermal circulation at ultraslow- and slow-spreading rifts (<5.5 cm/yr) is more restricted. Ultraslow- and slow-spreading rifts are formed not only by magmatic processes, but also by significant amounts of nonmagmatic seafloor generation and tectonic spreading (e.g. Dick et al., 2003; Cannat et al., 2006). Hydrothermal fluids can potentially penetrate and cool the oceanic crust deeper, due to the lack of permanent magma chambers and the lower temperatures of slow-spreading ridges (e.g. Harper, 1985; Detrick et al., 1990) that enables faulting to be more extensive and deeper and due to the existence of large normal faults (Harper, 1985; Cannat et al., 1991; Mével and Cannat, 1991; Stakes et al., 1991). P-wave tomography at the TAG hydrothermal field (Zhao et al., 2012) demonstrates hydrothermal circulation to at least 2 km, but potentially to 3½ km depth. Subsurface high-temperature alteration has been found in a few drill cores that have, however, a limited depth extent (<1600 m; e.g. Dick et al., 2000; Alt and Bach, 2006) and in tectonically exposed parts on the lower crust (Gillis et al., 1993) which have thus been exposed to seawater for extended

periods of time. But little direct evidence is available on hydrothermal alteration in the deeper parts of the crust at slow-spreading ridges and there is presently no consensus on the extent and maximum depth of hydrothermal circulation (e.g. Mottl, 2003).

2 Chlorine as a tracer for hydrothermal circulation

Evidence from fast-spreading ridges shows that hydrothermal activity and high-temperature alteration of the oceanic crust can indirectly be traced by the chemistry of mid-ocean ridge basalts (MORB) for which chlorine (Cl) is specifically indicative. Seawater entering the oceanic crust can increase its Cl content by hydrothermal alteration (Barnes and Cisneros, 2012), due to the vastly different Cl concentration of seawater (1.9 wt.%) and basaltic magma (generally <500 ppm; Michael and Schilling, 1989; Michael and Cornell, 1998). Assimilation of a hydrothermally altered crust or hydrothermal fluids by magma can consequently increase the Cl content of this magma that later can be recovered as basalt from the seafloor (Fig. 1; Michael and Schilling, 1989; Coogan et al., 2002a; Gillis et al., 2003). Models from fast-spreading ridges indicate that assimilation and Cl addition takes place by stoping in the interaction zone between the hydrothermal cell and magma at the roof of (shallow) axial magma chambers (Coogan et al., 2002a; Gillis et al., 2003; le Roux et al., 2006; France et al., 2009; France et al., 2010; Kendrick et al., 2013).

Chlorine addition due to interaction of basalts with hydrothermal fluids was previously identified at fast-spreading mid-ocean ridges (e.g. Michael and Schilling, 1989; Gillis et al., 2003), in ophiolites (Coogan et al., 2002a; Coogan, 2003), at back-arc basins (Kent et al., 2002; Sun et al., 2007), as well as in ocean island basalts (Kent et al., 1999a; Kent et al., 1999b).
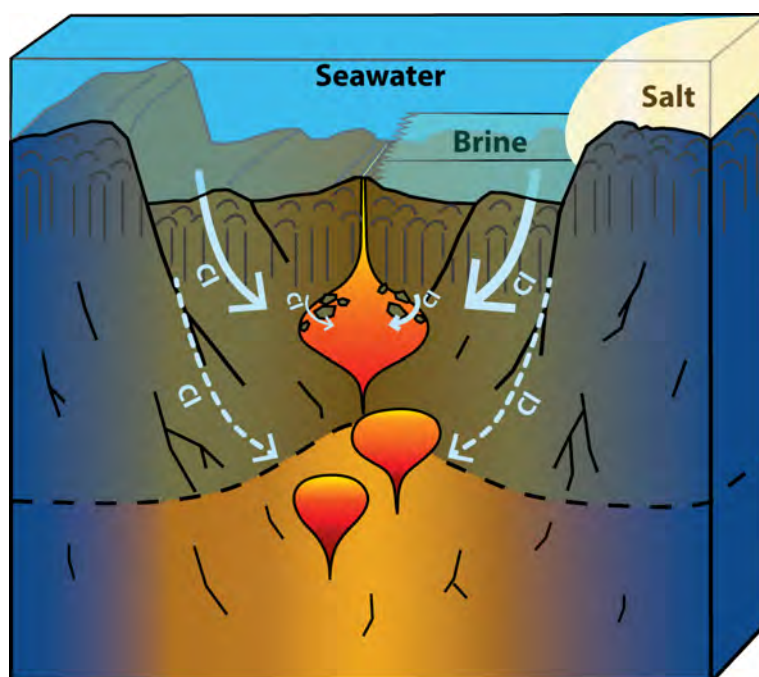
Fig. 1 – Schematic model of Cl addition by hydrothermal alteration and assimilation of this hydrothermally altered crust. Hydrothermal fluids from brines and evaporites at the surface have a higher potential to increase Cl.

In contrast, Cl concentrations of basalts from (ultra) slow-spreading ridges are generally lower (Cl ~50-200 ppm) and - apart from a few rifts with thick crust - no Cl addition was found (Michael and Cornell, 1998). This apparent lack of Cl addition was interpreted as an absence of assimilation of hydrothermally altered crust at slow-spreading ridges due to their on average much higher calculated crystallisation pressures (>300 MPa) when compared to fast-spreading ridges (Michael and Cornell, 1998). Michael and Cornell (1998) concluded that magma at slow-spreading ridges generally cools deeper (>3 kbar) than the maximum presumed depth of hydrothermal penetration (e.g. 6 km in the Oman ophiolite; Gregory and Taylor, 1981) and that hydrothermal circulation (at least at slow-spreading ridges) must occur shallow.

3 Objectives of this study

To date, studies of Cl in basalts measured by conventional microprobe methods have suffered from relatively large analytical uncertainties (15-20 ppm) and consequently high detection limits (Michael and Schilling, 1989; Jambon et al., 1995; Michael and Cornell, 1998). Small variations in the intrinsically low Cl concentrations of slow-spreading MORB that can reveal seawater-magma interaction could, therefore, not be resolved. Hence, the conclusion that assimilation of hydrothermally altered crust is not occurring at slow-spreading ridges might be the result of previous analytical uncertainties.

Based on the challenge to locate hydrothermal fields at slow-spreading ridges and in order to understand to which depth hydrothermal circulation plays a role in the cooling and formation of the crust, Cl studies at slow-spreading ridges are of interest. Because hydrothermal alteration leaves a chemical signature as a Cl contamination of the crust, assimilation of hydrothermally altered crust generates magmatic markers of present and past hydrothermal circulation and Cl contents can be used as a prospecting method for identifying past and present hydrothermal sites. Furthermore, by the use of petrologic arguments to establish at which depth Cl contaminated magma last crystallised, the minimum depth of assimilation and hydrothermal circulation can be determined. Therefore, this study was developed to investigate in detail Cl enrichment compared to e.g. K or Nb, due to assimilation of hydrothermally altered crust at slow-spreading ridges. The aim hereby was to resolve the following main questions:
1) How can Cl concentrations in basaltic glasses be measured with high precision (<2 ppm standard deviation) and low detection limits?
2) Is assimilation of hydrothermally altered crust and a resulting increase in Cl in basalts taking place at slow-spreading ridges?
3) Can Cl contents in basalts be used at slow-spreading ridges to predict where hydrothermal activity is most pronounced and where hydrothermal vent fields may be found?
4) What is the effect of rift morphology, fault intensity, volcanic activity and spreading rate on hydrothermal Cl addition?
5) What is the depth of hydrothermal circulation at slow-spreading ridges and what is the relation between Cl addition and last equilibrium crystallisation pressures?

To answer these questions, first a new method to measure Cl in basalts with high precision and accuracy was developed on the electron microprobe, since the microprobe is widely available and based on well-known physical principles. Together with an improvement of the measurement technique, the preparation procedure was optimized to avoid Cl contamination and the method was calibrated with international standards (see chapter 2).
The developed method was subsequently applied to basaltic glasses from three selected (ultra) slow-spreading ridges and studied together with major and trace elements and H_2O and CO_2 contents (see chapter 3 and 4). These ridges are:

A. The Red Sea Rift (10 – 16 mm/yr) has a relatively high seawater salinity (40 - 42‰ compared to 34.5‰ for average ocean water) and the presence of (hot) saline brine pools in several within-axis topographical 'Deeps' (Pierret et al., 2001) and thick evaporite sequences on the flanks of the active rift (e.g. Whitmarsh et al., 1974; Mitchell et al., 2010) that all have a high potential to increase magmatic Cl concentrations upon interaction (Fig. 1). The Red Sea Rift is therefore an extremely suitable place to test if Cl is added to basalts by interaction with hydrothermal fluids at slow-spreading ridges. Furthermore, no active hydrothermal fields have been imaged so far from the Red Sea and only three (inaccessible) inferred hydrothermal systems are known (e.g. Pierret et al., 2001; Gurvich, 2006; Swift et al., 2012). The use of Cl to predict where hydrothermal vents could be found would be, therefore, very valuable for this place (see chapter 3).

B. The southern Mid-Atlantic Ridge (SMAR) at 7-10 °S (~3 cm/yr) was selected as it has a varying crustal thickness, known hydrothermal fields, and contains both depleted and trace element enriched MORB (e.g. Möller, 2002; Hoernle et al., 2011), which show a range of crystallisation pressures (0-800 MPa; Almeev et al., 2008).

C. The arctic Gakkel Ridge at 6°W - 85°E (max. 1.5 cm/yr) was chosen because of its strongly tectonic character and very thin crust that has a large potential to form fluid pathways (Coakley and Cochran, 1998; Dick et al., 2003; Michael et al., 2003; see chapter 4).

In chapter 3, the relation between hydrothermal Cl addition and geological factors is closer examined in the Red Sea, by a comparison of the chemistry of the basalts to new high-resolution bathymetric maps of the Red Sea (Augustin et al., in review). To study the depth of Cl addition in more detail Cl measurements were, additionally to the glasses, performed on melt inclusions in minerals from the SMAR basalts (see chapter 4). Data from all three ridges were used to investigate how the differences between the ridges and MORB compositions affect Cl addition due to assimilation of hydrothermally altered crust (see chapter 4).

Chapter 2:

Precise measurement of low (<100 ppm) chlorine concentrations in submarine basaltic glass by electron microprobe

This chapter contains a publication in *Journal of Analytical Atomic Spectrometry* (2012) in its original form.

Authors:
FROUKJE M. VAN DER ZWAN, JAN FIETZKE AND COLIN W. DEVEY

Geomar Helmholtz Centre for Ocean Research Kiel, Germany

PAPER

Precise measurement of low (<100 ppm) chlorine concentrations in submarine basaltic glass by electron microprobe

Froukje M. van der Zwan,* Jan Fietzke and Colin W. Devey

There is a 2–3 order of magnitude difference between the chlorine concentrations of seawater and the magmas making up the oceanic crust. For this reason, chlorine is a key element for tracing present and past water–rock interactions. In order to trace processes such as assimilation of hydrothermally altered oceanic crust by mid-ocean ridge magmas, a high precision method with low detection limits is required, since conventional methods are not able to reveal variations in the intrinsically low chlorine content of these basalts. We present a new method to measure chlorine in basaltic glass by electron microprobe, using a combination of mapping and standard-sample bracketing techniques. Due to the high environmental background of chlorine, special emphasis is put on the influence of different preparation and cleaning procedures, as well as other possible effects on the measurements (*e.g.* sample size). Calibration of the method is performed by informational values of international standards and by minerals with a fixed chlorine content. Finally, new information on chlorine concentration values for commonly used standard reference materials (SRM) is provided. With this new method chlorine can be measured at very low detection limits (10's of ppm's) with a precision of 1–2 ppm standard deviation for low chlorine concentrations.

1 Introduction

In geochemistry usually a large set of elements (*e.g.*, the rare-earth elements) is used together to solve earth scientific problems. Nevertheless, some elements are specifically indicative of certain processes. Chlorine (Cl) is one such element, and its concentrations can be key in tracing present and past interaction between seawater and magmas and rocks of the oceanic crust, due to the high concentration of chlorine in seawater (1.9 wt%) compared to the low concentration (generally <500 ppm) in basaltic magma.[1,2] Consequently, seawater entering the oceanic crust can increase the chlorine content of the crust by hydrothermal alteration. Subsequent assimilation of this crust by rising magma can significantly increase the chlorine content of this basaltic magma that later can be recovered as basaltic rocks from the seafloor.[1,3,4] If we can use petrologic arguments to determine at which depth this assimilation took place, we can determine important information about the depth of seawater penetration into the crust – important for both mass and energy balances of the plate production process. Recycling of this altered crust by plate tectonic subduction can result in Cl anomalies in the mantle.

To date, studies of Cl in submarine basalts have been restricted to magmas with intrinsically high Cl concentrations or have accepted relatively large error margins.[1,3–5] Details of seawater–magma interaction in lower concentration samples could,

Geomar | Helmholtz Centre for Ocean Research, Kiel, Germany. E-mail: fzwan@geomar.de

therefore, not be explored with conventional (microprobe) methods due to their excessive analytical uncertainty (15–20 ppm[1,2,6]) and consequently high detection limit. A further problem with conventional microprobe methods is that calibration is often performed on standards with a much higher chlorine content than the samples that are to be measured (*e.g.* >1 wt% compared to <200 ppm for the basalts), and proof of linearity in the detector response over this concentration interval is lacking.

Apart from electron microprobe, there are several other methods that have been applied for measuring chlorine concentrations: (LA)-ICPMS, PIXE, INAA and SIMS,[7] or extraction by pyrohydrolysis in combination with TIMS[8] or ICPMS.[9] Some of these methods are not widely available or involve extensive sample preparation and so are not conducive to being used on a large suite of samples. For others, there are major concerns about the accuracy and precision. Also, when comparing results obtained by these different methods for the SRM "MPI-DING" glasses[7,10] there are large discrepancies between the results obtained by the different methods, *e.g.* the GeoReM database shows results for the ATHO-G SRM glass varying from 2 ppm for SIMS, 380 ppm for PIXE and between 320 and 600 ppm for EMP (see also Table 4). The differences between the results for the different methods show no clear systematics. Based on these data it is difficult to assess which is the most reliable method for determining Cl concentrations. Therefore we chose to attempt to develop a method with appropriate detection limits and precision for our aims using an analytical technique (the electron microprobe, EMP), which is based on basic physical principles, since it

makes use of element-specific X-ray emission after excitation by an electron beam. Additionally, of all the methods available for measuring Cl concentrations, the EMP is one of the most easily available around the world, and measurements can be obtained at relatively low cost. A significant improvement in the quality of EMP Cl measurement methods would therefore be a useful analytical achievement.

Our new analytical procedure enables us to reveal variations that could not be resolved before, which may be highly beneficial for the study of chlorine mid-ocean ridge basalts with lower Cl concentrations. In order to obtain accurate and precise values for low concentration chlorine samples, not only was the measurement technique of samples improved, but also the preparation of samples was evaluated to avoid contamination. Calibration of the samples was performed with international standards, which were re-evaluated, leading to new informational values proposed here.

2 Experimental

2.1 Preparation of samples

When analysing low concentrations of chlorine, it is crucial that samples do not get contaminated during preparation. Contamination of chlorine is a considerable possibility, since chlorine is present in appreciable concentrations in air, water and many materials/liquids that are used in regular microprobe preparation, not to mention in the operators themselves. All these are potential sources for chlorine contamination and thus a standardized, clean working procedure is required. Different sample preparation procedures were tested to determine the major sources of contamination.

Initially, the regular local preparation for microprobe samples was applied; this implies that pieces of volcanic glass >2 mm across were hand-picked and embedded in a ring with epoxy resin (Araldite 2020 (XW396/XW397)). All glasses were selected under a binocular microscope based on their fresh appearance and lack of visible vesicles, rims, inclusions or minerals. The complete sample mount was subsequently polished using increasingly fine-grained corundum and diamond grinding powder and cleaned between each grain-size change with demineralised water and dried with compressed air. The sample mount was finally cleaned with alcohol prior to carbon coating of the sample and before entering the microprobe with compressed air again.

In procedure 2 the samples were not cleaned with alcohol or compressed air, since both are potential sources of chlorine. We instead attempted to use demineralised (DeMi) water as a final cleaning step to wash off any chlorine that might have got onto the samples during polishing. To avoid any new chlorine contamination from the air (including compressed air) after cleaning, the samples were dried and stored in a desiccator with P_2O_5 as desiccant. We limited the time the sample spent outside the desiccator (for carbon coating and mounting of the samples in the sample holder, for example) as far as possible.

Procedure 3 consisted of the same steps as the second procedure. In addition, a set of dedicated polishing plates was acquired for the chlorine work to eliminate the possibility of cross-contamination by high chlorine samples during polishing. More importantly, the samples were cleaned extensively with Milli-Q water after polishing. This washing was carried out in a laboratory with good air filtration and where no use was made of hydrochloric acid for other analytical purposes. Finally, the time between final cleaning with Milli-Q water and carbon coating of the sample was kept as short as possible ($\sim$2 hours to dry the samples under vacuum).

With procedure 4 we tested the effect of using epoxy as a mounting material. Epoxy can be a potential contaminant because of its high chlorine concentration. Epoxy, if it became smeared over the sample surface during polishing, could not easily be removed by water. For this potential problem, a final surface cleaning was introduced, using an ESI New Wave Research "UP193FX" laser, with the sample placed in a sealed large format cell (LFC) sample chamber flushed with He (0.7 l m^{-1}). Grains were cleaned by scanning the surface with a laser fluence of 0.12 J cm^{-2}. Lines were scanned at 80 μm distance with a scan speed of 50 μm s^{-1}, a repetition rate of 10 Hz and a spot diameter of 100 μm. This intensity does not damage the glass surface, but, when aimed at the surrounding epoxy, it visually vapourized it, leading us to conclude that any epoxy present on the glass should be removed with this cleaning. The effect and requirements of this cleaning were tested by repeating 1, 20 or 100 times on different areas that were measured afterwards by microprobe. Laser cleaning was tested on a low, middle and high chlorine concentration sample ($\sim$60, 100 and 180 ppm respectively) and on 2 samples of pure silicon (<25 ppm). Additionally, a line was ablated on the high chlorine sample with a 3 J cm^{-2} fluence, a spot diameter of 20 μm, a scan speed of 20 μm s^{-1} and a repetition rate of 20 Hz, in order to determine if there was any chlorine loss due to the laser cleaning.

Several alternative mounting materials (polyester (Viapal UP 223 BS/65), pure indium and dental amalgam) were also tested for their chlorine content (for details see the discussion of sample preparation in Section 3.2).

2.2 Electron microprobe settings

2.2.1 Spot analyses tests. Chlorine measurements were made with a Jeol JXA-8200 "Superprobe" electron microprobe at GEOMAR using an acceleration voltage of 15 kV. Five spectrometers are available for simultaneous wavelength-dispersive X-ray analysis, of which two are equipped with PETH crystals suitable for analysing the chlorine signal. For the first tests several setups were applied, using the regular spot analyses, including varying beam current (30, 50, 80 and 100 nA; after a test of beam current stability over the measurement time), beam size (5, 20 and 30 μm) and measurement times (60 and 120 s). Calibration of the measurements was done using Smithsonian Standard NMNH R6600 (Scapolite; 1.43 wt% Cl).[11] The tests were performed on two unknown samples with average values (according to these measurements) of 64 ± 23 and 370 ± 28 ppm (2SD, $n = 45$). These results indicate the major drawback of the measurements that, depending on the settings, the results of measurements vary, which leads to poor reproducibility and which limits the accuracy of the measurements. For individual settings, 2SD vary between 11 and 40 ppm, a precision that is not sufficient for the concentration range considered here for basalts even with the settings that give the most reproducible results (in these tests, 80 nA, 5 μm, 120 s).

Consequently, we attempted to improve the beam settings and counting times further, based on these first test measurements. From considerations of counting statistics, it is required to obtain as many net counts as possible to improve the precision of the method, without damaging the sample/coating. Upon increasing the beam current the influence of the background signal becomes lower as the signal/background ratio increases and the precision should improve. This implies that for the measurement the highest possible current should be used. However, a second test measurement of 120 seconds on a spot already measured with a current of 100 nA gave significantly lower values, implying chlorine loss potentially due to heating of the sample. This was not observed for a beam current of 80 nA; therefore we concluded that improvement in the method by increasing the beam current is limited by chlorine loss and a maximum of 80 nA should be used.

In contrast to increasing the beam current, a slightly higher energy density of the beam is obtained by the smaller beam size and hence results in higher net counts. However, the minimum size is also limited, in this case by the material of the sample, since a focused beam will damage the basaltic glass and its carbon coating in the case of high applied currents and long measurement times. Although it is possible to apply a beam size of 5 μm, this did not significantly improve the test measurements and the risk of damage is severe. Therefore, we selected a defocused spot size of 10 μm for a better balance between spot size, applied energy and measurement time.

The largest increase in obtaining more net counts and hence improving precision can be achieved by increasing the measurement time (in the test measurements the 2SD improves from 26 ppm to 19 ppm on average in different beam settings when time is increased from 60 s to 120 s). However, measurements for a long time at the same spot might also cause damage of the sample/coating, as well as potential chlorine loss due to the heat produced. In order to solve this we investigated the effectiveness of the scanning analysis setting ("mapping") when compared to the spot analysis setting.

2.2.2 Mapping analyses. Mapping was performed with the EMP over a square area of 100 × 100 μm with a point size of 10 μm (same as the beam size) and a scan speed of 2 s/10 μm (by mechanical movement of the sample mount), *i.e.* an integration time (dwell time) of 2 seconds per point. Therefore the total measurement time for chlorine is 200 seconds, which might damage the sample when applied with spot analyses, particularly when smaller beam sizes are applied. In addition, mapping over a larger area gives a better average of the sample

and a single measurement will not likely be influenced by small heterogeneities. Chlorine was measured simultaneously on spectrometers 2 and 5 (PETH crystals) in order to double the total counts. On spectrometers 1, 3 and 4, the major elements aluminium, potassium and calcium were measured with TAPH, PETJ and PETJ crystals respectively. Measuring major elements simultaneously with chlorine gives a better control over any optically hidden minerals, inclusions, vesicles or errors during the measurements.

Each measurement of an area can be repeated in order to increase time further for a better counting statistic and, thus, better precision. After test measurements with different repetitions we found that 9 repetitions gave a good compromise between measurement time and sufficient counts to give a ~2 ppm precision of the measurements from counting statistics. The effect of multiple repetitions on a sample and potential chlorine loss was tested in a session in which for each sample first 1, then 3, 3, 9 and 3 repetitions were measured on the same area. Since the 3 repetitions before and after the 9 repetitions always gave the same average counts, we conclude that 9 repetitions do not appear to lead to chlorine loss.

From each mapped area the raw counts of the maps were manually evaluated, together with the contemporaneously measured major elements, to establish if the area was homogeneous or if there were any deviations or outliers (that can be seen in all elements). In addition, the compositional maps are cross-checked with photographs of the measured areas to assess if there are visual deviations in the sample or the polishing (even though the optically most homogenous places were selected for each measurement) and if the carbon coating has remained intact, since a broken coating is a possibility with the high applied beam currents. After correcting, the averages of spectrometers 2 and 5 for chlorine were summed up.

Calibration of the samples (*i.e.* calculating the raw counts to concentrations) and correction of slightly different measurement conditions and machine drift are done by a sample-standard bracketing correction method as often applied in ICP-MS measurements, where the concentration of a sample is calculated with the aid of the raw counts and known concentrations of two standards that are measured before and after a sample. Ideally these standards are at the high and low end of the expected concentration range (in this case, around 50 and 400 ppm), potentially aided by a standard in the middle concentration range (~150 ppm). Taking this method as a fundamental, there are however different possible techniques of measuring (Table 1):

Technique 1: for each sample/standard, the nine repetitions are measured continuously in one measurement followed by the next

Table 1 Comparison of precision for different mapping and calibration techniques assessed in this study. # is the number of samples from which the average SD was taken and *n* is the number of measurements for each sample

| Technique | Content | | Average SD | # of samples for average | *n* per sample |
	Repetition style	Std used for calibration			
Spot analyses	n.a.		13	2	45
Mapping					
1	9 repetitions in a row	Bracketing std	3.5	26	2–3
2	9 × 1 repetition	Bracketing std	2.8	42	2–3
3	9 × 1 repetition	Session average of std	1.6	42	2–3

12

sample/standard (*i.e.* the sequence is 9× standard – 9× sample – 9× standard, *etc.*). Since in this way the measurements take a long time (∼35 min), a high and low standard should be measured before and after each of the two samples (one hour of measurement time) in order to be able to correct for machine drift. Therefore relatively many standards are measured in between the samples, which makes the overall measurement time relatively long.

Technique 2: each area is measured with 9 repetitions, however, these are not measured directly after each other, instead a complete measurement series is measured for one repetition before continuing with the next repetition (*i.e.* the sequence is 9× standard – sample – standard, *etc.*). In this case variations that occur due to machine drift are levelled out over time by later repetitions. This assures that there are fewer variations between the samples due to machine drift within one measurement session. In addition, the measurement times are shorter for one repetition of one sample (∼4 min); therefore, it is possible to measure more samples in between the standards, without significant machine drift. Hence fewer standards are required, decreasing the overall measurement time. For calculating the concentrations, from every mapped area the raw counts of each of the 9 repetitions were taken and integrated together for every single measured point. Those can subsequently be evaluated as in Technique 1.

Technique 3: the samples/standards are measured in the same manner as Technique 2; however, the calculation of the concentrations from the raw counts with the aid of the standards is done differently. In contrast to a common sample–standard bracketing, the concentration of a sample is not calculated with only the four neighbouring standard measurements (2 high, 2 low). This way can potentially introduce errors in the case of small inhomogeneities in the standards or due to statistical variation. A small deviation in a standard analysis might introduce a larger variation in the calculated concentration of the related samples than is actually present. Therefore, the average counts of the different measurements for each standard measured during a session might give more representative results. The standards are measured in between the samples, similar to the previous techniques and at least 15 measurements of each standard in one measurement session. This technique can be justified if there is no large machine drift between the different measurements within one session, which is likely because of the short measurement time between standard measurements and due to the spreading of the 9 repetitions, *i.e.* any systematic machine drift will be counterbalanced by later repetitions of the same spot. This technique also gives the opportunity to carefully evaluate all resulting counts of the measured standards and evaluate the data for outliers or any inhomogeneities. If needed, those points can be discarded from the average. With the average counts for the standards and the known concentration of the standards the concentrations of the samples are calculated from the measured counts. For a better control over the used standards, a standard of middle concentration can be added, although that was not done in these first tests, to better compare the results of the different techniques. Technique 3 can also be more time saving, since only a statistically sufficient amount of standards is required, which means that if more samples than normal are measured

together with these 15 standards, it is not required to add additional standards.

3 Results and discussion

3.1 Mapping analyses

For all three technique tests, measurements were done on a set of samples from the southern Mid-Atlantic Ridge at 7–10 degrees south.[12,13] According to preliminary spot analyses (with non-optimised settings of 30 nA, 5 μm and 30 s) these samples have chlorine concentration between 60 and 400 ppm (± on average 26 ppm 2SD). In all test measurements the samples were calibrated with MPI-DING glass standard ML3B-G (with a concentration of 54.7 ppm based on our own calibration of this standard, see Section 4) and Smithsonian glass standard NMNH 111240-52 (329.1 ppm based on our calibration). For the preparation of samples the regular procedure for microprobe samples was used (procedure 1). Although this might give an overall contamination of the samples and hence inaccurate true values, this does not affect the reproducibility for sample measurements that are measured within one measurement session, as was applied for the method tests. To compare the different techniques, for each method various samples were measured 2 or 3 times and the standard deviations of those measurements were calculated. In Table 1 the average standard deviation of those samples is presented, with # the number of samples from which this average was taken and *n* the number of measurements for each sample.

All techniques show a significant improvement compared to the spot analyses measurements of the same sample set. While for the routine spot measurement the standard deviation reproducibility was about 13 ppm, the mapping gives a standard deviation of <3.5 ppm reproducibility (Table 1). Due to this, much more variation between samples can be observed, and lower concentrations can be measured than was possible with the spot analyses. An enhanced average reproducibility of 2.8 ppm SD for technique 2, compared to 3.5 ppm for Technique 1, demonstrates that the method improves further when the 9 repetitions for a sample are not measured in a row, but rather by measuring all samples for one repetition and then for the next. This implies that the method is significantly improved when an internal correction for machine drift is applied. Finally, the 3rd technique shows with an improved average SD of 1.6 ppm that the influence of the uncertainties of individual standard runs is higher than the machine drift. Hence for the calibration of the samples, higher precision is obtained by relating all data to the session averages of the standards, rather than to the neighbouring standards. In addition, small heterogeneities in the standards can be excluded in this method.

Based on these results, the 3rd technique is determined to be the best measurement technique both in terms of analytical precision and machine time use. This technique proved itself to be reproducible over various measurement sessions (for samples with the same polishing that were properly stored) even when there were changes to the microprobe in the meantime (*e.g.* filament change, spectrometer repair, re-establishing of vacuum). Therefore, this is subsequently used in the measurements to test the preparation procedures. A final improvement was to add a 3rd standard to have a better control of the calibration.

13

3.2 Preparation of the samples

A consistent, uncontaminated preparation is relevant not only for the accuracy of the sample measurements, but also for the comparison of samples that are not mounted in the same block. If contamination occurs during preparation of samples this should be visible in the results, which might differ after repolishing of a sample, since the amount of contamination will likely vary each time. Since the samples are in different sample holders, only the standards were repolished and not the samples to test the effect of repolishing. Therefore, every systematic difference in the sample measurements is likely to come from repolishing of the standards. Standard deviations are taken over 3–11 measurements of a sample, measured in sessions with 2 or 3 different repolishing and cleaning steps in between. The results are presented in Table 2 and Fig. 1.

When regular preparation is used for (re)polishing of standards, with which the samples are calibrated, there is a strong variation in the calculated Cl concentrations in the same sample between different polishings (Table 2). This variation is systematic and hence not due to a counting variation of the measurement. This indicates that the concentrations of the standards changed compared to a previous polishing and hence got contaminated to varying extents during preparation. For the regular preparation procedure, this variation is very high and leads to an average standard deviation that is comparable to the regular spot analyses, implying that the issue of preparation is camouflaged by the precision limitation of the conventional spot analyses. Cleaning with DeMi-water and trying to prevent any contact with possible contaminants, according to procedure 2, markedly improves the standard deviation (Table 2), particularly at low sample concentrations (Fig. 1), which are the target concentrations of mid-ocean ridge basalt research. However, procedure 2 still gives a systematic variation due to the preparation that is larger than that due to the counting statistics. In addition, this variation is not observed when samples are measured over multiple sessions, without repolishing in between, even after storage for over a month in the desiccator, indicating that preparation is the source of this variation. Cleaning with Milli-Q water, following procedure 3, improves the average precision between different polishings to the same values as the measurement precision (1.6 ppm; Tables 1 and 2). In addition, variation is not systematic, implying that variation due to preparation is less than the variation coming from counting statistics.

The results of the laser cleaning test are presented in Fig. 2. The measurements of the different laser cleaned areas have small variations, but these are not systematic and not the same for all samples. Therefore it can be concluded that epoxy was not
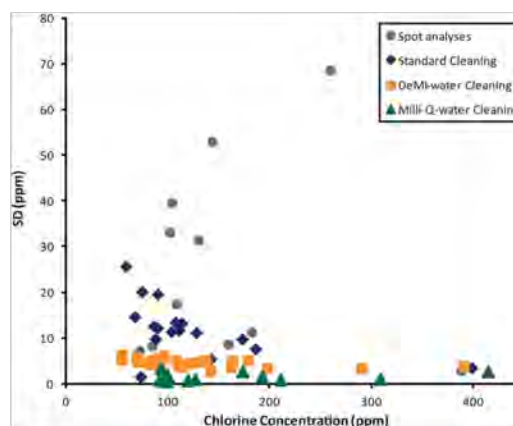
Fig. 1 Relation between precision of chlorine measurements and the concentration of samples with various preparation procedures. All concentrations benefit from improved cleaning, however this is most important for low concentration samples.
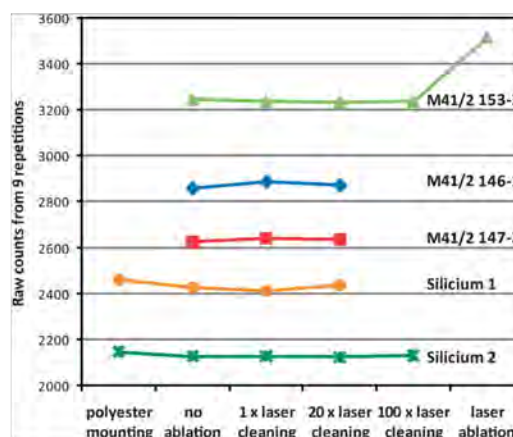
Fig. 2 Resulting raw counts for different laser cleaning steps. Little and no systematic variation implies that laser cleaning has no additional benefit.

present on the samples, and is hence not a possible source of chlorine contamination and laser cleaning is not required. Ablation of the samples has an obvious effect; however, this

Table 2 Comparison of precision for different preparation procedures. # is the number of samples from which the average SD was taken and *n* is the number of measurements for each sample

Procedure	Cleaning	Systematic offset between cleanings	Average SD	# of samples for average	*n* per sample
Spot analyses		n.a.	13	2	45
Mapping					
1	Regular	20–30 ppm	12	17	3–11
2	DeMi-water	7–15 ppm	4.6	26	3–11
3	Milli-Q-water	No offset	1.6	12	3–11

Table 3 Potentially chlorine free materials tested in this study

	Conc. (ppm)	2SD	n
Chlorine free materials			
Brass holder microprobe[a]	674	43	3
Copper holder ring[a]	972	137	3
Amalgam[a]	1394	66	4
Copper stripe[a]	634	41	2
Pure indium[a]	683	115	4
Pure rhenium[a]	897	34	3
Pure silicon 1[a,b]	22	12	14
Silicon 2[a,b]	−32	14	12
Polyester[a,c]	−226	—	1
Olivines			
Eifel, Meerfelder Maar Quarry Deudesfeld[a]	23	7	9
Lanzarote El4a, El4b, KLSJ2, KLSJ7[a]	16	11	24
Gran Canaria HAT9153, HAT9154[a]	26	31	6
Hawaii HX1801[a,15]	45	28	3
Auvergne, Maar de Beaunit[a]	22	3	3
Tahiti group 1 xenoliths[a,e,16]	42	17	12
Tahiti group 2 xenoliths[a,e,16]	60	34	6
Tanzanian xenoliths			
Grt Hz 89-675[d,17]	2.6	3.8	8
Hz 89-773[d,17,18]	−1.9	5.1	8
Dunite 89-778[17,18]	6.5	3.2	8
Hz LB26[d,19]	−0.1	4.9	7
Lz LB39[19]	7.2	5.9	8
Grt Hz LB4[d,19]	−1.1	10.9	7
Kimberley, South Africa xenoliths[20]			
Grt Hz AT1020clot[d]	2.0	4.0	8
Grt Hz AT1039Hz[d]	3.8	7.4	7
Grt Hz AT1039clot	5.7	6.7	8
Grt Hz AT1040clot[a]	35	24	3
Grt Hz AT1020Hz[a]	19	7	3

[a] Samples prepared in an earlier phase with procedure 2, hence absolute values might vary and error variations are higher. [b] Pure silicon as used for computer chips; silicon 2 is a natural mineral with a rough surface, hence the negative values. [c] Due to its soft nature, polyester could not be measured correctly, hence the negative values. [d] Selected for determination of 0 standard. [e] Group 1: T89-3, T89-13-x1, T89-21-x1, T89-24-x1; group 2: T89-14, T89-17.

leads to higher net Cl counts than expected. As a result, there is no chlorine loss due to heating, but rather a relief/edge effect is observed. Alternative mounting materials were also evaluated; they do however still contain significant amounts of chlorine, and they are mechanically considerably less suitable for mounting glass chips than epoxy (Table 3).

These tests underline the importance of a good and clean preparation and storage of the samples, in which a final cleaning step with Milli-Q water is required (procedure 3). However, the good reproducibility indicates that this clean preparation is feasible.

3.3 Selection of the measurement area

Apart from a clean preparation of the samples a good selection of the measurement area is important to avoid an additional contribution to the signal by excitation of chlorine from the underlying epoxy. This effect was discovered serendipitously during the test measurements. An increase in counts of several standards after repolishing was observed that was however not the same for all standards in the same mount, and hence was grain-specific rather than preparation related. Examination of these standards under the microscope revealed them to be very

thin and led us to suspect that fluorescence from the chlorine contained in the epoxy underneath the grain contributed to the total counts. This hypothesis was tested by a transect measured over standard ATHO-G, which was thinner at one side (transect A in Fig. 3). In this test, the thinner side is clearly seen to give higher counts. That this is not a heterogeneity effect of the standard itself is shown by a second, perpendicular transect (transect B in Fig. 3). Moreover, heterogeneity was in general not
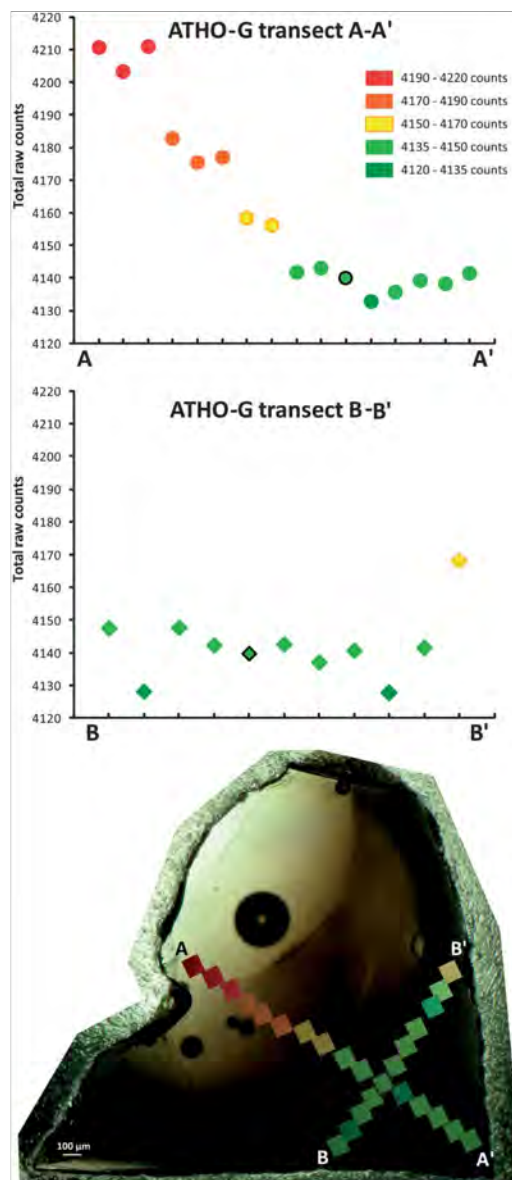
Fig. 3 Effect of thickness of a sample on the results. Samples that are too thin will have higher results due to the underlying epoxy.

15

displayed in any of the glass samples that were measured and so it can be concluded to be mostly lower than the counting statistics. It is therefore important that all measured samples as well as standards have a sufficient size so that the measured area is both underlain and bounded by sufficient material so that fluorescence from the epoxy can be ruled out. We recommend based on our experiments that areas at least 1 mm thick and at least 0.1 mm from the grain margin be used for measurements. In addition, measurement areas should be selected very carefully, in order to not measure close to bubbles or heterogeneities.

4 Calibration of the method

The concentration of measured samples can be obtained by calibration using international chlorine standards. However, for the low chlorine concentrations in basalts that are of interest to us, no certified international glass CRMs exist. Only some SRMs with informational values, or measured values reported in the literature, are available. We tested several of these standards with informational values to assess how their counts derived by our preferred method relate to their literature values. We hoped that a consistent calibration line could be determined by which the concentration (in ppm) can be calculated for samples as well as potentially better values for the standards. The standards that were measured are preferentially of basaltic composition, but also several more mafic or felsic magmatic rock compositions were added, in order to cover the complete range of possible chlorine concentrations in basalts. This proved necessary due to the paucity of basaltic glass standards for chlorine, particularly for the higher chlorine concentrations. The standards are listed in Table 4 (MPI-DING Glasses[7] and Smithsonian glasses[14]).

The results of the raw counts *versus* the reported concentrations from the literature are given in Table 4 and Fig. 4. It is apparent from Fig. 4 that the standard values reported in the literature are not well correlated with the raw counts. Although a calibration line can be drawn, this line has a high uncertainty. This situation is exacerbated when we consider the poorly defined values of the SRM, *i.e.* different methods give alternative values,[7,10] which if used would result in different calibration lines. Since it is difficult to assess which of the standards and which of their reported values in the literature is correct, the calibration line should ideally be fixed by an independent chlorine-free material at the lower end. As there is no defined chlorine-free standard, we tested several pure materials which we expected to contain no chlorine (see Table 3: pure metals, pure silicon in two forms, rhenium, indium and amalgam). However these 'pure' materials turned out to give generally high counts for chlorine (*i.e.* much higher than the basaltic samples) which we have converted into possible chlorine concentrations in Table 3 using a calibration based on our final resulting calibration line as discussed later in this paragraph. The silicon gave low but inconsistent values between the two different sample kinds (Table 3), probably due to matrix effects. Therefore, a more matrix-matched mineral was sought as the chlorine-free endpoint. Using geological reasoning we concluded that olivine (an Mg–Fe island silicate with simple stoichiometry and very low affinity for all trace elements except some transition metals) derived from the terrestrial mantle (which over geological time has lost a significant proportion of its chlorine to the hydrosphere) and recovered from within-plate settings (to minimize contamination by ocean water) should have the lowest chlorine content of all geological materials. We chose olivines from trace-element depleted mantle xenoliths from various geological environments: from kimberlite diatremes from South Africa[20] and Tanzania[17–19] (silica enriched and regular cratonic mantle); from lava flows on Tahiti (locality as in ref. 16), Hawaii,[15] Lanzarote and Gran Canaria (hotspot ocean islands); and from the Auvergne and Eifel (intracontinental volcanic provinces). All olivines have generally high Mg#, though they are highest for the olivines from cratonic mantle xenoliths. This is

Table 4 Literature values for the measured standards together with raw counts and calibrated values obtained here

Standard	Glass composition/ mineral	Calibrated value (ppm)	2SD (ppm)	Informational value[a]	Literature range[b]	Average counts[c]	SD counts	n
Zero standard	Olivines	0.0	5.8	0 ppm[d]		2381.2	15.4	42
M60/3-33GTV-18	Atacamite	165 999.0	3788.7	16.6[d] wt% (ref. 21)	16.22–16.8 wt% (ref. 21 and 22)	879 851.8	10 013.5	28
MPI-DING standard glasses[7,10]								
BM90/21-G	Peridotite	10.9	2.6	0.7 ppm	0.7–20 ppm	2438.9	6.8	9
GOR128-G	Komatiite	41.4	2.0	12 ppm	11.7–50 ppm	2600.0	5.3	9
KL2-G	Basalt	54.3	2.7	26 ppm	22.4–110 ppm	2668.4	7.2	9
ML3B-G	Basalt	54.7	2.4	7.5 ppm	7.5–110 ppm	2670.5	6.4	9
StHs6/80-G	Andesite	199.5	2.9	231 ± 50 ppm[e]	184–290 ppm	3435.6	7.8	9
T1-G	Quartz–diorite	222.2	4.0	113 ± 37 ppm[e]	86–135 ppm	3555.6	10.5	8
ATHO-G	Rhyolite	370.9	5.2	430 ppm	2–600 ppm	4341.8	13.9	8
Smithsonian reference glasses								
NMNH 113498-1	Basalt	271.3	8.7		200–212 ppm (ref. 23–26)	3815.3	23.1	4
NMNH 111240-52	Basalt	329.1	10.0		270 ppm −0.04 wt% (ref. 23, 24, 27–32)	4120.8	26.3	6
NMNH R6600	Scapolite (meionite)	13 907.9	49.1	1.43 wt%		75 898.3	129.8	4
Internal standards								
138-3	Basalt	413.6	3.4	High		4567.7	8.9	53
147-2	Basalt	61.4	2.2	Low		2705.9	5.8	61
157-3	Basalt	149.4	2.9	Middle		3170.8	7.5	63

[a] Informational value in the sense of Jochum *et al.*[7] [b] Values reported in the literature; standard deviation per value can be larger than the total range.[7,11] [c] Raw counts from 4 measurement sessions were normalised relative to the average counts obtained. [d] No informational value but based on low trace element contents for Ol and structural crystallography for Atc. [e] Reference value.[7]
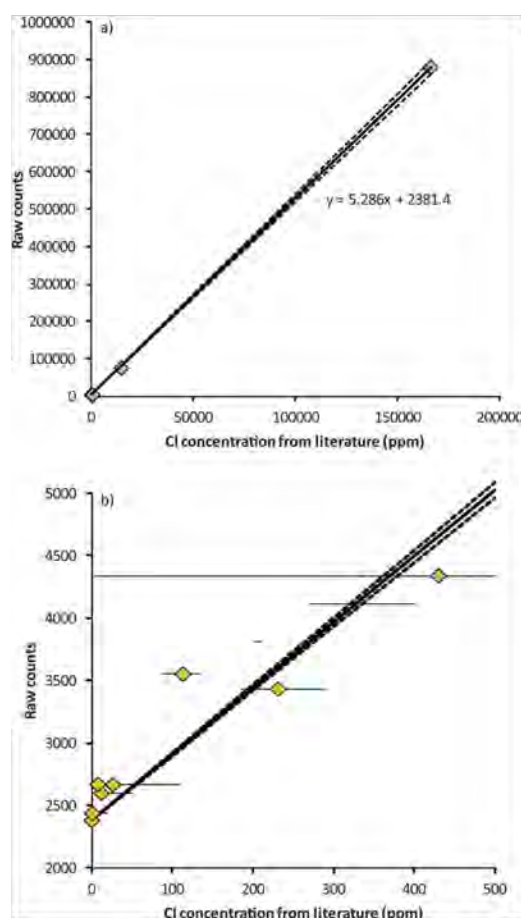
Fig. 4 Calibration line together with the raw counts and literature values of international standards. (a) Complete calibration line, including NMNH R6600 and Atc. (b) Blow up to low concentration range. Horizontal error bars give the variation for the samples found in the literature, while the orange diamante gives the informational value. Vertical error bars are smaller than the symbols. Dashed lines indicate the variation in the calibration line due to uncertainty of Atc (see text for more info).

consistent with the lowest chlorine values for these samples, which are in addition all quite similar. From the South African and Tanzanian mantle olivines, we carefully selected the samples showing the lowest chlorine counts to use as the zero point for the calibration line (Table 4). Even in these olivines the overall spread is relatively large (9.2 ppm 2SD), probably due to relatively many inhomogeneities in the olivine and a natural variation between the grains. In addition, some of the olivines are small and background epoxy might be a problem. Therefore, data from single grains of a selected sample with consistently higher values were removed from the zero-point average, with this excluding higher concentration grains. All data points were carefully evaluated for the thickness of the samples, and anomalously high data points on thinner areas were rejected. The resulting counts are in good agreement with

being lower than the BM90/21-G standard that, according to the literature, should have 0.7 ppm chlorine.[7] The variation of the olivine data is slightly higher than for higher concentration glasses, but too low to affect the slope of the calibration line (and the concentrations of samples/standards relative to each other). Only the absolute values are influenced, meaning that all standard/samples can vary in their absolute value by 5.8 ppm (2SD for olivine). Also for the higher end of the calibration line a fixed standard is required, particularly because the high chlorine standard NMNH R6600 only exists in small grain sizes, and hence its analysis might contain an additional chlorine signal from the embedding epoxy. Again using geological/mineralogical reasoning we chose the mineral atacamite ($Cu_2Cl(OH)_3$) as a high chlorine calibration point as it has chlorine in its structural crystal formula and contains stoichiometrically 16.6 wt% Cl.[21] For this study, atacamite derived from the Logatchev hydrothermal field (M60/3-33GTV-18)[22] was used. This is a natural mineral and hence variations occur, *e.g.* 16.8 wt% Cl was reported,[22] while spot analyses on the actual sample used yielded 16.9 ± 0.4 wt%, $n = 29$. However, due to the high Cl concentration of the atacamite, these variations in concentration do not significantly change the slope of the calibration line for the low concentrations (Fig. 4). For a 0.38 wt% difference in the selected value for atacamite (representing the 2SD for atacamite of the mapping method) the variation in the calibration becomes less than the standard deviation of the method at values of <130 ppm (and <1.5 ppm 2SD at <60 ppm), the target concentrations of this method. Therefore, a value of 16.6 wt% Cl was chosen, since this is the stoichiometric value for atacamite.

With a calibration line based on these geologically defined standards with high and low concentrations that is in agreement with informational and measured values of international SRM (Fig. 4), new values for the SRM can be calculated (see Table 4). Although some of the informational values vary significantly from the values presented here, all new values of the combined calibration for MPI-DING glasses and Smithsonian glasses are, except for T1-G and NMNH 113498-1, well within the respective ranges reported in the literature[7,10,21–32] (Table 4). Moreover, the systematics of the results, the basic physics of the method and the reproducibility of the standards under various machine conditions argue for accurate values obtained here.

For measurements of samples, 3 internal standards need to be used, since a set of standards is required in each block of samples to confirm contamination-free preparation and the use of international standards for this is not appropriate. Here, 3 samples from the test suite were chosen (M41/2 147-2, 157-3 and 138-3). The internal standards are measured together with the international standards and calibrated to values of 61.4, 149.4 and 413.6 ppm respectively. Long term reproducibility (~½ year) of these internal standards over multiple sessions with various repolishings is 2.5, 2.8 and 3.7 ppm 2SD for the lowest, middle and highest concentration respectively (>105 measurements per internal standard over 7 different measurement sessions). This underlines the robustness of the method, also over a long period of measurements.

5 Conclusions

Electron microprobe is capable of measuring chlorine at very low concentrations, when a method is used which provides high beam

17

currents over long times without damaging the sample or coating. Using a combination of beam scanning (element mapping) and standard–sample bracketing techniques, chlorine can be measured at <10 ppm levels with a precision of 1–2 ppm SD. Long term precision is similar to what can be obtained within one session. Very important for obtaining good results is a clean preparation, involving cleaning with Milli-Q water as the last step, after which the samples need to be stored under dry conditions. Clean preparation should always be confirmed by measuring internal standards prepared with the samples. Although epoxy is an appropriate mounting substance from the preparation standpoint, chlorine measurements should be performed on glass pieces thicker than 1 mm to avoid fluorescence from chlorine in the underlying epoxy from contaminating the measurement. Due to a lack of certified international chlorine standards at the concentrations of interest and large variations in the published values for SRM, the method is calibrated on geological materials with fixed concentrations of chlorine at 0 and 16.6 wt%. This calibration is in agreement with informational literature values of SRM. Using our new method it is now possible to study chlorine systematics in basaltic glasses at concentrations $\ll$100 ppm, providing insights into interactions between seawater and the oceanic crust and the behaviour of chlorine during mantle melting in general. In addition, this method provides a new approach for measuring element concentrations with high precision by electron microprobe that could be adapted, with appropriate standards, to other elements of interest. This may open up new fields of geochemical investigation for this widely available analytical tool.

Acknowledgements

References

1 P. J. Michael and J.-G. Schilling, *Geochim. Cosmochim. Acta*, 1989, **53**, 3131–3143, DOI: 10.1016/0016-7037(89)90094-x.

2 P. J. Michael and W. C. Cornell, *J. Geophys. Res.*, 1998, **103**, 18325–18356, DOI: 10.1029/98jb00791.

3 K. M. Gillis, L. A. Coogan and M. Chaussidon, *Earth Planet. Sci. Lett.*, 2003, **213**, 447–462, DOI: 10.1016/s0012-821x(03)00346-7.

4 L. A. Coogan, N. C. Mitchell and M. J. O'Hara, *J. Geophys. Res.*, 2002, **108**, 2002, DOI: 10.1029/2001jb001171.

5 L. A. Coogan, *Geology*, 2003, **31**, 1065–1068, DOI: 10.1130/g20129.1.

6 A. Jambon, B. Déruelle, G. Dreibus and F. Pineau, *Chem. Geol.*, 1995, **126**, 101–117, DOI: 10.1016/0009-2541(95)00112-4.

7 K. P. Jochum, B. Stoll, K. Herwig, M. Willbold, A. W. Hofmann, M. Amini, S. Aarburg, W. Abouchami, E. Hellebrand, B. Mocek, I. Raczek, A. Stracke, O. Alard, C. Bouman, S. Becker, M. Dücking, H. Brätz, R. Klemd, D. de Bruin, D. Canil, D. Cornell, C.-J. de Hoog, C. Dalpé, L. Danyushevsky, A. Eisenhauer, Y. Gao, J. E. Snow, N. Groschopf, D. Günther, C. Latkoczy, M. Guillong, E. H. Hauri, H. E. Höfer, Y. Lahaye, K. Horz, D. E. Jacob, S. A. Kasemann, A. J. R. Kent, T. Ludwig, T. Zack, P. R. D. Mason, A. Meixner, M. Rosner, K. Misawa, B. P. Nash, J. Pfänder, W. R. Premo, W. D. Sun, M. Tiepolo, R. Vannucci, T. Vennemann, D. Wayne and J. D. Woodhead, *Geochem., Geophys., Geosyst.*, 2006, **7**, Q02008, DOI: 10.1029/2005gc001060.

8 A. J. Magenheim, A. J. Spivack, P. J. Michael and J. M. Gieskes, *Earth Planet. Sci. Lett.*, 1995, **131**, 427–432, DOI: 10.1016/0012-821x(95)00017-7.

9 J. Fietzke, M. Frische, T. H. Hansteen and A. Eisenhauer, *J. Anal. At. Spectrom.*, 2008, **23**, 769–772.

10 GeoReM database: http://georem.mpch-mainz.gwdg.de; Application version 14; 04/01/2012.

11 E. Jarosewich, J. A. Nelen and J. A. Norberg, *Geostand. Geoanal. Res.*, 1980, **4**, 43–47, DOI: 10.1111/j.1751-908X.1980.tb00273.x.

12 R. Almeev, F. Holtz, J. Koepke, F. Parat and R. E. Botcharnikov, *Am. Mineral.*, 2008, **92**, 670–674, DOI: 10.2138/am.2007.2484.

13 H. Möller, PhD Dissertation, Christian-Albrechts-Univeristät, Kiel, 2002.

14 E. Jarosewich, J. A. Nelen and J. A. Norberg, *Geostand. Geoanal. Res.*, 1980, **4**, 43–47.

15 A. V. Sobolev and I. K. Nikogosian, *Petrology*, 1994, **2**, 111–144.

16 R. J. Tracy, *Earth Planet. Sci. Lett.*, 1980, **48**, 80–96, DOI: 10.1016/0012-821x(80)90172-7.

17 R. L. Rudnick, W. F. McDonough and A. Orpin, Kimberlites, Related Rocks and Mantle Xenoliths, in *Proceedings of the 5th International Kimberlite Conference*, ed. H. O. A. Meyer and O. H. Leonardos, 1994, pp. 336–353.

18 R. L. Rudnick, W. F. McDonough and B. W. Chappell, *Earth Planet. Sci. Lett.*, 1993, **114**, 463–475, DOI: 10.1016/0012-821x(93)90076-l.

19 C.-T. Lee and R. L. Rudnick, in *Proceedings of the 7th International Kimberlite Conference*, ed. J. Gurney and S. R. Richardson, 1999, pp. 503–521.

20 L. J. Wasch, F. M. van der Zwan, O. Nebel, M. L. A. Morel, E. W. G. Hellebrand, D. G. Pearson and G. R. Davies, *Geochim. Cosmochim. Acta*, 2009, **73**, 6894–6917, DOI: 10.1016/j.gca.2009.07.038.

21 J. W. Anthony, R. A. Bideaux, K. W. Bladh and M. C. Nichols, *Handbook of Mineralogy*, Mineral Data Publishing, 1997.

22 V. Dekov, T. Boycheva, U. Hälenius, S. Petersen, H. Billström, J. Stummeyer, G. Kamenov and W. Shanks, *Chem. Geol.*, 2011, **286**, 169–184, DOI: 10.1016/j.chemgeo.2011.05.002.

23 J. C. M. de Hoog, P. R. D. Mason and M. J. van Bergen, *Geochim. Cosmochim. Acta*, 2001, **65**, 3147–3164, DOI: 10.1016/s0016-7037(01)00634-2.

24 M. Laubier, P. Schiano, R. Doucelance, L. Ottolini and D. Laporte, *Chem. Geol.*, 2007, **240**, 129–150, DOI: 10.1016/j.chemgeo.2007.02.002.

25 S. Moune, O. Sigmarsson, T. Thordarson and P.-J. Gauthier, *Earth Planet. Sci. Lett.*, 2007, **255**, 373–389, DOI: 10.1016/j.epsl.2006.12.024.

26 M. J. Streck and S. Wacaster, *J. Volcanol. Geotherm. Res.*, 2006, **157**, 236–253, DOI: 10.1016/j.jvolgeores.2006.03.040.

27 D. Baker, *Contrib. Mineral. Petrol.*, 2008, **156**, 377–395, DOI: 10.1007/s00410-008-0291-3.

28 M. L. Coombs, T. W. Sisson and J.-I. Kimura, *Earth Planet. Sci. Lett.*, 2004, **217**, 297–313, DOI: 10.1016/s0012-821x(03)00631-9.

29 M. A. Elburg, V. S. Kamenetsky, J. D. Foden and A. Sobolev, *Chem. Geol.*, 2007, **240**, 260–279, DOI: 10.1016/j.chemgeo.2007.02.015.

30 V. Kamenetsky and A. Gurenko, *Contrib. Mineral. Petrol.*, 2007, **153**, 465–481, DOI: 10.1007/s00410-006-0160-x.

31 M. Portnyagin, R. Almeev, S. Matveev and F. Holtz, *Earth Planet. Sci. Lett.*, 2008, **272**, 541–552, DOI: 10.1016/j.epsl.2008.05.020.

32 W. D. Sun, R. A. Binns, A. C. Fan, V. S. Kamenetsky, R. Wysoczanski, G. J. Wei, Y. H. Hu and R. J. Arculus, *Geochim. Cosmochim. Acta*, 2007, **71**, 1542–1552, DOI: 10.1016/j.gca.2006.12.003.

1974 | *J. Anal. At. Spectrom.*, 2012, **27**, 1966–1974

This journal is © The Royal Society of Chemistry 2012

18

Chapter 3:

Hydrothermal activity at the slow-spreading Red Sea Rift traced by chlorine in basalt

This chapter consist of a manuscript, which is currently in review at *Geochimica et Cosmochimica Acta.*

Authors:
FROUKJE M. VAN DER ZWAN[1*], COLIN W. DEVEY[1], NICO AUGUSTIN[1], RENAT R. ALMEEV[2], RASHAD A. BANTAN[3] AND ALI BASAHAM[3]

[1] Geomar Helmholtz Centre for Ocean Research Kiel, Germany
[2] Institut für Mineralogie, Universität Hannover, Germany
[3] Faculty of Marine Science, King Abdulaziz University, Jeddah, Saudi Arabia

Abstract

The process of assimilation of hydrothermally altered crust at mid-ocean ridges by rising magma can be traced by measuring chlorine (Cl) enrichment in the erupted lavas. This process has been shown for erupted basalts from fast spreading ridges (Cl concentrations up to 1200 ppm), but not so far for slow-spreading ridges, where the basalts generally show lower Cl values (~50-200 ppm), which makes variations harder to measure. The Red Sea Rift provides an opportunity to study assimilation of hydrothermally altered crust at an ultra slow-spreading ridge (max. 1.6 cm/yr) by Cl, as the Red Sea seawater itself is relatively saline (40 - 42‰, cf. 35‰ in open ocean water), the rift axis contains (hot) brine pools (up to 270‰ salinity and 68°C) and the young rift is flanked by thick evaporite sequences. Absolute chlorine concentrations (up to 1300 ppm) and Cl concentrations relative to minor or trace elements of similar mantle incompatibility (e.g. K, Nb) are much higher in Red Sea basalts than for average slow-spreading ridges. Homogeneous within-sample Cl concentrations, high Cl/Nb compared to H_2O/Ce contents, the decoupling of Cl enrichment from other trace elements and its independence on the presence of highly saline seafloor brines at the site of eruption indicate that neither seafloor weathering nor magmatic enrichment/fractionation can account for these Cl variations. Instead we find high Cl enrichment to be spatially closely correlated with evidence of hydrothermal activity, suggesting that assimilation of hydrothermally altered crust is the dominant Cl-enrichment process. A proximity to both evaporite outcrops and bathymetric signs of volcanism on the seafloor enhances Cl enrichment. The spreading rate, the intensity of seafloor fracturing and the calculated depth of last crystal fractionation do not seem to play a role. The basaltic Cl enrichment can be used as a tracer to predict where hydrothermal activity can be expected. Sites of particular interest for future hydrothermal research are the Thetis-Hadarba-Hatiba Deeps (specially their large axial domes), the northern Port Sudan Deep and the dome in Mabahiss Deep.

1 Introduction

Hydrothermal circulation occurs when water interacts with a hot magma/rock; at mid-ocean ridges seawater interacting with the magma and rocks forming the new oceanic crust leads to both heat- and element-transfer with the young oceanic lithosphere. This can lead to focused seafloor venting of hot fluids that leads to the creation of habitats for chemosynthetic communities and the deposition of resources in the form of seafloor massive sulphides. Hydrothermal activity occurs at all ridges, but the along-axis frequency of high-temperature hydrothermalism appears to increase with spreading rate (e.g. Baker and German, 2004; Hannington et al., 2011). Active high-temperature fields can be found by detecting their effluent in the overlying water column, while the detection of extinct fields, which are economically more interesting, is at best extremely challenging.

An alternative prospection method for finding active and extinct hydrothermal sites is to trace hydrothermal alteration of the crust through the chlorine (Cl) contents of erupted basalts (Michael and Schilling, 1989; Gillis et al., 2003), since the Cl contents of seawater and magma are vastly different and interaction with seawater will increase the Cl content of a magma. Models from fast-spreading ridges indicate an interaction zone between water and magma at the roof of shallow axial magma chambers (Coogan et al., 2002a; Gillis et al., 2003; France et al., 2009; France et al., 2010). Assimilation of hydrothermally altered oceanic crust with a high Cl content (Barnes and Cisneros, 2012) by magma stoping will hence increase the Cl content of a rising magma, both when recently altered crust beneath an active hydrothermal field is assimilated as well as when inactive, previously altered crust is incorporated. These processes generate magmatic markers of present and past hydrothermal circulation. Chlorine enrichment is best observed by the use of ratios of Cl against elements of similar magmatic incompatibility such as potassium (K) or niobium (Nb). Very high Cl/K ratios (up to 0.7) and Cl contents (up to 1200 ppm) have previously been found at fast spreading (>10 cm/yr) mid-ocean ridges (Michael and Schilling, 1989; Gillis et al., 2003), at back-arc basins (Kent et al., 2002; Sun et al., 2007), in ophiolites (Coogan et al., 2002a;

Coogan, 2003), as well as in ocean island basalts (Kent et al., 1999a; Kent et al., 1999b), compared to <0.08 Cl/K for uncontaminated MORB (Michael and Cornell, 1998; Stroncik and Haase, 2004).

At (ultra) slow-spreading ridges (<3.5 cm/yr) as well as at some medium spreading ridges (<7.5 cm/yr, e.g. Southeast Indian Ridge, Austral-Antarctic Discordance) Cl concentrations of basalts are generally lower (Cl ~50-200 ppm; Cl/K 0.01-0.09 (e.g. Michael and Cornell, 1998)). This apparent lack of Cl enrichment was interpreted as implying that assimilation of hydrothermally altered crust was not occurring at slow-spreading ridges due to the absence of a shallow and continuous magma lens (Michael and Cornell, 1998). Calculations of the depth of last equilibrium crystallisation suggest that magma at slow-spreading ridges generally cools deeper (>3 kbar) than the maximum presumed depth of hydrothermal penetration observed in e.g. the Oman ophiolite (6 km in Gregory and Taylor, 1981) and rises relatively rapidly to the surface, without the possibility to interact with the shallow altered oceanic crust (Michael and Cornell, 1998). The only higher Cl/K ratios (up to 0.5) found at slow-spreading ridges are from ridges with a thick crust (and hence presumably higher magma flux) and low crystallisation equilibrium pressures, e.g. at Kolbeinsey and Reykjanes Ridges and AMAR (Michael and Cornell, 1998).

The intrinsically low Cl concentrations in slow-spreading MORB and the relatively large analytical uncertainty (15-20 ppm (Michael and Schilling, 1989; Jambon et al., 1995; Michael and Cornell, 1998)) and high detection limits of the methods with which Cl was measured in the past made it difficult to resolve small variations in Cl concentrations. Hence, the conclusion that assimilation of hydrothermally altered crust is not occurring at slow-spreading ridges might be the result of analytical problems. Here, we apply a new, highly precise Cl measurement method (van der Zwan et al., 2012), which enables us to analyze chlorine with a precision of 1-2 ppm and a much lower detection limit of below 10 ppm. The possibility to measure small variations between samples gives us the opportunity to test if Cl enrichment by assimilation of hydrothermally altered crust is also taking place at slow-spreading ridges.

One place extremely suitable for testing the importance of assimilation of hydrothermally altered crust through Cl enrichment of basalts is at the young, opening Red Sea (Fig. 1), because of its relatively high seawater salinity (40 - 42‰ compared to 34.5‰ for average ocean water), the presence of (hot) saline brine pools in several within-axis topographical 'Deeps' (up to 270‰ salinity (e.g. Pierret et al., 2001; Gurvich, 2006)), and the thick evaporite sequences on the flanks of the active rift (e.g. Whitmarsh et al., 1974; Mitchell et al., 2010). The Red Sea Rift (RSR) exhibits ultra slow-spreading (max. 1.6 cm/yr (Chu and Gordon, 1998)) and its basalts, with an average Na_8 of 2.3 (PetDB database (Lehnert et al., 2000)), have similar characteristics as the basalt group from slow-spreading ridges with low Cl/K values (Michael and Cornell, 1998). However, the potential to increase magmatic Cl concentrations by interaction with seawater, brines or fluids that passed through evaporites is expected to be significantly higher in the Red Sea and if assimilation of hydrothermally altered crust takes place at slow-spreading ridges, it is likely most pronounced there.

Here we present the Cl contents (together with major and trace elements) of Red Sea basalts and use new high-resolution bathymetric maps of the Red Sea (Augustin et al., in review) to examine the relation between Cl enrichment and rift morphology, fault intensity, volcanic activity and spreading rate. We use the presence of Cl enrichment to predict where hydrothermalism should be most active and where hydrothermal vents could be found. This is important for the Red Sea as so far only fragments of smokers have been found at one place (Blum and Puchelt, 1991), although three more active hydrothermal systems have been inferred from high temperatures in brines and underlying sediments (e.g. Pierret et al., 2001; Gurvich, 2006; Swift et al., 2012). This number of occurrences is significantly less than expected over the ~1900 km length of the Red Sea Rift (at this spreading rate we would expect ca. 10 systems (cf. Hannington et al., 2011), which implies that there may be more vent fields to be discovered).
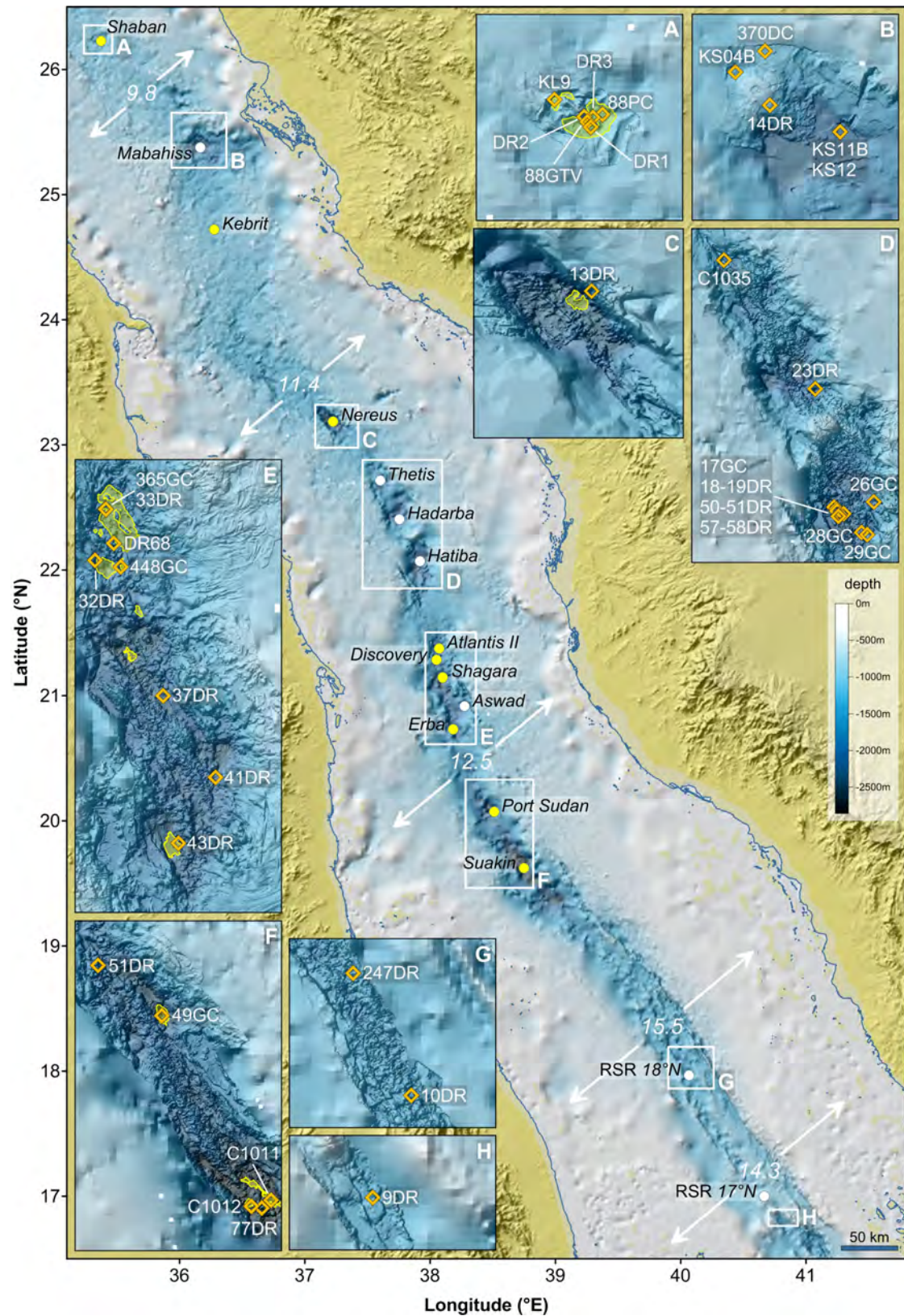
Fig. 1 – Overview map of the central Red Sea with the positions of the Red Sea Deeps. White circles mark brine-free Deeps without brines; yellow circles mark Deeps with brines. Spreading rates (white arrows) are given in mm/yr (Chu and Gordon, 1998). Insets A-H show details of the areas marked by white squares in the overview map. Orange diamonds indicate the positions of sample locations; yellow shapes mark the surface areas of the brine pools (after Gurvich, 2006). The bathymetric colour scale is valid for all maps; the scale bar is only valid for the overview map.

1.1 Geological Setting of the Red Sea Rift

The Red Sea is a ~1900 km long, maximum 370 km wide, NNW-SSE trending, young opening ocean, characterised by a shallow main depression (400-1200 m deep) and a <60 km wide axial trough with depths up to 2850 m (Laughton, 1970; fig. 1). Current spreading rates vary between 10 and ~16 mm/yr, with the highest rate near 18°N and slower spreading rates towards N and S (Chu and Gordon, 1998). The Red Sea formed by extensional tectonics and a counter-clockwise rotation of the Arabian Shield compared to the African (Nubian) shield (e.g. Girdler, 1991; Sultan et al., 1993; Ghebreab, 1998; Cochran, 2005), potentially initiated by impingement of the Afar plume head at ~30 Ma and associated crustal thinning (e.g. Cochran, 2005 and reference therein). Fission track data indicate opening of the Red Sea along its complete length with the main phase of extension at 25-21 Ma (Omar and Steckler, 1995) accompanied by synrift sedimentation and the eruption of basaltic dikes all along the Red Sea coast (Féraud et al., 1991; Bosworth et al., 2005). The start of oceanic seafloor spreading is somewhat uncertain; the oldest (~5 Ma) basaltic seafloor present in the axial trough occurs at 17°N (e.g. Courtillot, 1982; Cochran, 1983), but seafloor spreading may have begun sooner (8-12 Ma: (Izzeldin, 1987; Augustin et al., in review) with its magmatic products buried beneath the thick (up to 7 km) cover of Miocene evaporites and younger hemipelagic sediments which have flowed and slumped towards the axis from the basin margins.

In the southern part of the Red Sea (S of 19.5°N) the axial valley is continuous and well developed with parallel normal faulting and extensive volcanism (e.g. Roeser, 1975; Augustin et al., in review). Between 19.5°N and 23.5°N basalt occurs in wide troughs and basins, the Red Sea Deeps (e.g. Bäcker and Schoell, 1972; Pautot, 1983; Bonatti, 1985; fig. 1). The Deeps are separated by shallower intertrough zones that are covered by the same sediment cover as on the flanks of the main trough (e.g. Tramontini and Davies, 1969; Searle and Ross, 1975; Izzeldin, 1989; Ligi et al., 2012; Augustin et al., in review). North of 23.5°N the Deeps are more isolated and basalt is only found at Bannock, Mabahiss and Shaban Deeps (Bonatti et al., 1984; Pautot et al., 1984; Guennoc et al., 1988). The seafloor in the Deeps is strongly faulted and more tectonically influenced than that found in the southern Red Sea, although abundant evidence for volcanism is still present, including the localised occurrence of large (7-13 km in diameter) axial dome volcanoes at Mabahiss, Thetis, Hatiba and Aswad Deeps (Augustin et al., in review; fig. 1). The bathymetry of the volcanic Deeps displays all typical features of slow-spreading axes (e.g. Michael et al., 2003; Searle and Escartin, 2004)).

All magmatic samples previously analysed from the Red Sea Deeps are tholeiitic mid-ocean ridge basalts derived from a pure asthenospheric source with no indication of continental input (e.g. Altherr et al., 1990; Haase et al., 2000) and thus typical for (slow-spreading) mid-ocean ridge basalts (MORB). Basalts from the southern RSR (south of 19°N) vary in composition from tholeiites to alkali-basalts. The basalt trace element geochemistry indicates the presence of T-MORB and N-MORB in the North changing to E-MORB and OIB trace element signatures in the South, indicating variations along the RSR in the mantle sources of the magmas as well as in the degree of melting. The N-MORB with the highest degrees of melting occurs in the central part of the Red Sea (18°N-23°N (Altherr et al., 1988; Volker et al., 1993; Haase et al., 2000)). The mantle source of the Northern Red Sea basalts is influenced by an Indian Ocean component (Haase et al., 2000), while the Southern Red Sea mantle source is influenced by a plume component (Ramad enriched component (Barrat et al., 1990; Volker et al., 1993)). The trace element data are in agreement with He-isotope ratios that are MORB-like at Mabahiss Deep and have a stronger Afar plume component in the Southern Red Sea (Moreira et al., 1996).

Several of the Red Sea Deeps contain highly saline brines (Fig. 1). These vary in temperature from similar to Red Sea Deep Water (ca. 22°C) up to at present 68°C in the Atlantis II Deep (Swift et al., 2012) and are often associated with metalliferous sediments (Gurvich, 2006 and reference therein). At Atlantis II Deep, the metalliferous sediments and their sulphur isotope compositions together with the temperature and composition of the brine were taken to indicate hydrothermal input into the brine (Brewer and Spencer, 1969; Bäcker and Richter,

1973; Shanks and Bischoff, 1980; Hartmann, 1985; Pierret et al., 2001; Laurila et al., 2014). A N-S temperature gradient in the Atlantis II brine as well as gradients in the metal contents of the brine and in metalliferous sediments indicate that the strongest hydrothermal activity takes place in the SW-basin of this Deep (Brewer and Spencer, 1969; Bäcker and Richter, 1973; Schoell and Hartmann, 1973; Monin et al., 1981). Metalliferous sediments and higher temperatures of brines are also found in the neighbouring Discovery Deep and at Nereus Deep and Port Sudan Deep, indicating hydrothermal activity there as well (Pierret et al., 2001; Gurvich, 2006; Swift et al., 2012). Metalliferous sediments in some of the Deeps with ambient temperature brines (e.g. Shagara, Suakin Deep) or without brines (e.g. Thetis Deep) might suggest the former occurrence of hydrothermal activity there (Gurvich, 2006 and reference therein; Pierret et al., 2010). Due to the limited accessibility of the brines for modern camera sampling systems, no active vent fields have been confirmed so far by observation. Only inactive black smoker fragments have been reported from Kebrit Deep (Blum and Puchelt, 1991).

2 Sampling and analytical technique

Samples were collected along the RSR between 25.5°N to 16.5°N during expeditions R/V Poseidon 408-1 (January 2011) and R/V Pelagia 64PE350/351 (March-April 2012). Dredging over tracks of 200-900 m length yielded basaltic rocks or glass fragments from 23 sites at 10 different Deeps and at 17°N and 18°N along the Red Sea rift (Table 1; fig. 1). To complement this sample set, basalt samples from previous cruises M31/2, SO29, NORGMRO and DUF73 (Altherr et al., 1988; Moreira et al., 1996; Haase et al., 2000; Bézos, 2003) were measured as well as glass fragments collected from the base of sediment cores VA29-365 and SO02-448, stored at GEOMAR, Kiel. The basalts were derived from Deeps that show both presence and absence of brines (to study the relation of basalt Cl content to the brine pools), and from various distances from the evaporitic cover on the rift flanks.

For each rock at least 3 pieces of volcanic glass >2 mm across were selected. In the case of glass from sediment traps and cores, up to 15 fragments were analysed in case they originated from different eruptions. All glasses were selected under a binocular microscope based on their fresh appearance and lack of visible vesicles, rims, inclusions or minerals. The mounted glass was prepared, polished and finally cleaned with Milli-Q water following the procedures in van der Zwan et al. (2012) to avoid Cl contamination.

Major elements and chlorine measurements were carried out with a Jeol JXA-8200 ''Superprobe'' electron microprobe at GEOMAR, Kiel using an acceleration voltage of 15 kV. Chlorine was measured with a beam current of 80 nA and a beam diameter of 10 µm using the mapping technique described in van der Zwan et al. (2012). Concurrently with Cl, potassium (K) was measured (with a PETJ crystal) and calibrated with zero-potassium-olivines, MPI-DING standard glasses (Jochum et al., 2006) and Smithsonian reference glasses (Jarosewich et al., 1980). The Cl and K results are the average of up to 8 measurements per sample. The error (2SE) for Cl is generally <3 ppm, for K 2SE is <30 ppm. Major elements were measured with a defocused spot of 5 µm diameter and a beam current of 10 nA. Counting times were 20/10 s (peak/background) for Si, Ti, Al, Fe, Mg, Ca, Na and P and 30/15 s for Mn. For calibration and monitoring of data quality, natural reference samples from the Smithsonian Institute were used (Jarosewich et al., 1980). Relative analytical precision is generally <2.5 %, but up to 5% for Na and ~30% for Mn and P.

Trace element analyses were carried out at GEOMAR, Kiel by LA-ICP-MS using a 193 nm Excimer laser system (GeoLasPro from Coherent) operating at 5 J/cm^2 fluency and 10 Hz repetition rate and coupled to a double-focusing, high-resolution magnetic-sector mass spectrometer (AttoM from Nu Intruments). Point ablation (carried out under He carrier gas, subsequently mixed with Ar carrier gas) induced 300 shots per 90 µm spot, after pre-ablation at a 120 µm spot size. The reference sample NIST610 (Jochum et al., 2011) was analysed at 32 µm spot size. MPI-DING reference samples (Jochum et al., 2006) were analysed as unknowns to control the accuracy of the measurements. Relative analytical precision is typically <2–5% (one standard deviation), except for Li, B, U (<10%) and Be, Cs (<40%).

Glass H_2O and CO_2 concentrations were determined using a Fourier Transformation Infrared (FTIR) Bruker IFS88 spectrometer coupled with an IR Scope II microscope at the Institute of Mineralogy, Leibniz University of Hannover. Glass chips approximately 1 mm² in size were mounted in ceramic rings and doubly polished. Their thickness (150 to 50 μm) was measured with a digital micrometer Mitutyo (precision ± 2 μm (Behrens, 2009)) at 3 points for every polished glass fragment. Absorption spectra in the mid-infrared (MIR) range were collected using a spot size of 100 x 100 μm (average of 50 scans). The operating conditions for MIR were: globar light source, KBr beam splitter, MCT (HgCdTe) detector, 4 cm^{-1} spectral resolution, spectral range 13000 to 0 cm^{-1}. The H_2O concentration was measured at the peak that is attributed to the OH stretch vibration (3550 cm^{-1}) using a molar absorption coefficient of 67 L·cm^{-1}·mol^{-1} (Stolper, 1982). The CO_2 concentration was measured at the peak doublet with maxima at 1430 and 1510 cm^{-1} using a molar absorption coefficient of 317 L·cm^{-1}·mol^{-1} (Shishkina et al., 2010). Glass densities were calculated using the equation of Yamashita et al. (1997) for basaltic compositions: $\rho = 2819 - 20.8 \cdot CH_2O$. The H_2O and CO_2 concentrations were calculated based on the Lambert-Beer law using the peak height, which was determined by reference to a straight tangential base line. Three measurements per sample were performed to account for possible variations in thickness due to polishing. The average values of the measurements were used to calculate the H_2O and CO_2 contents of the glasses, with a standard deviation usually less than 0.02 and 0.003 wt.% respectively.

Pressure and temperature conditions calculated for the point of last crystallization equilibrium are based on major elements and H_2O concentrations of the glasses and calculated with the software COMAGMAT, version 3.57 (Ariskin and Barmina, 2004) using inversed modeling (see Almeev et al., 2008). Recent experimental calibrations take into account the effect of small amounts of H_2O on crystallisation (Almeev et al., 2007a; Almeev et al., 2007b; Almeev et al., 2012). The pressure models of COMAGMAT have an uncertainty of ±100 MPa and are comparable with models used in Michael and Cornell (1998) (Almeev et al., 2008).

3 Results

3.1 Petrology of the samples

The samples consist generally of basalts (sheet- and lobate flows, pillows; table 1) with a glassy rim, which varies from a few mm to cm's in thickness. The sheet and lobate flows have often glass on top and bottom and irregular shapes, including flow structure, drips and pockets, of which some are filled with sediments that may also be mingled with the glass or basalt. Internal flow structures are also visible in the glass. Sections of the samples are generally fresh and alteration seems restricted to the outer surfaces and pore spaces, mainly in the form of palagonite rims or carbonate precipitations. Samples from Erba Deep (43DR) appear to be freshest and display no visible alteration, samples from Atlantis II (33DR) and Shaban Deep are strongest altered, but still contain fresh glass. The glass samples from Nereus and Suakin Deeps appear to be relatively old as they were embedded in solid carbonates and coated with a 2-3 mm manganese crust respectively. Strong salt crystallisation upon drying of the samples from Erba and Northern Atlantis II Deeps (33DR and 43DR) indicate that they were recovered from beneath a brine. In addition, samples from Atlantis II where topped by hydrothermal barite crusts. All basaltic samples show generally low (<5%, often in zones at the top) vesicularity although a few samples reach 20%. Up to 5% phenocryst (0.2-4 mm) are present in the basalt and glass, and consist mostly of plagioclase, apart from Port Sudan samples (49GC, 51DR) that also contain olivine phenocrysts. Olivine and plagioclase groundmass crystals (<0.2 mm) are present in all samples (1-10%) and may contain inclusions of melt and/or opaque minerals. Some minerals from the pumpellyite group are found in samples from the large volcano at Mabahiss Deep (14DR).

Glass fragments from sediment traps appear fresh and are mixed with hemipelagic sediments, and sometimes with manganese oxide fragments. Gravity cores with glass fragments from Hatiba Deep (26SL, 28SL, 29SL) contain hemipelagic sediments; the cores from Atlantis II Deep contain metalliferous sediments.

Table 1
Overview of positions and lithologies of the sample stations

Station[a]	Geographic location	Start position (Lat./Long.)	End position (Lat./Long.)	Depth	Lithology
M31/2-KL9[b]	Shaban Deep	26°15.1'N/35°18.8'E	-	1362	basalt and glass fragments
M31/2-88PC[b]	Shaban Deep	26°13.9'N/35°22.7'E	-	1474	glass fragments
M31/2-DR3[b]	Shaban Deep	26°13.7'N/35°21.95'E	26°13.6'N/35°21.88'E	1464 - 1324	pillow basalts
M31/2-DR2[b]	Shaban Deep	26°13.5'N/35°21.2'E	26°14.0'N/35°21.0'E	1225	pillow basalts
M31/2-88GTV[b]	Shaban Deep	26°13.3'N/35°21.4'E	-	1280	basalt and glass fragments
M31/2-DR1[b]	Shaban Deep	26°12.4'N/35°21.7'E	26°13.4'N/35°21.4'E	1497-1224	pillows and sheet flow basalts
SON0029-370DC[b]	Mabahiss Deep	25°32.88'N/36°05.22'E	-	-	-
NORGMRO-KS04B[b]	Mabahiss Deep	25°30.7'N/36°02.27'E	-	1420	-
64PE351-14DR	Mabahiss Deep	25°27.35'N/36°05.84'E	25°27.55'N/36°05.59'E	1180 - 1100	sheet lavas and blocky basalts
NORGMRO-KS11B[b]	Mabahiss Deep	25°25.2'N/36°13.2'E	-	2150	-
NORGMRO-KS12[b]	Mabahiss Deep	25°24.71'N/36°12.78'E	-	2150	-
64PE351-13DR	Nereus Deep	23°12.53'N/37°16.03'E	23°12.83'N/37°16.36'E	1830 - 1417	altered basalt + glass in solidified carbonates
DUF0073-C1035[b]	Thetis Deep	22°48.10'N/37°33.10'E	-	1695	-
64PE350-23DR	Hadarba Deep	22°23.57'N/37°50.37'E	22°23.95'N/37°50.22'E	2098 - 1980	pillows, lobate, sheet flow basalts
POS408/1-26GC	Hatiba Deep	22°02.42'N/38°01.34'E	-	2008	glass fragments
POS408/1-50DR	Hatiba Deep	22°01.29'N/37°53.72'E	22°01.57'N/37°54.05'E	2450 - 2173	sheet flow basalts
POS408/1-57DR	Hatiba Deep	22°00.96'N/37°54.24'E	22°01.13'N/37°54.45'E	2235 - 2234	glass fragments
POS408/1-19DR	Hatiba Deep	22°00.60'N/37°54.23'E	22°00.83'N/37°54.67'E	2222 - 2230	sheet flow basalts
POS408/1-51DR	Hatiba Deep	22°00.00'N/37°55.46'E	22°00.30'N/37°55.79'E	2362 - 2294	glass fragments
POS408/1-58DR	Hatiba Deep	21°59.92'N/37°54.74'E	22°00.22'N/37°54.90'E	2212 - 2219	lobate and sheet flow basalts
POS408/1-18DR	Hatiba Deep	21°59.73'N/37°54.58'E	21°59.76'N/37°54.93'E	2220 - 2216	lobate and sheet flow basalts
POS408/1-17GC	Hatiba Deep	21°59.67'N/37°54.67'E	-	2219	glass fragments
POS408/1-28GC	Hatiba Deep	21°56.65'N/37°59.02'E	-	2081	glass fragments
POS408/1-29GC	Hatiba Deep	21°56.24'N/38°00.10'E	-	1962	glass fragments
64PE350-33DR	N. Atlantis II Deep	21°24.01'N/38°03.04'E	21°24.30'N/38°03.03'E	2132 - 2011	salty basalt blocks, barite crusts, silica crusts
VA29-365GC[b]	N. Atlantis II Deep	21°24.04'N/38°03.04'E	-	2099	glass fragments

Sample	Location	Coordinates	Coordinates		Lithology
DUF0073-DR68[b]	S. Atlantis II Deep	21°20.00'N/38°04.00'E	-	2000	-
64PE350-32DR	Discovery Deep	21°17.95'N/38°01.77'E	21°17.86'N/38°01.84'E	1860 - 1820	glass fragments
SON02-448GC[b]	S. Atlantis II Deep	21°17.17'N/38°04.85'E	-	2073	basalt and glass fragments
64PE350-37DR	Shagara Deep	21°01.83'N/38°09.87'E	21°01.96'N/38°09.88'E	2288 - 2270	glass fragments
64PE350-41DR	Aswad Deep	20°52.02'N/38°16.13'E	20°52.23'N/38°16.13'E	2281 - 2246	glass fragments
64PE350-43DR	Erba Deep	20°44.05'N/38°11.73'E	20°44.41'N/38°11.73'E	2378 - 2283	salty pillow basalts
64PE350-51DR	Port Sudan Deep	20°11.46'N/38°21.37'E	20°11.59'N/38°21.31'E	1941 - 1890	pillow, blocky, sheet flow basalt
64PE350-49GC	Port Sudan Deep	20°04.23'N/38°30.60'E	-	2701	basalt and glass fragments
DUF0073-C1011[b]	Suakin Deep	19°37.40'N/38°46.50'E	-	2746	-
DUF0073-C1012[b]	Suakin Deep	19°36.50'N/38°43.60E	-	2777	-
64PE350-77DR	Suakin Deep	19°36.06'N/38°45.19'E	19°36.28'N/38°45.18'E	2596 - 2477	basalt glass coated by Mn crust
SON0029-247DR[b]	RSR 18°N	18°09.0'N/39°59.58'E	-	-	-
64PE351-10DR	RSR 18°N	17°58.32'N/40°04.59'E	17°58.26'N/40°04.60'E	1670 - 1630	glass fragments
64PE351-9DR	RSR 17°N	16°46.98'N/40°48.97'E	16°46.83'N/40°48.96'E	1389 - 1341	basaltic sheet flows

[a] DR = Dredge, GC = Gravity corer, PC = piston corer, GTV = Video controlled grab.
[b] Sampling locations and lithology after Altherr et al. (1988), Moreira et al. (2000), Haase et al. (1996), Bézos (2003) and PREUSSAG core data.

3.2 Geochemistry

The chlorine, major and trace element data are presented in Fig. 2 and Table 2. All glasses are very homogeneous in major and trace elements and no gradient is observed in the glasses from the centre of a sample to the rim attached to sediment. Trace element patterns are strongly variable between samples and differ from N-MORB to E-MORB, with the exception of the sample from 17°N, which displays an OIB signature. There is no continental input visible in most of the basaltic samples (Fig. 2a). The trace element concentrations are consistent with the range for Red Sea samples described in Altherr et al. (1988).

Chlorine concentrations in the Red Sea basalts range from 58.7 ppm up to 1398.5 ppm and are higher than average for slow-spreading ridges (generally <600 ppm for enriched samples, but <200 ppm for depleted samples (Michael and Schilling, 1989)). No correlation between Cl and MgO is observed (Fig. 2b), nor between Cl and any other element (Table 2). Relative to K and Nb, Cl concentrations are also high with values of up to 1.7 for Cl/K and 530 for Cl/Nb. These values are much higher than for average slow-spreading ridges (e.g. Cl/K <0.1), but also higher than observed at e.g. Kolbeinsey Ridge and at fast spreading ridges (Fig. 2c; Cl/K <0.6 and <0.8 respectively (Michael and Cornell, 1998). Cl/K against Cl/Nb displays a general covariation (R^2=0.8; fig. 2d), indicating a relation between K and Nb and an increase in Cl, rather than a change in only K or Nb, confirmed by the lack of a negative correlation between Cl/K against K or Cl/Nb against Nb (Fig. 2e). As K is more mobile and more easily affected by alteration processes and Nb is closer to Cl in its distribution coefficient (Sun et al., 2007), we will focus on Cl/Nb in the following discussions, although Cl/K displays the same relations.

Chlorine concentrations and Cl/Nb in a basalt sample are homogeneous within a glass chip and mostly also homogeneous over three glass chips of the same sample. There are a few exceptions: 370DC-RS107 displays a variation of ~110 ppm

Cl between glass chips and a variation in Cl content of less than 30 ppm is observed for 13DR-2c, 50DR-1, 50DR-4, 50DR-5 and 33DR-5, with variations in Cl/Nb or Cl/K close to analytical error. To study if there is a difference between the top (T) and bottom (B) glass rim of a basalt sample, we measured for 9DR-1 (RSR17°N) and 19DR-1 (Hatiba Deep) Cl on glass from both sides. For 19DR-2 no difference in the Cl concentration is observed, for 9DR-1 the bottom layer is 20 ppm Cl higher. The variation in Cl/K and Cl/Nb for these samples is close to analytical error. Additional and sometimes larger differences can be observed in KL9-2, 23DR-9, 29SL, 32DR, 448GC, 37DR, 57DR and 51DR. However, those samples consist either of different rock pieces, or loose glass recovered by sediment traps in the dredges or cores. As these Cl variations are often accompanied by variations in major and trace elements, these glass chips are in most cases presumably not derived from the same rock, but represent different rock samples (i.e. from different eruptions of magma).

As with the absolute Cl contents, Cl/Nb is decoupled from MgO and all other measured elements (Fig. 2f; table 2). No correlation is observed for Cl/Nb with element ratios that can either identify magmatic processes and source variations (e.g. CO_2/Nb, Na_8, La/Sm, Pb/Ce, U/Nb (e.g. Hofmann et al., 1986; Langmuir et al., 1992; Miller et al., 1994; Saal et al., 2002; see fig. 2g,h) or could be influenced by seawater alteration or hydrothermal interaction (e.g. U/Th, Sr/Eu, Sr- and Eu-anomalies; table 2). Only a weak negative correlation between the fertility of the samples and chlorine enrichment can be observed; very high Cl/Nb or Cl/K values (<50 and <0.11 respectively) are not observed for the more fertile samples, i.e. with K/Ti >0.25 (Fig. 2c).

The highest Cl/Nb values (>100) are found in the Hadarba, Hatiba, Southern Atlantis II, Discovery and Port Sudan Deeps. The lowest values (Cl/Nb <50) are found at Shaban, Nereus, Northern Atlantis II, Shagara, Suakin Deeps and at RSR 18°N and 17°N (Fig 3). There is no strong relation between Cl/Nb and the sampling latitude. Although the highest Cl/Nb are mainly found in the Central Red Sea between 20°N and 23°N, low Cl/Nb are also found there. Chlorine enrichment can vary on the scale of a Deep at e.g. Shaban, Mabahiss, Hatiba and Atlantis II Deeps, and also within one dredge or core (e.g. 29SL, 32DR, 37DR, 448GC; fig 3; table 2). Chlorine enrichment is not related to the presence or absence of a brine in a Deep, for example low Cl/Nb occurs both in the brine-filled Shaban Deep and at the brine-free RSR, while high Cl/Nb occurs both in the brine-filled Atlantis II Deep and the non-brine filled Hadarba Deep. Atlantis II, Discovery and Port Sudan Deeps that all contain high temperature brines have high Cl/Nb samples. There is no relation between Cl/Nb and sampling depth.

Calculations of the depth of last equilibration of the lava with the three-phase olivine-plagioclase-clinopyroxene assemblage using the inverse method described in Almeev et al. (2008), yield equilibration pressures between 10-570 MPa. Samples from RSR 17° N have an OIB geochemical signature with high H_2O contents (0.9-1.3 wt.%) - our calculations of partial crystallization pressures for these melts demonstrate strong suppression of plagioclase and olivine crystallization relative to clinopyroxene, with the latter being the only phase observed in equilibrium with such "hydrous" melt compositions. Additionally, some of the samples studied have magmatic MgO >8 and so may not have fractionated sufficiently to reach the three-phase cotectic before eruption, invalidating one of the basic assumptions of the calculations. These samples might then give false pressure estimates (marked in very light blue if fig. 2j). The average pressure of all Red Sea samples is 251 ±124 MPa (238 MPa for samples <8 MgO). There is no relation between Cl enrichment and calculated depth of last crystallization (Fig. 2j).
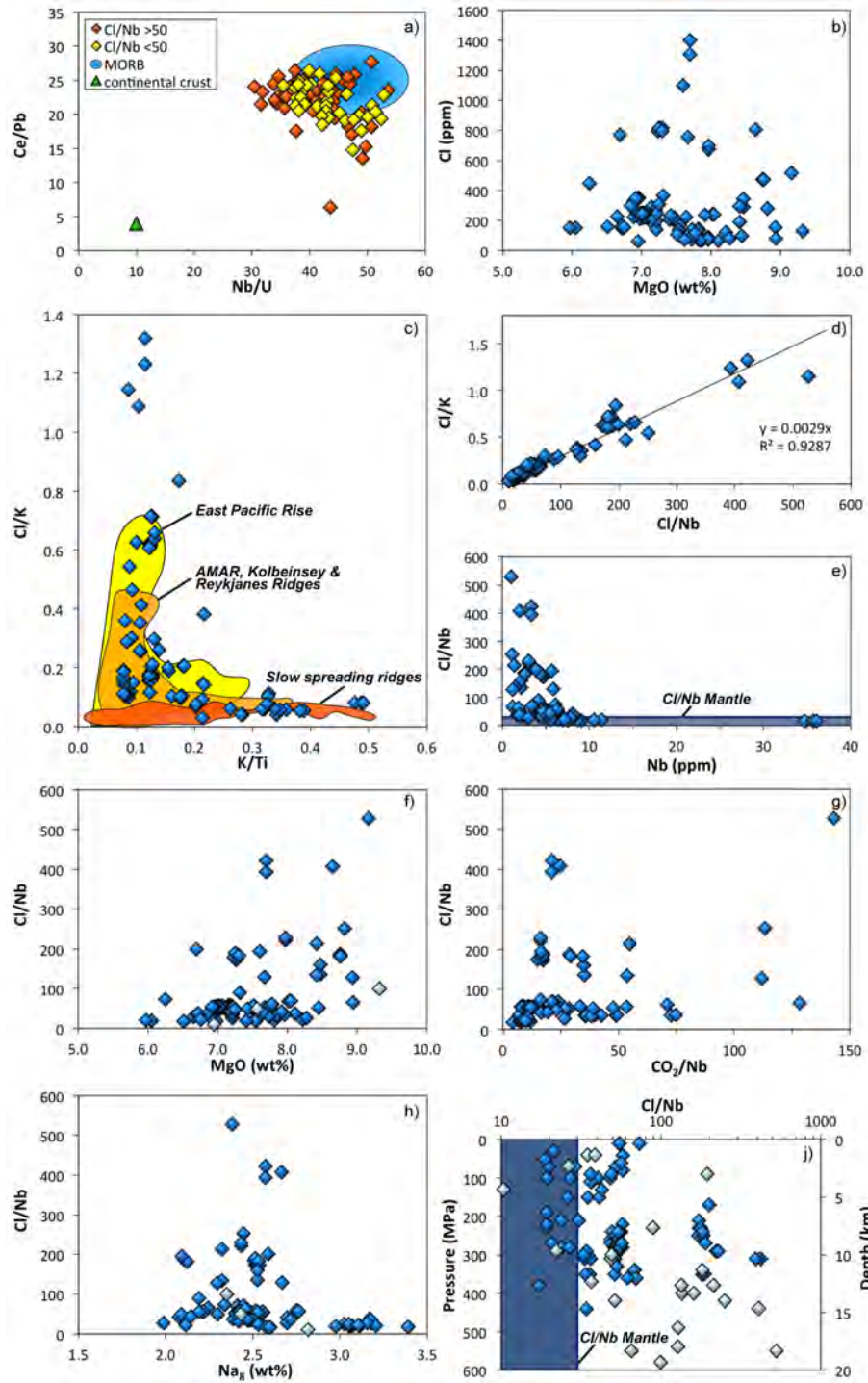
Fig. 2 – Chlorine, major and trace element compositions of the Red Sea basalt glasses. **(a)** Ce/Pb vs. Nb/U indicate that almost all samples overlap the MORB field of Hofmann et al. (1986), regardless of Cl enrichment. **(b)** No correlation can be observed between Cl and indicators of differentiation (MgO). **(c)** Cl/K ratios in Red Sea basalts are much higher than reported for both slow and fast spreading ridges (data from Michael and Cornell, 1998). Trace element enriched samples with K/Ti ratios >0.25 do not have high Cl/K ratios. **(d)** A positive correlation between Cl/K and Cl/Nb show a relative enrichment in Cl compared to both K and Nb for many of the samples. **(e)** Cl/Nb of most samples is significantly higher than Cl/Nb of the mantle. The lack of a negative correlation of Cl/Nb with Nb indicates that high Cl/Nb is the effect of Cl enrichment rather than Nb depletion. **(f-h)** Cl/Nb is not related to indicators of differentiation (MgO), degassing (CO_2/Nb) or melting (Na_8). For the light coloured samples Nb was not measured and Cl/Nb is based on the relation with Cl/K. **(j)** Cl enrichment displays not relation to calculated last crystallisation pressure. Light coloured samples have higher uncertainties due to estimated H_2O values (by H_2O/K relation) or MgO>8.

29

Table 2
Chlorine, volatile and major element data[a]

Sample[b]	Cl	2SE Cl	K	Nb	Cl/K	Cl/Nb	SiO$_2$	TiO$_2$	Al$_2$O$_3$	FeO	MnO	MgO	CaO	Na$_2$O	P$_2$O$_5$	H$_2$O	CO$_2$
M31/2 KL9-1[c]	166.9	3.0	2057	4.5	0.08	37.0	50.7	1.66	15.2	8.4	0.18	7.2	11.8	3.4	-	0.46	40
M31/2 KL9-2 (1,2)[c]	137.3	1.1	2025	5.3	0.07	26.1	50.1	1.67	15.5	8.7	0.15	7.2	12.2	3.4	-	0.46	42
M31/2 KL9-2 (3)[c]	196.4	2.4	2133	5.6	0.09	35.0	50.1	1.67	15.5	8.7	0.15	7.2	12.2	3.4	-	0.46	42
M31/2 88PC[c]	156.4	1.2	3803	9.1	0.04	17.3	51.5	1.86	16.6	8.8	0.15	6.5	9.3	3.9	-	0.69	38
M31/2 DR3-1[c]	166.1	0.5	2869	7.0	0.06	23.8	50.3	1.34	15.3	8.2	0.15	7.5	12.0	3.2	-	0.39	64
M31/2 DR3-2[c]	166.6	0.6	2872	8.6	0.06	19.3	50.7	1.38	15.5	8.3	0.17	7.6	11.9	3.2	-	0.44	103
M31/2 DR3-3[c]	133.8	0.4	2181	7.0	0.06	19.2	50.5	1.39	15.4	8.2	0.13	7.5	12.0	3.2	-	0.32	51
M31/2 DR2-1[c]	148.2	1.8	3559	7.6	0.04	19.5	51.7	2.10	15.4	9.6	0.18	6.1	9.7	3.8	-	0.62	b.d.l.
M31/2 DR2-2[c]	147.8	0.7	3603	7.4	0.04	19.9	51.3	2.15	15.2	9.4	0.20	6.0	9.7	3.6	-	0.70	b.d.l.
M31/2 88GTV[c]	215.1	0.9	3975	11.4	0.05	18.9	51.0	1.71	15.3	8.2	0.15	7.0	11.6	3.3	-	0.56	b.d.l.
M31/2 DR1-1[c]	133.5	1.5	2242	5.6	0.06	24.0	50.3	1.17	15.4	8.3	0.13	7.8	12.2	3.1	-	0.29	61
M31/2 DR1-2[c]	204.0	2.0	3771	10.5	0.05	19.4	50.4	1.65	15.6	8.0	0.15	7.4	11.7	3.3	-	0.49	79
M31/2 DR1-3[c]	143.1	1.1	2328	5.3	0.06	27.0	50.7	1.15	15.6	8.2	0.15	7.8	12.2	3.2	-	0.29	46
M31/2 DR1-4[c]	134.4	1.1	2231	6.4	0.06	20.9	50.5	1.18	15.4	8.0	0.14	7.8	12.2	3.2	-	0.28	51
SON0029-370DC RS107 (1)	327.9	13.4	2888	8.1	0.11	40.5	50.9	1.47	14.7	10.2	0.20	6.9	11.4	3.0	0.12	0.33	62
SON0029-370DC RS107 (2,3)	219.9	1.3	2872	8.1	0.08	27.2	50.9	1.47	14.7	10.2	0.20	6.9	11.4	3.0	0.12	0.33	62
SON0029-370DC RS108	297.1	1.8	2880	8.2	0.10	36.3	51.2	1.47	14.7	10.3	0.19	6.8	11.3	3.0	0.11	0.34	58
NORGMRO-KS04B[c]	225.9	2.2	2900	7.8	0.08	28.9	51.5	1.50	14.9	10.2	0.18	6.6	11.2	2.8	0.12	0.38	-
64PE351 14DR-1	273.6	2.1	1925	4.7	0.14	58.0	50.8	1.48	14.7	9.7	0.17	7.2	12.2	3.0	0.10	0.27	43
64PE351 14DR-2	271.9	2.6	1916	5.2	0.14	52.2	51.0	1.48	14.6	9.9	0.18	7.2	12.1	2.9	0.10	0.27	50
64PE351 14DR-3	287.3	3.0	1936	5.0	0.15	57.9	50.9	1.50	14.5	10.0	0.18	7.1	12.2	3.0	0.10	0.28	40
64PE351 14DR-4	272.5	2.8	1919	4.8	0.14	56.3	50.8	1.48	14.5	9.9	0.19	7.2	12.2	3.0	0.10	0.27	38
NORGMRO-KS11B[cde]	58.7	1.1	1891	-	0.03	10.3	51.1	1.48	14.7	10.1	0.19	7.0	11.2	3.1	0.17	0.32	-
NORGMRO-KS12[c]	63.8	0.7	635	1.7	0.10	36.7	49.7	1.23	15.6	10.4	0.21	8.1	12.1	2.4	0.09	0.43	-
64PE351 13DR-2c (1,2)[d]	144.9	1.4	1513	4.2	0.10	34.7	51.1	1.44	14.2	11.6	0.20	6.7	11.5	2.8	0.12	0.26	-
64PE351 13DR-2c (3)[d]	161.7	2.3	1537	4.2	0.11	38.8	51.1	1.44	14.2	11.6	0.20	6.7	11.5	2.8	0.12	0.26	-
DUF0073 C1035[d]	365.7	0.7	1398	4.1	0.26	89.1	49.8	1.68	14.7	11.3	0.19	7.3	11.7	2.3	0.14	0.24	-
64PE350 23DR-1	812.9	3.0	1312	4.7	0.62	173.1	49.7	1.77	14.6	11.6	0.20	7.3	11.6	2.7	0.15	0.27	82
64PE350 23DR-2	814.2	2.1	1305	4.7	0.62	172.3	49.8	1.77	14.5	11.5	0.21	7.3	11.6	2.7	0.16	0.28	82
64PE350 23DR-3	814.4	2.3	1311	4.4	0.62	184.7	50.0	1.77	14.6	11.5	0.18	7.3	11.7	2.7	0.15	0.23	76
64PE350 23DR-4	808.6	1.9	1315	4.7	0.61	173.7	50.0	1.77	14.5	11.5	0.22	7.3	11.6	2.7	0.15	0.28	70
64PE350 23DR-5	794.4	0.2	1308	4.4	0.61	178.6	49.8	1.78	14.6	11.6	0.22	7.2	11.6	2.7	0.15	0.27	75

Sample[b]	Cl	2SE Cl	K	Nb	Cl/K	Cl/Nb	SiO_2	TiO_2	Al_2O_3	FeO	MnO	MgO	CaO	Na_2O	P_2O_5	H_2O	CO_2
64PE350 23DR-6A	811.0	2.2	1312	4.3	0.62	189.6	49.6	1.77	14.7	11.5	0.21	7.2	11.6	2.7	0.16	0.27	75
64PE350 23DR-7	795.5	0.8	1310	4.3	0.61	183.2	49.8	1.79	14.5	11.6	0.21	7.3	11.6	2.7	0.15	0.27	75
64PE350 23DR-9 (1)	1398.5	5.4	1060	3.3	1.32	421.6	49.7	1.54	14.7	11.1	0.19	7.7	11.9	2.6	0.12	0.22	70
64PE350 23DR-9 (2,3)	1305.6	5.0	1060	3.3	1.23	393.6	49.7	1.54	14.7	11.1	0.19	7.7	11.9	2.6	0.12	0.22	70
POS408/1 26GC	767.3	2.5	1224	3.8	0.63	199.8	49.2	2.04	13.9	12.5	0.19	6.7	11.0	2.9	0.16	0.30	b.d.l.
POS408/1 50DR-1 (1,2)	238.9	0.5	1357	4.2	0.18	56.3	49.7	1.86	14.6	11.8	0.16	7.0	11.3	2.6	0.17	0.30	50
POS408/1 50DR-1 (3)	232.0	0.4	1357	4.2	0.17	54.7	49.7	1.86	14.6	11.8	0.16	7.0	11.3	2.6	0.17	0.30	50
POS408/1 50DR-2	212.2	1.9	1351	4.3	0.16	49.6	49.7	1.86	14.6	11.9	0.15	7.0	11.3	2.7	0.16	0.30	48
POS408/1 50DR-3	211.4	1.1	1354	4.3	0.16	48.8	49.6	1.84	14.7	11.8	0.19	7.0	11.3	2.6	0.17	0.29	72
POS408/1 50DR-4 (1,2)	212.9	0.5	1350	4.2	0.16	51.2	49.3	1.79	14.5	11.8	0.21	7.1	11.1	2.6	0.16	0.29	68
POS408/1 50DR-4 (3)	220.1	0.0	1350	4.2	0.16	53.0	49.3	1.79	14.5	11.8	0.21	7.1	11.1	2.6	0.16	0.29	68
POS408/1 50DR-5 (1,3)	216.5	2.2	1352	4.4	0.16	48.7	49.6	1.85	14.7	11.9	0.17	7.0	11.3	2.7	0.18	0.29	52
POS408/1 50DR-5 (2)	248.7	2.2	1368	4.4	0.18	55.9	49.6	1.85	14.7	11.9	0.17	7.0	11.3	2.7	0.18	0.29	52
POS408/1 50DR-6	220.3	2.0	1355	4.2	0.16	51.9	49.4	1.80	14.6	11.8	0.19	7.1	11.1	2.6	0.17	0.30	71
POS408/1 57DR (1,2,4)	219.2	2.5	1324	4.3	0.17	51.5	49.5	1.79	14.9	11.9	0.19	7.5	11.3	2.7	0.14	0.30	122
POS408/1 57DR (3)	234.1	3.1	1393	4.5	0.17	51.7	49.7	1.86	14.8	12.2	0.23	7.1	11.4	2.7	0.14	0.30	122
POS408/1 19DR-1	232.7	0.8	1386	4.4	0.17	52.7	49.6	1.81	14.6	11.7	0.21	7.1	11.1	2.7	0.17	0.29	69
POS408/1 19DR-2T	231.2	2.1	1376	4.3	0.17	53.2	49.1	1.86	14.4	12.1	0.18	7.2	11.2	2.7	0.17	0.31	51
POS408/1 19DR-2B	230.8	1.3	1377	4.5	0.17	51.3	49.0	1.88	14.3	12.1	0.15	7.1	11.2	2.7	0.17	0.31	50
POS408/1 19DR-3	230.8	1.3	1377	4.5	0.17	51.4	49.4	1.82	14.5	11.8	0.23	7.2	11.0	2.7	0.16	0.30	68
POS408/1 19DR-4	232.0	1.6	1381	4.4	0.17	52.2	49.6	1.82	14.5	11.8	0.23	7.2	11.0	2.6	0.18	0.29	67
POS408/1 19DR-5	232.3	1.5	1384	4.3	0.17	54.2	49.1	1.85	14.3	12.0	0.16	7.2	11.2	2.7	0.16	0.31	49
POS408/1 51DR (2)[e]	225.5	4.2	1361	4.4	0.17	51.4	49.6	1.83	14.8	12.0	0.20	7.2	11.4	2.7	0.15	*0.30*	-
POS408/1 51DR (1,3)[e]	213.2	0.6	1361	4.4	0.16	48.6	49.6	1.83	14.8	12.0	0.20	7.2	11.4	2.7	0.15	*0.30*	-
POS408/1 58DR-1	244.3	1.9	1385	4.5	0.18	53.8	49.5	1.83	14.5	11.8	0.21	7.0	11.1	2.7	0.17	0.30	66
POS408/1 58DR-2	246.4	1.4	1386	4.5	0.18	54.9	49.3	1.83	14.5	11.7	0.22	7.0	11.0	2.7	0.16	0.30	69
POS408/1 58DR-3	245.1	0.9	1387	4.6	0.18	53.0	49.8	1.89	14.7	11.8	0.19	6.9	11.2	2.7	0.18	0.30	47
POS408/1 58DR-4	245.1	1.7	1359	4.6	0.18	53.4	49.8	1.84	14.6	11.6	0.18	7.2	11.1	2.7	0.17	0.30	49
POS408/1 58DR-5	247.5	2.9	1394	4.6	0.18	54.4	49.7	1.88	14.6	11.9	0.16	7.0	11.2	2.7	0.16	0.31	37
POS408/1 58DR-6	245.7	2.1	1389	4.5	0.18	55.1	49.4	1.83	14.6	11.9	0.20	7.0	11.1	2.7	0.18	0.30	64
POS408/1 58DR-7	246.2	1.0	1383	4.5	0.18	54.2	49.5	1.83	14.5	11.9	0.23	7.0	11.0	2.7	0.17	0.30	72
POS408/1 18DR-1	248.1	0.2	1389	4.3	0.18	57.5	49.4	1.83	14.5	11.8	0.21	7.1	11.1	2.7	0.18	0.29	64
POS408/1 18DR-2	244.2	2.5	1389	4.4	0.18	55.9	49.3	1.83	14.5	11.7	0.23	7.0	11.0	2.7	0.17	0.29	64
POS408/1 18DR-3	245.2	1.7	1384	4.3	0.18	57.3	49.3	1.88	14.3	12.0	0.18	7.0	11.3	2.7	0.16	0.31	47

Sample[b]	Cl	2SE Cl	K	Nb	Cl/K	Cl/Nb	SiO$_2$	TiO$_2$	Al$_2$O$_3$	FeO	MnO	MgO	CaO	Na$_2$O	P$_2$O$_5$	H$_2$O	CO$_2$
POS408/1 18DR-4	245.7	2.5	1384	4.5	0.18	54.9	49.3	1.86	14.4	12.0	0.16	7.0	11.2	2.8	0.17	0.31	47
POS408/1 17GC	241.7	0.3	1385	4.5	0.17	53.9	49.2	1.88	14.3	12.0	0.16	7.0	11.2	2.7	0.17	0.31	50
POS408/1 28GC	277.3	2.0	510	1.1	0.54	251.4	49.2	0.97	15.5	9.2	0.15	8.8	13.2	2.3	0.06	0.09	125
POS408/1 29GC (1)	290.2	2.0	823	2.1	0.35	135.4	49.9	1.29	14.8	10.6	0.20	8.5	12.0	2.4	0.08	0.09	75
POS408/1 29GC (2,3)	344.5	4.2	834	2.2	0.41	159.9	49.9	1.29	14.8	10.6	0.20	8.5	12.0	2.4	0.08	0.09	75
POS408/1 29GC (5)	292.6	4.3	630	1.4	0.46	212.8	50.0	1.13	15.0	10.5	0.16	8.4	12.5	2.2	0.09	0.09	75
POS408/1 29GC (6)	188.0	11.3	622	1.4	0.30	134.1	50.0	1.13	15.0	10.5	0.16	8.4	12.5	2.2	0.09	0.09	75
64PE350 33DR-2	239.1	1.4	933	3.4	0.26	69.7	49.7	1.45	14.9	11.2	0.21	8.0	12.1	2.4	0.10	0.19	82
64PE350 33DR-4	69.4	0.9	643	2.0	0.11	34.1	50.3	1.35	14.6	11.2	0.19	7.8	12.0	2.5	0.10	0.14	99
64PE350 33DR-5 (1)	87.6	0.9	746	2.5	0.12	35.6	49.8	1.38	14.6	11.2	0.20	8.0	11.9	2.5	0.09	0.14	98
64PE350 33DR-5 (2)	71.3	2.3	656	2.0	0.11	35.9	49.8	1.38	14.6	11.2	0.20	8.0	11.9	2.5	0.09	0.14	98
64PE350 33DR-5 (3)	78.4	1.2	703	2.3	0.11	34.0	49.8	1.38	14.6	11.2	0.20	8.0	11.9	2.5	0.09	0.14	98
64PE350 33DR-6	67.2	0.8	641	2.0	0.10	32.9	50.2	1.35	14.6	11.2	0.19	7.8	12.0	2.5	0.09	0.14	78
64PE350 33DR-7	238.4	1.1	928	3.5	0.26	68.4	49.7	1.46	14.9	11.0	0.20	8.0	12.1	2.4	0.11	0.19	76
64PE350 33DR-8	238.9	1.3	930	3.4	0.26	70.0	49.8	1.47	14.9	11.0	0.20	8.0	12.1	2.4	0.11	0.18	72
64PE350 33DR-10	68.5	1.2	644	2.0	0.11	34.2	50.2	1.35	14.6	11.2	0.21	7.9	12.0	2.5	0.09	0.14	71
64PE350 33DR-11	67.1	1.1	642	2.0	0.10	33.3	50.3	1.34	14.7	11.1	0.20	7.9	12.0	2.5	0.09	0.13	72
64PE350 33DR-12	70.5	0.6	643	1.9	0.11	36.3	50.0	1.33	14.6	11.0	0.21	7.8	12.0	2.5	0.09	0.14	76
64PE350 33DR-13	71.3	1.4	649	2.0	0.11	35.0	50.2	1.33	14.6	11.2	0.20	7.9	12.0	2.5	0.09	0.14	73
VA29-365GC_KII	71.8	1.0	643	2.1	0.11	34.2	50.1	1.32	15.1	11.1	0.20	7.7	11.6	2.6	0.09	0.09	152
DUF0073 DR68 [e]	755.7	3.7	1981	5.9	0.38	128.4	49.2	1.53	16.1	10.1	0.18	7.7	11.6	2.7	0.11	*0.33*	-
64PE350 32DR (1)	672.9	1.7	1052	3.0	0.64	220.9	49.8	1.34	15.0	10.4	0.20	8.0	12.4	2.4	0.09	0.27	49
64PE350 32DR (2)	695.4	2.7	1054	3.0	0.66	228.3	49.8	1.34	15.0	10.4	0.20	8.0	12.4	2.4	0.09	0.27	49
64PE350 32DR (3,4)	139.5	1.3	1354	4.6	0.10	30.6	50.3	1.40	14.6	11.0	0.21	7.7	12.0	2.5	0.11	0.27	49
64PE350 32DR (5,7)	122.3	2.2	1612	5.5	0.08	22.1	49.9	1.33	15.2	9.6	0.19	8.2	12.7	2.5	0.12	0.27	49
64PE350 32DR (6)	804.8	2.2	740	2.0	1.09	407.3	49.2	1.19	15.3	10.2	0.21	8.6	12.2	2.5	0.09	0.27	49
SO02-488GC (1)	152.6	3.0	423	1.2	0.36	127.6	49.3	0.87	16.1	9.5	0.14	8.9	13.0	2.1	0.06	0.08	134
SO02-488GC (2,12)	95.6	1.1	641	1.9	0.15	51.6	49.9	1.13	15.5	10.0	0.14	8.4	12.5	2.3	0.08	0.15	72
SO02-488GC (3,6) [de]	91.2	1.4	638	-	0.14	**49.3**	50.3	1.35	14.9	11.3	0.19	7.6	12.0	2.5	0.09	*0.14*	-
SO02-488GC (4,9)	100.0	1.8	619	1.9	0.16	53.0	50.2	1.31	15.0	11.1	0.18	7.7	12.0	2.5	0.09	0.14	90
SO02-488GC (5)	514.2	14.7	449	1.0	1.15	527.4	49.6	0.87	16.2	8.9	0.19	9.2	13.1	2.1	0.07	0.08	139
SO02-488GC (7,8,16)	96.6	1.4	626	1.7	0.15	55.7	50.0	1.34	14.6	11.2	0.21	7.7	12.2	2.5	0.09	0.14	93
SO02-488GC (10)	78.5	3.6	409	1.2	0.19	65.3	49.2	0.88	16.2	9.5	0.17	8.9	13.0	2.1	0.07	0.08	154
SO02-488GC (11)	107.8	5.7	641	1.9	0.17	56.8	50.4	1.38	14.8	11.2	0.22	7.5	12.0	2.5	0.10	0.15	63

Sample[b]	Cl	2SE Cl	K	Nb	Cl/K	Cl/Nb	SiO₂	TiO₂	Al₂O₃	FeO	MnO	MgO	CaO	Na₂O	P₂O₅	H₂O	CO₂
SO02-488GC (13)[de]	*129.3*	*2.3*	*449*	*-*	*0.29*	*99.3*	*49.7*	*0.90*	*16.3*	*8.8*	*0.13*	*9.3*	*13.0*	*2.1*	*0.05*	*0.08*	*-*
SO02-488GC (14,15)	114.8	3.7	611	1.9	0.19	61.9	50.2	1.31	15.0	11.0	0.19	7.8	12.0	2.5	0.09	0.13	132
64PE350 37DR (1,3)	71.3	2.6	628	2.0	0.11	36.4	50.0	1.35	14.1	11.5	0.22	7.6	12.2	2.6	0.10	0.34	146
64PE350 37DR (2)	305.6	0.9	1515	6.3	0.20	48.3	49.2	2.01	13.8	12.9	0.20	7.3	11.1	2.4	0.19	0.34	146
64PE350 41DR	447.9	1.8	1499	6.1	0.30	73.4	50.4	1.92	13.4	13.6	0.25	6.3	11.0	2.7	0.16	0.30	99
64PE350 43DR-1	349.0	1.6	1683	6.3	0.21	55.1	50.7	1.55	13.6	12.1	0.24	7.0	11.8	2.4	0.13	0.24	79
64PE350 43DR-2	343.1	2.2	1671	6.2	0.21	54.9	50.7	1.55	13.6	12.3	0.22	6.9	11.8	2.4	0.13	0.24	82
64PE350 43DR-3	346.6	2.1	1680	6.3	0.21	55.0	50.8	1.54	13.7	12.3	0.25	6.9	11.8	2.4	0.13	0.24	77
64PE350 51DR-1	469.9	1.7	660	2.5	0.71	187.2	49.8	0.87	15.2	10.1	0.18	8.8	13.2	2.0	0.06	0.10	72
64PE350 51DR-2	472.3	0.8	660	2.6	0.72	181.8	49.8	0.87	15.2	10.0	0.19	8.7	13.2	2.0	0.06	0.10	76
64PE350 51DR-3	472.0	1.1	661	2.6	0.71	182.0	49.7	0.88	15.2	9.9	0.20	8.8	13.2	2.0	0.05	0.10	90
64PE350 49GC-2	1097.6	0.5	1315	5.6	0.83	194.5	50.5	1.27	14.2	11.5	0.21	7.6	12.3	2.2	0.10	0.21	92
DUF0073 C1011	221.1	2.0	1170	5.4	0.19	41.1	51.1	1.26	14.4	11.7	0.21	7.6	11.3	2.1	0.11	0.30	89
DUF0073 C1012	230.9	1.8	1092	4.7	0.21	49.0	50.8	1.43	13.9	12.9	0.23	7.4	10.9	2.2	0.12	0.29	-
64PE350 77DR-1	234.3	0.7	1166	5.5	0.20	42.8	50.4	1.26	14.1	11.7	0.20	7.9	11.8	2.2	0.10	0.24	105
SON0029-247-RS37	154.3	0.9	1528	7.2	0.10	21.5	50.9	1.45	13.8	12.7	0.21	6.8	10.8	2.3	0.13	0.33	70
64PE351 10DR	78.2	0.9	675	3.0	0.12	26.4	51.1	0.91	14.5	10.0	0.18	8.3	13.3	1.9	0.07	0.14	79
64PE351 9DR-1T	560.5	0.8	6893	34.7	0.08	16.2	50.8	2.36	13.6	13.3	0.27	4.5	9.1	3.4	0.41	1.26	b.d.l.
64PE351 9DR-1B	581.6	1.5	7122	35.7	0.08	16.3	51.1	2.50	13.1	14.2	0.24	4.5	9.0	3.4	0.43	1.23	b.d.l.
64PE351 9DR-2	570.2	1.2	7011	36.1	0.08	15.8	50.9	2.39	13.5	13.5	0.24	4.4	9.0	3.4	0.42	0.90	b.d.l.

Table 2 continued
Trace element data

Sample	Li	Be	B	Ni	Sc	Rb	Sr	Y	Zr	Cs	Ba	La	Ce	Pr	Nd	Sm	Eu
M31/2 KL9-1[c]	-	-	-	78.3	52.4	4.8	191.0	30.1	108.0	0.09	39.4	5.1	14.3	2.3	11.7	3.7	1.33
M31/2 KL9-2 (1,2)[c]	6.0	0.79	2.4	72.3	41.0	5.8	187.1	28.6	109.4	0.06	40.3	5.4	15.1	2.4	12.8	4.0	1.48
M31/2 KL9-2 (3)[c]	6.6	0.71	2.7	58.3	42.7	6.0	188.8	30.2	116.0	0.04	42.6	5.6	16.5	2.7	13.3	4.3	1.54
M31/2 88PC[c]	8.4	1.05	4.3	53.9	32.3	10.4	164.1	44.0	184.9	0.09	66.7	8.6	25.4	4.0	19.6	6.3	1.95
M31/2 DR3-1[c]	-	-	-	97.9	35.7	6.9	158.0	24.0	76.3	0.10	62.1	5.6	13.1	1.9	9.5	2.8	1.07
M31/2 DR3-2[c]	5.7	0.59	2.1	65.3	37.8	9.2	153.6	24.6	79.6	0.09	67.5	6.0	14.7	2.1	10.2	3.1	1.17
M31/2 DR3-3[c]	-	-	-	133.0	37.0	6.8	173.0	23.6	78.3	0.15	60.9	5.4	12.9	1.9	9.1	2.8	1.06
M31/2 DR2-1[c]	-	-	-	65.9	34.5	8.5	185.0	47.4	189.0	0.15	64.4	8.4	24.0	3.9	20.0	5.9	1.92
M31/2 DR2-2[c]	-	-	-	63.8	33.9	8.3	181.0	46.3	188.0	0.14	64.7	8.4	23.8	3.8	19.4	6.0	1.87
M31/2 88GTV[c]	6.3	0.80	2.9	66.7	39.6	11.6	216.4	28.2	123.9	0.11	87.9	8.6	22.1	3.3	16.0	4.2	1.57

Sample	Li	Be	B	Ni	Cu	Zn	Sc	Rb	Sr	Y	Zr	Cs	Ba	La	Ce	Pr	Nd	Sm	Eu
M31/2 DR1-1 [c]	-	-	-	96.1	115.0	79.5	36.4	5.8	145.0	22.7	56.3	0.11	55.0	4.3	10.1	1.5	7.8	2.6	0.96
M31/2 DR1-2 [c]	5.5	0.85	2.5	71.9	86.8	90.3	38.5	10.4	210.8	26.2	113.0	0.09	80.1	8.1	20.4	2.9	13.3	4.0	1.37
M31/2 DR1-3 [c]	-	-	-	97.0	107.0	76.9	34.3	5.4	137.0	21.6	53.0	0.10	55.4	4.4	10.3	1.6	7.8	2.6	0.99
M31/2 DR1-4 [c]	5.1	0.44	1.7	79.2	137.8	91.9	36.7	7.0	137.4	20.9	55.6	0.06	55.5	4.3	10.5	1.6	7.8	2.6	1.01
SON0029-370DC RS107 (1)	6.0	0.45	1.7	47.5	173.4	107.9	41.1	10.3	119.7	28.4	69.4	0.08	71.3	5.4	12.8	1.9	9.6	3.3	1.22
SON0029-370DC RS107 (2,3)	6.0	0.45	1.7	47.5	173.4	107.9	41.1	10.3	119.7	28.4	69.4	0.08	71.3	5.4	12.8	1.9	9.6	3.3	1.22
SON0029-370DC RS108	6.0	0.35	1.7	48.0	176.9	106.9	41.5	10.4	120.9	28.5	70.6	0.08	70.5	5.3	12.6	1.9	10.0	3.4	1.24
NORGMRO-KS04B	6.1	0.52	1.7	45.5	179.7	103.4	42.1	10.4	122.0	29.7	71.9	0.04	74.6	5.7	12.4	1.9	9.2	3.3	1.29
64PE351 14DR-1	5.7	0.45	2.3	62.6	176.5	108.8	46.1	6.7	112.4	31.7	73.5	0.04	45.2	4.0	10.3	1.7	9.2	3.6	1.27
64PE351 14DR-2	5.5	0.40	1.9	86.5	158.2	104.6	43.7	5.0	130.7	28.3	75.2	0.04	39.6	4.3	11.6	1.8	9.2	3.3	1.22
64PE351 14DR-3	6.0	0.33	1.8	60.2	186.9	109.0	43.4	6.7	113.7	30.3	70.9	0.05	46.1	3.7	10.2	1.7	9.4	3.4	1.31
64PE351 14DR-4	6.0	0.45	1.9	62.6	184.4	107.7	44.3	6.5	112.2	30.2	70.8	0.05	45.9	3.7	10.1	1.6	9.4	3.2	1.28
NORGMRO-KS11B	-	-	-	-	-	-	-	-	-	-	-	-	-	-	-	-	-	-	-
NORGMRO-KS12	5.0	0.23	1.5	124.7	131.5	108.6	39.6	1.2	95.3	24.8	61.6	0.06	10.8	2.0	6.7	1.1	6.9	2.6	1.00
64PE351 13DR-2c (1,2)	6.4	0.38	1.9	55.4	204.0	116.4	45.2	4.0	97.8	31.1	65.0	0.06	30.6	3.3	8.7	1.5	8.1	3.1	1.13
64PE351 13DR-2c (3)	6.4	0.38	1.9	55.4	204.0	116.4	45.2	4.0	97.8	31.1	65.0	0.06	30.6	3.3	8.7	1.5	8.1	3.1	1.13
DUF0073 C1035	6.7	0.49	1.4	104.8	113.4	125.8	42.4	3.5	90.5	35.3	89.0	0.08	27.2	3.8	10.9	1.8	10.0	3.7	1.31
64PE350 23DR-1	7.3	0.39	2.1	106.9	107.7	132.1	40.7	3.6	97.8	34.2	92.9	0.03	24.7	4.2	13.3	2.2	11.2	4.0	1.45
64PE350 23DR-2	7.0	0.52	2.1	113.6	114.7	138.4	41.6	3.8	99.1	35.4	94.8	0.04	24.4	4.2	13.0	2.2	11.1	4.0	1.47
64PE350 23DR-3	7.1	0.39	2.2	102.3	106.3	129.7	38.5	3.4	94.0	33.4	88.1	0.03	24.5	4.0	12.2	2.1	10.6	3.8	1.35
64PE350 23DR-4	7.4	0.53	2.2	106.7	112.4	135.7	40.3	3.7	97.3	34.6	92.1	0.04	25.1	4.2	13.3	2.2	11.0	3.7	1.41
64PE350 23DR-5	7.1	0.55	2.1	103.3	110.9	131.6	42.2	3.5	93.1	38.0	99.9	0.05	23.6	4.1	12.2	2.1	10.8	3.8	1.40
64PE350 23DR-6A	6.9	0.47	2.0	101.3	107.0	128.9	42.1	3.5	96.1	39.4	99.9	0.03	23.6	4.1	12.0	2.1	11.1	4.1	1.41
64PE350 23DR-7	7.0	0.41	2.1	102.8	108.7	130.5	43.5	3.5	97.1	39.8	105.0	0.02	23.8	4.2	12.6	2.0	11.4	4.2	1.45
64PE350 23DR-9 (1)	6.4	0.39	2.0	119.4	113.0	123.6	41.4	2.9	88.3	33.5	82.4	0.03	19.5	3.2	9.8	1.7	9.1	3.4	1.24
64PE350 23DR-9 (2,3)	6.4	0.39	2.0	119.4	113.0	123.6	41.4	2.9	88.3	33.5	82.4	0.03	19.5	3.2	9.8	1.7	9.1	3.4	1.24
POS408/1 26GC	7.5	0.60	1.9	120.6	101.9	144.8	43.6	2.9	104.7	40.9	113.6	0.03	22.1	4.2	13.3	2.3	12.2	4.5	1.59
POS408/1 50DR-1 (1,2)	7.2	0.31	2.3	100.1	113.3	132.4	42.4	3.8	102.6	39.9	105.5	0.04	24.9	4.2	12.6	2.2	11.8	4.2	1.48
POS408/1 50DR-1 (3)	7.2	0.31	2.3	100.1	113.3	132.4	42.4	3.8	102.6	39.9	105.5	0.04	24.9	4.2	12.6	2.2	11.8	4.2	1.48
POS408/1 50DR-2	7.1	0.58	1.9	101.2	113.1	134.6	41.9	3.8	102.4	39.3	104.1	0.04	24.1	4.2	12.7	2.2	11.6	4.1	1.44
POS408/1 50DR-3	7.1	0.50	1.7	100.8	113.5	135.5	42.1	3.8	102.1	39.5	105.2	0.03	24.8	4.2	12.7	2.1	11.6	4.2	1.44
POS408/1 50DR-4 (1,2)	7.0	0.48	2.0	100.3	112.8	132.0	41.5	3.7	101.0	38.9	104.3	0.04	24.4	4.2	12.4	2.2	11.5	4.1	1.38
POS408/1 50DR-4 (3)	7.0	0.48	2.0	100.3	112.8	132.0	41.5	3.7	101.0	38.9	104.3	0.04	24.4	4.2	12.4	2.2	11.5	4.1	1.38
POS408/1 50DR-5 (1,3)	7.0	0.51	1.9	100.5	116.1	135.0	42.9	3.7	103.5	39.7	105.6	0.04	25.0	4.2	12.5	2.1	11.7	4.4	1.46

Sample	Li	Be	B	Ni	Cu	Zn	Sc	Rb	Sr	Y	Zr	Cs	Ba	La	Ce	Pr	Nd	Sm	Eu
POS408/1 50DR-5 (2)	7.0	0.51	1.9	100.5	116.1	135.0	42.9	3.7	103.5	39.7	105.6	0.04	25.0	4.2	12.5	2.1	11.7	4.4	1.46
POS408/1 50DR-6	7.2	0.35	2.1	101.0	107.6	135.6	41.6	3.8	101.9	39.1	104.7	0.04	24.7	4.3	12.3	2.1	11.3	4.2	1.43
POS408/1 57DR (1,2,4)	7.1	0.44	2.1	116.8	110.5	144.4	41.5	3.7	102.4	38.0	102.5	0.04	23.5	4.0	12.0	2.0	11.3	3.8	1.38
POS408/1 57DR (3)	7.2	0.44	2.3	99.8	109.4	147.5	42.2	3.8	103.8	39.4	107.9	0.04	25.1	4.4	13.0	2.2	11.6	4.1	1.47
POS408/1 19DR-1	7.1	0.55	2.1	107.0	108.9	135.3	41.1	3.8	102.2	38.1	103.4	0.04	24.8	4.3	12.9	2.2	11.9	4.2	1.43
POS408/1 19DR-2T	7.1	0.54	2.3	108.5	109.5	134.7	41.3	3.8	102.5	38.9	105.8	0.05	24.5	4.4	12.8	2.2	11.6	4.2	1.45
POS408/1 19DR-2B	7.3	0.66	2.1	106.7	108.4	143.0	42.4	3.8	104.8	40.2	109.7	0.06	24.9	4.5	13.2	2.2	11.9	4.2	1.47
POS408/1 19DR-3	7.1	0.55	2.1	108.4	110.3	144.3	41.0	3.9	103.3	38.3	104.2	0.06	24.2	4.4	13.2	2.2	11.8	4.3	1.43
POS408/1 19DR-4	7.0	0.48	2.2	109.7	108.4	142.6	42.2	3.8	104.6	40.0	108.1	0.03	24.6	4.4	13.5	2.3	11.5	4.3	1.50
POS408/1 19DR-5	7.1	0.46	1.9	108.0	108.8	134.2	40.8	3.7	102.1	38.6	104.2	0.04	24.6	4.3	13.0	2.2	11.8	4.1	1.44
POS408/1 51DR (2)	7.4	0.49	2.1	101.0	114.1	144.0	43.1	3.8	103.8	40.2	107.5	0.04	25.1	4.3	12.6	2.2	11.7	4.2	1.46
POS408/1 51DR (1,3)	7.4	0.49	2.1	101.0	114.1	144.0	43.1	3.8	103.8	40.2	107.5	0.04	25.1	4.3	12.6	2.2	11.7	4.2	1.46
POS408/1 58DR-1	7.4	0.41	2.0	102.6	107.5	138.4	42.8	3.8	105.4	39.6	109.2	0.05	24.5	4.6	13.3	2.3	11.7	4.3	1.50
POS408/1 58DR-2	7.1	0.46	2.1	100.3	107.7	136.3	41.5	3.8	103.7	39.4	107.5	0.04	25.1	4.4	13.0	2.2	11.8	4.1	1.52
POS408/1 58DR-3	7.2	0.43	2.1	102.0	111.7	132.1	43.6	3.8	107.3	41.4	111.0	0.03	26.0	4.6	13.3	2.2	11.9	4.5	1.50
POS408/1 58DR-4	7.3	0.66	1.9	115.4	112.5	130.5	43.0	3.6	106.7	40.6	108.8	0.04	25.1	4.5	13.2	2.2	11.6	4.4	1.55
POS408/1 58DR-5	7.3	0.55	2.4	101.6	108.0	141.3	42.4	3.9	104.8	39.7	107.6	0.04	25.8	4.5	13.0	2.2	12.0	4.2	1.54
POS408/1 58DR-6	7.5	0.56	2.5	103.5	102.2	132.7	42.8	3.8	107.1	40.7	110.4	0.03	25.4	4.6	13.2	2.3	12.0	4.4	1.52
POS408/1 58DR-7	7.5	0.53	2.2	102.2	102.5	133.4	43.2	3.8	108.1	41.4	110.1	0.03	25.8	4.6	13.6	2.3	12.1	4.4	1.52
POS408/1 18DR-1	7.5	0.60	2.0	100.8	108.9	137.5	42.4	3.7	103.2	39.9	109.1	0.04	25.1	4.5	13.3	2.2	11.9	4.1	1.48
POS408/1 18DR-2	7.2	0.54	2.1	101.1	108.6	138.3	41.8	3.8	102.0	39.8	107.3	0.03	24.0	4.3	12.9	2.2	11.7	4.1	1.45
POS408/1 18DR-3	7.4	0.53	2.1	99.9	109.1	140.5	41.8	3.7	103.1	38.2	105.3	0.04	24.5	4.3	13.1	2.2	11.6	4.1	1.44
POS408/1 18DR-4	7.1	0.66	1.9	101.8	109.2	143.5	42.0	3.7	104.2	39.2	106.3	0.06	24.8	4.4	13.6	2.2	11.8	4.2	1.49
POS408/1 17GC	7.5	0.49	2.1	102.1	111.2	140.6	41.5	3.8	102.5	39.1	106.5	0.03	25.3	4.3	13.0	2.2	12.0	4.3	1.43
POS408/1 28GC	4.6	0.20	1.2	141.0	134.6	94.0	40.6	1.3	80.1	21.8	42.9	0.01	10.0	1.4	4.5	0.8	5.1	2.0	0.84
POS408/1 29GC (1)	5.2	0.37	1.4	151.7	127.5	124.6	40.3	2.1	84.5	27.0	61.4	0.03	15.3	2.3	7.4	1.2	7.0	2.7	1.05
POS408/1 29GC (2,3)	5.5	0.28	2.2	150.4	125.9	122.3	40.4	2.0	84.0	27.3	60.1	0.03	14.8	2.2	7.2	1.2	7.4	2.6	0.98
POS408/1 29GC (5)	5.6	0.39	1.7	130.4	136.0	118.3	40.2	1.7	68.0	25.7	51.5	0.02	11.4	1.5	5.2	1.0	6.1	2.3	0.92
POS408/1 29GC (6)	5.6	0.19	1.3	128.9	128.0	111.8	42.4	1.5	77.4	25.4	50.9	0.02	11.0	1.6	5.1	1.0	5.7	2.3	0.93
64PE350 33DR-2	6.3	0.42	1.4	119.6	107.2	122.8	40.0	2.5	84.8	30.5	71.1	0.03	19.8	3.1	9.2	1.5	8.2	3.1	1.15
64PE350 33DR-4	6.3	0.32	1.5	93.6	116.0	117.3	43.1	1.3	91.0	29.6	64.2	0.02	11.6	2.2	7.3	1.3	7.2	2.8	1.10
64PE350 33DR-5 (1)	6.5	0.32	1.2	104.4	109.7	123.2	41.9	1.8	93.8	30.7	69.3	0.03	14.2	2.7	7.9	1.4	8.2	3.0	1.13
64PE350 33DR-5 (2)	6.3	0.25	1.4	99.3	114.2	116.7	41.5	1.3	93.5	27.9	62.2	0.01	12.5	2.3	6.9	1.3	7.5	2.8	1.08
64PE350 33DR-5 (3)	6.9	0.41	1.6	107.7	103.3	117.0	41.3	1.5	92.1	29.0	65.1	0.01	13.4	2.5	7.3	1.4	7.4	2.8	1.17

Sample	Li	Be	B	Ni	Cu	Zn	Sc	Rb	Sr	Y	Zr	Cs	Ba	La	Ce	Pr	Nd	Sm	Eu
64PE350 33DR-6	6.4	0.24	1.4	94.0	113.0	117.6	42.6	1.4	92.4	29.2	64.0	0.02	12.0	2.2	7.0	1.3	7.3	2.9	1.13
64PE350 33DR-7	6.2	0.33	1.6	123.7	107.5	119.6	41.5	2.5	85.2	32.6	73.9	0.02	20.0	3.3	9.1	1.5	8.8	3.2	1.15
64PE350 33DR-8	6.8	0.37	1.4	121.2	106.9	114.6	42.0	2.5	85.3	33.5	76.1	0.03	20.5	3.2	9.1	1.6	9.0	3.2	1.22
64PE350 33DR-10	6.3	0.33	1.3	94.7	121.5	118.4	42.2	1.3	92.2	28.2	62.0	0.02	12.0	2.1	7.1	1.3	7.1	2.7	1.11
64PE350 33DR-11	6.4	0.34	1.4	92.5	111.7	115.2	42.7	1.3	93.8	29.4	63.1	0.02	12.2	2.4	6.9	1.4	7.4	3.3	1.10
64PE350 33DR-12	5.9	0.22	2.9	94.9	116.7	123.3	42.8	1.3	91.2	29.1	63.4	0.02	11.5	2.2	6.6	1.3	7.4	2.9	1.09
64PE350 33DR-13	6.1	0.29	2.5	96.1	118.8	126.2	43.0	1.4	93.8	29.5	63.8	0.02	12.0	2.4	7.2	1.4	7.6	2.9	1.11
VA29-365GC_KII	6.4	0.34	1.4	93.1	115.7	126.9	43.9	1.3	96.5	29.5	65.4	0.03	12.5	2.4	7.5	1.4	7.7	3.0	1.19
DUF0073 DR68	4.7	0.54	1.6	130.5	138.4	100.1	37.2	6.4	149.7	23.7	63.8	0.08	53.7	4.2	10.3	1.6	8.7	2.8	1.06
64PE350 32DR (1)	5.8	0.36	2.0	122.3	107.9	123.5	42.2	2.4	111.4	26.9	73.9	0.02	20.7	3.3	9.5	1.6	8.3	2.9	1.11
64PE350 32DR (2)	5.8	0.36	2.0	122.3	107.9	123.5	42.2	2.4	111.4	26.9	73.9	0.02	20.7	3.3	9.5	1.6	8.3	2.9	1.11
64PE350 32DR (3,4)	6.2	0.43	1.7	89.9	122.2	126.2	43.2	3.3	113.0	28.8	76.2	0.03	29.4	4.1	11.6	1.8	9.2	3.1	1.17
64PE350 32DR (5,7)	5.4	0.39	1.9	111.9	129.9	104.8	42.4	3.6	149.9	25.7	79.4	0.04	35.5	4.9	13.0	1.9	9.3	3.0	1.15
64PE350 32DR (6)	5.4	0.30	1.4	153.0	111.3	115.6	40.7	1.5	105.5	25.3	64.5	0.01	13.2	2.3	7.6	1.3	7.2	2.7	0.97
SO02-488GC (1)	4.7	0.24	0.8	142.7	143.0	91.5	39.4	1.0	61.1	22.0	36.6	-	8.0	1.3	3.9	0.8	4.0	2.0	0.71
SO02-488GC (2,12)	5.7	0.53	1.6	85.2	115.5	116.2	44.5	1.3	81.9	30.3	68.8	0.03	10.4	2.1	6.9	1.3	7.3	3.0	1.02
SO02-488GC (3,6)	-	-	-	-	-	-	-	-	-	-	-	-	-	-	-	-	-	-	-
SO02-488GC (4,9)	5.9	0.36	1.1	91.0	121.7	110.0	46.4	1.3	89.9	31.2	70.5	-	9.8	2.2	7.0	1.3	7.9	3.2	1.13
SO02-488GC (5)	4.6		1.0	158.3	134.8	86.0	38.5	1.1	79.1	19.6	41.4	0.04	7.8	1.1	4.1	0.8	4.6	1.9	0.80
SO02-488GC (7,8,16)	5.9	0.18	1.2	90.5	118.5	105.9	44.8	1.4	85.8	29.9	67.5	0.03	10.9	2.1	6.4	1.2	7.6	2.5	1.05
SO02-488GC (10)	4.7	0.43	0.7	148.7	137.2	89.3	39.1	0.8	63.2	21.3	35.7	-	8.7	1.2	3.9	0.7	4.4	1.6	0.69
SO02-488GC (11)	6.5	0.48	1.7	87.3	125.4	119.2	46.5	1.4	89.1	33.0	72.7	-	11.7	2.4	7.8	1.5	7.5	3.2	1.15
SO02-488GC (13)	-	-	-	-	-	-	-	-	-	-	-	-	-	-	-	-	-	-	-
SO02-488GC (14,15)	5.6	0.30	1.5	92.1	115.0	112.7	44.6	1.3	84.4	29.8	67.0	0.04	11.0	2.0	6.7	1.3	7.1	3.0	1.07
64PE350 37DR (1,3)	6.3	0.37	1.3	75.8	120.5	126.7	45.4	1.2	92.1	30.4	64.8	0.01	11.9	2.2	7.1	1.3	7.5	2.8	1.14
64PE350 37DR (2)	8.3	0.59	2.3	112.5	92.6	159.1	41.8	4.1	96.4	42.2	119.5	0.04	32.8	5.8	15.9	2.5	13.1	4.5	1.53
64PE350 41DR	8.4	0.63	2.4	45.8	108.3	166.3	46.8	4.2	96.0	42.8	107.8	0.05	34.5	5.1	14.2	2.4	12.8	4.3	1.50
64PE350 43DR-1	6.8	0.27	2.9	55.8	124.8	142.7	47.5	5.1	92.5	33.4	75.6	0.04	43.7	4.7	12.0	1.9	9.5	3.4	1.20
64PE350 43DR-2	6.9	0.39	2.7	57.6	124.4	142.6	46.8	5.1	93.5	33.3	74.7	0.05	44.2	4.7	12.1	1.9	10.0	3.4	1.26
64PE350 43DR-3	6.8	0.30	2.1	56.8	124.3	141.3	47.2	5.3	96.4	33.4	76.8	0.05	44.9	4.8	12.1	1.8	9.6	3.4	1.19
64PE350 51DR-1	4.8	0.17	1.8	154.3	146.6	110.5	44.6	1.9	49.2	23.5	33.8	0.03	15.4	2.0	4.9	0.8	4.3	1.8	0.68
64PE350 51DR-2	5.3	0.19	1.7	150.4	146.6	107.3	45.4	1.9	51.3	23.5	35.8	0.02	15.9	2.0	5.2	0.8	4.4	1.8	0.75
64PE350 51DR-3	5.3	0.18	2.4	152.1	146.4	107.7	46.0	1.8	50.7	24.6	35.8	0.03	15.8	2.0	5.2	0.8	4.2	1.8	0.68
64PE350 49GC-2	6.1	0.28	2.2	107.4	135.3	138.2	45.6	3.9	64.9	30.0	60.8	0.05	32.0	4.1	9.9	1.5	7.4	2.7	0.92

Sample	Li	Be	B	Ni	Cu	Zn	Sc	Rb	Sr	Y	Zr	Cs	Ba	La	Ce	Pr	Nd	Sm	Eu
DUF0073 C1011	7.0	0.46	1.4	113.4	118.6	132.8	42.2	3.3	69.1	29.7	59.0	0.03	32.2	4.0	10.3	1.4	8.1	2.6	1.00
DUF0073 C1012	7.3	0.29	1.7	120.8	123.9	145.3	42.6	3.0	62.2	35.4	67.7	0.04	28.0	3.9	9.7	1.5	8.0	3.1	1.09
64PE350 77DR-1	6.4	0.39	2.5	128.6	124.6	133.7	42.6	3.5	72.9	30.0	58.1	0.04	33.0	4.3	10.5	1.6	7.9	2.8	1.04
SON0029-247-RS37	7.3	0.37	1.9	73.5	115.7	148.6	44.1	4.5	82.7	31.9	71.4	0.05	40.8	5.6	13.4	1.9	10.0	3.2	1.16
64PE351 10DR	5.5	0.14	2.1	119.4	142.8	109.2	48.4	1.9	61.8	23.7	36.9	0.02	18.3	2.4	6.0	0.9	5.1	2.1	0.78
64PE351 9DR-1T	9.1	1.33	4.4	18.1	124.1	161.8	40.6	22.5	221.4	42.1	174.0	0.27	209.7	27.1	53.3	6.5	25.9	6.2	2.00
64PE351 9DR-1B	9.3	1.44	4.6	15.4	122.4	170.8	39.3	23.3	227.5	42.2	176.8	0.28	216.8	28.0	54.4	6.5	26.8	6.2	2.05
64PE351 9DR-2	10.1	1.63	4.3	18.1	130.5	164.8	40.7	23.8	224.5	42.0	179.4	0.29	215.1	28.6	56.8	6.9	28.0	6.4	2.03

Table 2 continued

Trace element data, Na_8 and calculated Pressures and Temperatures of last equilibrium crystallisation.

Sample	Gd	Tb	Dy	Ho	Er	Tm	Yb	Lu	Hf	Pb	Th	U	Na8[f]	Pressure	Temperature
M31/2 KL9-1[c]	*4.5*	*0.76*	*5.2*	*1.04*	*3.0*	*0.42*	*2.7*	*0.40*	2.7	-	*0.37*	*0.13*	3.2	110	1157
M31/2 KL9-2 (1,2)[c]	4.8	0.79	5.2	1.13	3.2	0.47	3.0	0.42	2.8	0.76	0.39	0.11	3.2	150	1162
M31/2 KL9-2 (3)[c]	5.1	0.88	5.5	1.20	3.3	0.47	3.2	0.46	3.0	0.86	0.41	0.12	3.2	150	1162
M31/2 88PC[c]	7.4	1.23	8.0	1.69	4.9	0.66	4.6	0.70	4.7	1.26	0.69	0.20	3.4	380	1149
M31/2 DR3-1[c]	*3.6*	*0.62*	*4.0*	*0.84*	*2.5*	*0.35*	*2.3*	*0.34*	2.1	-	*0.59*	*0.16*	3.0	210	1173
M31/2 DR3-2[c]	4.0	0.68	4.6	0.91	2.6	0.37	2.4	0.36	2.1	0.75	0.64	0.17	3.1	190	1168
M31/2 DR3-3[c]	*3.5*	*0.61*	*4.0*	*0.84*	*2.4*	*0.33*	*2.2*	*0.33*	2.1	-	*0.57*	*0.17*	3.1	230	1178
M31/2 DR2-1[c]	*6.8*	*1.19*	*7.9*	*1.62*	*4.6*	*0.68*	*4.4*	*0.66*	4.9	-	*0.63*	*0.18*	3.2	100	1125
M31/2 DR2-2[c]	*6.9*	*1.21*	*7.8*	*1.63*	*4.7*	*0.66*	*4.3*	*0.64*	4.8	-	*0.63*	*0.19*	3.0	70	1121
M31/2 88GTV[c]	5.0	0.87	5.4	1.09	3.1	0.45	3.0	0.43	3.1	1.00	0.82	0.26	3.0	50	1146
M31/2 DR1-1[c]	*3.2*	*0.57*	*3.8*	*0.79*	*2.3*	*0.33*	*2.1*	*0.31*	1.8	-	*0.48*	*0.12*	3.1	280	1186
M31/2 DR1-2[c]	*4.8*	*0.74*	*4.7*	*1.01*	*2.8*	*0.41*	*2.8*	*0.36*	3.0	0.89	*0.77*	*0.23*	3.1	220	1166
M31/2 DR1-3[c]	*3.3*	*0.58*	*3.9*	*0.82*	*2.4*	*0.34*	*2.2*	*0.32*	1.7	-	*0.49*	*0.17*	3.2	280	1186
M31/2 DR1-4[c]	3.5	0.56	3.8	0.83	2.4	0.35	2.3	0.32	1.6	0.55	0.49	0.12	3.1	270	1184
SON0029-370DC RS107 (1)	4.4	0.75	5.1	1.11	3.2	0.47	3.0	0.42	2.2	0.56	0.62	0.15	2.7	100	1153
SON0029-370DC RS107 (2,3)	4.4	0.75	5.1	1.11	3.2	0.47	3.0	0.42	2.2	0.56	0.62	0.15	2.7	100	1153
SON0029-370DC RS108	4.4	0.77	5.2	1.07	3.2	0.45	2.9	0.45	2.3	0.59	0.63	0.16	2.7	110	1153
NORGMRO-KS04B	5.0	0.81	5.3	1.13	3.2	0.42	2.9	0.47	2.1	0.61	0.64	0.15	2.5	70	1147
64PE351 14DR-1	4.7	0.84	5.8	1.27	3.4	0.52	3.3	0.49	2.2	0.57	0.41	0.10	2.8	80	1162
64PE351 14DR-2	4.4	0.74	4.9	1.11	3.2	0.43	2.9	0.42	2.1	0.51	0.40	0.11	2.7	70	1161
64PE351 14DR-3	4.6	0.81	5.5	1.17	3.4	0.48	3.1	0.45	2.1	0.52	0.39	0.10	2.8	40	1157
64PE351 14DR-4	4.7	0.82	5.5	1.16	3.6	0.49	3.2	0.49	2.4	0.56	0.38	0.10	2.8	60	1160

Sample	Gd	Tb	Dy	Ho	Er	Tm	Yb	Lu	Hf	Pb	Th	U	Na_8^f	Pressure	Temperature
NORGMRO-KS11B	-	-	-	-	-	-	-	-	-	-	-	-	2.8	130	156
NORGMRO-KS12	3.7	0.66	4.5	0.95	2.7	0.37	2.6	0.41	2.1	0.27	0.13	0.05	2.4	370	184
64PE351 13DR-2c (1,2)	4.8	0.77	5.5	1.08	3.5	0.48	3.4	0.49	1.9	0.46	0.31	0.09	2.5	40	149
64PE351 13DR-2c (3)	4.8	0.77	5.5	1.08	3.5	0.48	3.4	0.49	1.9	0.46	0.31	0.09	2.5	40	149
DUF0073 C1035	5.3	0.92	5.9	1.34	4.0	0.64	3.9	0.59	2.8	0.51	0.28	0.12	2.2	230	170
64PE350 23DR-1	5.1	0.91	6.1	1.35	3.9	0.56	3.8	0.55	2.5	0.52	0.31	0.12	2.5	230	167
64PE350 23DR-2	5.1	0.97	6.1	1.32	3.9	0.56	3.7	0.56	2.6	0.55	0.31	0.11	2.5	250	167
64PE350 23DR-3	4.8	0.88	5.9	1.29	3.7	0.54	3.5	0.53	2.5	0.52	0.29	0.11	2.5	250	170
64PE350 23DR-4	5.0	0.93	6.1	1.36	3.9	0.56	3.7	0.55	2.6	0.56	0.31	0.12	2.5	210	164
64PE350 23DR-5	5.3	1.02	6.5	1.47	4.3	0.61	3.9	0.64	3.0	0.49	0.32	0.10	2.5	230	166
64PE350 23DR-6A	5.7	1.00	6.7	1.51	4.3	0.64	4.2	0.60	2.8	0.51	0.32	0.10	2.5	270	169
64PE350 23DR-7	5.7	1.03	7.0	1.63	4.5	0.66	4.2	0.65	3.1	0.51	0.33	0.11	2.5	240	167
64PE350 23DR-9 (1)	4.8	0.84	5.8	1.33	3.8	0.53	3.6	0.53	2.4	0.40	0.24	0.08	2.6	310	181
64PE350 23DR-9 (2,3)	4.8	0.84	5.8	1.33	3.8	0.53	3.6	0.53	2.4	0.40	0.24	0.08	2.6	310	181
POS408/1 26GC	6.0	1.12	7.4	1.61	4.5	0.69	4.6	0.69	3.3	0.55	0.30	0.13	2.6	170	150
POS408/1 50DR-1 (1,2)	5.9	1.01	6.8	1.48	4.4	0.62	4.4	0.64	3.1	0.51	0.31	0.11	2.4	240	162
POS408/1 50DR-1 (3)	5.9	1.01	6.8	1.48	4.4	0.62	4.4	0.64	3.1	0.51	0.31	0.11	2.4	240	162
POS408/1 50DR-2	5.7	1.04	7.0	1.54	4.3	0.62	4.0	0.67	3.0	0.59	0.32	0.11	2.5	240	162
POS408/1 50DR-3	5.8	1.21	6.8	1.54	4.3	0.63	4.0	0.62	3.0	0.57	0.32	0.12	2.4	260	163
POS408/1 50DR-4 (1,2)	5.7	1.01	6.7	1.42	4.3	0.61	4.1	0.59	3.0	0.56	0.31	0.10	2.4	280	166
POS408/1 50DR-4 (3)	5.7	1.01	6.7	1.42	4.3	0.61	4.1	0.59	3.0	0.56	0.31	0.10	2.4	280	166
POS408/1 50DR-5 (1,3)	5.7	1.01	7.0	1.50	4.5	0.64	4.3	0.64	3.0	0.52	0.32	0.11	2.4	270	165
POS408/1 50DR-5 (2)	5.7	1.01	7.0	1.50	4.5	0.64	4.3	0.64	3.0	0.52	0.32	0.11	2.4	270	165
POS408/1 50DR-6	5.6	1.04	6.7	1.47	4.3	0.63	3.9	0.61	3.1	0.49	0.32	0.11	2.4	280	165
POS408/1 57DR-1 (1,2,4)	5.4	1.02	6.7	1.48	4.3	0.63	4.1	0.62	3.1	0.50	0.31	0.11	2.5	350	173
POS408/1 57DR (3)	5.5	1.04	6.9	1.53	4.3	0.65	4.2	0.63	3.1	0.55	0.32	0.12	2.5	300	166
POS408/1 19DR-1	5.5	1.03	6.8	1.51	4.5	0.63	4.1	0.66	3.1	0.55	0.33	0.14	2.5	280	165
POS408/1 19DR-2T	5.9	1.02	7.1	1.47	4.4	0.65	4.1	0.64	3.2	0.61	0.34	0.12	2.6	270	163
POS408/1 19DR-2B	5.9	1.11	7.0	1.65	4.6	0.65	4.3	0.68	3.2	0.58	0.37	0.13	2.5	250	161
POS408/1 19DR-3	5.5	1.01	6.8	1.46	4.3	0.61	4.2	0.62	3.0	0.54	0.34	0.13	2.5	290	165
POS408/1 19DR-4	5.7	1.06	7.0	1.54	4.6	0.68	4.1	0.64	3.2	0.56	0.34	0.12	2.5	290	166
POS408/1 19DR-5	5.6	1.02	6.9	1.48	4.2	0.66	4.1	0.67	3.1	0.59	0.32	0.13	2.6	260	163
POS408/1 51DR (2)	5.8	1.05	7.2	1.57	4.7	0.67	4.3	0.68	3.2	0.48	0.32	0.11	2.5	310	168
POS408/1 51DR (1,3)	5.8	1.05	7.2	1.57	4.7	0.67	4.3	0.68	3.2	0.48	0.32	0.11	2.5	310	168

Sample	Gd	Tb	Dy	Ho	Er	Tm	Yb	Lu	Hf	Pb	Th	U	Na$_8^f$	Pressure	Temperature
POS408/1 58DR-1	5.7	1.04	7.0	1.61	4.5	0.65	4.2	0.62	3.2	0.61	0.33	0.11	2.4	260	1162
POS408/1 58DR-2	5.8	1.00	6.8	1.51	4.4	0.63	4.1	0.65	3.0	0.56	0.33	0.10	2.5	280	1164
POS408/1 58DR-3	5.8	1.08	7.4	1.52	4.6	0.68	4.4	0.65	3.3	0.50	0.33	0.12	2.5	260	1162
POS408/1 58DR-4	5.8	1.03	7.3	1.55	4.6	0.64	4.3	0.64	3.1	0.58	0.34	0.12	2.5	280	1166
POS408/1 58DR-5	5.9	1.07	6.9	1.48	4.5	0.62	4.1	0.62	3.1	0.53	0.34	0.11	2.5	260	1162
POS408/1 58DR-6	6.0	1.10	7.2	1.54	4.6	0.65	4.3	0.66	3.1	0.57	0.33	0.11	2.4	280	1164
POS408/1 58DR-7	6.0	1.08	7.2	1.61	4.7	0.69	4.3	0.66	3.0	0.62	0.33	0.10	2.5	270	1163
POS408/1 18DR-1	5.8	1.08	7.0	1.45	4.4	0.62	4.2	0.64	3.0	0.52	0.32	0.12	2.5	280	1165
POS408/1 18DR-2	5.7	1.04	7.0	1.44	4.6	0.66	4.0	0.64	3.0	0.60	0.32	0.11	2.4	270	1164
POS408/1 18DR-3	5.7	0.98	6.5	1.49	4.2	0.60	4.2	0.62	3.0	0.54	0.32	0.12	2.5	220	1159
POS408/1 18DR-4	5.9	1.02	6.9	1.53	4.4	0.64	4.2	0.65	2.9	0.58	0.35	0.12	2.6	240	1160
POS408/1 17GC	5.7	1.00	6.8	1.52	4.3	0.66	4.1	0.65	3.0	0.57	0.32	0.13	2.5	240	1160
POS408/1 28GC	3.2	0.57	3.9	0.87	2.4	0.38	2.4	0.35	1.4	0.21	0.09	0.03	2.4	420	1218
POS408/1 29GC (1)	4.1	0.69	5.0	1.04	3.2	0.45	3.0	0.44	1.8	0.38	0.15	0.05	2.5	400	1201
POS408/1 29GC (2,3)	4.1	0.71	4.8	1.09	3.2	0.42	2.8	0.46	1.9	0.35	0.16	0.05	2.5	400	1201
POS408/1 29GC (5)	3.6	0.66	4.8	0.97	3.0	0.46	2.8	0.43	1.6	0.34	0.10	0.03	2.3	380	1204
POS408/1 29GC (6)	3.5	0.66	4.4	1.00	3.0	0.42	2.7	0.39	1.6	0.26	0.10	0.03	2.3	380	1204
64PE350 33DR-2	4.4	0.78	5.4	1.20	3.4	0.51	3.2	0.50	2.2	0.37	0.25	0.07	2.4	300	1186
64PE350 33DR-4	4.2	0.74	5.1	1.10	3.2	0.46	3.0	0.47	1.9	0.36	0.15	0.05	2.5	310	1188
64PE350 33DR-5 (1)	4.3	0.77	5.3	1.13	3.2	0.51	3.3	0.51	2.2	0.30	0.19	0.06	2.5	310	1187
64PE350 33DR-5 (2)	4.0	0.73	4.9	1.13	3.3	0.44	3.1	0.46	2.0	0.33	0.15	0.05	2.5	300	1186
64PE350 33DR-5 (3)	3.9	0.74	4.9	1.06	3.2	0.47	3.1	0.45	1.8	0.29	0.17	0.05	2.5	360	1189
64PE350 33DR-6	4.3	0.75	5.0	1.11	3.2	0.47	3.2	0.48	2.0	0.33	0.14	0.05	2.5	290	1185
64PE350 33DR-7	4.5	0.85	5.5	1.28	3.6	0.51	3.4	0.53	2.3	0.35	0.25	0.07	2.4	350	1190
64PE350 33DR-8	4.6	0.83	5.7	1.29	3.7	0.54	3.4	0.54	2.4	0.45	0.26	0.08	2.4	350	1190
64PE350 33DR-10	4.1	0.72	4.8	1.07	3.1	0.42	3.0	0.46	1.9	0.31	0.14	0.05	2.5	350	1190
64PE350 33DR-11	4.0	0.72	5.3	1.14	3.1	0.48	3.0	0.44	2.0	0.47	0.15	0.04	2.5	300	1186
64PE350 33DR-12	3.9	0.76	5.1	1.11	3.3	0.47	3.0	0.47	2.0	0.28	0.15	0.05	2.5	340	1188
64PE350 33DR-13	4.2	0.73	5.3	1.11	3.2	0.49	3.2	0.47	2.0	0.30	0.14	0.06	2.5	360	1191
VA29-365GC_KII	4.3	0.80	5.2	1.13	3.3	0.49	3.2	0.49	1.9	0.36	0.16	0.05	2.5	440	1199
DUF0073 DR68	4.4	0.70	4.1	0.89	2.6	0.43	2.5	0.38	1.9	1.63	0.49	0.14	2.7	490	1191
64PE350 32DR (1)	4.0	0.72	4.8	1.04	3.0	0.41	2.9	0.43	2.0	0.40	0.22	0.07	2.4	290	1184
64PE350 32DR (2)	4.0	0.72	4.8	1.04	3.0	0.41	2.9	0.43	2.0	0.40	0.22	0.07	2.4	290	1184
64PE350 32DR (3,4)	4.4	0.75	5.0	1.12	3.4	0.48	3.1	0.46	2.2	0.50	0.33	0.11	2.4	210	1172

Sample	Gd	Tb	Dy	Ho	Er	Tm	Yb	Lu	Hf	Pb	Th	U	Na8[f]	Pressure	Temperature
64PE350 32DR (5,7)	4.1	0.71	4.7	0.98	2.9	0.41	2.7	0.39	2.2	0.53	0.41	0.14	2.5	290	1189
64PE350 32DR (6)	3.6	0.66	4.4	0.95	3.0	0.42	2.7	0.39	1.9	0.38	0.15	0.05	2.7	440	1199
SO02-488GC (1)	3.0	0.49	3.9	0.90	2.6	0.34	2.2	0.36	1.1	0.17	0.09	0.02	2.3	540	1228
SO02-488GC (2,12)	4.2	0.79	5.0	1.05	3.2	0.49	3.2	0.51	1.9	0.40	0.13	0.03	2.4	420	1206
SO02-488GC (3,6)	-	-	-	-	-	-	-	-	-	-	-	-	2.4	300	1184
SO02-488GC (4,9)	4.3	0.75	5.6	1.11	3.4	0.50	3.0	0.49	2.1	0.29	0.13	0.04	2.4	330	1188
SO02-488GC (5)	2.7	0.55	3.4	0.82	2.3	0.37	2.2	0.30	1.4	0.20	0.08	0.02	2.4	550	1231
SO02-488GC (7,8,16)	4.5	0.66	5.1	1.15	3.5	0.47	2.9	0.47	1.8	0.32	0.12	0.04	2.4	280	1185
SO02-488GC (10)	3.1	0.49	3.8	0.88	2.6	0.36	2.2	0.35	1.1	0.29	0.08	0.02	2.2	550	1228
SO02-488GC (11)	4.6	0.83	5.8	1.23	3.9	0.53	3.5	0.52	2.3	0.35	0.15	0.04	2.4	270	1181
SO02-488GC (13)	-	-	-	-	-	-	-	-	-	-	-	-	2.4	580	1235
SO02-488GC (14,15)	4.3	0.76	5.2	1.20	3.7	0.44	3.0	0.46	1.9	0.38	0.13	0.05	2.5	360	1192
64PE350 37DR (1,3)	4.5	0.77	5.5	1.15	3.5	0.49	3.2	0.50	1.9	0.34	0.14	0.05	2.5	90	1158
64PE350 37DR (2)	5.9	1.07	7.4	1.61	4.6	0.69	4.5	0.67	3.3	0.66	0.46	0.15	2.3	100	1145
64PE350 41DR	6.1	1.08	7.4	1.65	4.9	0.68	4.5	0.70	3.2	0.68	0.46	0.16	2.3	10	1130
64PE350 43DR-1	4.8	0.84	5.8	1.29	3.8	0.54	3.6	0.57	2.3	0.46	0.48	0.14	2.2	10	1146
64PE350 43DR-2	5.0	0.82	5.8	1.30	3.8	0.55	3.6	0.56	2.2	0.50	0.46	0.14	2.2	10	1146
64PE350 43DR-3	4.8	0.90	5.6	1.31	3.6	0.55	3.7	0.59	2.3	0.49	0.48	0.13	2.2	10	1146
64PE350 51DR-1	2.7	0.54	3.9	0.84	2.7	0.39	2.7	0.41	1.1	0.19	0.19	0.06	2.1	350	1209
64PE350 51DR-2	2.9	0.56	3.9	0.90	2.9	0.44	2.7	0.44	1.1	0.19	0.20	0.06	2.1	340	1208
64PE350 51DR-3	2.9	0.55	4.1	0.94	2.9	0.42	2.8	0.41	1.1	0.22	0.21	0.05	2.1	350	1209
64PE350 49GC-2	4.1	0.70	5.0	1.12	3.5	0.49	3.3	0.51	1.8	0.38	0.43	0.13	2.1	90	1166
DUF0073 C1011	4.2	0.77	5.4	1.24	3.5	0.55	3.5	0.49	1.9	0.58	0.43	0.11	2.1	150	1160
DUF0073 C1012	4.7	0.94	5.9	1.38	4.3	0.58	3.9	0.55	2.2	0.50	0.37	0.11	2.1	90	1148
64PE350 77DR-1	4.1	0.75	5.2	1.13	3.6	0.51	3.3	0.55	1.8	0.43	0.45	0.14	2.1	130	1165
SON0029-247-RS37	4.5	0.82	5.6	1.30	3.9	0.55	3.7	0.53	2.2	0.68	0.56	0.17	2.1	30	1138
64PE351 10DR	3.3	0.61	4.0	0.85	2.7	0.43	2.7	0.41	1.3	0.33	0.24	0.07	2.0	70	1181
64PE351 9DR-1T	6.9	1.15	7.2	1.57	4.3	0.64	4.1	0.66	4.4	2.51	3.29	0.92	2.6	Only Cpx on liquidus	
64PE351 9DR-1B	6.8	1.09	7.5	1.58	4.4	0.64	4.2	0.66	4.4	2.65	3.36	0.94	2.6	Only Cpx on liquidus	
64PE351 9DR-2	6.8	1.14	7.7	1.66	4.6	0.67	4.4	0.65	4.7	2.34	3.42	0.95	2.6	Only Cpx on liquidus	

[a] Major elements, H_2O are given in wt%; Cl, K, Nb, CO_2 and trace elements are given in ppm (µg/g); Temperature is in °C, Pressure in MPa.

[b] Samples from the same station but different endnumbers represent separate rocks. Numbers between brackets represent separate glass chips from the same rock/station.

[c] Data in *italics* represents literature data (Jambon et al., 1990; Haase et al., 2000; Bezos, 2003; Chavrit, 2010; Chavrit et al., 2012)

[d] H_2O data in ***bold italics*** is calculated from the K/H_2O relationship (Michael, 1995) and used for Pressure calculations.

[e] Cl/Nb data in **bold** is derived from the linear Cl/K-Cl/Nb relationship (fig. 2d).

[f] After Plank and Langmuir (1992).

4 Discussion

4.1. Chlorine enrichment

To determine the extent of Cl enrichment in the Red Sea samples it is important to estimate the uncontaminated Cl/Nb and Cl/K ratios. These ratios will be similar to the mantle Cl/Nb and Cl/K, as they are not strongly affected by melting processes. The Cl/K mantle ratio is relatively well constrained from previous studies on Cl in basalts (Jambon et al., 1995; Michael and Cornell, 1998; Saal et al., 2002; Stroncik and Haase, 2004; Kovalenko et al., 2006) and ranges between values of <0.01 to maximum 0.09. Cl/Nb values are less well constrained, with published values of e.g. 3 (Saal et al., 2002), 14 (le Roux et al., 2006), 25.8 (McDonough and Sun, 1995) up to 51 (Palme and O'Neill, 2003). Palme and O'Neill (2003) calculate a relatively high Cl mantle concentration (30 ppm) in comparison to Cl contents in studies that derived the mantle Cl concentration from basaltic melts and melt inclusions, which all produced values lower than 7 ppm (Ryabchikov, 2001; Saal et al., 2002; Salters and Stracke, 2004; Kovalenko et al., 2006; le Roux et al., 2006). Therefore, a Cl/Nb mantle value of 51 seems unrealistically high and a ratio of <26 may be more applicable. This is consistent with the relationship between Cl/Nb and Cl/K that indicates that samples with a Cl/K ratio of >0.09 have Cl/Nb of >30. This implies that, since most samples have Cl/Nb >30 and Cl/K >0.09 (Fig. 2c, e), relative Cl enrichment in the Red Sea basalts is widespread, although in varying intensities. A few non-enriched samples in both Cl/Nb and Cl/K occur at Shaban, Mabahiss and Discovery Deeps and at RSR 17°N (Fig. 3).
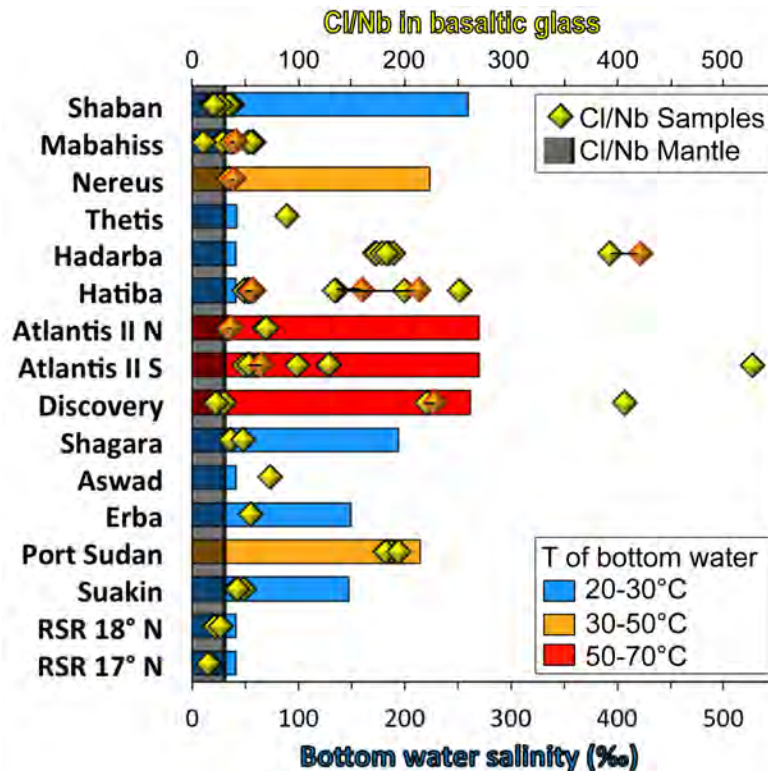
Fig. 3 – Cl/Nb contents of the basalt samples grouped after their latitude along the Red Sea Rift (N to S), compared to local bottom water salinities (brine pools have salinities >>50‰) and bottom water temperatures (temperature-ranges are indicated by different colours of the salinity bars). The mantle Cl/Nb value is indicated in dark blue. Brine salinities and temperatures are after Pierret et al. (2001); Eder et al. (2002); Gurvich (2006); Swift et al. (2012). Glass measurements in orange with a red rim might have been influenced by seafloor weathering and/or syneruptive Cl contamination (for details see text) and are connected by a tie-line to the fresh glass from the same sample. No relation can be observed between high Cl/Nb and the salinity; however, the brines with high temperatures are consistently Cl enriched.

4.2 Chlorine enrichment by magmatic processes?

Aside from interaction with seawater, Cl enrichment could potentially be due to fractionation during melting, crystallisation or degassing or result from source variations (Schilling et al., 1980). Degassing of the Red Sea basalts is clearly occurring, based on the vesicular character of some of the samples and CO_2/Nb values of <150, which is significantly lower than the values of 239 or ~530 for undegassed samples obtained by Saal et al. (2002) and Cartigny et al. (2008) respectively. However, degassing of Cl is thought to be important only at <400 m waterdepth (<40 bar (e.g. Unni and Schilling, 1978)) and therefore unlikely as all samples come from >1000 m depth (cf. Stroncik and Haase, 2004). More importantly, there is no relation observed between Cl enrichment and sampling depth or the amount of degassing (CO_2/Nb; fig. 2g).

The melting degrees of the basalts vary along the Red Sea (e.g. Altherr et al., 1988), but the lack of correlation between Cl/Nb and Na_8 (as well as Cl/Nb and La/Sm, not shown here), indicates that melting does not play a significant role in Cl enrichment. Neither is there a correlation between Cl enrichment and indicators of fractionation, like MgO (Fig. 2f). Therefore, we conclude that although melting or fractionation might influence the Cl concentrations themselves, they are not responsible for the observed strong Cl enrichment relative to K or Nb.

The lack of correlation between Cl/Nb and indicators of subduction such as Pb/Ce (Miller et al., 1994) demonstrates that the Cl enrichment is also not related to subduction processes. A Ce/Pb against Nb/U plot indicates that almost all RSR samples are close to the MORB field of Hofmann et al. (1986) and hence have experienced no significant continental input (Fig. 2a). Some exceptional samples display low Ce/Pb, related to high Pb, which is most likely due to low temperature alteration, as most of these samples come from sediment cores. However, even small variations in Ce/Pb or Nb/U are not related to a high or low Cl/Nb and thus Cl enrichment (Fig. 2a). The general lack of a correlation between Cl/Nb and various trace elements (e.g. LREE) indicates that Cl/Nb is not related to mantle source characteristics. The fact that predominantly the more trace element enriched samples (K/Ti >0.25) show less sign of Cl enrichment is probably a result of their intrinsically higher Cl contents, which are less easily affected by relatively limited amounts of Cl addition. In conclusion, the strong Cl enrichment compared to K and Nb and the decoupling of Cl from other trace elements argues for interaction with seawater (cf. Jambon et al., 1995).

4.3 Chlorine enrichment by interaction with seawater

Chlorine addition due to interaction with seawater could take place at three different points of magma evolution: (I) post-eruptive - by direct alteration of basalt at low temperatures on the seafloor (e.g. Hart et al., 1974), (II) syn-eruptive - by incorporation of vaporized seawater in lava flows during emplacement (Perfit et al., 2003; Soule et al., 2006), or (III) pre-eruptive - at high temperatures deeper in the crust by hydrothermal alteration of oceanic crust and subsequent assimilation by magma. The different effects that each of these interactions has on the petrology, homogeneity and trace element concentrations of the samples can help distinguishing between them.

4.3.1 Low temperature seafloor weathering
Due to the high sedimentation and carbonate precipitation rates in the Red Sea (locally up to 1 m/yr (Guennoc et al., 1988; Botz et al., 2007)) we can conclude that all basalts sampled by dredge from the seafloor are relatively young. Together with the fresh appearance of the glass and the lack of visible internal alteration except along cracks and veins, we expect that Cl-enrichment by simple seafloor alteration will not have had sufficient time to significantly infiltrate the intact glass margin. This is supported by the homogeneous Cl distribution even amongst different glass chips from the same sample and that some of the lowest (and hence uncontaminated) Cl/Nb values are found in the visually most altered hand specimens (from Shaban and Atlantis II Deep). The lack of a correlation between Cl enrichment and mobile

trace elements that would most likely be affected by seafloor weathering (e.g. U, Pb, Rb, Ba (e.g. Alt et al., 1986; Alt and Teagle, 2003; Schramm et al., 2005; Augustin et al., 2008)) and the strong grouping of the samples in Nb/U, Ce/Pb (Fig. 2a) argue against a strong influence of seafloor weathering on the Cl concentrations, with the potential exception of a few samples with low Ce/Pb (fig 2a).

As brine and seawater have very different Cl/H_2O ratios, we can distinguish the addition of seawater and e.g. the Atlantis II brine compared to other contaminants to an uncontaminated end member using a modified model of Kent et al. (1999a); le Roux et al. (2006). This is shown as a plot of Cl/Nb against H_2O/Ce in Fig. 4. The Cl/Nb to H_2O/Ce relations show that although some samples lie on a mixing line with seawater (high H_2O/Ce, low Cl/Nb) and could potentially be explained by seafloor weathering, these are mostly not the Cl enriched samples (Cl/Nb >30). The spread in H_2O/Ce in these samples is probably better explained by slight variations in the source composition (Michael, 1995), confirmed by a positive correlation between H_2O/Ce and e.g. La/Sm. Of the samples that have a higher Cl/Nb than mantle, only some samples from Shaban Deep (H_2O/Ce ~300) and one of the samples from Shagara Deep (H_2O/Ce 483) could potentially be explained by incorporation of a seafloor-weathering component. Seafloor weathering in a brine could theoretically explain some of the higher Cl/Nb in the Atlantis II Deep samples but it will not work for any of the samples that have Cl/Nb>100 (Fig. 4). We note also that samples recovered from close to or within brine pools do not show a tendency to have higher Cl/Nb ratios (Fig. 3, 4) and some of the highest Cl/Nb ratios are found in the brine-free Hadarba deep, which suggests that contamination by contact with water at the seafloor is not a significant process for altering the Cl concentrations.

Fig. 4 – Indications on the nature of the contaminant derived from Cl/Nb ratios and H_2O/Ce compositions of the glasses together with models of the addition of different contaminants to an uncontaminated endmember (after le Roux et al., 2006). The endmember from le Roux et al. (2006) is derived as a local for the EPR, but seems fitting for the Red Sea as well. The model has been adapted by increasing the salinity of Red Sea deep water to 41‰, while for altered oceanic crust recent values of Barnes and Cisneros (2012) are used. Furthermore, we included the effect of adding the most saline brine (Atlantis II: 270‰ (Gurvich, 2006)) to an uncontaminated sample. Trace element concentrations for Red Sea seawater and Atlantis II brine are from Klauke (2000). Samples with a red rim may be influenced by alteration based on their low Ce/Pb ratios. Based on their Cl/Nb and H_2O/Ce contents also the marked samples from Shagara, Shaban and Atlantis II Deeps may be explained by seawater or brine weathering on the seafloor. All other samples require the addition of up to 0.3% hydrothermal brines. For discussion see text.
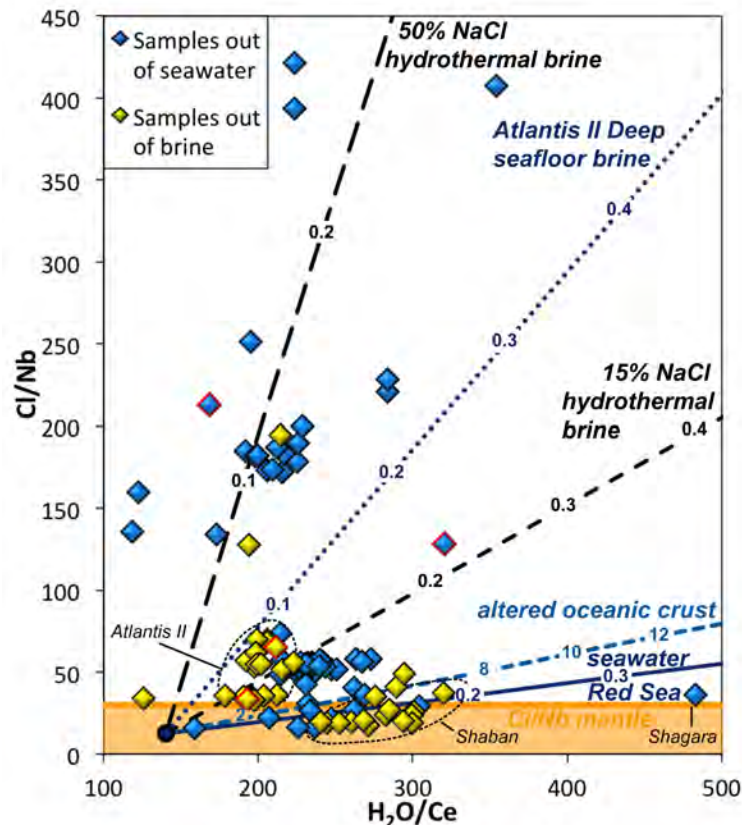
4.3.2 Syn-eruptive seawater-lava interaction

Chlorine incorporation by syn-eruptive interaction of (vaporized) seawater with erupting magma can take place if vaporized seawater is trapped in pockets underneath a lava flow (Soule et al., 2006) or lava sinks into or disrupts sediments (Maicher and White, 2001). Due to the high temperature of the lava, the fluid is heated and phase separation can occur, leading to a high Cl/H_2O brine (Soule et al., 2006) that could explain the high Cl/Nb compared to H_2O/Ce values in the Red Sea basalts (Cl/Nb >100 for H_2O/Ce <300; Fig. 4). Important to note is that samples that can be affected by these processes are mainly sheet flows and lobate magma flows characterized by glass rims on both top and bottom with drips, flanges and septa (glass ridges in between close-spaced voids) at the bottom of the samples (Perfit et al., 2003; Soule et al., 2006). These characteristics have, however, not been found in pillow lavas (Soule et al., 2006), which excludes syn-eruptive Cl contamination for the pillow and blocky samples of northern Atlantis II, Erba Deeps and most of the high Cl samples of Hadarba Deep. Samples from Mabahiss, Hatiba Deeps, RSR 17° and some at Hadarba and Port Sudan Deeps show hand-specimen signs of magmatic contact with water and sediments, but direct interaction with sediment did not affect the glass chemistry, as can be observed from the MORB-like trace elements and from the lack of any chemical gradients in the glass. Contamination by vapor intrusion from the sediments cannot be ruled out, but should result in fluid lines and highly localised and heterogeneous Cl enrichment. Most samples display homogeneous Cl contents and so are unlikely affected by syn-eruptive contamination.

To further avoid any possible effects of syn-eruptive vapor incorporation we tried to sample glass from the top of samples where their orientation could be determined and from there the glass chips lowest in vesicles. For samples where top and bottom glass could be analysed we found differences of maximum 30 ppm. This increase in Cl is in agreement with a maximum variation of 30 ppm between glass chips in sheet flows from Hatiba Deep and one sheet flow from Atlantis II Deep (sample 33DR-5) that display heterogeneous Cl contents. Only glass from 370DC-RS107 displays a larger Cl variation with homogeneous trace elements, although due to the unknown sample petrography, we cannot certainly ascribe this to syn-eruptive contamination although it would be consistent with the large 2SE (13.4 ppm) within a glass chip that indicates local chlorine enrichment.

In conclusion, the action of syn-eruptive contamination seems to be limited and although it can explain some small-scale heterogeneous Cl variations within a sample (mostly up to 30 ppm, in a rare case also higher), it cannot explain the overall homogeneous strong enrichment in Cl displayed in the majority of the samples.

4.3.3 Assimilation of hydrothermally altered crust

The homogeneous high Cl/Nb compared to H_2O/Ce in many Red Sea lavas suggests interaction with a highly saline brine component that becomes well mixed in a magma (addition of hydrothermal brines in Fig. 4). The presence of brines in hydrothermal systems is indicated by fluid inclusion studies in MOR gabbros (with brines up to 50% salinity (Kelley and Delaney, 1987)) and by the analyses of hydrothermal vent fluids at MOR (e.g. Berndt and Seyfried Jr, 1990; Von Damm et al., 2003). Hydrothermal brines are generated by phase separation of a fluid into a brine and vapor phase at high temperatures (Bischoff and Rosenbauer, 1987; Fournier, 1987; Berndt and Seyfried Jr, 1990). These highly saline fluids could either be directly 'tapped' by rising magma, or be trapped as fluid inclusions in hydrothermally altered rocks, particularly in hydrothermally formed minerals (e.g. amphiboles (Gillis et al., 2003; Barnes and Cisneros, 2012)), that are subsequently assimilated by magma (e.g. Michael and Schilling, 1989; Jambon et al., 1995)). The latter would be in agreement with a boron isotope study of Kent et al. (1999a), which shows that altered oceanic crust is assimilated, although this crust is not sufficiently Cl-rich to raise the Cl/Nb ratios relative to low H_2O/Ce ratios by itself (Fig. 4). The fact that no other possible indicators of seawater alteration (e.g. Sr- or Eu-anomalies, Sr/Eu or boron (cf. Kent et al., 1999a; Gillis et al., 2003) are correlated to Cl/Nb in the magmas studied here might argue for Cl input from the evaporites flanking the rift rather than from altered crust, or simply imply that variations in Sr, Eu or boron produced by melting processes are more important than those produced by

assimilation of hydrothermally altered crust. The only other element, which could have been significantly added to the melts during assimilation, is Na. This would not be visible in the measurements, however: the addition of the amount of brine that is required to explain the highest Cl/Nb ratios (maximum 0.3 wt.% of a 50% NaCl brine – Fig. 4) would add maximum 0.06 wt.% of Na to a magma, which is within the error margins of the microprobe measurements.

The interpretation of Cl enrichment being due to hydrothermal interaction is consistent with high Cl/Nb basalts being found at the sites in the Red Sea where hydrothermal venting is implied either at the present day by high temperature brines (Atlantis II, Discovery and Port Sudan; Fig. 3) or in the past by the presence of metalliferous sediments (Thetis, Shagara and Suakin Deeps). In detail, the strongest Cl enrichment in basalts from Atlantis II Deep is found in samples close to the SW basin and in the W flank of Discovery Deep, in agreement with the indications for the presence of the hydrothermal vents in the SW basin of Atlantis II Deep and in Discovery Deep (Fig. 3 (Brewer and Spencer, 1969; Bäcker and Richter, 1973; Schoell and Hartmann, 1973; Monin et al., 1981)). High Cl/Nb in samples from the volcano at Mabahiss Deep is in accordance with the presence of some pumpellyite minerals that indicate hydrothermal activity there (Mevel, 1981). At the same time, samples from the Shaban Deep reveal no Cl enrichment consistent with a low temperature brine and the lack of any evidence for hydrothermalism. Only the sample from the Nereus Deep (which has a high temperature brine of 30.2°C (Gurvich, 2006)) does not fit this pattern. Note, however, that this sample was embedded in sedimentary rock and appears to be much older and thus unrelated to the present high temperature of the brine. We conclude, therefore, that Cl enrichment appears to be a good indicator of hydrothermalism in the Red Sea.

4.4 Geological influences on chlorine enrichment

4.4.1 The effect of crystallisation pressure and spreading rate in the Red Sea
The strong Cl enrichment in basalts from the Red Sea due to magmatic assimilation of hydrothermally altered crust is unexpected at this ultra slow-spreading ridge, where magma fractionation (and hence liberation of latent heat allowing assimilation of oceanic crust) is expected to occur deeper than hydrothermal circulation was thought to reach (Michael and Cornell, 1998). In contrast to what is seen at fast-spreading ridges, the process does not appear to involve coupled assimilation and fractional crystallisation (AFC) as Cl shows no correlation with MgO (Fig. 2f). This is similar to what is seen at other Cl-enriched slow-spreading ridges e.g. Kolbeinsey and Reykjanes Ridges. The Red Sea is different to the Kolbeinsey or Reykjanes ridges however, in that its magma flux (degree of melting (15% after (Langmuir et al., 1992) multiplied by spreading rate (<16 mm/yr (Chu and Gordon, 1998)) is, at maximum 2.4, similar to that of not Cl-enriched slow-spreading ridges (which lie in the range 1-6 (Michael and Cornell, 1998)).

The average crystallisation pressure calculated for the Red Sea basalts is slightly lower (at 2.5 kbar) than those described for other slow-spreading ridges with low Cl/K (>3 kbar) by Michael and Cornell (1998)). This could be taken to indicate that Red Sea basalts are fractionating closer to the seafloor and so can become more Cl contaminated. In detail, however, Cl enrichment is not correlated with crystallization pressures for individual Red Sea samples and Cl enrichment is much higher than found in any other MORB (Fig. 2c, j), implying that, instead of crystallisation pressures, other geological factors are causing the extreme Cl enrichment in Red Sea basalts.

We observe also no relationship between spreading-rate variations and Cl enrichment, indicating that other factors are of larger influence on Cl contamination than local spreading rate (Fig. 5a).

4.4.2 The influence of brine pools, evaporites, faults and magmatic activity on chlorine enrichment
The extreme Cl enrichment related to assimilation of hydrothermally altered crust in the Red Sea is potentially linked to the intensity of faulting (providing pathways for fluids to alter the

crust) and magmatism (providing heat) or the presence nearby of evaporites (providing high-Cl brines). To examine these influences, we combined the Cl/Nb data with geomorphological analyses based on high-resolution bathymetric maps of the RSR (Fig. 5; Augustin et al., in review). We have seen that Cl enrichment in basaltic samples is unrelated to the presence or absence of saline brines on the present-day seafloor (Fig. 3), which suggests that the brines are not the cause of the very high magmatic Cl/Nb. To study the role of the evaporites in the extreme basaltic Cl enrichment we plotted Cl/Nb versus the distance of the sampling positions to the nearest salt glacier fronts (Fig. 5b - based on salt glacier mapping of Augustin et al. (in review)). We see that all samples with extreme Cl enrichment (Cl/Nb >100) were collected within 5 km of a salt glacier. Samples collected at >5 km away display only minor to moderate maximum Cl enrichment (Cl/Nb <60). This level of Cl enrichment may indicate Cl enrichment due to assimilation of crust, which has been hydrothermally altered by seawater without any additional Cl from the evaporites. The association of extreme Cl enrichment with evaporite proximity may indicate that the path length of hydrothermal recharge is ≤ 5 km. Whether this recharge occurs across or along axis is not discernable from our data, however, as both the rift flanks and the inter-trough zones are covered by evaporites (e.g. Tramontini and Davies, 1969; Ligi et al., 2012).

Cl enrichment in respect to the total bathymetrically traceable fault length per km² shows a negative relation (Fig. 5c). This negative relation is probably an artifact that merely reflects the masking effect of faults by evaporite glaciers and sedimentation and so is a proxy for the "proximity to evaporites" relationship seen previously.

Hydrothermal circulation at spreading centres is almost exclusively driven by magmatic heat (Allen and Seyfried Jr, 2004). To investigate the presence of a link between the proximity to magmatic heat sources and Cl enrichment, we attempted to estimate variation in intensity of volcanic activity in the Red Sea by calculating the relative area (in %) of volcanic edifices and
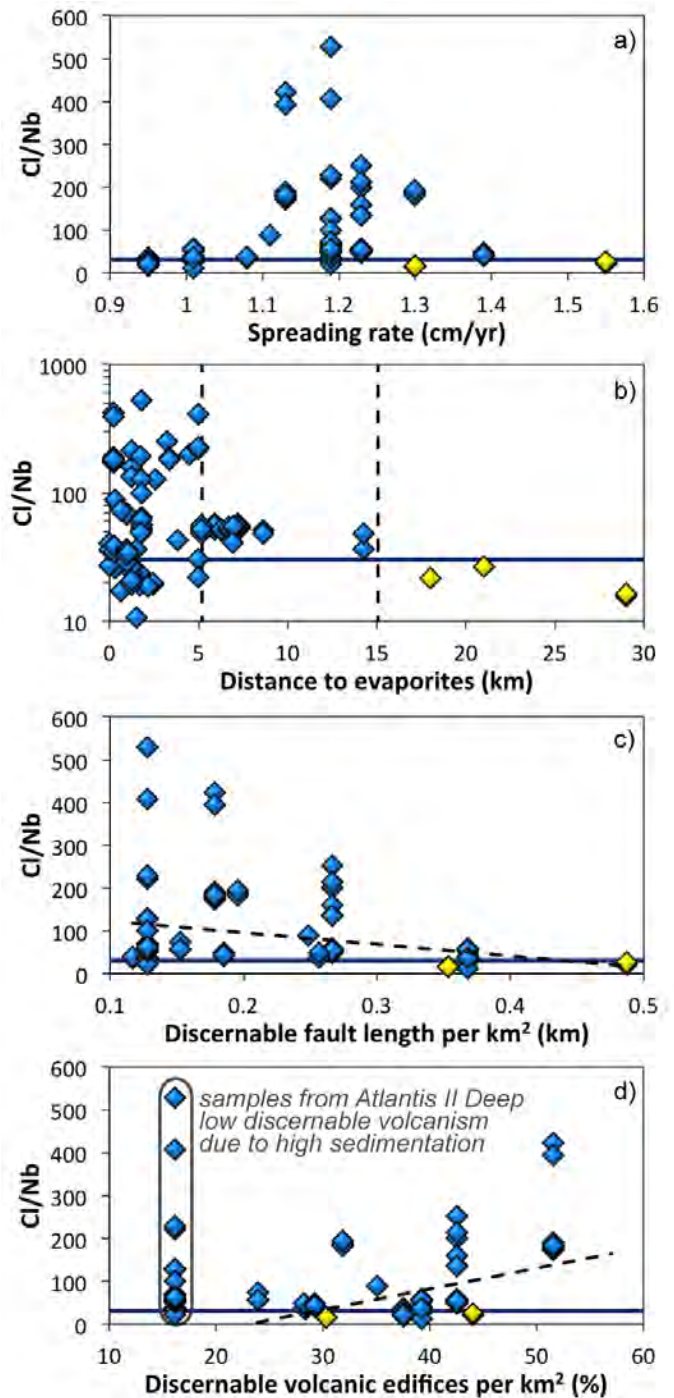

Fig. 5 - Cl/Nb relation to various geological and morphological parameters **(a)** Spreading rate after Chu and Gordon (1998). **(b)** Distance of sampling location to the nearest evaporite flow front. **(c)** Length of discernable bathymetric faults. **(d)** Area of morphologically discernable volcanic edifices and hummocky volcanics. **(e)** High Cl/Nb is highest in the Thetis-Hadarba-Hatiba area, where recent volcanic activity (high backscatter area) is high, while volcanic inactive Suakin area is low in Cl/Nb. Samples that have no or very little additional Cl due to a large distance to the evaporites of more than 15 km (in b) are marked yellow in all plots. Blue lines represent the maximum Cl/Nb mantle value. Evaporite flow front locations, fault and volcanics statistics were derived from bathymetric grids with a spatial resolution of 20 to 35 m.

hummocky volcanics identifiable from the bathymetric maps (Fig. 5d). This method does not recognise sheetflows, nor does it distinguish between fresh and older edifices and so could lead to biases in heat estimates if the mode of volcanism changes or large hiatuses in volcanic activity occur. Nevertheless, fig. 5d shows a generally positive correlation between Cl/Nb and number of volcanoes if we exclude the samples from Atlantis II Deep, where most volcanic edifices are probably buried by enhanced (chemical) sedimentation and evaporite inflow. In addition, all large dome volcanoes found in the Red Sea in Mabahiss, Thetis, Hatiba and Aswad Deeps are associated with Cl enrichment.

In summary, the high Cl enrichments relative to Nb in the Red Sea basalts appear to be related to the proximity to an evaporitic Cl source and the presence of magmatic heat.

4.5 Chlorine as tracer for hydrothermalism

The local, strong Cl enrichment of basalts in the Red Sea due to the interplay of fluids passing through evaporites and assimilation of hydrothermally altered crust, makes it possible in the Red Sea to locate the highest Cl/Nb regions (Fig. 6) and use Cl as a tracer of hydrothermal activity to predict where (past or recent) hydrothermal activity can be expected. This is the case for the technologically mostly inaccessible brine-filled Deeps, but more importantly also for the accessible, but so far less studied brine-free areas of the RSR.

4.5.1 Brine-filled Deeps

The high brine temperatures and presence of metalliferous sediments signal the presence of hydrothermal activity at Atlantis II, Discovery and Port Sudan Deeps - the high Cl/Nb of the basalts there serves to confirm this. At Shagara, Erba and Suakin Deeps the situation is slightly different - the brines are near (within 5°C) ambient bottom-water temperatures but metalliferous sediments are still present in Shagara and Suakin Deeps, again reflected in elevated Cl/Nb values. At Erba, which also has a cool brine, no metalliferous sediments are known but basaltic Cl/Nb is elevated. The high Cl/Nb indicate that hydrothermal activity has occurred here, but low temperature and the relatively small volumes of the Erba and Shagara brines (<0.2 km^3) compared to the large basins (>800 km^2) suggest that hydrothermal activity probably did not occur within the brine pool. The area within and around these Deeps represents a particularly good target for further hydrothermal exploration with the prospect of finding a non-brine-covered vent field and macrofaunal vent animal assemblages. High basaltic Cl/Nb and metalliferous sediments in the narrow Suakin Deep indicate hydrothermal activity at some point of its history, but at present there seem to be little volcanic activity (only 5% high multibeam backscatter data), while one of the measured basaltic samples was covered by manganese crust. Therefore hydrothermal activity is now possibly extinct, consistent with the current low temperature of both brines.

Shaban Deep, the most northerly known to have basalts, has evaporites very close (<2.5 km) but shows Cl/Nb ratios below mantle values, suggesting no hydrothermal activity there. This is supported by the low temperature of its large (2.5 km^3) brine pool and by a lack of hydrothermally induced metalliferous sediments (Blum and Puchelt, 1991). The presence of a brine pool is therefore in itself not an indication of hydrothermal activity, and so cannot be explained exclusively by hydrothermal circulation of fluids (Shanks and Bischoff, 1980; Zierenberg and Shanks III, 1988; Winckler et al., 2000). Instead, the explanation of brine formation by evaporite dissolution (e.g. Manheim, 1974; Pierret et al., 2001) appears more likely.

4.5.2 Brine-free Red Sea Rift

At present, there is little information on the occurrence of hydrothermal vents on the parts of the RSR that do not contain a brine, although these would be more accessible for exploration using standard instrumentation. By the use of the basaltic Cl data and mapping of the evaporite distribution, we can now assess the likeliness of hydrothermalism in these areas.
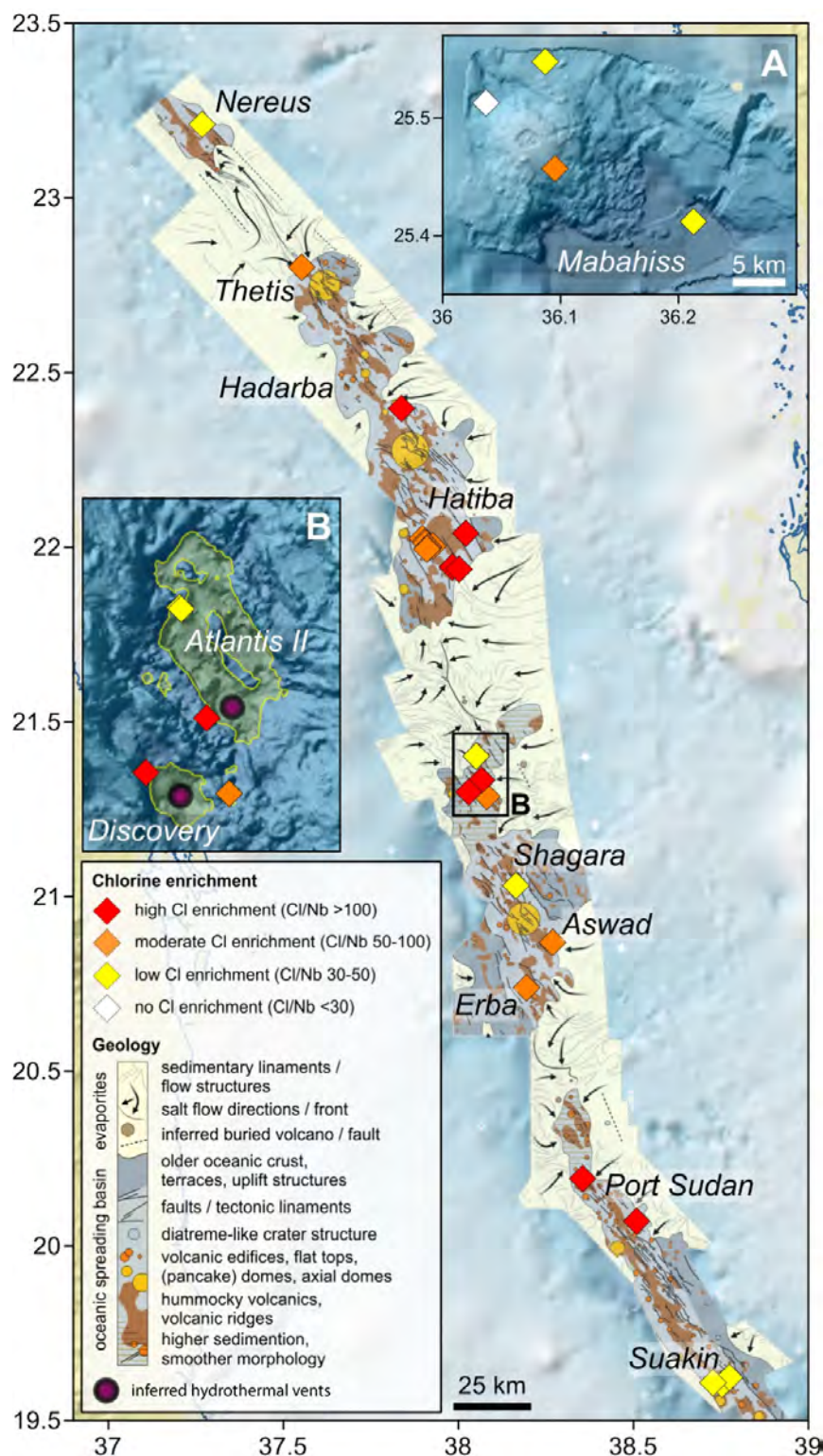
Fig. 6 – Locations of Cl enrichment indicating hydrothermal activity. The base map and colour codes are as in fig. 1; geological map is from Augustin et al. (in review). Samples with the highest Cl enrichment come from the Thetis, Hadarba and Hatiba Deeps that are characterised by high volcanic activity and/or evaporites closeby. Inset A (north of the base map): The strongest Cl enrichment at Mabahiss Deep can be observed at the SE flank of the dominant volcanic edifice. Inset B (black box in the base map): The strongest Cl enrichment in the Atlantis II area is found close to the suggested places of hydrothermal venting in the SW basin of Atlantis II Deep and the Discovery Deep (Brewer and Spencer, 1969; Bäcker and Richter, 1973; Schoell and Hartmann, 1973; Monin et al., 1981; Swift et al., 2012).

The strongest candidate for recent hydrothermal activity and a primary target for hydrothermal exploration is the Thetis-Hadarba-Hatiba Deeps area, where the highest Cl/Nb ratios are found (Fig. 3, 6). A strong chance of finding hydrothermal activity in Thetis Deep is consistent with metalliferous sediments and indications for high volcanic activity over the whole Thetis-Hadarba-Hatiba area. This area displays a comparable shallow rift axis and discernable volcanic edifices cover 44% (average of the RSR is ~33%), while 20% of the area appears to be recent (displays high multibeam backscatter). The highest Cl/Nb found in our study come from the Hatiba Dome (Fig. 6), the largest volcano described in the RSR so far and a main hydrothermal target. Other large volcanoes on the RSR appear also to be good targets, due to their strong association with Cl enrichment, i.e. the domes in Thetis, Aswad and Mabahiss Deeps. High Cl/Nb at Mabahiss Deep (>50) is restricted to relatively fresh samples from its dome, in contrast to samples with low Cl/Nb from other parts of the Mabahiss Deep (Fig. 6). This could reflect that the dome provides the heat source for hydrothermal circulation.

A main target for exploration in the southern Deeps, unrelated to any brine, is the northernmost part of Port Sudan Deep, 20 km N of its brine, where basalts shows strong Cl enrichment (Fig. 6). This Cl enrichment indicates a second hydrothermal system in Port Sudan Deep that, in contrast to the one related to the hot brine, is not venting into a brine.

Due to the lack of evaporites close to the neovolcanic zone, Cl signals in the southern Red Sea Rift are much more subtle. Nevertheless, the slight increase, compared to mantle values, in Cl/K ratios of basalts at 18°N may indicate hydrothermal circulation, although this is less clear in the basaltic Cl/Nb ratios and requires a better determination of mantle Cl/Nb ratios. Samples from 17°N do not show any sign of Cl enrichment. However, we cannot distinguish if this is due to the lack of hydrothermalism, or that Cl enrichment due to assimilation of hydrothermally altered crust is invisible, compared to the high initial Cl contents of these trace element enriched samples.

5 Conclusions

The Red Sea basalts are generally characterized by elevated Cl values and e.g. Cl/Nb ratios compared to basalts from other slow-spreading ridges. These high Cl contents cannot be explained by source enrichment, crystal fractionation or seafloor weathering processes. The good agreement of indications of hydrothermal fields in the Red Sea with the sample locations of Cl enriched basalts shows that chlorine enrichment due to assimilation of hydrothermally altered crust can also be observed at slow-spreading ridges. The extent of Cl enrichment does not appear to be controlled by spreading rate or the petrologically derived depth of last crystallisation, nor is it related to the presence of highly saline brines on the seafloor or the extent to which that seafloor is faulted. Instead, extreme Cl enrichment appears to be linked to two factors - evidence for recent volcanism and/or hydrothermalism and proximity to evaporitic deposits on the rift flank. We conclude that the elevated Cl contents in the magmas reflect the assimilation of crust, which has previously been hydrothermally altered by Cl-rich brines derived from the evaporites. Individual magmas in any one hydrothermal area are not all Cl enriched to the same extent, implying that the degree of hydrothermal alteration of the crust (and hence its Cl content) is highly variable.

Based on these relationships, we can use the Cl/Nb contents of basalts as an indicator of the location of likely hydrothermal activity. Our data give strong indications for widespread hydrothermal activity in the Red Sea rift both at the sites where high temperatures of brines indicate hydrothermalism, but also outside of the brines. Sites of particular interest for future hydrothermal research are the Thetis-Hadarba-Hatiba Deeps (and especially their large volcanic domes), the northern Port Sudan Deep, the dome at Mabahiss Deep and the Shagara-Aswad-Erba Deeps.

The more subtle enriched Cl values (Cl/Nb 30-100) at the more open and non-brine filled parts of the RSR, e.g. at Shagara-Aswad-Erba Deeps or 18°N indicates that with the here used method small variations in Cl due to assimilation of hydrothermally altered crust, can be

resolved even without an increase in Cl due to evaporites. Since we can resolve these variations, this method can potentially also be used at other slow-spreading ridges and aid there in the search of hydrothermal systems, even if chlorine enrichments will most likely not be as extreme as in the Red Sea.

Acknowledgments

Chapter 4:

Lower crustal hydrothermal circulation at slow-spreading ridges – evidence from chlorine in Arctic and South Atlantic basalt glasses and melt inclusions

This chapter consist of a manuscript, which is prepared to be submitted at *Contributions to Mineralogy and Petrology*.

Authors:
Froukje M. van der Zwan[1*], Colin W. Devey[1], Thor H. Hansteen[1], Renat R. Almeev[2], Nico Augustin[1], Matthias Frische[1] and Rashad A. Bantan[3]

[1] Geomar Helmholtz Centre for Ocean Research Kiel, Germany
[2] Institut für Mineralogie, Universität Hannover, Germany
[3] Faculty of Marine Science, King Abdulaziz University, Jeddah, Saudi Arabia

Abstract

Hydrothermal circulation at slow-spreading ridges is important for cooling of the oceanic crust but the depth to which this occurs is uncertain. Hydrothermal activity increases the chlorine (Cl) content of the crust. Therefore, if magma assimilated such crust, hydrothermal alteration can be determined by raised Cl contents of erupted basalts. The depth and extent of these processes can be quantified when the Cl data is combined with chemical thermobarometry. Previous global studies on Cl in mid-ocean ridge basalts did not find Cl addition in the deep crystallizing basalts (>300 MPa) from slow-spreading ridges and indicated, therefore, a restricted depth for hydrothermal circulation. However, new high-precision Cl data from the slow-spreading Red Sea demonstrate that significant variations are present among the intrinsically low Cl concentrations (~50-200 ppm), which provide evidence for Cl addition by assimilation processes. To examine the depth extent of hydrothermal circulation in the oceanic crust at slow-spreading ridges, we performed high-precision Cl measurements on basaltic glasses and melt inclusions from the Southern Mid-Atlantic Ridge (SMAR; ~3 cm/yr) and the Gakkel Ridge (max. 1.5 cm/yr).

The measured Cl contents of basalt glass cover a range of 40 to 400 and 700 ppm for the SMAR and Gakkel Ridge respectively, whereas SMAR melt inclusions cover a range between 20 and 460 ppm. Many of the samples display elevated Cl compared to elements of similar incompatibility (e.g. K, Nb). Cl/Nb ratios higher than mantle ratios in 75% of the samples (up to 62 and 36 compared to mantle ratios of 20 and 18.5 for SMAR and Gakkel Ridge respectively) are interpreted to indicate assimilation of hydrothermally altered crust, since there is no geochemical evidence for magmatic or seafloor Cl addition, e.g. there is no correlation between Cl/Nb and trace elements and Cl distribution is homogeneous in the analysed glass samples. Assimilation of hydrothermal fluids and crust is evident from the large range of Cl/K ratios in glasses and in melt inclusions in phenocrysts and further supported by resorption and re-equilibration textures of phenocrysts and the abundant occurrence of xenocrysts and gabbroic fragments in the rocks.

Lower crustal crystallization depths (10-13 km) are indicated by crystallization pressures calculated from Cpx-melt equilibrium pairs. In contrast, calculated pressures based on glass compositions alone cover the full depth range down to the mantle typical for slow-spreading ridges, but assume merely crystallization under equilibrium conditions. We demonstrate that this assumption is not valid as the samples typically show disequilibrium between glasses and minerals and were affected by assimilation processes. Therefore, barometry based on melt compositions only is unreliable and should not be used. Based on the Cpx crystallization pressures, petrographic and geochemical indications for assimilation in magma chambers, combined with and earlier petrologic and thermodynamic evidence for lower crustal melt-rock reactions and crystallization, we envisage a model in which assimilation of hydrothermally altered crust takes place down to a depth of at least 10 km. Such assimilation depths imply that hydrothermal circulation goes down to the lower crust at slow-spreading ridges, probably aided by extensive faulting. Circulation of fluids enhances crystallization and assimilation processes and the resulting deep cooling of the crust adds support to the sheeted sill model to form the lower oceanic crust at slow-spreading ridges.

The lower Cl/Nb at slow-spreading ridges compared to fast-spreading ridges is likely due to localised and comparatively less intensive circulation of hydrothermal fluids at depth and the lack of large shallow magma chambers where contamination can occur almost continually. Cl/Nb increase in basalts is enhanced at slow-spreading ridges by the occurrence of evaporites and high magmatic activity. Trace-element-enriched magmas (with higher primordial Cl) and samples from areas with a cool and thin crust display comparatively low increases in Cl/Nb due to assimilation processes. Nevertheless hydrothermal plumes are associated with samples at <10 km distance with Cl/Nb ratios that are higher than mantle values and thus Cl/Nb can be used as a tracer for the exploration of (active or extinct) hydrothermal fields.

1 Introduction

New oceanic crust is formed at mid-ocean ridges by magmatic processes, which focus magma from a large volume of asthenospheric melting into a narrow region (Forsyth, 1992) comprising eruptive rocks underlain by feeder systems, a more or less ephemeral magma chamber and a thick body of crystal mush. Although there is fairly convincing evidence that hydrothermal circulation of seawater cools the upper parts of this system, it is not completely understood how the deeper parts of the intrusive magmatic system are cooled rapidly enough to form the lower oceanic crust, because this also appears to require advection of heat by fluid or rock movement (e.g. Maclennan et al., 2005; VanTongeren et al., 2008). At present, two competing endmember models exist for cooling the lower oceanic crust, mostly taking fast-spreading ridges into account. The *gabbro glacier model* postulates crystallisation of all lower crustal rocks in a shallow melt lens followed by plastic downward flow of the cumulates. It was originally developed under the assumption that hydrothermal circulation does not penetrate and cool the crust beneath the shallow melt lens, although it does not exclude deep hydrothermal circulation (Nicolas et al., 1988; Henstock et al., 1993; Morgan and Chen, 1993; Quick and Denlinger, 1993; Chen, 2001; Coogan et al., 2002b). The *sheeted sill model*, in contrast, requires deep cooling by hydrothermal circulation as melt lenses cool and crystallise at several depths, down to the base of the crust (Kelemen et al., 1997; Korenaga and Kelemen, 1997; Kelemen and Aharonov, 1998; Lissenberg et al., 2004). Up to present there is, however, no consensus on the maximum depth that hydrothermal circulation may occur in newly formed oceanic crust (e.g. Mottl, 2003) and it is further uncertain what role hydrothermal circulation plays in the cooling of slow-spreading ridges.

Indications for deep circulation of hydrothermal fluid at fast-spreading ridges come from studies of ophiolites or oceanic drill sections (Gregory and Taylor, 1981; McCulloch et al., 1981; Stakes and Vanko, 1986; Nehlig and Juteau, 1988; Nehlig et al., 1994; Lecuyer and Reynard, 1996; Kawahata et al., 2001; Coogan, 2003; Nicolas et al., 2003; Bosch et al., 2004; Koepke et al., 2011) which display high temperature alteration of the lower crust. Deep cooling due to deep hydrothermal circulation is consistent with constant calculated cooling rates as a function of depth (e.g. VanTongeren et al., 2008), with thermodynamic models that indicate steep crustal isotherms beneath the spreading axis (Cherkaoui et al., 2003; Maclennan et al., 2005; Hasenclever et al., 2014), seismic evidence (Dunn et al., 2000) and microfracture mechanisms that permit fluids to penetrate into the hotter and ductile lower-crustal regions (above ~700°C up to 1000°C (Lister, 1974; Manning et al., 2000; Nicolas et al., 2003; Koepke et al., 2005)). At (ultra) slow-spreading ridges (<5.5 cm/yr), seafloor is produced by tectonic as well as magmatic processes (e.g. Dick et al., 2003; Cannat et al., 2006). Due to the lack of permanent magma chambers and the lower temperatures of slow-spreading ridges (e.g. Harper, 1985; Detrick et al., 1990), faulting can be more extensive and deeper. Deep normal faults that formed as shear zones during early stretching of the lithosphere can penetrate into the lower crust and form deep pathways for hydrothermal fluids (Harper, 1985; Cannat et al., 1991; Mével and Cannat, 1991; Stakes et al., 1991). P-wave tomography underneath the TAG hydrothermal field indicates hydrothermal circulation, related to the detachment fault, extending at least 2 km, but potentially 3½ km deep (Zhao et al., 2012). Other direct information on the depth of penetration of hydrothermal circulation at slow-spreading ridges is only available from drill-cores that have a limited depth extent (e.g. <1600 m in Alt and Bach, 2006) or from tectonically exposed parts on the lower crust (Gillis et al., 1993), which have thus been exposed to seawater for extended periods of time.

Deep hydrothermal alteration of the oceanic crust can indirectly be traced by raised chlorine (Cl) contents of erupted basalts, if it can be demonstrated that the magma assimilated high-Cl, hydrothermally altered crust (Michael and Schilling, 1989; Michael and Cornell, 1998; Kent et al., 1999a; Coogan et al., 2002a; Gillis et al., 2003; Sun et al., 2007; France et al., 2009; van der Zwan et al., in review; see chapter 3). Both active hydrothermal cells and ancient, now inactive hydrothermal circulation can be identified this way. Assimilation of crustal rocks by rising MORB magmas has been shown to take place (Bédard et al., 2000 and references therein), but the depth and/or hydrothermal alteration state of these rocks is

uncertain so far. If we can use petrologic evidence to determine at which depth Cl contamination due to assimilation of hydrothermally altered crust took place, by using chemical thermobarometers to determine the last crystallisation depth, we can gain important information about the depth of seawater penetration – which is important for mass and energy balances during the generation of oceanic crust.

Models derived from fast-spreading ridges indicate enrichment in Cl compared to trace elements of similar incompatibility (e.g. K or Nb) at the roof of a shallow (100-300 MPa) axial magma chamber, where magma interacts with fluids of the shallower hydrothermal circulation cell (Coogan et al., 2002a; Gillis et al., 2003; le Roux et al., 2006; France et al., 2009; France et al., 2010; Kendrick et al., 2013). In contrast, Michael and Cornell (1998), did not find Cl addition to basaltic magmas from most slow-spreading ridges (i.e. they have low Cl/K). These magmas have on average much higher calculated crystallisation pressures (>300 MPa) than those at fast-spreading ridges. Therefore, they concluded that hydrothermal circulation (at least at slow-spreading ridges) must occur at pressures lower than 300 MPa. In contrast, high precision Cl measurements on basalt glasses from the ultra slow-spreading Red Sea Rift (max. 1.6 cm/yr) indicate that hydrothermal circulation could lead to Cl enrichment compared to e.g. Nb (Cl/Nb of >30) in basalts from slow-spreading ridges, which in the case of the Red Sea is enhanced as a result of hydrothermal circulation through thick evaporite sequences that neighbour the active rift (van der Zwan et al., in review; see chapter 3). More importantly, there is no relation observed in the Red Sea basalts between Cl/Nb and calculated pressures of last equilibration. Instead, high Cl/Nb is observed both in samples with low crystallisation pressures and in samples that reveal significantly higher calculated pressures (up to 600 MPa) than the Cl enriched samples found by Michael and Cornell (1998) and thus would indicate deep hydrothermal circulation.

To understand if the discrepancy in Cl addition between the Red Sea and various other slow-spreading ridges constitutes a real difference or is an effect of systematic bias in earlier studies due to poor precision of Cl measurements at low concentration levels, we performed high precision Cl measurements (van der Zwan et al., 2012) on glassy basalt samples from two other slow-spreading ridges in addition to the Red Sea (Fig. 1). The southern Mid-Atlantic Ridge (SMAR) at 7-10 °S was selected as a slow-spreading ridge (~3 cm/yr) as it has both depleted and trace element enriched samples that display varying crystallisation pressures (0-800 MPa; Almeev et al., 2008). The arctic Gakkel ridge at 6 °W - 85 °E was chosen as an ultra-slow-spreading ridge (max. 1.5 cm/yr) as it has a strongly tectonic character and possesses a very thin crust (Coakley and Cochran, 1998; Dick et al., 2003; Michael et al., 2003). The new Cl data are directly compared to the data of the Red Sea (van der Zwan et al., in review; see chapter 3) and put into context with the previous Cl studies (e.g. Michael and Cornell, 1998). With the Cl information from glasses of those three ridges we can study the relationships between last crystallisation pressure and Cl/Nb as well as other influencing factors such as spreading rate, melting percentages and basalt compositions. To study Cl addition in three dimensions and thus obtain information on the full depth range of melts, we analysed Cl both in glasses and in melt inclusions in minerals from the SMAR basalts. If Cl addition due to assimilation of hydrothermally altered crust can be identified, we can use petrologic pressure calculations to indicate the depth extent of hydrothermal circulation at slow-spreading ridges, and thus confine the depth of cooling due to hydrothermal circulation.

2 Geological background

2.1 Southern Mid-Atlantic Ridge

The southern Mid-Atlantic Ridge (SMAR) between 7° and 10°S, east of Ascension Island, is a mature ridge with slow-spreading rates of 31-32 mm/yr (DeMets et al., 2010; fig. 1a). The area is bounded to the north by the Ascension Fracture Zone and to the south by the Bode Verde Fracture Zone. The region is divided into four segments that are separated by

overlapping spreading centres and show varying morphologies (A1-A4; Bruguier et al., 2003). Segment A1 has a typical slow-spreading ridge character with a well-developed deep rift valley of >2950 m, while segment A2 represents a shallower axial high and is 2100-3000 m deep (Fig. 1a; Bruguier et al., 2003). The shallower ridge of segment A2 is associated with a thicker crust of ~11 km, compared to ~5 km under A1 (Minshull et al., 1998; Bruguier et al., 2003). Segment A1 displays microseismicity at 2-4 km depth and teleseismicity (Grevemeyer et al., 2013), while segment A2 shows little earthquake activity, thought to indicate a higher temperature of the crust (Fig. 1a; Devey et al., 2010). However, the thick and warm crust at segment A2 appears associated with former high magmatic activity as the most recent lava flows are tectonised, in contrast to the shallowest segment A3, which seems currently highly active (Devey et al., 2010). The samples used in this study were sampled during the Meteor cruise M41/2 and are well studied in terms of their major and trace elements and isotope compositions and crystallisation pressures (Möller, 2002; Almeev et al., 2008; Paulick et al., 2010; Hoernle et al., 2011). The samples in this study come from segments A1 and A2 as these samples display the largest range in calculated last crystallisation pressures up to the highest depths (200-900 MPa; Almeev et al., 2008). The geochemical studies show mixing between a depleted unradiogenic MORB source and radiogenic, trace element enriched sources. Hoernle et al. (2011) recognised 3 different enriched sources over the whole segment (from which 2 are identified in samples from segments A1 and A2), all of the HIMU type. The enriched samples display higher H_2O contents and nearly isobaric crystallisation pressures (100-300 MPa) and occur mostly in segments A2 and A3, while the more depleted samples show lower H_2O contents and a range of calculated last crystallisation pressures (200-900 MPa) and occur mainly in segments A1, A2 and A4 (Almeev et al., 2008). Hydrothermal circulation in the studied area is known from the Nibelungen hydrothermal field and two indications of plume activity at 7°57'S and 8°17'S (Fig. 1a; German et al., 2002; Devey et al., 2005; Melchert et al., 2008). Further south at segment A3 the Lilliput hydrothermal field occurs (German et al., 2002; Haase et al., 2009).
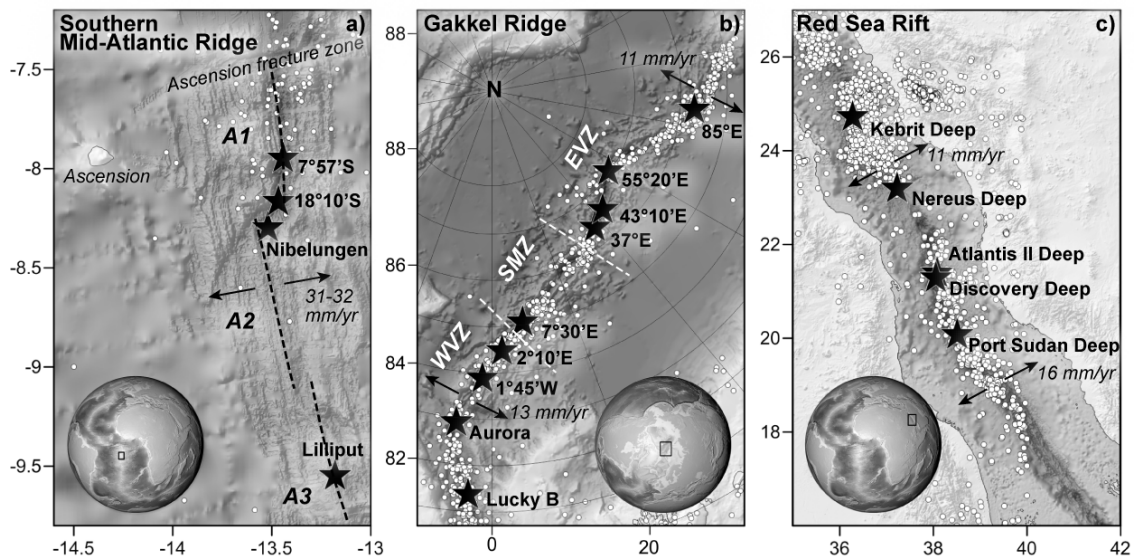
Fig. 1 – Overview of studied areas on the **(a)** SMAR, **(b)** Gakkel Ridge compared to the **(c)** Red Sea Rift. The SMAR study area is subdivided in various segments (after Bruguier et al., 2003; samples are from A1 and A2). The Gakkel Ridge is segmented into 3 zones (after Michael et al., 2003): western volcanic zone (WVZ), sparsely magmatic zone (SMZ) and eastern volcanic zone (EVZ). White dots indicate earthquake hypocenters with M≤3 (from ISC, 1960 to present). Note the lack of earthquakes in SMAR segment A2. Black stars indicate hydrothermal activity after German et al., 2002, Baker et al., 2004 and Gurvich 2006. Spreading rates (after DeMets et al., 2010 and Chu & Gordon; 1998) are indicated by arrows.

2.2 Gakkel Ridge

The Gakkel ridge (6 °W - 85 °E) shows the lowest orthogonal spreading rate on Earth at 11-13 mm/yr (DeMets et al., 2010) and lacks transform offsets (Fig. 1b). The Gakkel Ridge has a very deep rift (>4600 m) with thin estimated crustal thickness (<4 km; Coakley and Cochran, 1998; Jokat et al., 2003). The Gakkel Ridge can be subdivided in three different magmato-tectonic terrains (Fig. 1b; Michael et al., 2003). The Western Volcanic Zone (WVZ; 7°W-3°E) is a volcanic area with many small cones on the ridge and displays a larger extent of melting that the other two segments. The Sparsely Magmatic Zone (SMZ; 3°E-28°E) in contrast consists mostly of peridotitic "crust", with only rare basalts or volcanic features. The Eastern Volcanic Zone (EVZ; 29°E-85°E) contains large (~30 km) widely-spaced volcanic centres of which some show recent activity. Basalts from the Gakkel Ridge from the AMORE 2001 cruise (with PFS Polarstern and USCGC Healy) are generally enriched in trace elements with high Ba/TiO_2 ratios, however with a large variability between the different segments and also between samples (Michael et al., 2003). Isotopically two distinct sources were identified: samples from the WVZ have a DUPAL-signature attributed to a contribution of sub-continental lithospheric mantle, while samples from the EVZ have a signature similar to Atlantic-Pacific MORBs (Goldstein et al., 2008). In this model the boundary between the different mantle domains is represented by the SMZ. Hydrothermal activity at the Gakkel Ridge seems to be high compared to other (ultra)slow-spreading ridges (Edmonds et al., 2003; Michael et al., 2003). Although only one active vent site was confirmed by visual observations (Aurora), 8-11 more vent sites were inferred by light scattering, temperature and Mn data in the water column (Fig. 1b; Edmonds et al., 2003; Baker et al., 2004). Teleseismic earthquakes are present along the whole ridge (Fig. 1b).

2.3 Red Sea Rift

The Red Sea Rift occurs in a comparatively young ocean (<30 Ma), and, although ultra slow-spreading (10-16 mm/yr; fig. 1c; Chu and Gordon, 1998), has an average crustal thickness of ~5-6 km (Makris et al., 1991). Samples vary from depleted and trace element enriched tholeiitic basalts to alkali-basalts with OIB signatures south of 17°N and represent varying mantle sources and degrees of melting (Altherr et al., 1988; Volker et al., 1993; Haase et al., 2000). The Red Sea water itself has a high salinity and contains highly saline brines at the bottom of some of the so-called Red Sea Deeps (Gurvich, 2006 and references therein) and evaporite sequences at the flanks of the neovolcanic rift and in intertrough zones (e.g. Tramontini and Davies, 1969; Izzeldin, 1989; Searle and Escartin, 2004; Ligi et al., 2012; Augustin et al., in review). Hydrothermalism is not visually confirmed anywhere in the Red Sea, apart from an extinct smoker fragment (Blum and Puchelt, 1991) but inferred by metalliferous sediments and high temperatures and metal concentration of the seafloor brines (Fig. 1c; Brewer and Spencer, 1969; Bäcker and Richter, 1973; Shanks and Bischoff, 1980; Hartmann, 1985; Pierret et al., 2001; Gurvich, 2006; Laurila et al., 2014). Cl/Nb in volcanic rocks is extreme in the Red Sea (higher than at fast-spreading ridges), related to the places that show indications of active hydrothermalism, indicating assimilation of hydrothermally altered crust in most of the Red Sea Rift (van der Zwan et al., in review; see chapter 3). The highest Cl/Nb is observed at the sample locations close to evaporite sequences and with high magmatic activity. No relation between Cl/Nb and crystallisation pressures is observed.

3 Analytical methods

Measurements were performed on glassy basaltic samples from collections of expeditions R/V Meteor 41/2 (SMAR; e.g. Möller, 2002; Almeev et al., 2008; Hoernle et al., 2011) and AMORE 2001 (Gakkel Ridge; e.g. Michael et al., 2003; Goldstein et al., 2008), and compared to those from Red Sea basalts (van der Zwan et al., in review; see chapter 3). For

basaltic glass measurements, 3 pieces of glass >2 mm across were selected per rock under a binocular microscope based on their fresh appearance and lack of visible vesicles, alteration rims or minerals. The mounted glass was prepared, polished and then cleaned with Milli-Q water following the procedures in van der Zwan et al. (2012) to avoid Cl contamination. Optically clear SMAR Ol, Pl and Cpx minerals were prepared in a same procedure. For selected SMAR samples with elevated Cl/Nb glass contents, Ol and Pl minerals with melt inclusions were mounted in UHU Hart glue mixed with aceton and doubly polished sections (~60 µm thick) were prepared. Melt inclusions were selected based on homogeneity and large sizes/thicknesses and with a good surface.

Major elements and Cl measurements were carried out with a Jeol JXA-8200 ''Superprobe'' electron microprobe at GEOMAR, Kiel using an acceleration voltage of 15 kV. Chlorine and potassium (K) were measured with a beam current of 80 nA and a beam diameter of 10 µm using the mapping technique described in van der Zwan et al. (2012) and van der Zwan et al. (in review; see chapter 3). The Cl and K results are the average 2-8 measurements per sample and have a uncertainty of <3 and <20 ppm for Cl and K respectively (2SE). For the Cl and K measurements of the melt inclusions, the method was slightly adapted by a reduced beam current of 50 nA and a mapping repetition of 14 times, in order to avoid a strong Cl signal of the mounting material through the thin samples. Internal glass standards show a reproducibility of on average 3.2 ppm (2SD) for this method. Nevertheless, an additional signal from the mounting material is visible in the Cl data of the melt inclusions and corrected for, but results in a higher uncertainty of 19.2 ppm 2SD. This higher uncertainty does however not influence the main conclusions derived from Cl data of the melt inclusions. Any measurements that show discrepancies (e.g. inhomogeneous Cl, mostly due to bubble forming) were discarded.

Major elements of the glasses were measured with a defocused spot of 5 µm and a beam current of 10 nA. Counting times were 20/10 s (peak/background) for SiO_2, TiO_2, Al_2O_3, FeO, MgO, CaO, Na_2O and P_2O_3 and 30/15 s for MnO. For calibration and monitoring of data quality, we used natural reference samples from the Smithsonian Institute (Jarosewich et al., 1980). The average was taken of 9 analyses per sample to assure homogeneity. Relative analytical precision is generally <2.5 %, but up to 5% for Na_2O and ~30% for MnO and P_2O_3. Additionally, available (literature) data for the samples were used; for the SMAR data is utilized from Möller (2002) and data measured by K.M. Haase (pers. comm.) with a CAMECA SX-50 at GEOMAR and a JEOL JXA8900 Superprobe at the Institut für Geowissenschaften, University of Kiel. Settings were the same as above and accuracy and precision are better than 5% apart for MnO and P_2O_3. Additional major element data measured by J.E. Snow on a Jeol JXA 8900RL electron probe microanalyzer at the University of Mainz was used for Gakkel Ridge basalts. Mineral point analyses and transects were measured with a focused beam spot. Plagioclase and Cpx were measured with a beam current of 20 nA and counting times of 20/10 s, apart for K_2O in Pl (40/20 s) and Cr_2O_3 and TiO_2 in Cpx (30/15 s). Olivine was measured with a beam current of 100 nA and 20/10 s counting times for SiO_2, Al_2O_3, MgO, FeO, 30/15 s for MnO, Cr_2O_3, 60/30 s for CaO and 40/20 s for NiO.

For consistency trace element glass analyses were analysed for all samples and carried out at GEOMAR, Kiel by LA-ICP-MS using a 193 nm Excimer laser system (GeoLasPro from Coherent) coupled with a double-focusing, high-resolution magnetic sector mass spectrometer (AttoM from Nu Intruments), operating at 5 J/cm^2 fluency and 10 Hz repetition rate. Point ablation induced 300 shots per 90 µm spot, after pre-ablation at a 120 µm spot size and carried out under He carrier gas, subsequently mixed with Ar carrier gas. The reference sample NIST610 (Jochum et al., 2011) was operated at 32 µm spot size. MPI-DING reference samples (Jochum et al., 2006) were also analysed to evaluate the measurements. Relative analytical precision is typically <2–5% (one standard deviation), except for Li, B, U (<10%) and Be, Cs (<40%).

Glass H_2O and CO_2 concentrations were determined using a Fourier Transformation Infrared (FTIR) Bruker IFS88 spectrometer coupled with an IR Scope II microscope at Institute of Mineralogy, Leibniz University of Hannover. H_2O and CO_2 concentrations were measured on

doubly polished glass chips (~1 mm² in size) that had a thickness of 150 to 50 μm, measured with a digital micrometer Mitutyo (precision ± 2 μm (Behrens, 2009)) by 3 points for every polished glass fragment. Absorption spectra in the mid-infrared (MIR) range were collected using a spot size of 100 x 100 μm (average of 50 scans) and using the following operating conditions: globar light source, KBr beam splitter, MCT (HgCdTe) detector, 4 cm⁻¹ spectral resolution, spectral range 13000 to 0 cm⁻¹. The H_2O concentration was measured at the peak that is attributed to the OH stretch vibration (3550 cm⁻¹) using a molar absorption coefficient of 67 L·cm⁻¹·mol⁻¹ (Stolper, 1982). The CO_2 concentration was measured at the peak doublet with maxima at 1430 and 1510 cm⁻¹ using molar absorption coefficient of 317 L·cm⁻¹·mol⁻¹ (Shishkina et al., 2010). Glass densities were calculated using the equation of Yamashita et al. (1997) for basaltic compositions: $\rho = 2819 - 20.8 \cdot C_{H_2O}$. The H_2O and CO_2 concentrations were calculated based on the Lambert-Beer law using the peak height, which was determined by reference to a straight tangential base line. The average values of three measurements per sample were used to calculate the H_2O and CO_2 contents of the glasses, with a standard deviation usually less than 0.02 and 0.003 wt.% respectively.

Pressure and temperature conditions at the point of last crystallization equilibrium are calculated by two different methods. Pressures for all samples were calculated with the software COMAGMAT version 3.57 that is based on empirical models calibrated with an experimental database (Ariskin and Barmina, 2004). Here we used inversed modelling (see Almeev et al., 2008) of the major elements and H_2O concentrations of the glasses. The effects of small amounts of H_2O on crystallisation were taken into account by incorporating recent experimental calibration coefficients (Almeev et al., 2007a; Almeev et al., 2007b; Almeev et al., 2012). The pressure models of COMAGMAT have an uncertainty of ±100 MPa and are comparable with models used in Michael and Cornell (1998) (Almeev et al., 2008). For the samples that contain Cpx, pressures were also calculated using equilibrium exchange between Cpx and the melt (Putirka et al., 1996; Putirka, 2008), determined by analysing the compositions of Cpx-rims and their host glasses; the uncertainty of this method is ±170 MPa.

4 Results

4.1 Geochemistry of the Glasses

The major and trace elements together with the Cl data are given in Table 1 and 2. The Cl concentrations of the basalt glasses are highly variable with values of 43-704 ppm for the Gakkel ridge and 52-459 for the SMAR, although the majority of the samples lie below 200 ppm (Fig. 2a). These values are not as high as observed in the Red Sea (up to 1400 ppm; van der Zwan et al., in review; see chapter 3) and rather fall in the same range as literature data for other slow-spreading ridges (mostly <200 ppm; Michael and Cornell, 1998). High Cl contents at the SMAR are found at both segments of the studied area (A1 and A2; fig. 1a). High Cl contents at Gakkel ridge occur mostly at the SMZ, while samples from the EVZ and WVZ display Cl contents of <250 and <150 ppm respectively.

In contrast to samples from the Red Sea, there is a weak relation between Cl and MgO, with slightly lower Cl values for higher MgO contents (Fig. 2a); this trend is, however, poor (R^2 = 0.22; n = 117) and not parallel to fractionation models ((log(Cl_8/Cl) = 0.12*(MgO-8) from Weaver and Langmuir (1990), assuming unfractionated Cl concentrations of 50, 100 or 150 ppm at 8 wt.% MgO; fig. 2a). Moreover, there is a positive correlation between Cl and several incompatible elements, e.g. K, Rb, Ba, Th, U, Nb, Ta, La, Ce, Pr, Nd and H_2O, from which the best correlation exists between Cl and Nb (R^2 = 0.87; fig. 2b,c). In addition, for samples from the SMAR there is a correlation observed between high Cl contents and radiogenic Sr, Nd and Pb isotopes (isotope data from Hoernle et al. (2011); fig. 2d). No correlation is observed between Cl and indicators of degassing, melting processes or source variations (e.g. CO_2/Nb, Na_8, Pb/Ce, U/Nb; correlation with Cl gives R^2 <0.2 (cf. Hofmann et al., 1986; Langmuir et al., 1992; Miller et al., 1994; Saal et al., 2002) and the relation between H_2O and Ce indicates no significant addition or loss of H_2O (Fig. 2e).
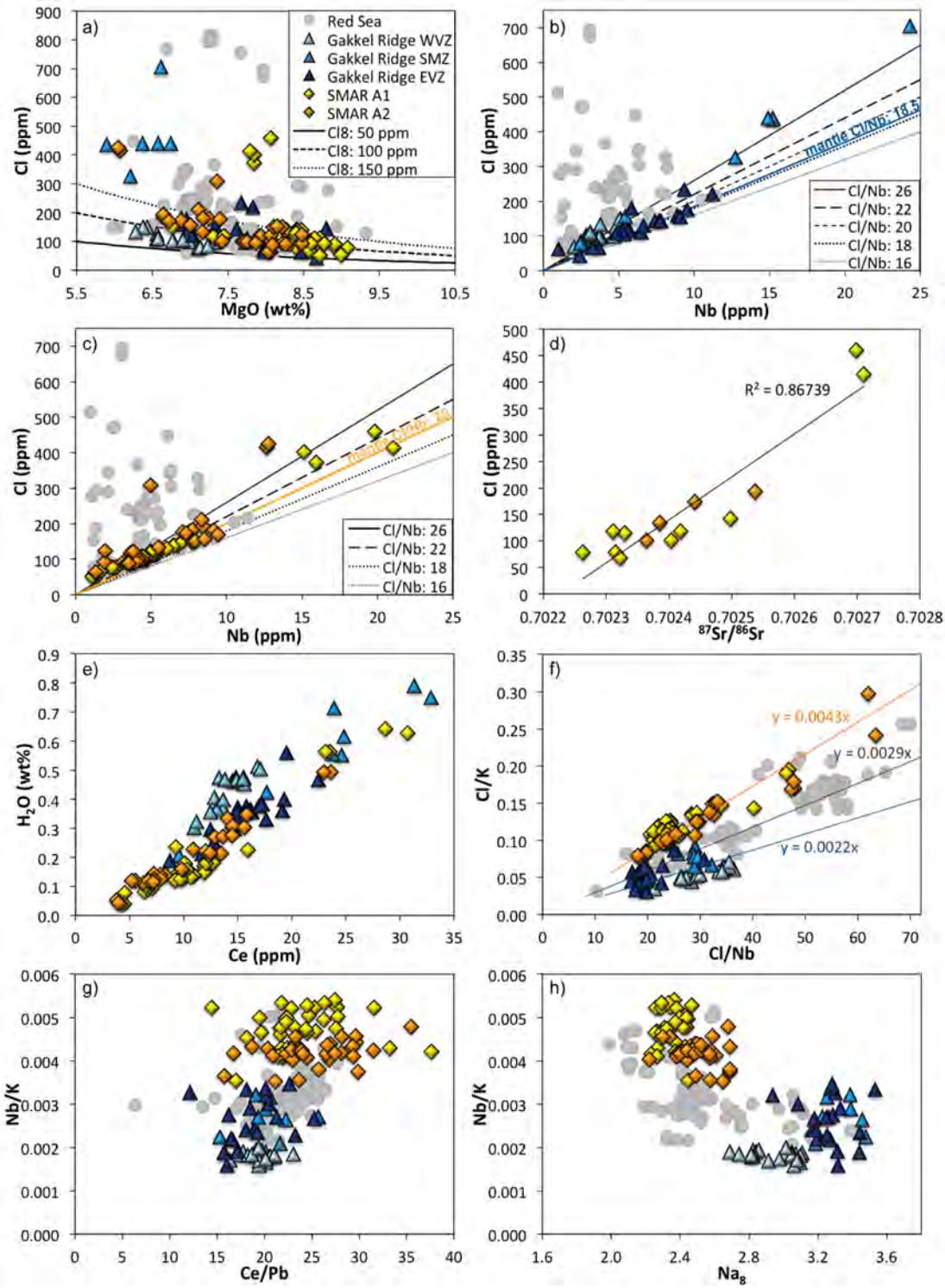
Fig. 2 – Chlorine compositions of SMAR and Gakkel Ridge basalt glasses compared to major and trace element compositions. **(a)** Cl vs. MgO compared to fractionation trends for Cl compositions of 50, 100 or 150 ppm at 8 wt.% MgO (black lines). Cl vs. Nb for **(b)** Gakkel Ridge and **(c)** SMAR samples together with lines of various Cl/Nb ratios. The most likely (see discussion) mantle Cl/Nb ratio for the two locations is highlighted. Note that many samples lie above these mantle values. **(d)** H_2O and Ce contents are relatively well correlated. **(e)** Chlorine concentrations are related to radiogenic isotope ratios (i.e. $^{87}Sr/^{86}Sr$). **(f)** Cl/K and Cl/Nb are correlated for each sample suite, but display different trends between the suites. Variations in Nb/K between the samples suites are correlated to **(g)** Ce/Pb and **(h)** Na_8.
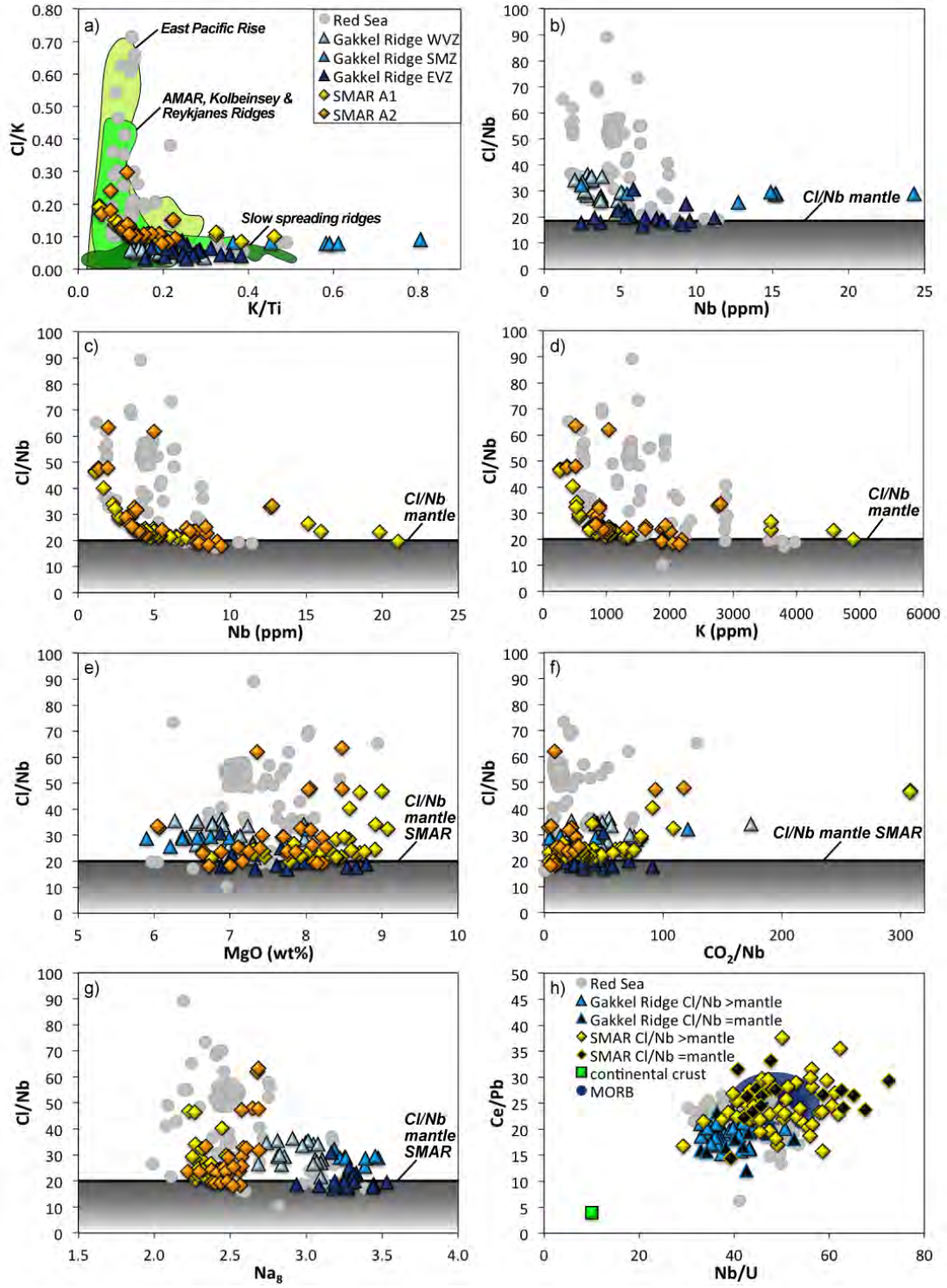
Fig. 3 – Indicators of hydrothermal Cl addition (Cl/Nb, Cl/K) in basaltic glass plotted against major and trace element data. **(a)** Cl/K ratios reach higher values than previously observed for average slow-spreading ridges, but are not as high as observed for Red Sea Rift basalts or fast-spreading ridges. High Cl/K (>0.1) is not observed for samples with K/Ti >0.22. Numerous **(b)** Gakkel Ridge and **(c)** SMAR samples have Cl/Nb above the Cl/Nb mantle ratio. Samples from Gakkel Ridge show high Cl/Nb over the complete range of Nb; at the SMAR this is mainly for samples with low Nb. **(d)** Cl/Nb versus K shows no smooth mixing trend. **(e)** Cl/Nb is not related to MgO (fractionation), **(f)** CO_2 (degassing), **(g)** Na_8 (melt degree) or **(h)** Ce/Pb and Nb/U (continental influence). Gakkel Ridge samples reveal low Cl/Nb and high Na_8.

Table 1
Southern Mid-Atlantic Ridge chlorine, volatile and major element data[a]

Sample	Latitude	Longitude	Cl	2SE	K	Nb	Cl/K	Cl/Nb	SiO2	TiO2	Al2O3	FeO	MnO	MgO	CaO	Na2O	P2O5	H2O	CO2
Segment A1																			
132 DS-1 [b]	7.666	13.456	140.8	2.2	1297	6.8	0.11	20.7	50.2	1.31	15.0	10.1	0.14	8.4	11.8	2.3	0.15	0.17	270
132 DS-2	7.666	13.456	139.3	1.1	1303	6.4	0.11	21.6	50.4	1.34	15.1	10.1	0.19	8.5	12.0	2.3	0.11	0.16	246
132 DS-5 [b]	7.666	13.456	139.1	1.1	1296	6.8	0.11	20.6	50.8	1.33	15.2	10.0	0.17	8.3	11.8	2.2	0.25	0.17	274
132 DS-6 [b]	7.666	13.456	138.6	0.2	1299	6.5	0.11	21.3	50.1	1.32	14.5	10.0	0.15	8.4	11.7	2.4	0.16	0.17	261
133 DS-1	7.718	13.444	99.4	0.9	994	4.7	0.10	21.1	50.9	1.27	15.1	9.5	0.17	8.2	12.5	2.3	0.10	0.15	229
133 DS-4 [b]	7.718	13.444	111.0	0.4	1136	4.8	0.10	23.0	49.2	1.16	15.4	9.2	0.17	8.7	12.3	2.4	0.14	0.18	353
133 DS-7 [b]	7.718	13.444	105.3	0.4	1057	4.3	0.10	24.4	49.8	1.16	15.5	9.3	0.19	8.1	12.2	2.4	0.25	0.24	179
133 DS-8 [b]	7.718	13.444	111.7	2.2	1128	4.8	0.10	23.0	48.9	1.14	15.9	9.1	0.19	8.6	12.3	2.4	0.14	0.18	348
133 DS-9 [b]	7.718	13.444	129.9	0.4	1395	6.0	0.09	21.5	49.2	1.24	15.5	9.5	0.17	8.4	12.2	2.4	0.15	0.15	264
136 DS-1 [b]	7.773	13.432	99.9	1.0	855	4.5	0.12	22.4	49.3	1.22	14.9	9.8	0.14	8.1	12.1	2.2	0.14	0.13	214
136 DS-3 [b]	7.773	13.432	100.8	1.3	847	4.6	0.12	22.0	50.2	1.20	15.1	9.6	0.18	8.2	12.1	2.3	0.13	0.13	222
137 DS-2 [b]	7.820	13.427	77.1	1.1	571	2.7	0.14	28.4	50.5	1.11	15.2	9.8	0.15	8.4	12.0	2.3	0.23	0.10	222
137 DS-3	7.820	13.427	77.1	0.6	579	2.7	0.13	28.4	50.6	1.11	15.2	9.8	0.20	8.6	12.4	2.2	0.07	0.10	219
137 DS-4 [b]	7.820	13.427	78.0	0.3	572	2.7	0.14	29.3	50.0	1.10	15.1	9.7	0.17	8.5	12.1	2.2	0.11	0.09	218
138 DS-1 [b]	7.867	13.431	459.4	1.9	4583	19.8	0.10	23.2	48.8	1.66	16.0	9.4	0.16	8.1	11.6	2.4	0.36	0.64	96
138 DS-2_1,2	7.867	13.431	372.8	2.7	3601	15.9	0.10	23.4	49.2	1.85	15.4	9.9	0.17	7.8	12.2	2.4	0.21	0.56	240
138 DS-2_3	7.867	13.431	401.6	2.9	3595	15.1	0.11	26.5	49.2	1.85	15.4	9.9	0.17	7.8	12.2	2.4	0.21	0.56	240
138 DS-3	7.867	13.431	414.0	1.5	4898	21.0	0.08	19.7	47.5	2.13	16.5	9.7	0.14	7.8	11.5	2.5	0.27	0.63	95
139 DS-2 [b]	7.919	13.411	116.7	0.6	1016	5.3	0.11	22.0	50.3	1.31	14.9	10.1	0.18	7.9	11.9	2.3	0.13	0.14	208
139 DS-3 [b]	7.919	13.411	117.9	2.6	1014	5.4	0.12	21.8	50.3	1.31	14.8	10.1	0.17	7.9	11.9	2.3	0.13	0.13	193
140 DS-1 [b]	7.965	13.399	77.5	1.5	529	2.3	0.15	34.1	49.0	1.01	15.7	9.3	0.17	8.9	12.3	2.2	0.12	0.08	93
140 DS-2 [b]	7.965	13.399	78.0	1.4	524	2.4	0.15	32.3	49.3	1.02	15.8	9.3	0.17	9.1	12.2	2.2	0.10	0.10	263
141 DS-1 [b]	7.986	13.431	66.6	1.1	468	1.7	0.14	40.2	52.3	0.83	16.3	7.6	0.12	8.6	10.7	2.4	0.10	0.08	151
141 DS-2 [b]	7.986	13.431	89.3	0.2	815	3.7	0.11	24.1	50.4	1.16	14.4	9.5	0.16	8.3	12.5	2.3	0.14	0.14	240
142 DS-1 [b]	8.019	13.430	92.7	2.0	733	3.8	0.13	24.2	50.1	1.24	15.2	9.6	0.17	8.6	11.9	2.3	0.24	0.12	229
142 DS-3	8.019	13.430	91.0	0.6	739	3.7	0.12	24.4	50.6	1.25	15.0	9.7	0.17	8.9	12.0	2.3	0.09	0.12	238
142 DS-7	8.019	13.430	92.1	1.4	734	3.9	0.13	23.5	50.1	1.24	15.1	9.6	0.16	8.8	12.1	2.2	0.08	0.13	263
143 DS-1	8.055	13.417	52.5	1.2	270	1.1	0.19	46.8	48.7	0.91	15.9	10.8	0.21	9.0	12.6	2.1	0.04	0.04	346
143 DS-2 [b]	8.055	13.417	51.7	0.5	272	1.1	0.19	46.3	48.8	0.92	16.2	10.6	0.21	8.7	12.1	2.2	0.23	0.04	344
144 DS-1 [b]	8.090	13.453	114.5	2.3	1067	5.3	0.11	21.6	50.5	1.63	14.4	11.0	0.19	7.5	11.7	2.5	0.17	0.20	175
145 DS-1 [b]	8.125	13.411	116.8	0.2	1037	5.2	0.11	22.5	50.8	1.61	14.3	10.9	0.19	7.3	11.8	2.5	0.16	0.18	154

Sample	Latitude	Longitude	Cl	2SE	K	Nb	Cl/K	Cl/Nb	SiO₂	TiO₂	Al₂O₃	FeO	MnO	MgO	CaO	Na₂O	P₂O₅	H₂O	CO₂
145 DS-2_1,2 [b]	8.125	13.460	121.3	0.7	1039	5.0	0.12	24.5	51.1	1.55	14.6	10.9	0.20	7.3	11.6	2.5	0.30	0.18	170
145 DS-2_3 [b]	8.125	13.460	116.8	0.3	1033	5.2	0.11	22.7	51.1	1.55	14.6	10.9	0.20	7.3	11.6	2.5	0.30	0.18	170
145 DS-3	8.125	13.460	118.4	1.1	1043	5.0	0.11	23.7	51.0	1.58	14.2	10.9	0.22	7.4	11.9	2.5	0.12	0.18	158
145 DS-4 [b]	8.125	13.460	150.1	1.1	1347	7.1	0.11	21.1	50.3	1.83	13.9	11.5	0.21	6.8	11.2	2.6	0.16	0.23	126
146 DS-1 [b]	8.167	13.446	108.6	1.4	947	4.4	0.11	24.6	50.4	1.26	15.0	9.9	0.16	8.2	12.2	2.3	0.15	0.16	297
146 DS-2 [b]	8.167	13.446	106.3	0.7	949	4.6	0.11	22.9	50.8	1.27	15.1	9.8	0.21	8.2	11.8	2.4	0.26	0.16	271
146 DS-3 [b]	8.167	13.446	107.0	0.2	944	4.5	0.11	23.9	50.6	1.27	15.2	9.8	0.18	8.1	12.2	2.3	0.20	0.16	339
Segment A2																			
147 DS-1 [b]	8.314	13.607	132.8	0.9	1322	5.5	0.10	24.2	51.3	1.43	14.0	10.9	0.21	7.2	11.6	2.5	0.15	0.23	153
147 DS-2 [b]	8.314	13.607	63.4	0.8	375	1.3	0.17	47.9	50.6	1.17	15.8	10.0	0.14	8.1	10.5	2.6	0.10	0.06	156
147 DS-3 [b]	8.314	13.607	63.7	2.7	378	1.3	0.17	47.3	50.8	1.14	15.8	10.0	0.16	8.0	10.5	2.6	0.10	0.04	126
147 DS-4 [b]	8.314	13.607	179.2	0.7	1881	7.6	0.10	23.6	51.1	1.38	14.3	10.1	0.17	7.2	11.8	2.3	0.17	0.21	94
148 DS-4 [b]	8.345	13.600	183.3	0.8	1920	7.7	0.10	23.7	51.6	1.61	13.5	11.0	0.17	6.6	11.1	2.6	0.17	0.33	95
148 DS-6 [b]	8.345	13.600	192.4	1.4	2003	8.4	0.10	22.8	51.6	1.67	13.5	11.2	0.18	6.6	10.9	2.6	0.17	0.35	104
149 DS-1 [b]	8.374	13.616	414.8	2.3	2765	12.6	0.15	32.8	51.0	2.09	13.9	12.1	0.19	6.1	10.4	2.8	0.25	0.49	55
149 DS-4	8.374	13.616	425.3	1.6	2802	12.8	0.15	33.3	51.6	2.10	13.9	12.2	0.22	6.1	10.5	2.6	0.22	0.49	75
151 DS-1 [b]	8.451	13.590	101.0	1.6	806	3.5	0.13	29.3	51.9	1.30	15.2	10.1	0.14	7.7	11.0	2.5	0.12	0.12	87
151 DS-2 [b]	8.451	13.590	100.4	1.3	806	3.4	0.12	29.8	52.0	1.35	15.0	9.9	0.13	7.4	10.9	2.5	0.21	0.13	86
151 DS-3	8.451	13.590	99.2	2.0	798	3.4	0.12	29.3	51.7	1.26	15.6	10.2	0.17	7.7	10.7	2.6	0.09	0.12	85
152 DS-1 [b]	8.508	13.564	98.6	0.3	1006	4.4	0.10	22.3	51.1	1.37	15.3	10.3	0.16	7.8	11.5	2.5	0.15	0.14	95
152 DS-2 [b]	8.508	13.564	99.0	0.6	1001	4.2	0.10	23.8	50.7	1.35	14.7	10.3	0.16	7.8	11.4	2.6	0.14	0.14	110
153 DS-1 [b]	8.555	13.550	210.6	1.1	1931	8.4	0.11	25.2	51.2	1.69	14.4	11.1	0.16	7.1	11.1	2.6	0.19	0.30	89
153 DS-3 [b]	8.555	13.550	176.7	1.5	1618	7.1	0.11	24.8	51.1	1.57	14.0	10.6	0.18	7.4	11.4	2.6	0.17	0.27	99
154 DS-1 [b]	8.608	13.535	173.1	1.8	1612	7.3	0.11	23.6	51.7	1.75	14.2	11.3	0.19	6.9	11.0	2.4	0.26	0.27	149
155 DS-1 [b]	8.693	13.543	91.7	0.5	866	3.2	0.11	29.0	50.4	1.06	16.1	10.1	0.19	8.2	11.6	2.5	0.12	0.11	85
156 DS-1 [b]	8.749	13.503	119.4	0.5	890	3.7	0.13	32.6	50.4	1.24	16.1	10.6	0.18	7.9	10.7	2.6	0.14	0.14	84
156 DS-3 [b]	8.749	13.503	94.6	0.3	942	4.0	0.10	23.6	50.2	1.16	15.7	10.5	0.18	7.9	11.9	2.5	0.18	0.13	103
156 DS-4 [b]	8.749	13.503	122.1	1.4	889	3.8	0.14	31.8	50.2	1.28	15.6	10.5	0.16	8.1	10.7	2.7	0.13	0.13	82
157 DS-1 [b]	8.808	13.496	150.1	0.6	1878	7.7	0.08	19.5	50.8	1.50	15.5	9.0	0.14	8.1	12.0	2.4	0.16	0.21	76
157 DS-2 [b]	8.808	13.496	149.3	0.2	1874	7.8	0.08	19.1	50.5	1.50	15.0	8.9	0.13	8.2	11.9	2.4	0.16	0.22	80
157 DS-3 [b]	8.808	13.496	151.7	1.1	1875	7.9	0.08	19.1	51.0	1.49	15.8	9.0	0.15	8.2	11.8	2.4	0.30	0.22	79
158 DS-2 [b]	8.838	13.495	181.1	0.7	2190	9.1	0.08	19.8	51.3	1.73	13.9	10.2	0.17	7.2	11.4	2.6	0.18	0.31	71
159 DS-2	8.909	13.468	308.5	1.3	1040	5.0	0.30	62.0	51.7	1.51	15.3	10.4	0.12	7.4	10.1	2.8	0.10	0.16	46
160 DS-1_1 [b]	8.968	13.460	92.2	0.9	515	1.9	0.18	47.8	50.7	1.13	15.6	9.6	0.13	8.5	10.6	2.6	0.11	0.12	-

Sample	Latitude	Longitude	Cl	2SE	K	Nb	Cl/K	Cl/Nb	SiO_2	TiO_2	Al_2O_3	FeO	MnO	MgO	CaO	Na_2O	P_2O_5	H_2O	CO_2
160 DS-1_2,3 [b]	8.968	13.460	124.1	3.1	516	2.0	0.24	63.4	50.7	1.13	15.6	9.6	0.13	8.5	10.6	2.6	0.11	0.12	-
161 DS-2 [b]	9.013	13.457	88.4	0.4	837	3.4	0.11	25.8	49.9	1.15	16.0	10.0	0.17	8.1	11.4	2.6	0.24	0.12	97
161 DS-3	9.013	13.457	89.4	1.7	833	3.5	0.11	25.3	50.2	1.17	15.9	9.9	0.15	8.3	11.4	2.5	0.08	0.12	105
162 DS-1 [b]	9.080	13.445	156.7	0.8	2056	8.5	0.08	18.3	51.2	1.74	14.3	10.9	0.16	7.0	11.3	2.7	0.18	0.28	75
162 DS-2 [b]	9.080	13.445	169.8	0.8	2151	9.4	0.08	18.1	51.5	1.82	13.9	11.4	0.19	6.7	11.2	2.7	0.14	0.30	55

Table 1 continued
Trace element data

Sample	Li	Be	B	Ni	Cu	Zn	Sc	Rb	Sr	Y	Zr	Cs	Ba	La	Ce	Pr	Nd	Sm	Eu	Gd	Tb	Dy	Ho	Er	Tm	Yb
Segment A1																										
132 DS-1	6.2	0.35	1.4	144.3	79.2	111.6	37.0	4.2	100.4	26.8	63.9	0.04	43.7	5.2	11.9	1.8	8.9	2.9	1.06	4.1	0.70	4.6	1.09	3.0	0.42	2.8
132 DS-2	5.7	0.26	1.1	142.9	77.8	110.4	36.3	4.1	99.4	26.5	63.4	0.04	42.4	5.1	12.0	1.7	8.5	2.6	1.01	4.0	0.66	4.8	0.97	2.9	0.43	3.0
132 DS-5	6.0	0.44	1.6	145.6	76.9	108.2	37.3	4.0	102.2	27.5	65.1	0.04	43.4	5.3	12.3	1.8	8.7	2.8	1.03	3.8	0.75	5.0	0.98	3.2	0.49	2.8
132 DS-6	5.9	0.35	1.6	143.4	78.3	111.8	36.3	4.1	101.3	26.5	63.4	0.05	42.6	5.0	12.3	1.8	8.8	2.8	1.04	3.7	0.66	4.7	1.08	3.1	0.43	2.8
133 DS-1	5.7	0.44	1.4	108.5	88.5	102.4	40.4	2.8	96.7	26.9	63.9	0.04	29.8	4.0	10.5	1.7	8.5	2.9	1.02	4.1	0.68	4.8	1.02	2.9	0.43	3.1
133 DS-4	5.0	0.23	1.2	145.1	99.2	94.9	38.5	3.0	108.2	23.5	61.5	0.04	30.3	4.0	10.1	1.6	8.4	2.4	0.94	3.4	0.59	4.2	0.89	2.7	0.39	2.5
133 DS-7	4.8	0.21	1.2	103.6	96.3	102.3	36.2	2.7	120.5	21.5	51.9	0.03	27.7	3.5	9.2	1.4	7.4	2.4	0.97	3.4	0.59	4.0	0.79	2.5	0.31	2.2
133 DS-8	5.1	0.27	1.5	145.5	101.8	96.1	38.4	3.2	106.8	23.3	58.8	0.04	29.0	3.9	10.1	1.6	7.7	2.7	0.94	3.3	0.60	3.9	0.91	2.7	0.39	2.5
133 DS-9	5.2	0.54	1.6	133.3	90.2	100.4	38.2	3.8	115.5	24.9	65.4	0.06	37.9	5.0	11.9	1.8	8.4	3.0	0.99	3.6	0.64	4.5	0.93	2.8	0.41	2.6
136 DS-1	5.5	0.28	1.2	119.0	85.5	107.0	38.5	2.7	84.6	25.3	55.5	0.02	28.8	3.7	9.7	1.5	7.7	2.6	1.00	3.5	0.67	4.5	0.99	2.8	0.41	2.7
136 DS-3	5.8	0.19	1.3	122.9	86.4	109.4	39.8	2.8	86.9	26.5	57.4	0.02	28.9	3.9	9.9	1.5	7.8	2.6	1.03	3.6	0.68	4.8	1.01	2.9	0.43	2.8
137 DS-2	5.7	0.21	1.1	136.8	86.5	108.8	39.4	1.6	71.3	25.6	47.9	0.02	17.2	2.5	7.1	1.2	6.4	2.5	0.95	3.7	0.66	4.5	0.95	2.9	0.42	2.8
137 DS-3	6.3	0.28	1.4	130.0	84.3	103.1	38.7	1.7	69.0	25.5	45.9	0.02	17.0	2.4	6.6	1.1	6.1	2.4	0.85	3.1	0.61	4.4	0.93	2.6	0.40	2.6
137 DS-4	5.8	0.14	1.0	127.3	82.0	113.1	37.7	1.6	68.2	24.4	45.4	0.02	17.4	2.5	6.7	1.1	5.8	2.3	0.88	3.2	0.61	4.3	0.96	2.7	0.40	2.6
138 DS-1	4.5	0.63	1.8	124.8	80.6	112.1	31.2	12.8	233.8	21.3	105.2	0.14	124.2	13.2	28.6	3.7	15.8	4.1	1.34	4.4	0.67	4.1	0.85	2.4	0.31	2.1
138 DS-2_1,2	4.8	0.48	1.5	101.9	91.4	-	35.9	10.0	186.6	22.4	92.3	0.10	100.2	10.9	23.5	3.2	13.6	3.6	1.20	4.3	0.67	4.3	0.83	2.5	0.36	2.2
138 DS-2_3	4.9	0.70	2.3	102.5	87.8	-	35.0	10.0	182.2	22.6	89.9	0.14	98.2	10.2	23.1	3.0	13.7	3.6	1.30	3.8	0.60	4.6	0.86	2.1	0.29	2.4
138 DS-3	4.8	0.72	1.8	130.7	72.4	112.6	29.6	13.4	242.4	21.1	108.1	0.14	133.6	13.8	30.7	3.9	16.7	4.1	1.39	4.3	0.65	4.2	0.82	2.2	0.31	1.9
139 DS-2	6.1	0.37	1.3	107.6	81.6	110.2	39.6	3.2	85.6	27.8	60.5	0.05	33.3	4.6	10.9	1.6	8.3	2.8	1.04	4.0	0.73	5.0	1.07	3.1	0.50	2.8
139 DS-3	6.2	0.21	1.4	105.0	81.5	117.8	40.0	3.4	86.7	28.2	60.5	0.04	33.3	4.4	10.6	1.6	8.4	2.9	1.07	4.1	0.72	4.7	1.03	3.2	0.44	3.1
140 DS-1	5.1	0.20	1.1	167.7	90.5	100.0	36.8	1.4	74.6	22.3	44.7	0.01	14.0	2.2	6.4	1.1	6.0	2.2	0.86	3.0	0.58	4.0	0.83	2.6	0.35	2.4
140 DS-2	5.3	0.22	1.1	167.5	93.1	99.5	37.4	1.4	75.3	22.7	45.2	0.02	13.9	2.3	6.5	1.1	5.9	2.1	0.87	3.3	0.57	4.0	0.88	2.5	0.35	2.5
141 DS-1	3.5	0.24	0.8	190.2	72.6	89.3	23.7	1.0	152.6	12.9	30.9	0.01	10.1	1.6	4.5	0.8	4.3	1.6	0.72	2.2	0.39	2.3	0.48	1.4	0.19	1.2
141 DS-2	5.6	0.29	1.4	99.8	94.3	107.5	39.9	2.3	86.2	24.7	56.3	0.02	22.9	3.3	9.1	1.5	7.3	2.4	0.98	3.5	0.62	4.4	0.95	2.8	0.41	2.7

Sample	Li	Be	B	Ni	Cu	Zn	Sc	Rb	Sr	Y	Zr	Cs	Ba	La	Ce	Pr	Nd	Sm	Eu	Gd	Tb	Dy	Ho	Er	Tm	Yb
142 DS-1	5.7	0.33	0.9	143.6	78.2	103.7	36.0	2.3	77.1	25.8	57.1	0.04	22.7	3.3	9.1	1.5	7.4	2.6	0.96	3.7	0.70	4.5	1.04	3.0	0.41	2.7
142 DS-3	5.9	0.44	1.5	142.8	82.2	106.0	37.2	2.2	77.0	25.8	57.5	0.03	24.3	3.4	9.2	1.5	7.5	2.5	0.96	3.6	0.67	4.6	1.02	2.9	0.44	2.7
142 DS-7	5.7	0.33	1.0	154.8	80.0	108.0	38.4	2.3	81.1	27.5	60.3	0.02	23.9	3.5	9.7	1.5	8.0	2.8	0.98	3.9	0.72	4.7	1.02	3.1	0.44	2.8
143 DS-1	4.9	0.25	1.0	141.5	121.9	95.3	44.7	0.6	78.7	23.0	34.2	0.01	6.2	1.3	4.5	0.8	4.2	1.6	0.69	2.8	0.51	4.0	0.90	2.8	0.43	2.8
143 DS-2	5.3	0.24	1.1	169.1	119.3	89.5	44.3	0.6	78.5	22.7	33.7	0.02	6.2	1.2	4.1	0.7	4.2	1.5	0.71	2.6	0.52	3.8	0.86	2.5	0.38	2.8
144 DS-1	7.4	0.40	1.6	84.0	74.4	131.4	41.3	3.3	89.8	32.7	80.8	0.03	32.5	4.8	12.8	2.0	10.7	3.6	1.24	4.8	0.85	5.9	1.25	3.5	0.55	3.5
145 DS-1	7.2	0.51	1.4	80.0	74.1	127.5	42.9	3.1	84.2	33.5	79.0	0.04	30.6	4.5	12.3	1.9	10.1	3.7	1.29	4.8	0.87	5.8	1.31	3.8	0.55	3.6
145 DS-2_1,2	7.0	0.29	1.3	80.8	72.3	118.6	40.5	3.1	81.5	31.7	75.1	0.03	29.2	4.4	12.0	1.9	9.3	3.3	1.18	4.7	0.79	5.4	1.11	3.5	0.51	3.4
145 DS-2_3	7.9	0.32	1.2	81.9	72.4	127.7	43.1	3.2	83.6	33.6	79.3	0.04	30.3	4.6	12.7	2.0	10.1	3.6	1.31	5.3	0.86	6.1	1.33	3.8	0.53	3.6
145 DS-3	6.5	0.39	1.7	79.1	73.2	122.8	41.3	3.1	81.7	32.2	77.0	0.05	28.7	4.5	12.1	1.9	9.8	3.6	1.26	4.6	0.90	5.7	1.23	3.7	0.52	3.5
145 DS-4	8.1	0.43	1.8	64.5	70.3	142.2	43.4	4.2	88.7	40.0	98.3	0.07	37.8	5.9	15.9	2.5	12.7	4.2	1.48	5.8	1.08	7.2	1.58	4.5	0.65	4.1
146 DS-1	5.8	0.19	1.6	116.4	81.7	112.6	37.9	2.7	85.3	25.5	59.9	0.03	26.1	3.7	9.9	1.6	7.7	2.7	0.95	3.7	0.64	4.4	0.99	2.7	0.40	2.7
146 DS-2	5.7	0.34	1.1	113.7	81.6	106.9	39.3	2.7	86.5	26.1	62.7	0.04	26.2	3.9	10.3	1.6	8.3	2.7	1.01	4.0	0.71	4.6	1.03	3.1	0.41	2.6
146 DS-3	5.9	0.31	1.3	117.6	82.7	104.7	39.0	2.6	88.2	26.8	63.4	0.04	26.6	3.9	9.9	1.6	8.0	2.7	1.03	3.9	0.69	4.6	0.95	3.0	0.38	2.8
Segment A2																										
147 DS-1	5.9	0.30	1.4	62.0	107.9	126.3	41.5	2.9	105.8	28.0	71.1	0.03	27.3	4.1	10.9	1.7	8.7	3.0	1.13	4.1	0.73	4.8	1.08	2.9	0.46	2.8
147 DS-2	4.7	0.41	0.8	191.1	125.9	120.0	28.9	0.6	112.7	18.3	44.2	0.02	5.9	1.2	3.8	0.7	4.1	1.9	0.83	2.8	0.51	3.5	0.71	2.0	0.28	1.8
147 DS-3	4.8	0.28	0.9	191.0	126.1	122.9	28.6	0.6	113.5	18.4	45.0	0.01	5.9	1.3	3.9	0.7	4.2	2.0	0.87	2.9	0.52	3.5	0.67	2.0	0.26	1.8
147 DS-4	5.8	0.48	1.6	64.3	95.4	115.7	38.7	4.6	122.7	24.5	75.3	0.06	43.2	5.4	13.5	2.0	9.6	3.1	1.09	3.9	0.67	4.2	1.01	3.0	0.41	2.6
148 DS-4	6.3	0.54	1.5	44.7	87.3	136.0	38.7	4.3	121.6	27.4	87.3	0.05	40.6	5.7	14.1	2.2	10.7	3.5	1.25	4.2	0.71	5.0	1.13	3.0	0.43	2.8
148 DS-6	6.6	0.50	1.8	44.5	80.2	-	39.3	4.5	125.2	28.8	92.3	0.04	43.8	6.1	15.8	2.3	11.8	3.5	1.29	4.9	0.80	5.1	1.13	3.3	0.44	3.0
149 DS-1	8.5	0.67	2.4	61.3	77.3	-	40.5	6.6	116.4	43.2	148.4	0.08	60.8	9.2	23.6	3.5	17.2	5.3	1.76	7.2	1.17	8.0	1.76	5.0	0.70	4.8
149 DS-4	8.8	0.71	2.6	60.1	79.4	160.7	40.0	6.9	113.4	42.2	145.5	0.06	58.7	9.2	23.0	3.5	17.1	5.3	1.73	6.9	1.19	7.6	1.66	5.0	0.70	4.4
151 DS-1	5.5	0.33	1.1	138.4	118.9	121.3	33.0	1.7	133.4	20.3	57.3	0.02	15.9	2.5	7.1	1.2	6.0	2.3	1.03	3.3	0.59	3.9	0.81	2.1	0.32	2.0
151 DS-2	5.1	0.39	1.2	122.4	128.1	-	32.7	1.6	129.2	20.2	58.2	0.02	15.4	2.4	6.8	1.2	6.0	2.5	1.00	3.4	0.61	4.0	0.81	2.5	0.32	1.9
151 DS-3	4.9	0.49	1.4	134.4	123.4	-	31.4	1.6	131.0	20.3	57.4	0.03	15.7	2.5	6.9	1.1	6.1	2.3	0.98	3.3	0.55	3.9	0.81	2.2	0.33	2.0
152 DS-1	5.0	0.42	1.1	117.4	159.4	119.9	36.1	1.9	134.9	20.7	59.7	0.03	20.2	2.9	8.3	1.3	6.9	2.4	1.00	3.3	0.60	4.0	0.84	2.3	0.31	2.0
152 DS-2	5.0	0.41	1.1	109.4	133.9	-	35.5	1.8	133.8	20.4	60.2	0.03	20.1	2.8	7.8	2.0	6.7	2.2	1.00	3.5	0.56	3.8	0.82	2.2	0.32	2.1
153 DS-1	6.2	0.53	1.8	82.9	76.3	-	38.2	4.0	125.4	28.7	93.1	0.05	41.4	5.6	14.5	2.3	11.0	3.6	1.27	4.6	0.76	5.1	1.13	3.1	0.44	2.9
153 DS-3	6.3	0.41	1.2	87.6	80.8	119.9	39.2	3.6	111.9	27.5	81.6	0.04	34.7	5.0	12.8	2.0	10.0	3.3	1.22	4.1	0.77	4.7	1.03	3.1	0.45	2.8
154 DS-1	7.1	0.51	1.9	68.1	78.5	-	40.9	3.6	101.4	31.4	92.4	0.04	33.4	5.1	13.6	2.2	10.9	3.7	1.30	5.2	0.83	5.7	1.19	3.6	0.51	3.3
155 DS-1	4.0	0.53	1.4	139.2	133.8	-	35.3	1.7	133.3	18.6	46.9	0.03	16.3	2.3	6.2	1.0	5.6	1.9	0.81	2.6	0.50	3.3	0.75	2.1	0.31	1.9
156 DS-1	4.6	0.35	1.3	161.6	120.3	123.8	31.6	1.8	132.8	20.3	56.5	0.03	17.2	2.6	7.2	1.2	6.3	2.4	0.87	3.1	0.58	3.6	0.72	2.4	0.29	2.2
156 DS-3	4.8	0.29	0.9	118.0	159.4	112.4	40.2	1.9	137.8	20.8	54.1	0.02	20.3	2.9	7.9	1.3	6.5	2.2	0.94	3.3	0.57	3.8	0.82	2.3	0.33	2.1

Sample	Li	Be	B	Ni	Cu	Zn	Sc	Rb	Sr	Y	Zr	Cs	Ba	La	Ce	Pr	Nd	Sm	Eu	Gd	Tb	Dy	Ho	Er	Tm	Yb
156 DS-4	4.5	0.31	1.4	166.4	118.3	116.0	31.9	1.8	136.1	20.5	56.5	0.03	18.2	2.7	7.2	1.2	6.3	2.3	0.94	3.0	0.59	3.7	0.74	2.1	0.31	2.0
157 DS-1	4.3	0.47	1.3	135.3	104.5	102.5	33.1	3.8	168.9	19.3	75.9	0.04	40.4	4.8	12.4	1.8	9.1	2.8	1.07	3.5	0.57	3.5	0.71	2.1	0.29	1.8
157 DS-2	4.6	0.55	1.5	133.1	104.1	100.1	34.2	3.7	171.8	19.8	76.6	0.04	40.3	4.7	12.0	1.8	9.2	2.8	1.05	3.7	0.59	3.5	0.72	2.0	0.30	1.9
157 DS-3	4.6	0.60	1.4	137.7	111.1	102.7	33.7	3.9	166.9	19.6	76.5	0.05	40.1	4.9	12.4	1.8	9.0	2.8	1.06	3.7	0.61	3.7	0.76	2.1	0.29	1.9
158 DS-2	6.1	0.47	1.2	69.1	91.0	121.1	37.8	4.5	158.8	23.6	88.8	0.04	47.4	5.8	14.5	2.2	10.8	3.2	1.23	3.9	0.71	4.3	0.90	2.7	0.37	2.4
159 DS-2	4.4	0.37	1.5	173.3	109.2	125.4	29.0	2.0	158.4	21.7	73.0	0.04	20.6	3.6	9.8	1.5	8.1	2.7	1.07	3.8	0.68	4.0	0.87	2.4	0.29	2.0
160 DS-1_1	3.9	0.35	0.9	194.4	122.8	-	29.9	0.8	129.4	17.6	47.6	b.d.l.	9.3	1.7	5.5	0.9	5.3	2.2	0.84	2.6	0.47	3.2	0.72	2.0	0.29	1.7
160 DS-1_2,3	4.0	0.40	0.7	195.6	122.5	-	29.2	0.8	129.4	17.5	48.2	b.d.l.	9.0	1.7	5.2	0.9	5.1	2.0	0.84	2.8	0.49	3.4	0.67	2.0	0.26	1.8
161 DS-2	4.1	0.32	1.0	153.0	128.9	106.5	35.1	1.6	119.2	20.3	52.2	0.03	16.2	2.5	6.7	1.1	5.7	2.0	0.89	2.9	0.53	3.6	0.80	2.2	0.31	2.0
161 DS-3	4.2	0.34	1.2	157.3	137.6	101.8	36.0	1.6	121.0	20.0	52.9	0.02	15.8	2.6	7.2	1.1	5.9	2.1	0.92	3.0	0.59	3.5	0.77	2.3	0.32	2.0
162 DS-1	5.4	0.48	1.5	63.3	106.1	127.7	38.1	4.3	169.8	24.1	90.1	0.05	42.2	5.6	14.5	2.1	10.5	3.5	1.26	4.0	0.69	4.7	0.90	2.5	0.35	2.4
162 DS-2	5.9	0.45	1.5	49.8	103.1	134.9	38.3	4.5	164.2	24.8	91.7	0.05	44.4	6.1	15.6	2.3	11.4	3.4	1.35	4.4	0.72	4.5	0.99	2.7	0.38	2.4

Table 1 continued

Trace element and isotope data, Na8 and calculated Pressures and Temperatures of last equilibrium crystallisation.

Sample	Lu	Hf	Pb	Th	U	$^{87}Sr/^{86}Sr$[c]	$^{143}Nd/^{144}Nd$[c]	$^{206}Pb/^{204}Pb$[c]	$^{207}Pb/^{204}Pb$[c]	$^{208}Pb/^{204}Pb$[c]	$^{207}Pb/^{206}Pb$[c]	$^{208}Pb/^{206}Pb$[c]	Na8[d]	Pressure[e]	Temperature[e]
Segment A1															
132 DS-1	0.41	2.0	0.43	0.49	0.14	0.702499	0.513138	18.8513	15.5534	38.3853	0.82506	2.03621	2.3	400	1200
132 DS-2	0.41	2.0	0.46	0.51	0.15								2.4	380	1196
132 DS-5	0.48	2.1	0.39	0.50	0.17								2.3	360	1193
132 DS-6	0.47	1.7	0.45	0.48	0.15								2.4	290	1186
133 DS-1	0.40	1.9	0.38	0.35	0.10								2.3	280	1194
133 DS-4	0.37	1.6	0.44	0.37	0.11								2.4	470	1211
133 DS-7	0.33	1.6	0.42	0.32	0.09								2.4	370	1195
133 DS-8	0.39	1.8	0.46	0.35	0.11								2.5	600	1225
133 DS-9	0.44	1.9	0.51	0.44	0.14								2.5	490	1211
136 DS-1	0.43	1.8	0.38	0.34	0.10	0.702404	0.513166	18.5702	15.5222	38.1240	0.83587	2.05297	2.3	400	1205
136 DS-3	0.42	1.8	0.36	0.35	0.11								2.4	400	1205
137 DS-2	0.41	1.6	0.33	0.20	0.06	0.702315	0.513231	18.3519	15.4966	37.8589	0.84441	2.06294	2.3	440	1209
137 DS-3	0.41	1.6	0.26	0.20	0.07								2.3	380	1206
137 DS-4	0.41	1.5	0.34	0.19	0.06								2.3	460	1214
138 DS-1	0.29	2.7	0.98	1.37	0.43	0.702699	0.513040	19.4228	15.6096	38.9960	0.80368	2.00775	2.4	450	1182
138 DS-2_1,2	0.32	2.3	0.79	1.07	0.35								2.4	250	1166
138 DS-2_3	0.38	2.4	0.61	1.07	0.30								2.4	250	1166

Sample	Lu	Hf	Pb	Th	U	$^{87}Sr/^{86}Sr^c$	$^{143}Nd/^{144}Nd^c$	$^{206}Pb/^{204}Pb^c$	$^{207}Pb/^{204}Pb^c$	$^{208}Pb/^{204}Pb^c$	$^{207}Pb/^{206}Pb^c$	$^{208}Pb/^{206}Pb^c$	$Na_8{}^d$	Pressure^e	Temperature^e
138 DS-3	0.27	2.7	0.92	1.44	0.44	0.702711	0.513038	19.4943	15.6168	39.0684	0.80109	2.00409	2.5	570	1188
139 DS-2	0.43	1.9	0.76	0.41	0.14								2.3	310	1191
139 DS-3	0.46	1.8	0.40	0.41	0.12	0.702418	0.513173	18.6558	15.5297	38.2130	0.83244	2.04832	2.3	350	1197
140 DS-1	0.38	1.3	0.28	0.17	0.05	0.702263	0.513249	18.1915	15.4873	37.7184	0.85135	2.07341	2.3	620	1234
140 DS-2	0.40	1.4	0.30	0.17	0.06								2.3	630	1233
141 DS-1	0.20	0.9	0.27	0.11	0.03	0.702322	0.513275	18.0579	15.4759	37.5946	0.85701	2.08189	2.4	600	1226
141 DS-2	0.38	1.7	0.50	0.26	0.08								2.3	200	1191
142 DS-1	0.41	1.7	0.40	0.28	0.08								2.4	450	1209
142 DS-3	0.44	1.8	0.37	0.27	0.08								2.4	390	1203
142 DS-7	0.47	2.0	0.44	0.31	0.09								2.3	420	1209
143 DS-1	0.41	1.0	0.20	0.08	0.03								2.2	670	1236
143 DS-2	0.43	1.1	0.19	0.08	0.03								2.3	700	1234
144 DS-1	0.53	2.3	0.58	0.39	0.13	0.702330	0.513160	18.3325	15.4939	37.8667		2.06555	2.4	200	1173
145 DS-1	0.54	2.3	0.55	0.37	0.12	0.702311	0.513214	18.3897	15.5003	37.9043	0.84288	2.06117	2.4	160	1171
145 DS-2_1,2	0.48	2.3	0.52	0.36	0.13								2.4	240	1176
145 DS-2_3	0.56	2.5	0.65	0.40	0.11								2.4	240	1176
145 DS-3	0.55	2.4	0.56	0.36	0.11								2.4	110	1165
145 DS-4	0.65	2.9	0.65	0.51	0.16								2.5	100	1156
146 DS-1	0.41	1.7	0.40	0.31	0.10								2.3	340	1198
146 DS-2	0.40	2.0	0.46	0.32	0.11								2.4	340	1192
146 DS-3	0.44	1.8	0.41	0.32	0.10								2.3	320	1192
Segment A2															
147 DS-1	0.43	2.0	0.49	0.32	0.10	0.702386	0.513210	18.6337	15.5348	38.1680	0.83370	2.04834	2.4	40	1158
147 DS-2	0.27	1.6	0.18	0.08	0.02								2.6	670	1222
147 DS-3	0.27	1.5	0.17	0.08	0.03								2.6	660	1221
147 DS-4	0.43	2.1	0.50	0.48	0.19								2.2	50	1161
148 DS-4	0.43	2.3	0.61	0.49	0.15								2.4 Pl undersaturated		
148 DS-6	0.44	2.7	0.55	0.50	0.16	0.702538							2.4 Pl undersaturated		
149 DS-1	0.72	4.4	0.80	0.84	0.27								2.6 Pl undersaturated		
149 DS-4	0.70	4.4	0.82	0.84	0.25								2.3 Ol undersaturated		
151 DS-1	0.30	1.8	0.35	0.18	0.06								2.5	400	1194
151 DS-2	0.32	1.8	0.24	0.18	0.06	0.702365	0.513215	18.8474	15.5506	38.2948		2.03184	2.5	350	1188
151 DS-3	0.31	1.8	0.22	0.18	0.06								2.6	500	1201
152 DS-1	0.31	1.8	0.31	0.21	0.07								2.5	420	1198

Sample	Lu	Hf	Pb	Th	U	$^{87}Sr/^{86}Sr$[c]	$^{143}Nd/^{144}Nd$[c]	$^{206}Pb/^{204}Pb$[c]	$^{207}Pb/^{204}Pb$[c]	$^{208}Pb/^{204}Pb$[c]	$^{207}Pb/^{206}Pb$[c]	$^{208}Pb/^{206}Pb$[c]	Na_8[d]	Pressure[e]	Temperature[e]
152 DS-2	0.32	1.8	0.47	0.21	0.14								2.6	330	1189
153 DS-1	0.44	2.5	0.49	0.47	0.14								2.5	140	1157
153 DS-3	0.41	2.3	0.55	0.38	0.12								2.5	30	1155
154 DS-1	0.55	2.7	0.59	0.41	0.13	0.702442	0.513237	18.6024	15.5354	38.1444		2.05051	2.3	50	1149
155 DS-1	0.30	1.3	0.40	0.15	0.05								2.5	630	1122
156 DS-1	0.29	1.7	0.35	0.19	0.06								2.6	670	1215
156 DS-3	0.34	1.6	0.35	0.21	0.06								2.5	440	1200
156 DS-4	0.30	1.7	0.39	0.19	0.07								2.7	600	1207
157 DS-1	0.25	2.2	0.42	0.35	0.11								2.4	350	1193
157 DS-2	0.27	1.9	0.45	0.37	0.12								2.4	290	1188
157 DS-3	0.28	2.0	0.52	0.37	0.12								2.4	410	1196
158 DS-2	0.33	2.2	0.53	0.48	0.15								2.5	10	1145
159 DS-2	0.28	2.1	0.28	0.25	0.08								2.7	450	1186
160 DS-1_1	0.26	1.6	0.18	0.09	0.03								2.7	590	1212
160 DS-1_2,3	0.26	1.5	0.20	0.09	0.04								2.7	590	1212
161 DS-2	0.31	1.5	0.27	0.18	0.06								2.6	600	1214
161 DS-3	0.33	1.6	0.30	0.18	0.07								2.5	590	1216
162 DS-1	0.33	2.6	0.60	0.43	0.14								2.6	80	1152
162 DS-2	0.35	2.3	0.59	0.45	0.16								2.5	10	1140

[a] Major elements, H_2O are given in wt%; Cl, K, Nb, CO_2 and trace elements are given in ppm ($\mu g/g$); Temperature is in °C, Pressure in MPa.

[b] Major elements in *italics* represents data from Möller (2000) and data measured by K.M. Haase.

[c] Isotope data from Hoernle et al., 2011

[d] After Plank and Langmuir (1992).

[e] Pressures and temperatures of least equilibrium are calculated by COMAGMAT and based on glass compositions. If those are modified by crustal assimilation (see text for discussion) they have no geological meaning.

Table 2

Gakkel Ridge chlorine, volatile and major element data[a]

Sample	Latitude	Longitude	Cl	2SE Cl	K	Nb	Cl/K	Cl/Nb	SiO₂	TiO₂	Al₂O₃	FeO	MnO	MgO	CaO	Na₂O	P₂O₅	H₂O	CO₂
Western Volcanic Zone																			
HLY0102 D08-13	82.889°N	6.259°W	79.9	1.8	1777	2.8	0.04	28.3	50.3	1.52	15.6	9.2	0.14	8.0	11.1	3.1	0.12	0.30	219
HLY0102 D11-9 [b]	82.999°N	6.318°W	99.4	1.4	2809	4.7	0.04	21.3	50.6	1.58	15.9	9.1	0.15	7.3	11.0	3.3	0.13	0.41	199
PS 59-218-36	83.080°N	5.750°W	105.0	1.3	1996	3.7	0.05	28.2	50.4	1.57	16.1	8.9	0.15	7.1	10.9	3.4	0.14	0.47	86
PS 59-222-3 [b]	83.280°N	5.660°W	127.0	1.4	2531	4.8	0.05	26.4	50.9	1.71	15.4	9.3	0.17	6.6	11.0	3.0	0.19	0.45	123
HLY0102 D12-1 [b]	83.340°N	4.998°W	98.9	1.4	1983	3.8	0.05	26.2	50.5	1.81	15.9	10.1	0.20	7.0	10.7	3.1	0.16	0.47	193
HLY0102 D12-14 [b]	83.340°N	4.998°W	97.1	1.5	1983	3.6	0.05	26.9	50.0	1.73	15.8	9.9	0.16	7.7	11.0	3.2	0.15	0.47	178
HLY0102 D12-17 [b]	83.340°N	4.998°W	100.4	0.8	1992	3.7	0.05	27.3	50.2	1.74	15.9	9.9	0.16	7.3	10.8	3.3	0.17	0.47	197
HLY0102 D12-7 [b]	83.340°N	4.998°W	98.0	0.6	1970	3.7	0.05	26.4	50.3	1.73	15.8	9.8	0.13	7.3	10.8	3.3	0.16	0.48	179
HLY0102 D14-2 [b]	83.426°N	4.438°W	149.4	0.8	2631	5.1	0.06	29.2	51.1	1.82	15.3	10.3	0.21	6.4	10.7	3.3	0.20	0.51	124
HLY0102 D14-7 [b]	83.426°N	4.438°W	150.1	0.9	2623	5.1	0.06	29.6	51.0	1.74	15.2	10.1	0.20	6.4	10.7	3.2	0.19	0.50	108
HLY0102 D18-12 [b]	83.697°N	2.907°W	76.9	0.5	1467	2.6	0.05	29.3	50.3	1.81	15.6	10.3	0.20	7.1	11.0	3.0	0.18	0.37	198
HLY0102 D18-8 [b]	83.697°N	2.907°W	79.5	1.4	1470	2.7	0.05	30.0	50.1	1.78	15.7	10.2	0.21	7.1	11.0	3.1	0.17	0.37	192
HLY0102 D19-15	83.758°N	2.527°W	102.9	0.5	1667	2.8	0.06	36.3	50.1	1.84	14.9	10.3	0.15	6.9	11.2	3.2	0.14	0.40	154
PS 59-226-11 [b]	83.697°N	2.198°W	102.7	0.4	1628	3.0	0.06	34.7	50.0	2.13	15.0	10.9	0.18	6.8	10.7	3.3	0.18	0.47	145
PS 59-226-17 [b]	83.697°N	2.198°W	101.8	0.6	1622	3.0	0.06	34.3	50.1	2.07	15.0	11.0	0.16	6.8	10.7	3.3	0.18	0.47	134
PS 59-226-3 [b]	83.697°N	2.198°W	105.9	1.3	1694	3.1	0.06	34.1	50.0	2.01	15.4	10.8	0.15	6.9	10.7	3.4	0.19	0.47	135
PS 59-226-4 [b]	83.697°N	2.198°W	108.2	2.1	1697	3.1	0.06	34.5	50.0	2.01	15.3	10.8	0.22	6.6	10.8	3.1	0.18	0.48	139
PS 59-226-6 [b]	83.697°N	2.198°W	110.4	0.6	1701	3.1	0.06	35.4	50.2	2.01	15.3	10.6	0.20	6.6	10.7	3.2	0.19	0.47	131
HLY0102 D21-4 [b]	83.860°N	1.947°W	134.4	1.7	1897	3.8	0.07	35.5	51.0	1.89	14.7	10.3	0.18	6.3	11.2	3.5	0.15	0.47	88
HLY0102 D22-2 [b]	83.915°N	1.286°W	83.8	1.6	1434	2.5	0.06	33.5	50.2	1.60	15.6	9.5	0.15	7.2	11.4	3.2	0.13	0.36	142
PS 59-233-3-3 [b]	84.270°N	1.470°E	69.2	1.0	1188	2.0	0.06	34.2	49.8	1.61	16.2	9.4	0.15	8.0	11.7	3.1	0.13	0.32	352
Sparsely Magmatic Zone																			
PS 59-243-55 [b]	84.970°N	10.162°E	78.7	1.2	1169	2.4	0.07	32.2	50.2	1.07	17.2	8.5	0.15	8.0	11.1	3.2	0.10	0.21	295
PS 59-244-5	85.030°N	11.050°E	704.9	2.3	7691	24.3	0.09	29.0	50.9	1.59	17.3	7.5	0.09	6.6	10.1	3.7	0.24	0.75	134
PS 59-244-8	85.030°N	11.050°E	157.1	0.7	2421	5.4	0.06	28.9	50.9	1.62	15.8	9.6	0.15	7.0	9.9	3.8	0.17	0.42	237
PS 59-244-13	85.030°N	11.050°E	436.6	1.3	5277	15.2	0.08	28.7	51.9	1.94	15.8	9.1	0.12	5.9	9.1	4.1	0.28	0.79	73
HLY0102 D37-2 [b]	85.293°N	11.492°E	326.6	2.1	3962	12.7	0.08	25.6	51.1	1.82	16.2	9.8	0.16	6.2	9.7	4.0	0.21	0.71	141

Sample	Latitude	Longitude	Cl	2SE Cl	K	Nb	Cl/K	Cl/Nb	SiO$_2$	TiO$_2$	Al$_2$O$_3$	FeO	MnO	MgO	CaO	Na$_2$O	P$_2$O$_5$	H$_2$O	CO$_2$
HLY0102 D36-64 [b]	85.259°N	12.332°E	439.3	1.8	5617	15.2	0.08	28.9	51.9	1.61	16.7	8.3	0.17	6.4	9.9	3.7	0.23	0.62	212
HLY0102 D36-66 [b]	85.259°N	12.332°E	439.7	1.5	5634	15.2	0.08	28.9	51.3	1.59	16.5	8.3	0.15	6.6	9.9	3.7	0.22	0.55	205
HLY0102 D36-68 [b]	85.259°N	12.332°E	439.4	1.6	5626	14.9	0.08	29.5	51.6	1.53	16.5	8.1	0.13	6.7	10.0	3.9	0.22	0.56	206
Eastern Volcanic Zone																			
HLY0102 D47-10	86.039°N	31.056°E	160.5	1.8	2973	8.9	0.05	18.0	50.6	1.79	15.5	9.3	0.12	6.9	11.2	3.4	0.20	0.40	203
HLY0102 D90-11 [b]	86.279°N	35.597°E	179.9	2.2	2430	5.9	0.07	30.7	50.3	1.59	15.8	9.1	0.14	6.9	11.4	3.5	0.16	0.37	293
HLY0102 D91-1 [b]	86.323°N	35.635°E	120.2	0.5	1814	5.3	0.07	22.8	49.5	1.75	15.9	9.5	0.16	7.0	10.8	3.6	0.16	0.34	243
PS 59-309-1	86.250°N	35.900°E	220.4	1.4	3424	11.2	0.06	19.7	50.4	1.83	15.5	9.5	0.16	7.8	10.3	3.4	0.22	0.47	200
PS 59-309-5 [b]	86.250°N	35.900°E	177.1	1.9	2981	9.6	0.06	18.5	50.5	1.74	15.9	9.3	0.18	7.0	10.6	3.2	0.24	0.36	248
HLY0102 D86-29 [b]	86.348°N	39.051°E	155.1	1.2	2702	9.1	0.06	17.0	50.4	1.59	16.2	8.8	0.14	7.3	10.8	3.5	0.18	0.33	454
HLY0102 D84-14	86.444°N	39.902°E	233.9	0.9	2699	9.3	0.09	25.0	49.9	1.85	15.2	9.9	0.13	7.7	10.3	3.4	0.22	0.56	199
PS 59-304-2	86.480°N	41.010°E	115.6	1.6	2081	5.7	0.06	20.2	50.1	1.55	16.1	9.0	0.14	8.0	11.0	3.3	0.16	0.34	288
PS 59-304-3	86.480°N	41.010°E	115.5	1.6	2089	5.6	0.06	20.5	50.2	1.57	16.3	8.9	0.15	7.9	11.0	3.3	0.17	0.37	261
HLY0102 D52-01	86.522°N	42.117°E	109.9	1.9	2432	6.5	0.05	16.9	50.2	1.49	16.2	8.2	0.13	7.8	11.6	3.3	0.17	0.36	218
HLY0102 D51-33	86.558°N	43.485°E	65.8	1.2	1693	3.7	0.04	17.9	49.7	1.39	17.1	8.0	0.13	8.5	11.4	3.1	0.13	0.25	213
PS 59-271-1 [b]	86.818°N	47.942°E	144.0	1.3	2214	7.4	0.07	19.5	50.0	1.77	15.6	10.5	0.17	7.0	10.3	3.9	0.17	0.36	266
PS 59-270-19	86.740°N	49.510°E	145.1	1.1	3295	7.7	0.04	18.8	49.4	1.54	16.3	8.3	0.10	8.8	10.9	3.2	0.17	0.38	248
PS 59-295-1	86.820°N	52.120°E	143.9	1.1	3553	7.8	0.04	18.5	50.2	1.55	16.8	8.3	0.13	7.6	11.2	3.3	0.18	0.38	331
PS 59-295-2	86.820°N	52.120°E	131.0	1.1	2897	6.6	0.05	19.8	49.8	1.44	16.5	8.2	0.11	8.1	11.3	3.2	0.18	0.38	264
PS 59-274-17 [c]	86.730°N	66.750°E	63.4	1.0	1547	1.0	-	-	49.8	1.05	17.3	8.8	0.17	8.5	11.1	2.9	0.05	0.19	165
HLY0102 D58-07	86.524°N	69.929°E	106.1	1.3	2227	5.3	0.05	19.8	49.9	1.51	16.3	8.4	0.12	7.9	11.5	3.2	0.15	0.30	175
HLY0102 D68-3 [b]	86.580°N	71.582°E	109.6	1.3	2530	4.9	0.04	22.6	50.3	1.56	16.6	8.4	0.13	7.4	11.2	3.5	0.16	0.35	195
HLY0102 D63-26 [b]	85.632°N	84.512°E	65.4	1.0	2089	3.3	0.03	19.8	49.6	1.38	17.0	8.2	0.15	8.0	11.2	3.3	0.15	0.30	237
HLY0102 D61-05	85.633°N	84.995°E	43.1	2.3	1287	2.4	0.03	17.7	49.6	1.37	17.2	8.1	0.11	8.7	11.2	3.2	0.14	0.21	222

Table 2 continued
Trace element data

Sample	Li	Be	B	Ni	Cu	Zn	Sc	Rb	Sr	Y	Zr	Cs	Ba	La	Ce	Pr	Nd	Sm	Eu
Western Volcanic Zone																			
HLY0102 D08-13	6.1	0.43	2.2	126.6	79.3	101.4	37.4	4.3	144.0	28.7	86.3	0.06	45.1	3.6	11.0	1.9	9.8	3.4	1.26
HLY0102 D11-9	6.0	0.58	2.3	117.0	74.5	98.3	37.0	8.5	170.1	28.3	93.0	0.11	72.2	4.5	12.9	2.1	10.5	3.4	1.29
PS 59-218-36	6.2	0.68	2.7	91.7	76.9	92.9	34.6	5.2	168.0	28.1	94.2	0.07	52.9	4.7	13.3	2.2	11.2	3.6	1.31
PS 59-222-3	6.0	0.86	2.6	68.8	76.0	103.8	39.9	6.9	159.3	31.9	106.3	0.09	74.0	5.7	15.6	2.5	12.0	4.1	1.42
HLY0102 D12-1	7.0	0.70	2.9	100.9	69.7	112.2	37.6	4.2	158.3	33.2	111.6	0.06	50.2	5.3	14.8	2.4	12.8	4.1	1.49
HLY0102 D12-14	6.7	0.50	2.8	101.0	68.6	114.0	36.4	4.2	156.4	32.9	107.7	0.06	47.9	5.2	14.8	2.4	12.3	4.1	1.48
HLY0102 D12-17	6.8	0.54	2.9	98.5	69.0	110.5	36.8	4.2	156.4	33.4	110.3	0.05	49.7	5.2	14.5	2.3	12.2	4.0	1.48
HLY0102 D12-7	6.9	0.51	2.9	104.3	71.0	114.8	35.5	4.3	157.7	31.9	106.9	0.06	49.5	5.2	14.9	2.4	12.3	4.1	1.45
HLY0102 D14-2	7.1	0.70	3.1	54.4	70.8	112.9	40.0	6.2	169.8	34.2	117.8	0.09	72.7	6.3	16.9	2.7	13.0	4.3	1.55
HLY0102 D14-7	6.9	0.72	3.2	55.5	73.0	113.9	40.4	6.2	172.9	35.0	119.0	0.08	74.1	6.6	17.1	2.7	13.4	4.3	1.58
HLY0102 D18-12	6.7	0.60	2.5	91.0	78.2	109.9	40.5	2.9	148.5	35.4	112.4	0.04	31.7	4.5	13.6	2.2	12.2	3.9	1.48
HLY0102 D18-8	6.8	0.74	2.9	90.4	77.8	110.6	39.0	3.0	146.8	34.5	110.8	0.05	31.8	4.2	13.1	2.3	11.7	4.0	1.47
HLY0102 D19-15	6.7	0.67	2.5	68.9	78.8	109.8	41.0	3.0	151.3	35.0	109.8	0.04	35.3	4.6	13.7	2.3	11.8	4.1	1.48
PS 59-226-11	7.2	0.53	3.0	66.5	79.2	123.3	40.8	2.8	141.3	38.8	131.7	0.05	29.3	4.7	14.8	2.5	13.6	4.9	1.61
PS 59-226-17	7.5	0.91	3.0	66.7	79.5	123.8	40.2	2.8	141.7	39.4	129.8	0.10	27.3	4.7	14.9	2.4	14.4	4.7	1.65
PS 59-226-3	7.4	0.77	3.0	74.2	79.5	114.8	40.9	3.1	147.8	39.5	127.2	0.04	33.3	4.9	15.5	2.5	13.5	4.5	1.65
PS 59-226-4	7.1	0.60	3.1	74.0	78.7	115.4	40.9	3.0	149.5	39.6	126.7	0.04	32.9	4.9	15.6	2.6	13.6	4.6	1.60
PS 59-226-6	7.3	0.71	3.1	76.8	79.8	115.0	39.5	3.0	146.7	37.6	125.6	0.05	31.8	4.7	13.8	2.5	13.3	4.5	1.58
HLY0102 D21-4	7.6	0.72	3.0	55.0	78.8	114.9	43.1	4.1	148.6	38.3	121.2	0.06	43.7	5.2	15.5	2.5	13.5	4.4	1.59
HLY0102 D22-2	6.0	0.53	2.5	88.8	83.7	101.4	40.2	2.7	150.8	32.2	102.4	0.03	30.9	4.1	12.5	2.1	10.8	3.7	1.38
PS 59-233-3-3	6.2	0.47	2.7	113.7	86.2	98.8	36.8	2.5	149.7	29.4	97.0	0.06	24.9	3.5	11.2	1.8	10.0	3.7	1.29
Sparsely Magmatic Zone																			
PS 59-243-55	5.3	0.52	1.1	130.9	89.7	83.0	34.0	4.5	143.8	23.2	69.2	0.06	36.5	3.2	9.6	1.4	7.6	2.7	1.05
PS 59-244-5	6.1	1.08	3.4	96.5	58.3	78.1	29.5	33.1	299.2	25.8	117.1	0.53	377.0	16.2	32.9	3.8	16.6	3.9	1.30
PS 59-244-8	7.4	0.76	2.1	95.9	67.2	108.8	34.6	10.2	158.8	34.2	129.1	0.10	78.3	6.4	17.7	2.7	14.4	4.0	1.49
PS 59-244-13	8.1	0.79	3.9	75.3	54.6	109.8	32.8	26.0	188.1	42.3	189.9	0.36	207.9	12.9	31.4	4.4	21.3	5.7	1.81
HLY0102 D37-2	8.6	0.63	3.1	91.9	58.3	124.1	32.7	15.3	170.8	36.5	143.8	0.22	143.2	9.9	23.9	3.3	16.3	5.1	1.60

Sample	Li	Be	B	Ni	Cu	Zn	Sc	Rb	Sr	Y	Zr	Cs	Ba	La	Ce	Pr	Nd	Sm	Eu
HLY0102 D36-64	6.8	0.62	1.8	99.5	62.7	98.4	32.4	25.4	209.1	31.2	131.4	0.41	257.0	11.5	24.8	3.3	14.2	3.9	1.40
HLY0102 D36-66	6.7	0.67	2.3	97.4	60.7	93.0	31.2	25.5	208.9	29.6	127.1	0.46	247.4	11.5	24.6	3.1	14.7	3.9	1.39
HLY0102 D36-68	7.0	0.90	2.6	95.4	60.6	92.8	31.3	25.4	202.4	29.5	127.0	0.39	243.0	11.1	23.8	3.2	14.7	3.9	1.36
Eastern Volcanic Zone																			
HLY0102 D47-10	7.2	0.76	2.2	79.1	82.9	103.2	36.0	7.6	154.1	34.3	129.5	0.10	75.5	7.6	19.3	3.0	14.1	4.3	1.53
HLY0102 D90-11	6.7	0.91	1.9	85.3	75.3	95.2	34.6	4.8	132.5	28.0	103.4	0.08	55.9	5.9	15.0	2.2	11.9	3.8	1.33
HLY0102 D91-1	7.1	0.62	1.7	109.8	67.9	108.9	34.1	3.9	118.2	37.4	125.8	0.05	37.7	5.0	14.8	2.6	13.1	4.5	1.45
PS 59-309-1	6.2	0.73	2.5	136.0	64.6	103.9	32.9	8.9	173.8	34.3	129.1	0.07	95.2	9.2	22.5	3.0	14.9	4.7	1.49
PS 59-309-5	6.5	0.74	2.1	116.4	67.5	111.0	34.0	7.7	167.1	33.4	120.3	0.07	81.7	7.7	19.1	2.7	13.6	4.0	1.47
HLY0102 D86-29	6.0	0.73	1.9	142.3	86.2	122.9	31.6	7.6	159.9	34.1	142.9	0.09	68.8	6.8	17.6	2.8	12.8	4.0	1.34
HLY0102 D84-14	7.0	0.72	2.0	150.7	80.6	105.8	33.1	6.7	150.4	35.6	137.3	0.08	63.4	7.6	19.5	2.8	14.2	4.4	1.40
PS 59-304-2	6.2	0.63	1.7	136.2	72.2	99.4	33.0	4.0	166.7	28.5	108.2	0.05	44.9	5.3	14.9	2.3	12.0	3.6	1.39
PS 59-304-3	6.0	0.83	1.6	136.9	76.2	92.3	33.3	4.4	168.1	29.6	110.3	0.07	44.0	5.8	16.2	2.3	12.0	3.7	1.32
HLY0102 D52-01	5.3	0.66	1.7	103.7	76.3	80.3	36.7	3.7	202.0	26.3	106.5	0.08	44.8	5.9	15.1	2.3	11.9	3.3	1.31
HLY0102 D51-33	4.8	0.44	1.6	151.1	74.1	80.5	31.4	1.9	208.2	23.0	98.2	0.06	20.4	4.7	12.8	2.0	9.9	3.2	1.15
PS 59-271-1	7.4	0.81	2.1	128.1	80.7	142.7	33.3	6.2	155.2	43.4	139.1	0.07	60.0	6.0	16.3	2.7	13.1	4.4	1.48
PS 59-270-19	5.2	0.85	1.9	175.2	67.6	82.2	31.4	5.2	226.2	24.3	105.6	0.10	58.0	6.7	16.9	2.5	11.8	3.4	1.23
PS 59-295-1	5.8	0.86	2.2	124.5	78.3	84.0	32.2	5.4	199.1	26.3	106.4	0.10	62.5	6.9	17.3	2.5	11.7	3.6	1.27
PS 59-295-2	6.1	0.52	2.6	142.3	75.4	84.7	33.0	5.0	190.8	25.9	101.1	0.11	58.1	6.0	15.8	2.3	11.5	3.6	1.22
PS 59-274-17	6.8	0.35	2.9	152.6	105.0	105.5	31.9	6.6	111.3	23.8	75.6	0.28	34.9	3.0	8.7	1.4	7.3	2.3	0.87
HLY0102 D58-07	5.4	0.55	2.2	113.3	84.8	91.3	34.1	3.5	184.5	25.3	105.4	0.05	38.7	5.4	14.7	2.4	11.5	3.3	1.22
HLY0102 D68-3	5.4	0.77	2.1	114.7	74.2	85.3	33.8	3.4	185.2	23.2	99.7	0.06	37.2	5.8	15.7	2.3	11.8	3.5	1.28
HLY0102 D63-26	4.8	0.56	1.6	131.2	61.1	73.8	30.8	1.7	187.5	18.9	77.7	0.03	22.4	4.7	12.5	1.8	9.9	2.6	1.12
HLY0102 D61-05	4.8	0.74	1.8	170.1	71.0	83.9	29.8	1.0	206.7	22.7	94.4		13.2	4.0	11.7	1.9	9.6	3.0	1.05

Table 2 continued
Trace element data, Na_8 and calculated Pressures and Temperatures of last equilibrium crystallisation.

Sample	Gd	Tb	Dy	Ho	Er	Tm	Yb	Lu	Hf	Pb	Th	U	Na_8[d]	Pressure[e]	Temperature[e]
Western Volcanic Zone															
HLY0102 D08-13	4.4	0.77	5.1	1.11	3.2	0.44	2.8	0.43	2.4	0.57	0.22	0.07	3.1	460	1193
HLY0102 D11-9	4.6	0.77	5.3	1.06	3.0	0.45	2.9	0.44	2.6	0.64	0.29	0.09	3.1	410	1180
PS 59-218-36	4.8	0.75	5.0	1.07	3.0	0.46	2.9	0.44	2.6	0.84	0.31	0.09	3.1	410	1178
PS 59-222-3	5.2	0.88	5.7	1.23	3.5	0.50	3.3	0.47	2.8	0.88	0.45	0.13	2.7	190	1157
HLY0102 D12-1	5.2	0.93	6.1	1.33	3.8	0.51	3.3	0.51	3.2	0.76	0.35	0.10	2.8	420	1173
HLY0102 D12-14	5.4	0.89	6.1	1.28	3.8	0.51	3.4	0.49	3.0	0.78	0.35	0.10	3.1	450	1180
HLY0102 D12-17	5.4	0.92	5.7	1.29	3.9	0.51	3.2	0.50	3.0	0.76	0.35	0.10	3.1	440	1177
HLY0102 D12-7	5.3	0.90	6.0	1.29	3.7	0.47	3.6	0.52	2.9	0.74	0.35	0.11	3.0	400	1173
HLY0102 D14-2	5.4	0.94	6.2	1.31	3.8	0.51	3.5	0.50	3.1	0.88	0.48	0.14	2.9	190	1148
HLY0102 D14-7	5.7	0.96	6.2	1.33	4.0	0.55	3.5	0.55	3.2	0.86	0.49	0.13	2.8	180	1149
HLY0102 D18-12	5.4	0.98	6.1	1.33	4.0	0.56	3.5	0.55	3.0	0.65	0.24	0.08	2.8	420	1179
HLY0102 D18-8	5.6	0.92	6.1	1.36	3.8	0.56	3.6	0.52	2.9	0.63	0.24	0.08	2.8	440	1181
HLY0102 D19-15	5.6	0.91	6.3	1.34	3.8	0.56	3.6	0.52	3.0	0.70	0.26	0.08	2.9	240	1162
PS 59-226-11	6.5	1.04	7.5	1.52	4.2	0.60	4.0	0.64	3.7	0.81	0.23	0.08	3.0	260	1154
PS 59-226-17	6.3	1.07	7.3	1.43	4.5	0.67	4.0	0.66	3.6	0.80	0.22	0.09	3.0	260	1154
PS 59-226-3	6.1	1.06	7.2	1.50	4.2	0.60	3.9	0.60	3.4	0.74	0.25	0.09	3.0	350	1162
PS 59-226-4	6.1	1.05	7.0	1.46	4.4	0.63	4.0	0.62	3.5	0.68	0.26	0.08	2.7	300	1159
PS 59-226-6	6.2	0.98	6.6	1.45	4.1	0.55	3.8	0.63	3.2	0.82	0.25	0.08	2.8	300	1159
HLY0102 D21-4	5.9	1.02	6.6	1.42	4.3	0.61	3.9	0.56	3.4	0.80	0.32	0.09	3.0	100	1144
HLY0102 D22-2	4.9	0.85	5.7	1.23	3.6	0.49	3.2	0.49	2.8	0.62	0.23	0.07	3.0	370	1182
PS 59-233-3-3	4.4	0.84	5.5	1.22	3.6	0.47	3.2	0.47	2.4	0.69	0.19	0.05	3.1	550	1203
Sparsely Magmatic Zone															
PS 59-243-55	3.5	0.56	4.3	0.85	2.6	0.38	2.4	0.40	2.2	0.44	0.19	0.06	3.2	750	1227
PS 59-244-5	4.3	0.67	4.8	1.02	3.0	0.44	2.9	0.42	2.9	1.60	2.12	0.56	3.3	410	1161
PS 59-244-8	5.5	0.94	6.0	1.17	3.8	0.56	3.6	0.58	3.2	1.16	0.48	0.15	3.5	400	1167
PS 59-244-13	6.9	1.21	7.6	1.57	4.8	0.66	4.4	0.73	4.3	1.56	1.40	0.38	3.4	100	1116
HLY0102 D37-2	6.0	0.98	6.7	1.54	4.4	0.53	3.8	0.62	3.8	1.25	1.08	0.27	3.4	290	1140

Sample	Gd	Tb	Dy	Ho	Er	Tm	Yb	Lu	Hf	Pb	Th	U	Na₈[d]	Pressure[e]	Temperature[e]
HLY0102 D36-64	5.0	0.80	5.4	1.20	3.2	0.44	3.1	0.46	3.3	0.97	1.46	0.37	3.2	330	1154
HLY0102 D36-66	4.6	0.84	5.7	1.18	3.3	0.47	3.2	0.44	3.1	1.27	1.39	0.36	3.3	390	1163
HLY0102 D36-68	4.7	0.84	5.1	1.06	3.0	0.49	2.9	0.52	3.0	1.07	1.41	0.33	3.5	330	1158
Eastern Volcanic Zone															
HLY0102 D47-10	5.1	0.91	6.2	1.22	3.3	0.50	3.5	0.45	3.7	0.94	0.67	0.20	3.1	270	1166
HLY0102 D90-11	5.0	0.79	5.6	1.20	3.5	0.43	2.9	0.48	2.9	0.79	0.47	0.14	3.2	320	1174
HLY0102 D91-1	5.7	0.88	7.0	1.56	3.8	0.53	4.0	0.57	3.2	0.80	0.43	0.15	3.3	500	1186
PS 59-309-1	5.7	1.02	6.5	1.26	3.5	0.54	3.9	0.53	3.4	1.85	0.87	0.26	3.3	380	1168
PS 59-309-5	5.2	0.88	6.0	1.31	3.7	0.50	3.5	0.55	3.3	0.95	0.71	0.20	2.9	440	1180
HLY0102 D86-29	4.9	0.84	5.5	1.16	3.3	0.49	3.3	0.51	3.0	0.87	0.61	0.19	3.3	510	1191
HLY0102 D84-14	5.7	0.98	6.3	1.36	4.0	0.55	3.7	0.54	3.7	0.86	0.67	0.22	3.3	300	1156
PS 59-304-2	4.8	0.80	5.5	1.18	3.1	0.46	2.8	0.50	2.7	0.92	0.40	0.13	3.3	550	1198
PS 59-304-3	4.5	0.74	5.2	1.06	3.0	0.42	3.1	0.45	2.6	0.76	0.41	0.13	3.2	550	1197
HLY0102 D52-01	4.0	0.72	4.6	0.83	2.8	0.36	2.6	0.37	2.6	0.60	0.41	0.15	3.2	460	1195
HLY0102 D51-33	3.9	0.70	4.5	0.93	2.5	0.38	2.3	0.34	2.3	0.77	0.23	0.09	3.3	770	1232
PS 59-271-1	5.9	0.96	6.4	1.36	4.0	0.58	3.8	0.54	3.2	0.90	0.46	0.14	3.5	440	1172
PS 59-270-19	4.3	0.65	4.2	0.94	2.5	0.39	2.7	0.36	2.6	0.88	0.54	0.18	3.4	610	1206
PS 59-295-1	4.1	0.74	4.6	1.17	3.0	0.41	2.6	0.41	2.9	1.05	0.56	0.20	3.2	570	1199
PS 59-295-2	4.0	0.73	5.0	0.97	2.8	0.40	2.7	0.37	2.4	0.68	0.49	0.18	3.3	600	1206
PS 59-274-17	3.3	0.54	3.7	0.77	2.4	0.38	2.1	0.36	1.8	1.46	0.48	0.13	3.0	840	1239
HLY0102 D58-07	4.6	0.76	4.7	0.93	2.9	0.41	2.3	0.39	2.7	0.81	0.38	0.13	3.2	560	1206
HLY0102 D68-3	4.4	0.79	4.7	1.02	3.0	0.41	2.9	0.40	2.8	0.91	0.39	0.14	3.3	530	1196
HLY0102 D63-26	3.6	0.66	4.3	0.93	2.4	0.33	2.3	0.33	2.6	0.78	0.29	0.10	3.3	710	1219
HLY0102 D61-05	3.9	0.64	4.4	0.94	2.4	0.38	2.4	0.29	2.5	0.74	0.15	0.07	3.4	840	1239

[a] Major elements, H₂O are given in wt%; Cl, K, Nb, CO₂, and trace elements are given in ppm (μg/g); Temperature is in °C, Pressure in MPa.
[b] Major elements in *italics* represents data measured by J. E. Snow.
[c] High Ce/Pb and Nb/U indicate alteration or continental input and this sample is not considered further for Cl.
[d] After Plank and Langmuir (1992).
[e] Pressures and temperatures of least equilibrium are calculated by COMAGMAT and based on glass compositions. If those are modified by crustal assimilation (see text for discussion) they have no geological meaning.

To study possible Cl addition unrelated to mantle melting or source processes, we compare Cl to trace elements of similar incompatibility, i.e. Cl/K and Cl/Nb ratios. Cl/K and Cl/Nb are positively correlated but form subparallel trends between samples from Gakkel Ridge, the SMAR and the Red Sea (Fig. 2f). These trends are consistent with variations in Nb/K between the different sample suites that are correlated to Ce/Pb and Nb/U and display a weak negative correlation to Na_8 (Fig. 2g,h).

Cl/K and Cl/Nb are lower than in the Red Sea and lower than observed at fast-spreading ridges, but Cl/K of SMAR samples reach a maximum of 0.3, which is higher than at most slow-spreading ridges (Michael and Cornell, 1998; fig. 3a), while Gakkel Ridge samples have lower Cl/K (<0.09; fig. 2g). High Cl/K ratios mostly occur in trace element depleted samples, indicated by low K/Ti and Ba/Ti (Fig. 3a), consistent with a negative relation between Cl/Nb and Nb or K (Fig. 3b,c) and with a similar pattern for Cl/Nb against other incompatible trace elements (e.g. P, K, Rb, Zr, Cs, Ba, REE; fig. 3d). This trend is particularly strong for the SMAR samples, while samples from Gakkel Ridge display a larger scatter with some higher Cl/Nb values also in more trace element enriched samples. Cl/Nb is not correlated to MgO or CO_2/Nb (Fig. 3e,g). Samples from Gakkel Ridge all have Cl/Nb below 37 and Na_8 above 2.6. Of these samples, EVZ samples have the lowest Cl/Nb and Na_8 generally above 3.1 (Fig. 3g). Variations in Ce/Pb and Nb/U are not related to high Cl/Nb (Fig. 3h). High Cl/Nb is observed in both segments of the SMAR and in the WVZ and SMZ of the Gakkel Ridge. The EVZ of the Gakkel Ridge in contrast, displays comparatively few high Cl/Nb samples.

4.2 SMAR mineral textures and chemistry

Phenocryst textures and chemistry may offer supplementary evidence to understand the processes that influence the magmatic compositions. Phenocrysts are up to 2 mm in size and mostly comprise olivine (Ol) and plagioclase (Pl), with minor clinopyroxene (Cpx) observed in only 5 of the samples. Olivine and Pl phenocrysts in both trace element enriched and depleted samples show a range of textures from euhedral, well formed minerals to anhedral crystals that display resorption at the mineral rims and occasionally sieve textures (Fig. 4a-e). A few of the Ol grains display undulose extinction (Fig. 4f). Melt inclusions are present in both Ol and Pl and can be up to ~200 μm in diameter; in the Pl they are frequently located along growth zones, but also along healed cracks. Olivine and Pl crystals often show clustering and intergrowth of multiple minerals that probably represent rock fragments (Fig. 4c-h).

The forsterite (Fo) contents in Ol vary between 83.4 and 91.8%, but intra-sample variations are less than 5.5% both between different grains and within single Ol grains. Chemical profiles from core to rim over several selected Ol reveal three compositional groups, comprising a) grains that display a constant composition, and b) those that are normally zoned, of which some may include diffusion profiles (e.g. in 143-2 and 149-1) and c) reversely zoned grains (e.g. in 143-2, 147-2; fig 5a). Comparison of the Ol rim Fo-contents to theoretical Ol Fo-contents that would be in equilibrium with the host glasses (using the equilibrium constant of 0.3 ±0.03 from Roeder and Emslie (1970)), show disequilibrium for many of the Ol that have higher Fo-contents than Ol in equilibrium with melt (77.2 – 88.4%; fig, 5b) and thus imply a xenocrystic origin for most Ol. This is the case for both trace element enriched and depleted samples. The rare Cpx that occur in samples 147-2, 149-1, 149-4, 162-1 and 16-2 have a composition of $Wo_{36-41}En_{51-55}Fs_{6-10}$. Rim to core profiles across Cpx grains display zoning in some of the minerals (fig. 5c). Similarly, two profiles over Pl show one unzoned crystal and one reversly-zoned crystal (fig. 5d).

The phenocryst minerals (Pl, Ol, Cpx) of 22 selected samples from the SMAR (comprising samples with both low and high Cl/Nb ratios in the glasses) were analysed in order to obtain high precision Cl and K data (supplementary table A1). As might be expected, their respective concentrations are very low (0-45 ppm Cl and <420 ppm K) and display a large and seemingly unsystematic scatter in Cl concentrations and Cl/K ratios between samples covering the whole Cl/Nb range observed in the glasses. The Cl contents in the minerals thus do not reflect the Cl contents of the glasses. Only a systematic variation between the various

mineral species can be observed: Cpx displays consistently the highest Cl contents and Cl/K ratios (on average 35 and 0.7), Ol contains on average 16 ppm Cl with a Cl/K ratio of 0.5, while Pl has on average 9 ppm Cl and a Cl/K ratio of 0.2, unfortunately sufficient and consistent distribution coefficients for Cl in these minerals are not available and an interpretation of these Cl contents is difficult.
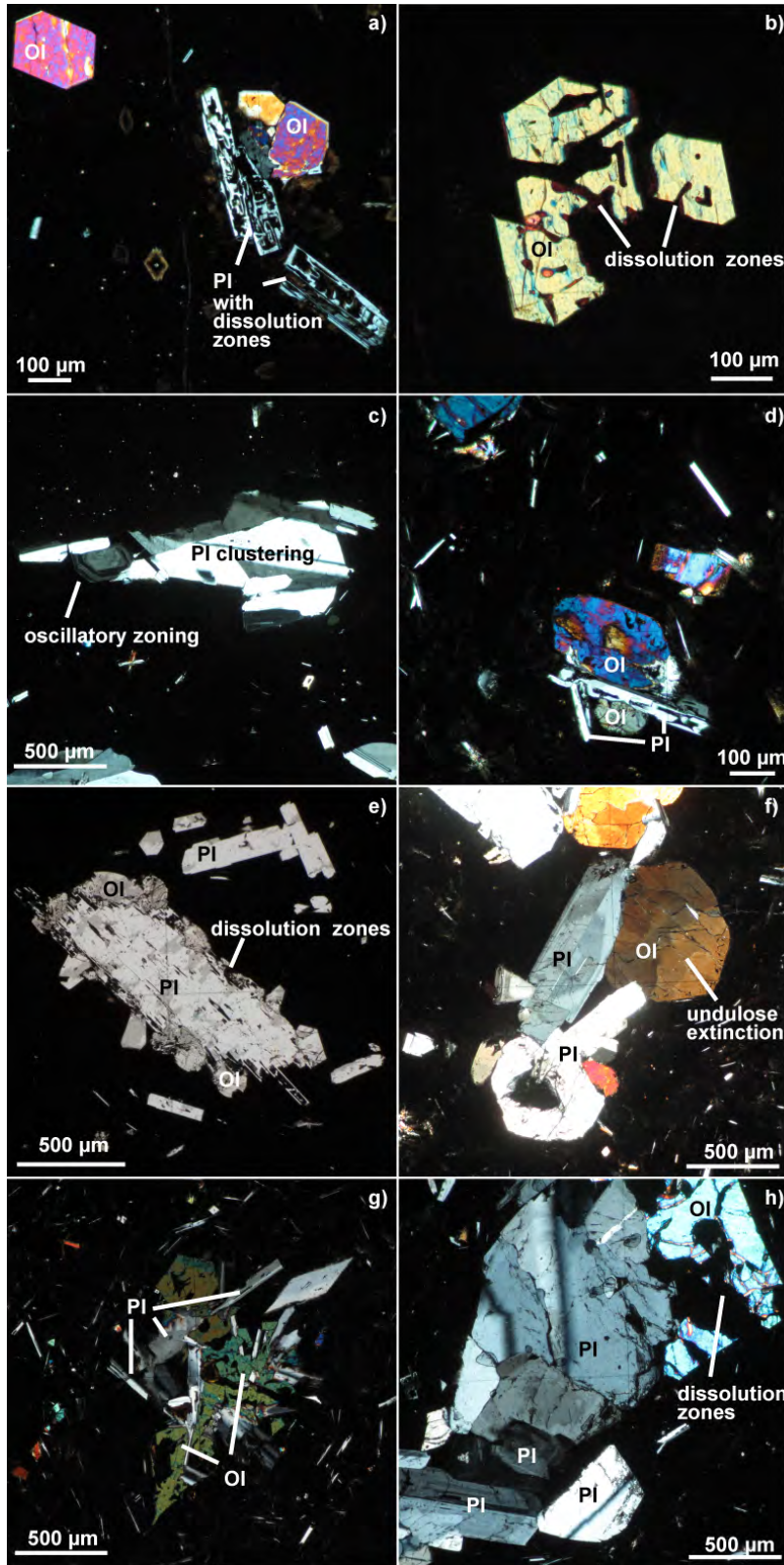
Fig. 4 – Photomicrographs of thin sections from SMAR samples 149-1 **(a, c-f, h)**, 142-7 **(b)** and 145-3 **(g)** in cross-polarized light **(a-d, f-h)** and plane-polarized light **(e)**. **(a)** Euhedral Ol occurs together with highly dissolved and skeletal Pl and **(b,h)** Ol. **(c-h)** Clusters of different types of Pl **(c)**, or Pl and Ol **(d-h)** with complex intergrowth structure of Pl and Ol **(e,g)** and undulose extinction in Ol **(f)** indicate xenocrystic fragments that formed by in situ crustal growth of minerals together and subsequent assimilation of these fragments.
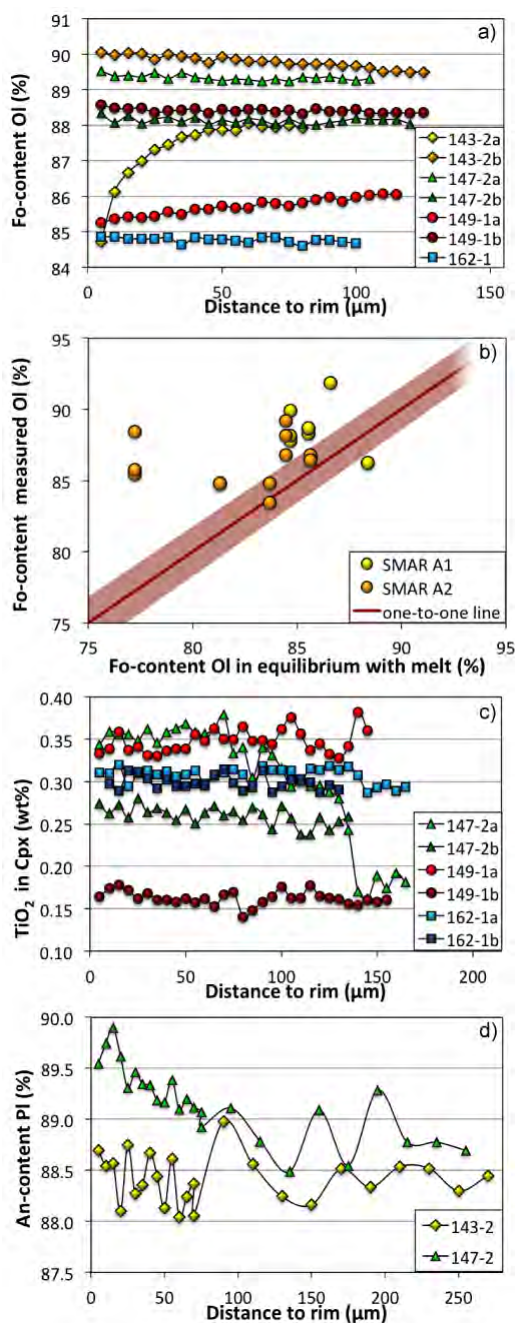
Fig. 5 – Mineral composition data. **(a)** Transects over Ol grains from rim to core show unzoned Ol together with normally and reversely zoned Ol. **(b)** Fo-content of the Ol plotted against the Fo-content of Ol that would be in equilibrium with their host glasses (applying the equilibrium constant of 0.3 ±0.03 from Roeder & Emslie, 1970). Olivines in equilibrium fall onto the one-to-one line or within the red field that represents the variation of the equilibrium constant. **(c)** Transects over Cpx crystals show various zonation patterns from limited zoned to complexly zoned crystals. **(d)** Plagioclase transects display large scatter (potentially oscillatory zoning), but display a generally reversely zoned trend (147-2) and an unzoned trend (143-2).

4.3 High-precision chlorine measurements on SMAR melt inclusions

Melt inclusions in both Ol and Pl crystals were measured in selected samples from the SMAR that display high Cl/Nb (28-48) ratios of the glasses (137-3, 143-1, 143-2, 147-2, 147-3, 149-1, 149-4 and 151-3; supplementary table A2). For analytical reasons, only Cl and K were measured with high precision in the melt inclusions. The absolute Cl and K concentrations obtained for the melt inclusions in 9-14 minerals per sample are both lower and higher than their corresponding host glasses, but extend to lower minimum and maximum concentration than observed in all SMAR glasses (20-234 ppm Cl, 67-2256 ppm K; fig. 6a). Chlorine concentrations vary between 20 and 168 ppm for inclusions in Ol and between 30 and 234 ppm for Pl-hosted inclusions. The SMAR melt inclusions display a general positive trend between Cl and K, but with more scatter than observed in Cl-K of the glasses (Fig. 6a). However, Cl/K ratios vary between 0.08 and 0.56 for inclusions in Ol and between 0.08 and 0.49 for inclusions in Pl, and thus extend to both lower and higher values than observed in the host glasses (0.12-0.19 and 0.07-0.30 for all SMAR glasses). Also for individual samples, Cl, K and Cl/K of the melt inclusions vary to higher and lower values than the host glass (Fig. 6b). The exceptions are the trace element enriched samples 149-1 and 149-4, that display a larger variation of the melt inclusions in Cl/K, but both Cl and K are considerably lower than the host glass and overlap with the more depleted samples and thus probably hosted by xenocrysts (Fig. 6c). The highest Cl/K values in the melt inclusions are observed in 143-1 and 143-2 that also have the highest Cl/K of their host glasses (0.19).

76

4.4 Pressures of equilibrium crystallisation

The COMAGMAT pressures of last equilibrium crystallisation vary between 5 and 700 MPa for samples from the SMAR and between 100 and 84 MPa for samples from the Gakkel Ridge (Table 1,2). The average pressures are 357 and 426 MPa respectively, which is higher than observed in the Red Sea (251 MPa; van der Zwan et al., in review; see chapter 3) and typical for slow-spreading ridges that do not display high Cl/K (Michael and Cornell, 1998). At the SMAR, the northern ridge segment A1 has slightly higher crystallisation pressures than the southern shallower segment A2 with on average 385 MPa and 322 MPa respectively. At Gakkel Ridge, the highest average pressures are found in the Eastern Volcanic Zone (538 MPa), while the Western Volcanic Zone and Sparsely Magmatic Zone display lower pressures (340 and 375 MPa respectively).

For the rare samples that contain Cpx (SMAR 147-2, 149-1, 149-4, 162-1, 162-2) we also calculated pressures using the formulations for Cpx-melt equilibrium of Putirka et al. (1996), which are given in Table 3. Equilibrium was assessed by comparing the predicted and observed values for the Cpx components (cf. Putirka, 2008) and by comparing the observed and predicted values for $K_D(Fe\text{-}Mg)^{cpx\text{-}liq}$ (Supplementary Fig. A1; Table 3). In terms of the Cpx components, the calculated and observed compositions were within 5% and indicate equilibrium. Samples 147-2 and 162-2 show, additionally, equilibrium between Fe-Mg, while samples 149-4 and 162-1 display only minor disequilibrium of the Cpx with the glass. This disequilibrium indicates minor late-stage modification of the glass and is thus not significant for the calculation, as it is the Cpx
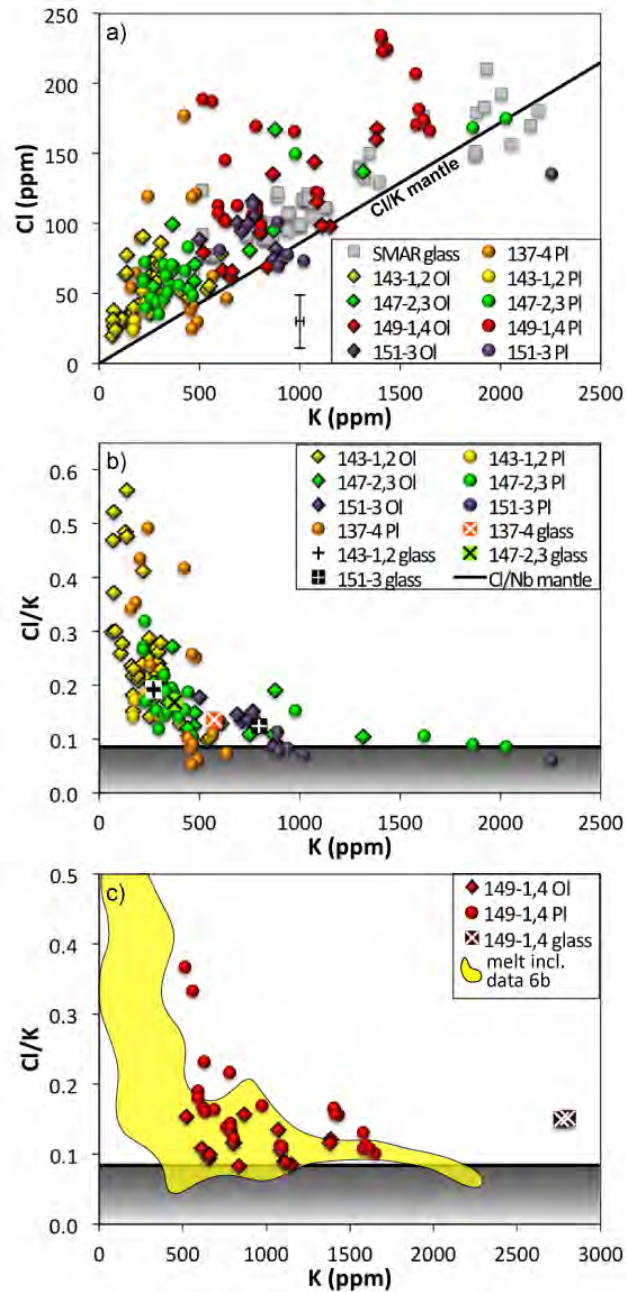
Fig. 6 – Melt inclusion Cl and K data. **(a)** Melt inclusions in Ol (diamonds) and Pl (circles) show a similar trend in Cl and K as the SMAR glasses, but with larger scatter. There is no systematic difference between melt inclusions in Ol or Pl. **(b)** Cl/K vs. K for melt inclusions (filled symbols) together with their host glasses (crosses; colours distinguish samples). Melt inclusions in minerals hosted in trace element depleted glasses display both lower and higher Cl/K and K than their host glasses. Note that the most K-depleted inclusions show extremely high Cl/K ratios, exceeding the range in their host glasses. **(c)** Melt inclusions from trace-element-enriched (high K) glass sample 149-1 have lower Cl and K than their host and overlap with concentrations of melt inclusions in trace element depleted samples **(b)**.

compositions (which are in equilibrium) that influence the pressure calculations the most. All these four samples give pressures between 300 and 400 MPa and therefore, are taken as significant crystallization pressures. These calculated pressures are not consistent with the pressures calculated by COMAGMAT (Table 3). Sample 149-1 shows strong Fe-Mg disequilibrium (0.12) between Cpx and melt, and are thus excluded from the calculations.

Table 3
Pressure calculations based the formulations for Cpx-melt equilibria compared to COMAGMAT pressure calculations.

Sample	Cl/Nb	Pressure Putirka et al. (1996)	K_D (Fe-Mg)	Pressure COMAGMAT	∂ Pressure
147-2_1	47.9	361 MPa	0.25	670 MPa	-309 MPa
147-2_2	47.9	316 MPa	0.24	670 MPa	-354 MPa
147-2_3	47.9	324 MPa	0.23	670 MPa	-346 MPa
149-1_1[a]	*32.8*	*-13 MPa*	*0.12*	*5 MPa*	*-18 MPa*
149-1_2[a]	*32.8*	*53 MPa*	*0.12*	*5 MPa*	*48 MPa*
149-4	33.3	375 MPa	0.17	5 MPa	370 MPa
162-1_1	18.3	387 MPa	0.20	80 MPa	307 MPa
162-1_2	18.3	403 MPa	0.20	80 MPa	323 MPa
162-1_3	18.3	373 MPa	0.20	80 MPa	293 MPa
162-2_1	18.1	340 MPa	0.24	10 MPa	330 MPa
162-2_2	18.1	364 MPa	0.25	10 MPa	354 MPa

[a] The low/negative pressures together with the low K_d (Fe-Mg) indicate disequilibrium and geologically non significant pressures fort his sample.

5 Discussion

5.1 Chlorine enrichment and magmatic and seafloor processes

In order to identify Cl addition due to assimilation of hydrothermally altered crust, it is necessary to ascertain that Cl was not degassed during eruption or that Cl was not enriched as a result of mantle variations, magmatic melting/fractionation processes or surficial processes. Significant Cl degassing of the samples is unlikely due to sampling depths of >2000 m, as Cl degassing is generally believed to be important only at <400 m depth (<40 bar; e.g. Unni and Schilling, 1978; Stroncik and Haase, 2004). There is evidence from the samples that they have experienced degassing of CO_2, as CO_2/Nb of the samples is mostly <200 (Fig. 3f), which is significantly lower than values of 239 or ~530 for undegassed magma derived by Saal et al. (2002) and Cartigny et al. (2008) respectively. However, CO_2 degassing did apparently not reduce Cl, since we see no correlation between the Cl in the samples and their sampling depth, nor is there a correlation between Cl and CO_2/Nb ratios. Although fractional crystallisation might influence the Cl concentrations, the poor relation between Cl and Mg together with the misfit with fractionation models (Fig. 2a), shows that fractionation cannot be the main source of variations in the Cl data. The correlation of Cl to many incompatible trace elements, particularly those that have a compatibility close to Cl (e.g. Nb), and to Sr-, Nd- and Pb- radiogenic isotopes in the case of the SMAR (Fig. 2b,c,d), does, however, indicate that most of the variations in the absolute Cl concentrations between the samples can be explained by source processes. Mantle source variations at the SMAR were described by e.g. Almeev et al. (2008) and Hoernle et al. (2011) and were attributed to mixing between a depleted mantle source (with low Cl concentrations) and several enriched (HIMU) mantle sources (with higher Cl concentrations), while variations in mantle source compositions at the Gakkel Ridge were identified by e.g. Michael et al. (2003) and Goldstein et al. (2008).
A close relation between Cl and Nb or K in basalts is predicted by their similar distribution coefficients (e.g. Sun et al., 2007) that cause those elements to behave alike during magmatic

processes, such as melting, fractional crystallization, consistent with the lack of a correlation between Cl/Nb and e.g. MgO, Na_8 (Fig. 3e,g). The relation between Nb and K is constant, supported by the positive correlation of Cl/Nb and Cl/K for each of the sample suites (Fig. 2f). The difference in Nb/K between the sample suites are due to source variations as indicated by the correlation of Nb/K to e.g. Ce/Pb and Na_8 (Fig. 2g,h). There is, however, no relation between Cl/Nb and source variations (e.g. Ce/Pb or U/Nb; fig. 3h). Nb is closer in incompatibility to Cl than K (Sun et al., 2007) and has the advantage that it is more resistant against weathering and alteration processes. Thus processes that formed the source have more likely modified the K content (e.g. Hart et al., 1974; Alt and Teagle, 2003; Schramm et al., 2005). Therefore, Nb is the most representative proxy for the original magmatic Cl concentrations and we thus mainly use Cl/Nb here to assess variations in Cl. Despite being more easily modified, Cl/K follows a similar trend as Cl/Nb and is for analytical reasons used for the melt inclusion, and also to compare our data to older studies, where mostly only major elements were measured.

A decoupling of Cl compared to Nb and K in both SMAR and Gakkel Ridge basalts (i.e. a range in Cl/Nb and Cl/K; fig. 2f, 3a-d) shows that processes additional to source melting and closed system fractional crystallisation. Since Cl/Nb is also unrelated to degassing (CO_2/Nb; fig. 3f), interaction with seawater is indicated as it can significantly increase the Cl concentrations compared to Nb and K (e.g. Jambon et al., 1995). Chlorine addition by surficial processes (seafloor alteration or syn-eruptive magma-seawater interaction, e.g. Hart et al., 1974; Soule et al., 2006) can be ruled out as playing a significant role for the following reasons: a) Homogeneous but anomalously high Cl concentrations of all but two of the SMAR and Gakkel Ridge glasses, even between different glass chips from a sample, suggest that Cl was added prior to mixing and homogenization in a magma chamber. b) The lack of a correlation between Cl/Nb and elements that are easily affected by alteration, e.g. U, Th, Ba (e.g. Alt et al., 1986; Alt and Teagle, 2003; Schramm et al., 2005; Augustin et al., 2008) argues against Cl addition due to alteration (Table 1,2). c) SMAR melt inclusions display even higher Cl/K than observed in the glasses (Fig. 3a, 6). The Cl in these inclusions must have been incorporated before eruption and during crystal growth and indicate deep Cl contamination. Deep addition of Cl thus argues for the direct or indirect incorporation of Cl-rich fluids (brines) that could have formed due to phase separation of hydrothermal fluids (Bischoff and Rosenbauer, 1987; Fournier, 1987; Berndt and Seyfried Jr, 1990) at high temperatures (see also van der Zwan et al., in review; see chapter 3). These brines could either be directly 'tapped' by rising magma, or be 'recycled in hydrothermally altered crustal rocks, particularly in hydrothermally formed minerals (e.g. amphiboles; Gillis et al., 2003; Barnes and Cisneros, 2012; Kendrick et al., 2013) that are subsequently assimilated by magma.

5.2 Cl/Nb mantle value

To determine the extent of Cl enrichment compared to K or Nb, we need to determine the mantle Cl/Nb and Cl/K ratios. Cl/Nb mantle ratios are not well constrained and cover a large range in the literature: Palme and O'Neill (2003) suggest the highest Cl/Nb of 51, McDonough and Sun (1995) propose 25.8, le Roux et al. (2006) favour 14 with a spread between 1 and 26, Salters and Stracke (2004) choose 6.9 and Saal et al. (2002) give a ratio of 3. However, Palme and O'Neill (2003) calculate a relatively high Cl mantle value (30 ppm) compared to values that were derived from basaltic melts and melt inclusions that are all lower than 7 ppm (e.g. Ryabchikov, 2001; Saal et al., 2002; Salters and Stracke, 2004; Kovalenko et al., 2006; le Roux et al., 2006). If we assume mantle concentrations of 0.3-0.6 for Nb (Hofmann, 1988; McDonough and Sun, 1995; Donnelly, 2002; Palme and O'Neill, 2003) and a Cl concentration of < 7 ppm, then mantle Cl/Nb ratios are not higher than the value obtained by McDonough and Sun (1995) of 25.8. Therefore, a maximum Cl/Nb mantle ratio of 26 is indicated, which is consistent with the Cl/Nb-Cl/K relationship in the samples investigated in this study (Fig. 2f), which shows that samples with Cl/Nb <26 have Cl/K <0.09, a value which overlaps with published Cl/K mantle values of 0.01-0.09 (Jambon et al.,

1995; Michael and Cornell, 1998; Saal et al., 2002; Stroncik and Haase, 2004; Kovalenko et al., 2006).

Our data show, however, many basalts with a Cl/Nb ratio of <26 (Fig. 3b-d). Since neither magmatic processes, nor interaction with seawater can explain a lower Cl/Nb than the Cl/Nb mantle ratio, these lowest values most likely represent the local Cl/Nb mantle ratios. At Gakkel Ridge, basalts with low Cl/Nb are observed over almost the complete range of Nb concentrations. Their Cl/Nb ratios group around 18.5±1.5 (Fig. 2b, 3b). This Cl/Nb ratio thus represents the local mantle ratio at Gakkel Ridge and all samples with Cl/Nb above this value are taken to show elevated Cl enrichment. SMAR samples with low Cl/Nb and Nb >4.5 ppm fall on a line with Cl/Nb of 20±2, suggesting this is the local SMAR mantle value (Fig. 2c, 3c,d). All depleted SMAR basalts (Nb <4.5) show high Cl/Nb ratios (Fig. 3c), which suggest that they are all affected by Cl addition, to which they are inherently more sensitive due to their low magmatic Cl. This is consistent with stronger elevated Cl/Nb of trace element depleted samples compared to trace element enriched samples observed in the other sample suites (Fig. 3a-d). Alternatively the trend observed in Cl/Nb against Nb at the SMAR could be interpreted as mixing of magma from a trace element depleted (low Nb) source with high Cl/Nb (~50) and a trace element enriched magma with low Cl/Nb. Although we cannot completely rule out this option due to a lack of low Nb samples with mantle Cl/Nb (in contrast to Gakkel Ridge), mixing appears less credible as a the depleted source Cl/Nb of 50 would not be compatible with a lower Cl/K of depleted mantle sources than of enriched mantle sources (Michael and Cornell, 1998; Stroncik and Haase, 2004) and we see no positive correlation between Cl/Nb and element pairs with a similar compatibly relation (e.g. Zr/Hf; Nb/Zr). Additionally, the smoothness of the curve observed in a Cl/Nb against Nb plot is an artifact of plotting the ratio of an element against the same element, and the samples do not follow a mixing line when Cl/Nb is plotted against e.g. K (Fig. 3d). Therefore, we reject mixing of sources with varying Cl/Nb as the cause of high Cl/Nb for depleted samples and apply a constant Cl/Nb mantle ratio for the SMAR samples.

A Cl/Nb mantle ratio of 18.5±1.5 and 20±2 for the Gakkel Ridge and SMAR respectively, means that ~75% of the measured samples on both the Gakkel Ridge and SMAR show hydrothermal Cl enrichment compared to Nb (Table 1,2). At the SMAR, Cl/Nb values are more extreme (up to 63) than at Gakkel Ridge, where the effect is comparatively subtle and all samples have Cl/Nb below 37. The SMAR melt inclusions show an even stronger enrichment of Cl compared to K, with Cl/K up to 0.56 (implying a Cl/Nb ratio of 130 based on the correlation regression shown in Fig. 2f). But neither ridge has Cl/Nb basalt ratios as extreme as the Red Sea (Cl/Nb >100; van der Zwan 2014).

5.3 High Cl/Nb and sites of hydrothermal activity

To study the relationship between high Cl/Nb and active hydrothermal vents, we compared the sampling locations of high Cl/Nb basalts with the bathymetry and positions of active hydrothermal venting and/or indirect indications for hydrothermal activity (Fig. 7). At both the SMAR and Gakkel Ridge there are distinct areas of high Cl/Nb, expressed in multiple samples. These areas are most apparent on the SMAR (Fig. 7a), where, within 10 km of a known hydrothermal site or plume, samples with elevated Cl/Nb are always seen. High Cl/Nb are also seen at the summit of A2 (8°57'S) and the relatively shallow area in the north of A1 (7°51'S), although no plume or hydrothermal deposits are known from there (Fig. 7a; Devey et al., 2010). Axial highs and domes are volcanic structures with a higher average potential to host hydrothermal systems due to the higher topography, a relative high magmatic activity over longer time scales (compared to small axial, monogenetic cones and flat tops volcanoes), and higher crustal heat flows (Fouquet, 1997). The summit of A2 was, however, earlier interpreted to be a remnant of past high magmatic activity (Devey et al., 2010). We take the high Cl/Nb basalts at the summit of A2 and in the north of A1, therefore, to indicate that alteration of the crust took place there previously by ancient, now inactive hydrothermal systems, which makes these areas good targets for the search for extinct hydrothermal vent fields.
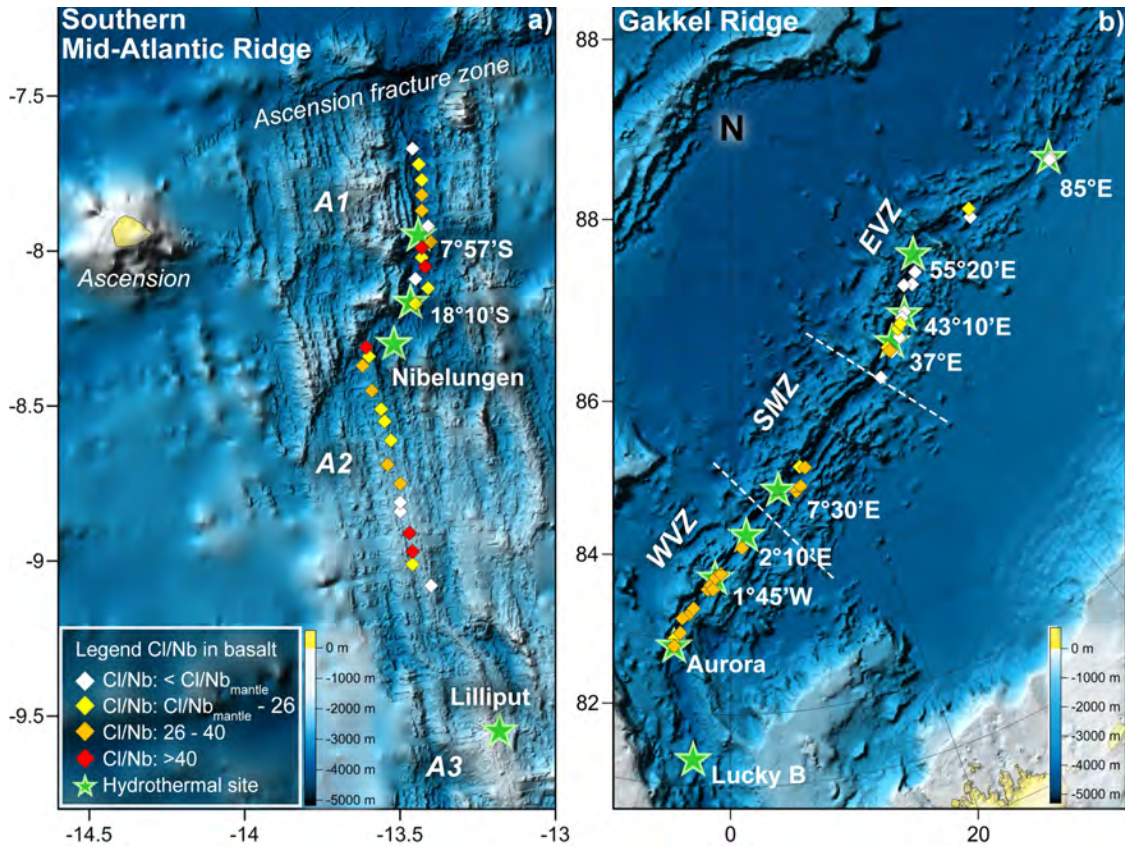
Fig. 7 – Locations of high Cl/Nb samples and hydrothermal sites at the **(a)** SMAR and **(b)** Gakkel Ridge. Note within 10 km of a known hydrothermal site there are always samples taken with elevated Cl/Nb ratios with the exception of 43°10'E and 85°E at Gakkel ridge, where independent evidence suggests that the hydrothermal activity is very recent and probably younger than the magmas sampled (for discussion see text). The axial high at SMAR segment A2 (8°57'S) yielded high Cl/Nb samples but lacks any recent hydrothermal activity, which suggests that the high Cl/Nb results from former, now inactive hydrothermal activity.

At Gakkel Ridge the correlation of high Cl/Nb basalts with areas of hydrothermal activity is less straightforward, due to the poorer sample spacing and the highly uncertain locations for most of the hydrothermal fields (Baker et al., 2004). Nevertheless, consistent with the observations at the SMAR, the visually confirmed Aurora hydrothermal field at 6°20'W and plume sites at 1°45'W and 37°E have samples, which display high Cl/Nb collected within 10 km (Fig. 7b). The samples taken closest to the suggested plume sites at 2°10'E, 7°30'E and 55°20'E are 20-27 km away and display both high and low Cl/Nb, suggesting that the plumes may have been detected relatively far from their sources or are unrelated to samples at distance. The fact that our samples from <10 km from 85°E, an area which is known to host present-day hydrothermal activity (Baker et al., 2004; Pontbriand et al., 2012) do not exhibit elevated Cl/Nb (Fig. 7b), implies that the sampled glasses, which come from visibly older lava flows than the young glassy eruptives observed on the seafloor by Pontbriand et al. (2012), are unrelated to the present hydrothermal activity. Both the young lavas and hydrothermal activity were linked by them to an eruption in 1999, which seems to suggest that the 85°E system is a new hydrothermal system, established at the initiation of a new period of magmatic activity. Also low Cl/Nb samples <10 km from the plume at 43°10'E are visibly not the youngest glasses in the area and likely erupted before the present hydrothermal activity.

In summary, the lack of high Cl/Nb in basalts give no guarantee that there is no hydrothermal activity present, as the magmas may have erupted before hydrothermal activity took place. High Cl/Nb, in contrast, likely always indicates that there is active or recently extinct

hydrothermal activity in the vicinity and as such represents an exploration tool for active and fossil hydrothermal fields.

5.4 Hydrothermal circulation in relation to crystallization depths

Michael and Cornell (1998) suggested that the depth of last equilibrium crystallization determines the possible amount of hydrothermal Cl addition. They did not find high Cl/K at slow-spreading ridges that display average crystallization pressures of >300 MPa, which they assumed indicated that hydrothermal circulation is shallower. Our work shows that basalts from slow-spreading ridges with high average calculated crystallisation pressures do show on average significantly elevated Cl/Nb (Gakkel Ridge: Cl/Nb of 26 at 426 MPa; SMAR: Cl/Nb of 27 at 357 MPa and the Red Sea Rift: Cl/Nb of 81 at 251 MPa), which implies that the precision of previous data was not high enough to distinguish between small, but significant variations in Cl/Nb. In addition, high Cl/Nb due to hydrothermal influence is visible at all three ridges over the complete range of calculated COMAGMAT pressures (0-800 MPa), with high Cl/Nb basalts having calculated last equilibrium crystallisation pressures of >500 MPa (~15 km; table 1,2).

When estimated crustal thicknesses of ~5 (A1) to ~11 km (A2), <4 km and ~5-6 km at the SMAR, Gakkel Ridge and Red Sea Rift respectively, are compared to the high calculated COMAGMAT pressures (and also pressures calculated by Michael and Cornell (1998)), hydrothermal circulation down into the mantle would be indicated. The implied deep hydrothermal circulation raises doubt on the reliability of the pressures. In addition, the discrepancies (-300 to +300 MPa; table 3) between the COMAGMAT pressures and the pressures calculated with the model of Putirka et al. (1996) on the same samples, indicate that at least one pressure estimate is wrong. To test the validity of the pressure calculations we assessed their major assumptions, mainly based on data from the SMAR, although the same probably applies to the other ridges too.

5.5 Validity of pressure calculations

5.5.1 Comparison of COMAGMAT to other models

Pressure calculations of the SMAR ridge glass samples derived with COMAGMAT were discussed by Almeev et al. (2008), and shown to correspond within the given uncertainties to pressures calculated by empirical models for anhydrous compositions of Danyushevsky et al. (1996), Yang et al. (1996), Herzberg (2004) and Villiger et al. (2007), with the most overlap with the model of Yang et al. (1996). The crystallisation pressures for SMAR samples given here, although they use improved calibration coefficients for the effect of H_2O contents on Ol, Cpx and Pl crystallisation and take measured H_2O values into account (Almeev et al., 2007a; Almeev et al., 2007b; Almeev et al., 2012), follow the same trend as for the older calculations, but with consistent offsets to lower pressures of between ~100 MPa (for higher pressure estimates) and ~150 MPa (for lower pressure estimates). The new results are, however, more consistent with results calculated by the methods of Danyushevsky et al. (1996), Herzberg (2004) and Villiger et al. (2007). Compared to the method of Yang et al. (1996), (used by Michael and Cornell (1998) to identify different pressure and Cl/K groups), our COMAGMAT results show consistently lower values of on average 88 MPa that are however on a parallel trend and within the analytical uncertainty of the methods.

5.5.2 The effect of water contents

The COMAGMAT model is relatively sensitive to the water concentrations of the melts. Water concentrations are potentially subject to post-crystallisation modification by loss due to degassing (which results in an overestimation of P) or by addition due to alteration (which results in a P underestimation). The relatively good correlation of H_2O with elements of similar magmatic incompatibility, e.g. Ce ($R^2 = 0.86$) indicates little H_2O loss or addition (Fig. 2e). Nevertheless, even if we use the highest measured H_2O content of an SMAR sample (0.64 wt.%) to calculate minimum crystallisation pressures, the reduction of ~220 MPa that

this yields still places the highest pressures within the mantle and the unsystematic and large differences to the Cpx-melt pressure calculations are still present. Late addition of seawater due to alteration is not consistent with the homogeneous Cl distribution in the glasses (see above) and would lead to unrealistic deep pressures and larger differences to some of the Cpx-melt pressures.

5.5.3 Equilibration extent of the samples and the influence of crustal assimilation
More doubtful is the assumption, inherent in all phase equilibrium models, that the melts have followed a simple crystallization history and were in equilibrium with Ol, Cpx and Pl at the cotectic without subsequent modification. Mineral rim data of the SMAR samples display profound disequilibrium between glasses and many of the phenocrysts, particularly for Ol, implying they are partly xenocrystic (Fig. 5b). The optical microscopy and mineral transect data show the presence of complex or reverse zoning, dissolution zones and deformation in some of the minerals (Fig. 4,5). Thus a more complex history for the melts is implied. Magma mixing is indicated by isotope data (Hoernle et al., 2011) and by the melt inclusion data, which show both higher and lower Cl and K concentrations than the host glasses (Fig. 6). Higher K and Cl contents of trace element enriched glasses 149-1 and 149-4 compared to any of their melt inclusions indicate late addition of the trace element enriched component to the system before eruption (Fig. 6c). Also, disequilibria between melts from all samples and many Ol rims imply addition of at least part of the Ol to the melts shortly before eruption, as Ol diffusion profiles form at these temperatures within a few days (cf. Klügel, 1998; Shaw and Klügel, 2002). Even the one observed diffusion profile with a diffusion length of <50 μm (sample 143-2; fig. 4a), indicates a short residence time of the Ol in the melt of a few weeks (cf. Shaw and Klügel, 2002). Moreover, the lack of Cpx in most of the samples, as observed in many MORB samples, is inconsistent with the assumption that the melts are at a multiply saturated cotectic with Ol, Pl and Cpx. A positive correlation between Ca and Mg in most MORB magma suites has been used as evidence for Cpx crystallization, with the lack of Cpx explained by multiple melt events at different depths, magma mixing, deep Cpx crystallization and/or polybaric and low-pressure crystal fractionation (e.g. Dungan and Rhodes, 1978; Bence et al., 1979; Rhodes et al., 1979; Bryan et al., 1981; Francis, 1986), although an alternative explanation for Ca fractionation trends involves assimilation of (lower) crustal rocks and melt-rock reactions (syntaxis; Bédard et al., 2000 and references therein). Assimilation of (altered) oceanic crust in the samples studied here is demonstrated by the high Cl/Nb data of the glasses (cf. Bédard, 1991; Bédard and Hébert, 1996), by the occurrence of xenocrysts and solid rock fragments that partially show deformation in the SMAR samples (Fig. 3, 5) and at Gakkel Ridge by U-series data (Elkins et al., 2014).
Melt-rock reactions in the lower crust may significantly change lower crustal cumulates (e.g. Meyer et al., 1989; Bédard, 1991; Bédard, 1993; Bédard and Hébert, 1996; Natland and Dick, 1996; Bédard et al., 2000; Coogan et al., 2000; Dick et al., 2002; Ridley et al., 2006) and are thought to occur at slow-spreading ridges by porous flow through lower crustal rocks, in ephemeral magma chambers or during magma ascent (e.g. Kelemen et al., 1995; Kvassnes and Grove, 2008; Lissenberg and Dick, 2008). The assimilated crust consists of similar components as the assimilant and therefore the original melt composition and extent of assimilation cannot be determined straightforwardly by backwards modeling, and particularly not if the exact composition of the crust is unknown. Kvassnes and Grove (2008) and Lissenberg and Dick (2008) showed, however, by experiments and forward modeling that assimilation of various types of oceanic crust has a significant effect on the composition of the melts and their Al_2O_3-CaO-Si-MgO relations. Therefore, they concluded that any method that uses the composition of a melt (glass) alone to determine e.g. crystallization pressure or temperature from a melt can be erroneous. Lissenberg and Dick (2008) further showed that calculated pressures increase with increasing assimilation of lower crustal troctolite (up to 25%) and that the full range of crystallization pressures observed in MORB (100-800 MPa) can be achieved by reaction of melts with the lower crust. This relation is consistent with the basalt data from the SMAR, where mainly high Cl/Nb is observed for the samples that display high pressures (>300 MPa; table 1). Assimilation seems to be a more reasonable explanation

for calculated high (i.e. mantle) pressures than merely crystallization due to the difficulties to transport melts unmodified from these depths. Crystallisation in the mantle is further considered unrealistic due to the lack of abundant gabbroic rocks there, while cumulates are present in the lower crust (see discussion in Lissenberg and Dick, 2008).

As all samples that indicate assimilation by high Cl/Nb likely have modified major element compositions, which invalidate all melt-based pressure calculation-models, these pressure calculations cannot be used to determine the depth of Cl addition and the previously observed correlation between Cl/K and apparent melt-based crystallization pressures (Michael and Cornell, 1998) is hence invalid. Pressure calculations based on Cpx-melt element exchange (Putirka, 2008) can give a better control on the crystallization pressures, as the degree of equilibrium between glass and Cpx can be assessed and the Cpx compositions dominate the pressure calculations more than the (potentially changed) melt compositions. Magma changed by assimilation can thus be recognized and relevant crystallization pressures of the Cpx can be derived, although a statistical relation between Cl/Nb and crystallization pressures cannot be determined due to the lack of Cpx in most samples. Unfortunately due to the undersaturation of volatiles, no fluid inclusions are present in the samples that could give additional pressure information (Hansteen and Klügel, 2008).

5.6 The depth of assimilation of hydrothermally altered crust

The pressures obtained from samples containing Cpx, by the formulations of Cpx-melt equilibria of Putirka et al. (1996) all give values in the same range (316-403 MPa ≈ 10-13 km; table 3). For a crustal thickness of ~11 km on segment A2 (Bruguier et al., 2003) where these samples originate, these pressures imply crystallization at lower crustal depths or close to the Moho. The complete equilibrium observed for 147-2 and 162-2 between the Cpx phenocrysts and melt, and the Cl enriched melt inclusions, imply an increase of Cl/Nb happened prior to crystallization and inclusion formation, with no substantial modification of the melt subsequently to Cpx crystallization. Thus the Cl/Nb content of the glass in sample 147-2 must have been increased before or at the crystallization depth of the Cpx, which infers a minimum depth of ~10 km for the hydrothermal circulation in this region. The range in Cl, K and Cl/K in the melt inclusion implies the mixing of melts from different mantle sources and various degrees of assimilation during crystallization (Fig. 6). This indicates Cl addition in magma pockets, where magma can crystallise and interact with the crust. As many Ol grains are xenocrystic, they must have crystallised from earlier batches of melt that already partly assimilated Cl compatible with the high Cl/K of the melt inclusions in the Ol. Hence, the various Cl/Nb and Cl/K observed in the glass and melt inclusions from one rock probably represent multiple cycles of hydrothermal alteration, assimilation of crust and crystallisation, rather than processes occurring all to the same magma batch.

At Gakkel Ridge, deep pooling of melt was indicated in samples from 85°E by homogeneous major and trace elements in melt inclusions and their H_2O-CO_2 saturation pressures (Shaw et al., 2010), while U-series data indicates melt-rock reactions at depths <15 km (Elkins et al., 2014). Crystallization and crustal assimilation in (ephemeral or permanent) magma chambers in the lower crust is consistent with the evidence of gabbroic samples and melt-rock reactions in the lower crust at e.g. the slow-spreading South-West Indian Ridge and the MAR 30°N (e.g. Dick et al., 2000; Expedition Scientific Party, 2005). In addition, both thermodynamic models and inferred temperature gradients indicate more effective conductive cooling at slow-spreading ridges and predict a cooler crust and increase the probability for magma chambers to be present at greater depths than at fast-spreading ridges (Reid and Jackson, 1981; Niu and Hekinian, 1997; Dick et al., 2003; Montési and Behn, 2007).

The investigated samples that show minor disequilibrium in Fe-Mg between the Cpx and glass indicate modification of the host melt after crystallization of the Cpx (Table 3). Thus, theoretically an increase in Cl of the glass could have occurred at shallower depths as well. Although we cannot rule out that Cl can be further enriched by melt-rock reactions during the ascent of magma, the cooler upper crust at slow-spreading ridges (Reid and Jackson, 1981; Dick et al., 2003; Montési and Behn, 2007) requires that rising of magma must be relatively

fast to not crystallize, in agreement with the lack of diffusion profiles in the Ol (Rutherford, 2008). Hence, assimilation of crust is less likely to happen here and the main assimilation of (hydrothermally altered) crust probably occurs in the lower crust. Some of the samples that display lower crustal Cpx crystallization pressures do not have high Cl/Nb, which indicates that not all magmas cooling at depth are contaminated by altered crust.

Circulation of hydrothermal fluids down to the lower crust in slow-spreading ridges can be aided by the cooler, more brittle crust, which may lead to a comparatively strong effect of tectonics and faults (Dick et al., 2003). These faults can provide prominent pathways for fluids and additionally to e.g. microfractures (Lister, 1974; Nicolas et al., 2003; Koepke et al., 2005) penetrate into the ductile regime (Harper, 1985; Mével and Cannat, 1991). The depth of the faults and their brittle activity can be investigated by earthquake data. For the SMAR, microseismicity is found on segment A1 down to 2-4 km within the 5 km thick crust (Grevemeyer et al., 2013). The teleseismic earthquake database from the International Seismological Centre of this area (1960 to present; International Seismological Centre, 2011), however, also records events at depths of ~10 km with a few earthquakes recorded up to depths of ~30 km and 62 km. Although the depth estimate of these earthquakes is not very precise (Engdahl et al., 1998), the >3 magnitude of these earthquakes indicate that the faults causing them must be large and thus have the potential to extent to larger depths (Fig. 1). In segment A2 earthquakes are only present in the northern part, while the southern part is characterized by aseismicity, which suggests a relatively ductile crust, potentially related to extensive magmatism (Devey et al., 2010; fig. 1). This lack of teleseismic earthquakes in the last ~50 years is consistent with the lack of active hydrothermal plumes in this area and our interpretation that high Cl/Nb samples from the A2 summit may be the result of former, now inactive hydrothermal interaction. From Gakkel Ridge generally less teleseismic earthquakes are recorded, but they are present at all sample locations (Fig. 1,7). Earthquake depths scatter around 10 km, but with depths up to 32 km, thus indicating the activity of deep faults here as well, that can be pathways for hydrothermal circulation down to the lower crust.

5.7 Differences between slow- and fast-spreading ridges

Our data show that Cl contamination by assimilation of hydrothermal fluids or hydrothermally altered crust is not restricted to fast-spreading ridges or ridges with a thick crust as suggested by Michael and Cornell (1998), but occurs also at slow-spreading ridges. However, there is still a difference in the Cl/Nb content of basalts from the two types of ridges. While Cl/Nb at fast-spreading ridges is high (~250 based on Cl/Nb-Cl/K relation) and present in most samples (e.g Michael and Cornell, 1998; Saal et al., 2002; le Roux et al., 2006; Kendrick et al., 2013), Cl/Nb at slow-spreading ridges is highly variable and significantly lower (<70), in the absence of evaporites (Fig. 3a).

Two reasons can explain this difference: First, the generally shallower occurrence of melts at fast-spreading ridges makes it possible to assimilate hydrothermally altered crust at shallower levels (<3 km; le Roux et al., 2006; Kendrick et al., 2013) than the depths observed here for slow-spreading ridges (at least 10 km at the SMAR A2). If hydrothermal activity decreases with depth as suggested by e.g. Dick et al. (2000) and Coogan (2003), deeper assimilation of crust will result only in a subtly elevated Cl/Nb. To confirm that lower Cl/Nb is due to a decrease in hydrothermal activity, however, more independent pressure data from different ridges are needed or better constraints on the relative decrease of hydrothermal alteration in the lower crust. Secondly, the larger permanent magma chambers that exist on fast-spreading ridges provide the opportunity for more extensive mixing and assimilation of the crust over a larger area. Therefore, the chemical signature of assimilation of hydrothermally altered crust should always be present (cf. Saal et al., 2002; Kendrick et al., 2013). In contrast, slow-spreading ridges display a much higher compositional variety (e.g. Dick et al., 2000), and magma chambers are probably small and ephemeral, which implies that assimilation processes are more localized and that either there is less homogeneous interaction of magma with the crust, or that the degree and location of alteration is more heterogeneous (cf. Dick et al., 2000).

Differences in Cl/Nb ratios in basalts between slow-spreading ridges are also observed and do not change systematically with spreading rate. Extremely high Cl/Nb from samples of the Red Sea are attributed to extra Cl addition from evaporites (van der Zwan et al., in review; see chapter 3). The relatively trace element enriched character of Gakkel Ridge samples (Michael et al., 2003; Goldstein et al., 2008) can explain in part at least the moderate Cl/Nb of <37 over the whole ridge, as Cl addition due to assimilation is harder to detect in incompatible trace element enriched samples (e.g. with high K/Ti, Nb, K; Fig. 3a-d). Alternatively, the ultra-slow-spreading and cool crust at Gakkel Ridge (Reid and Jackson, 1981; Dick et al., 2003; Montési and Behn, 2007) may also play a role if the cooler crust causes assimilation to occur on average at deeper levels with potentially lower hydrothermal circulation, or if melt degrees and the amount of assimilation are reduced below limits that can be detected in Cl/Nb. Low melt fractions were indicated by the thin crust (Reid and Jackson, 1981; Coakley and Cochran, 1998; Dick et al., 2003; Jokat et al., 2003) and high Na_8 (>3.1; fig. 3g), although the latter can be modified by assimilation (Kvassnes and Grove, 2008; Lissenberg and Dick, 2008).

6 Implications

The depth of hydrothermal circulation is important for the cooling of the crust and for formation mechanisms of the lower crust (e.g. Dungan and Rhodes, 1978; Bence et al., 1979; Rhodes et al., 1979; Bryan et al., 1981; Francis, 1986). With our data, we can demonstrate that hydrothermal fluids circulate at slow-spreading ridges down to the lower crust till at least 10 km depth at segment A2 of the SMAR. Lower crustal hydrothermal circulation implies that cooling of the deep crust at slow-spreading ridges is aided by hydrothermal fluids, which further has important implications for cooling models and makes the cooling by ductile movement of cumulates as stated in the gabbro glacier model (Maclennan et al., 2005; VanTongeren et al., 2008) not necessarily. The lower Cl/Nb at slow-spreading ridges than at fast-spreading ridges indicate a stronger influence of conductive cooling. Together with cooling by deep hydrothermal circulation this provides a mechanism to remove heat produced by crystallisation in the lower crust. In agreement with the lack of permanent magma chambers at most slow-spreading ridges, this makes the sheeted sill model (Nicolas et al., 1988; Henstock et al., 1993; Morgan and Chen, 1993; Quick and Denlinger, 1993; Chen, 2001; Coogan et al., 2002b) the more likely model applicable for the formation of the lower crust at slow-spreading ridges.

Our work shows that crustal assimilation occurs at slow-spreading ridges and can be identified by Cl/Nb. Although the lack of high Cl/Nb does not mean that crustal assimilation did not take place, melts that do show high Cl/Nb did interact with the crust and care should be taken when using their major element data for e.g. pressure or melt degree calculations.

Hydrothermal circulation down to the lower crust can increase the Cl budget and to a smaller extent the H_2O budget of an altered oceanic slab and thus the potential of Cl to subduct, although we cannot determine with the present data the Cl content and distribution of the altered crust and so cannot give a realistic estimate of the total Cl content of the crust. The increase in Cl due to hydrothermal circulation is particularly important if the oceanic crust is covered by evaporites, which are a common feature at the early stages of opening oceans (e.g. Rona, 1982). Most other elements occur in too low concentrations in hydrothermal fluids to significantly change the composition of the basalts. Only H-isotopes, B and noble gasses may be significantly changed (Kent et al., 1999a; Gillis et al., 2003; Kendrick et al., 2013) and thus any study on those elements should take into account the effect of hydrothermal circulation and assimilation of hydrothermally altered rocks.

Finally, Cl/Nb can be used to indicate potential locations for massive sulfide deposits that can be the surface expression of the hydrothermal system, even if those systems are not presently active, but therefore economically more interesting. They provide a means to average over longer time scales the hydrothermal activity, which has influenced the crust and so could be a potentially good prospecting tool on- and off-axis.

7 Conclusions

Novel high-precision Cl measurements of glasses and melt inclusions in basalts from the slow-or ultra-slow spreading Southern Mid-Atlantic Ridge and Gakkel Ridge show a range of magmatic Cl contents. Basaltic Cl/Nb and Cl/K ratios are higher than mantle values and so cannot be explained by magmatic processes such as degassing, melting, fractionation or source variations, a conclusion supported by the lack of a correlation of Cl/Nb or Cl/K with other trace elements. Modification of Cl contents by seafloor processes can be excluded because melt inclusions measurements also show high Cl/K and analysed glass chips all have homogeneous Cl content. The assimilation of hydrothermal brines or hydrothermally altered rock appears to be the most likely cause of the elevated Cl contents in the magmas. The overall high Cl/Nb implies that these processes also occur at slow-spreading ridge in contrast to conclusions drawn from early studies based on lower precision Cl data.

Assimilation of altered crust changes the magma major element composition in such a way that barometers based on the glass compositions alone and experimentally calibrated phase equilibria cannot be used to determine the Cl contamination depth. Cpx-melt pairs are more reliable and yield Cl contamination depths and thus hydrothermal circulation in the lower crust. In the case of SMAR segment A2 hydrothermal fluids extend to depths of at least 10 km. Deep assimilation with hydrothermal cooling is consistent with independent earlier evidence for lower crustal crystallization and melt-rock reactions and extensive and deep faulting at slow-spreading ridges and appears to support a sheeted sill mechanism for formation of the lower oceanic crust at slow-spreading ridges.

Compared to fast-spreading ridges, the Cl/Nb ratios at slow-spreading ridges, although elevated, are less extreme. This can be explained by the general lack of large and shallow magma chambers beneath slow-spreading ridges, leading to a larger component of conductive cooling there and to assimilation processes and circulation of hydrothermal fluids acting on a more localized scale. Cl/Nb at slow-spreading ridges is enhanced by heat supply, visible as high magmatic activity, and reduced in areas with cool and thin crust such as the EVZ of Gakkel Ridge. The high intrinsic magmatic Cl contents of enriched magmas mask the effects of Cl addition.

The effects of deep hydrothermal circulation should be taken into account for the Cl budget of the oceanic crust, particularly at passive margins where evaporites might be present. In addition, the signatures of H-isotopes, B and noble gasses may be modified by hydrothermal alteration and crustal assimilation. All MORB basalts that display high Cl/Nb were at some point in time affected by hydrothermal fluids. Thus Cl/Nb can be used for the exploration of hydrothermal vent fields, which is particularly interesting for inactive systems.

Supplementary table A1

High precision Cl and K Ol, Pl and Cpx mineral data (ppm)[a]

Sample	Glass		Olivine				Plagioclase				Clinopyroxene			
	Cl/Nb	Cl/K	Cl	2SE	K	Cl/K	Cl	2SE	K	Cl/K	Cl	2SE	K	Cl/K
133-1	21.1	0.10	23.3	0.5	30.7	0.76	13.3	0.4	70.9	0.19				
136-1	22.4	0.12	14.4	0.5	23.6	0.61	13.5	0.1	41.9	0.32				
137-3	28.4	0.13	12.5	0.6	25.7	0.49	13.1	0.3	40.3	0.32				
137-4	29.3	0.14	13.7	1.1	24.5	0.56	12.7	0.4	51.0	0.25				
138-2	23.4	0.11					14.2	0.5	37.3	0.38				
138-3	19.7	0.08					12.5	0.4	42.3	0.30				
139-2	22.0	0.11	13.7	1.5	22.7	0.60	11.2	1.0	41.6	0.27				
139-3	21.8	0.12	15.3	1.9	26.7	0.58	11.3	0.9	41.4	0.27				
140-1	34.1	0.15	-0.5	0.0	9.1	-0.05	11.0	0.8	28.3	0.39				
141-1	40.2	0.14	18.9	0.4	31.7	0.60	8.3	0.2	31.1	0.27				
143-1	46.8	0.19	11.1	1.7	21.8	0.51	10.0	1.3	44.6	0.22				
							7.6	N/A	172.3	0.04				
143-2	46.3	0.19	12.2	1.0	23.9	0.51	12.1	0.8	37.6	0.32				
146-2	22.9	0.11					8.4	1.4	65.2	0.13				
							3.6	N/A	109.1	0.03				
147-2	47.9	0.17	11.6	1.2	25.5	0.46	8.7	0.4	42.6	0.20	35.0	1.2	51.2	0.68
							6.5	N/A	61.6	0.11				
147-3	47.3	0.17	19.1	0.0	32.7	0.58	6.2	0.4	48.8	0.13				
149-1	32.8	0.15	20.5	0.4	32.3	0.63	9.8	0.7	76.6	0.13	37.0	0.7	47.7	0.78
			11.1	2.3	21.1	0.53								
149-4	33.3	0.15	8.6	1.9	14.6	0.59	6.7	1.5	106.8	0.06	45.3	N/A	28.7	1.58
151-3	29.3	0.12	28.0	5.7	43.5	0.64	6.9	1.6	158.5	0.04				
							11.9	N/A	82.2	0.15				
157-2	19.1	0.08	17.4	0.9	25.2	0.69	6.6	N/A	189.6	0.04				
160-1	47.8	0.24	19.6	0.5	30.6	0.64	5.9	0.6	129.0	0.05				
162-1	18.3	0.08	26.8	0.9	37.8	0.71	12.2	N/A	141.0	0.09	41.5	0.6	55.4	0.75
							1.6	0.7	332.0	0.00				
162-2	18.1	0.08	32.4	0.1	44.5	0.73	-2.6	0.5	415.5	-0.01	43.5	0.8	54.6	0.80

[a] Averages based on 2-3 measurements on different minerals, apart for the samples without 2SE. Samples with high 2SE may represent different groups of minerals.

Supplementary table A2
Melt inclusion Cl and K data

Sample [a] 137-4	Cl (ppm)	K (ppm)	Cl/K
Glass	78	572	0.14
Melt inclusions in Plagioclase			
137-4_1a	46	634	0.07
137-4_1b	62	564	0.11
137-4_1c	177	424	0.42
137-4_2	64	182	0.35
137-4_3a	38	454	0.08
137-4_3b	29	489	0.06
137-4_3c	25	463	0.05
137-4_4a	45	440	0.10
137-4_4b	42	465	0.09
137-4_5	61	255	0.24
137-4_6	121	480	0.25
137-4_7	89	205	0.44
137-4_8	119	462	0.26
137-4_9a	54	158	0.34
137-4_9b	119	242	0.49

Sample [a] 143-1	Cl (ppm)	K (ppm)	Cl/K
Glass	53	270	0.19
Melt inclusions in Olivine			
143-1_1a	72	251	0.29
143-1_1b	62	250	0.25
143-1_1c	52	217	0.24
143-1_2a	63	288	0.22
143-1_2b	37	170	0.22
143-1_2c	26	169	0.15
143-1_2d	47	446	0.11
143-1_3a	64	131	0.49
143-1_3b	65	136	0.48
143-1_3c	73	273	0.27
143-1_3d	71	294	0.24
143-1_4a	31	170	0.18
143-1_4b	40	175	0.23
143-1_5a	37	258	0.14
143-1_5b	36	253	0.14
143-1_5c	41	195	0.21
143-1_5d	42	192	0.22
143-1_5e	78	607	0.13
143-1_6a	53	538	0.10
143-1_6b	56	550	0.10
143-1_7a	70	289	0.24
143-1_7b	58	285	0.21
143-1_7c	71	307	0.23
143-1_8a	78	298	0.26
143-1_8b	86	309	0.28
143-1_8c	91	221	0.41
143-1_8d	77	138	0.56
Melt inclusions in Plagioclase			
143-1_9a	43	298	0.14
143-1_9b	24	169	0.14
143-1_10d	38	221	0.17

Sample [a] 143-2	Cl (ppm)	K (ppm)	Cl/K
Glass	52	272	0.19
Melt inclusions in Olivine			
143-2_1	52	403	0.13
143-2_2a	50	275	0.18
143-2_2b	45	306	0.15
143-2_3a	38	160	0.24
143-2_3b	28	108	0.26
143-2_4	32	114	0.28
143-2_5a	27	72	0.37
143-2_5b	38	72	0.52
143-2_5c	20	67	0.30
143-2_5d	32	67	0.47
143-2_6	53	263	0.20
143-2_7	51	240	0.21
143-2_8	62	303	0.21
143-2_9	24	81	0.30
143-2_10a	46	264	0.17
143-2_10b	65	358	0.18
Melt inclusions in Plagioclase			
143-2_11	30	176	0.17
143-2_12a	52	283	0.19
143-2_12b	51	264	0.19

Sample [a] 147-2	Cl (ppm)	K (ppm)	Cl/K
Glass	63	375	0.17
Melt inclusions in Olivine			
147-2_1	137	1316	0.10
147-2_2	71	477	0.15
147-2_3	167	876	0.19
Melt inclusions in Plagioclase			
147-2_4	39	231	0.17
147-2_5	83	443	0.19
147-2_6a	70	362	0.19
147-2_6b	66	427	0.15
147-2_7	150	975	0.15
147-2_8a	35	297	0.12
147-2_8b	46	322	0.14
147-2_9	72	226	0.32
147-2_10a	63	332	0.19
147-2_10b	51	338	0.15

Sample [a] 147-3	Cl (ppm)	K (ppm)	Cl/K
Glass	64	378	0.17
Melt inclusions in Olivine			
147-3_1	58	346	0.17
147-3_2a	95	870	0.11
147-3_2b	81	749	0.11
147-3_3	59	473	0.12
147-3_4	53	443	0.12
147-3_5	55	270	0.20
147-3_6	100	367	0.27
Melt inclusions in Plagioclase			
147-3_7	60	225	0.27
147-3_8	47	257	0.18
147-3_9	71	323	0.22
147-3_10a	48	464	0.10
147-3_10b	44	286	0.15
147-3_11a	60	221	0.27
147-3_11b	58	220	0.27
147-3_12a	172	1619	0.11
147-3_12b	175	2027	0.09
147-3_12c	168	1861	0.09
147-3_13a	56	397	0.14
147-3_14a	68	358	0.19
147-3_14b	69	374	0.18

Sample [a] 149-1	Cl (ppm)	K (ppm)	Cl/K
Glass	415	2765	0.15
Melt inclusions in Olivine			
149-1_1a	168	1385	0.12
149-1_1b	160	1382	0.12
149-1_2a	99	1107	0.09
149-1_2b	98	1149	0.08
149-1_3a	93	803	0.12
149-1_3b	94	803	0.12
149-1_4	70	838	0.08
149-1_5	98	1114	0.09
149-1_6	135	866	0.16
149-1_7	67	615	0.11
149-1_8a	61	657	0.09
149-1_8b	66	662	0.10
Melt inclusions in Plagioclase			
149-1_9a	224	1434	0.16
149-1_9b	232	1408	0.16
149-1_10	98	805	0.12
149-1_11a	165	975	0.17
149-1_11b	234	1406	0.17
149-1_11c	223	1412	0.16
149-1_12a	187	560	0.33
149-1_12b	169	780	0.22
149-1_12c	189	514	0.37

Sample [a] 149-4	Cl (ppm)	K (ppm)	Cl/K
Glass	425	2802	0.15
Melt inclusions in Olivine			
149-4_1	79	520	0.15
149-4_2	115	1087	0.11
149-4_3	144	1073	0.13
Melt inclusions in Plagioclase			
149-4_4	103	619	0.17
149-4_5a	113	592	0.19
149-4_5b	107	593	0.18
149-4_5c	105	761	0.14
149-4_5d	113	785	0.14
149-4_6a	104	789	0.13
149-4_6b	109	785	0.14
149-4_7	207	1578	0.13
149-4_8a	122	1082	0.11
149-4_8b	122	1094	0.11
149-4_9	170	1580	0.11
149-4_10a	166	1647	0.10
149-4_10b	181	1594	0.11
149-4_10c	174	1618	0.11
149-4_10d	113	687	0.16
149-4_10e	145	626	0.23
149-4_11	101	631	0.16

Sample [a] 151-3	Cl (ppm)	K (ppm)	Cl/K
Glass	99	798	0.12
Melt inclusions in Olivine			
151-3_1	89	498	0.18
151-3_2a	95	712	0.13
151-3_2b	100	689	0.15
151-3_2c	105	772	0.14
151-3_2d	100	741	0.14
151-3_3a	82	880	0.09
151-3_3b	75	870	0.09
151-3_3c	73	905	0.08
151-3_4	116	765	0.15
Melt inclusions in Plagioclase			
151-3_5a	101	890	0.11
151-3_5b	78	938	0.08
151-3_5c	69	891	0.08
151-3_6	114	764	0.15
151-3_7	73	1020	0.07
151-3_8	135	2256	0.06
151-3_9	81	598	0.14

[a] Numbers behind the sample number represent different minerals in which the melt inclusions were measured, different letters represent different melt inclusions or different measurements on the same melt inclusion.
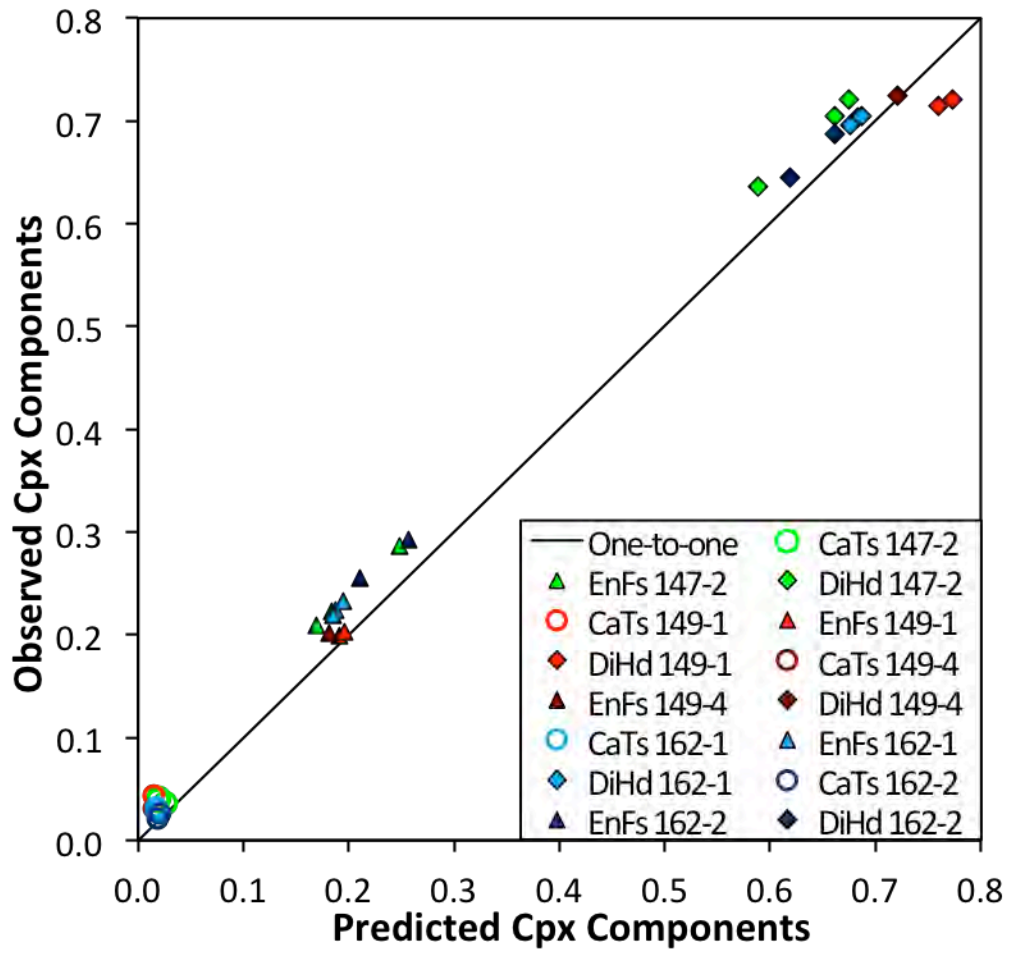
Supplementary Fig. A1 – Cpx components predicted by the barometers from Putirka et al., 1996 versus the observed components. As all samples are close to the one-to-one line, they show equilibrium of the Cpx.

Chapter 5:

Conclusions

This study investigated the chlorine (Cl) contents in basalts from three (ultra) slow-spreading ridges using novel high-precision electron microprobe measurements. Basalt samples from the Red Sea Rift, Southern Mid-Atlantic Ridge and Gakkel Ridge were selected to examine Cl addition by assimilation of hydrothermally altered oceanic crust at slow-spreading ridges. The following main conclusions result from this work:

1)   Because of the low Cl concentrations in basalt glasses from slow-spreading ridges (<200 ppm), accurate and highly precise Cl measurements are necessary to be able to observe variations in Cl contents in these rocks. The small variations can be measured by electron microprobe when the newly developed mapping method is applied that measures with high beam currents over a long time without sample damage and achieves a high precision of 1-2 ppm SD with detection limits of <10 ppm. Sample-standard bracketing techniques and a calibration of the method with geological materials with fixed Cl concentrations of 0 wt.% (depleted olivine) and 16.6 wt.% (atacamite) and with international Standard Reference Material ensure the accuracy of the method. Essential for good Cl glass measurements is a clean preparation of the samples with Milli-Q water and dry storage to avoid any Cl contamination as well as a sufficient sample thickness to avoid an additional Cl signal from the underlying mounting material.

2)   Absolute Cl concentrations in the glasses partially correlate with other mantle-incompatible trace elements and are therefore to a certain extent source dependent. However, in addition to the range in magmatic Cl concentrations, a decoupling of Cl is observed to elements of similar compatibility (K, Nb), particularly in Red Sea basalts. Cl/K and Cl/Nb ratios that lie above mantle ratios cannot be explained by source enrichment, fractional crystallisation, melting, degassing or seafloor weathering processes. Instead they require assimilation of a hydrothermal brine component, either by direct assimilation of the fluids or by the assimilation of crust that was previously hydrothermally altered. Consistently, at all three ridges investigated here, independent indications for hydrothermal activity at the seafloor are spatially related to basalts with elevated Cl/Nb ratios. Assimilation of hydrothermally altered crust appears therefore not to be restricted to fast-spreading ridges, but also to take place at slow-spreading ridges. Hydrothermal contamination of magmas seems widespread as more than 75% of the measured glass samples have Cl/Nb higher than mantle values. High Cl/K is also detected in melt inclusions in olivine and plagioclase, which indicates that Cl addition occurs before final crystallisation.

3)   Since all samples that have Cl/Nb above mantle ratios experienced interaction with hydrothermal fluids, elevated Cl/Nb can be used as an indicator of present or former hydrothermal activity and Cl/Nb in basalts can be employed as an exploration tool for both active hydrothermal vent fields and for inactive fields, and their associated massive sulphide deposits. Important discovered target areas for future hydrothermal research in the Red Sea are the Thetis-Hadarba-Hatiba Deeps, particularly their large dome volcanoes, and also the northern Port Sudan Deep and the volcanic dome in Mabahiss Deep. A major objective for a former, now inactive hydrothermal vent field is the axial high at the SMAR segment A2 (8°57'S).

4)   Cl/Nb ratios in basalts at slow-spreading ridges are highly variable between samples, sometimes even between samples from the same dredge. High Cl/Nb is related to large volcanic structures and recent volcanic activity, consistent with expectations of hydrothermal activity at those locations. Faulting is important to form fluid pathways, but the number of faults detectable in bathymetric maps is not correlated to Cl/Nb and hence implies that major faults are not a limiting factor for hydrothermal circulation at slow-spreading ridges. Chlorine addition can be enhanced by fluid flow through evaporite sequences as can be observed at the Red Sea Rift, while high magmatic Cl contents (due to a trace element enriched source; present at all three ridges) decrease the probability of detecting hydrothermal Cl addition as the change in absolute Cl concentrations is minimal. Spreading rate has no significant effect on Cl within a ridge, but there is a difference in the extent of Cl addition between fast- and slow-spreading ridges. Fast-spreading ridges show ubiquitous Cl addition to all samples probably as they have permanent, large and shallow magma chambers that assimilate the crust on a larger scale. In contrast, the lower and highly variable Cl/Nb in basalts at slow-spreading ridges indicates the action of more heterogeneous and smaller scale magmatic and alteration processes deeper in the crust. The local action of these processes limits the amount of Cl addition. Most extreme in this respect is the ultra-slow-spreading Gakkel Ridge with a cool and thin crust that displays the smallest extent of Cl/Nb elevation.

5)   The depth of hydrothermal circulation is difficult to determine with pressure calculations derived from glass compositions alone, as their major element contents and thus the calculated crystallization pressures are highly sensitive to modification by assimilation of crustal cumulates and gabbroic rocks. Such assimilation is indicated by disequilibrium textures and xenocrysts in the basalts. All samples that have elevated Cl/Nb have experienced assimilation and so their pressure calculations should be taken with care. More reliable, but sparse, Cpx-melt pressure calculations (using the equilibrium between Cpx and the glass) indicate lower crustal crystallization depths of 10-13 km for SMAR segment A2. Melt inclusions with high Cl/K in SMAR magmas imply Cl addition by magma chamber and assimilation processes during crystallization and thus hydrothermal circulation down to the lower crust at a minimum depth of 10-13 km. Lower crustal hydrothermal circulation and assimilation is consistent with melt-rock reactions found in lower crustal cumulates elsewhere and deep faulting at slow-spreading ridges. Hydrothermal circulation over the whole crustal range has important implications for the Cl and H_2O budget of the crust, particularly for young spreading oceans, where the crust can be additionally contaminated in Cl if hydrothermal fluids crossed evaporite sequences as in the Red Sea. Deep hydrothermal circulation can further aid lower crustal cooling and promote crystallization at all crustal depths. Therefore, the sheeted sill model is supported by the Cl data as a mechanism to cool the lower crust at slow-spreading ridges.

Acknowledgements

Further thanks I like to express to all people that provided all different kind of samples or helped me organise them: Dr. Antoine Bézos, Prof. Dr. Gareth Davies, Dr. Armin Freundt, Anna Krätschell, Richard Mühe, Jan Sticklus and Prof. Roberta Rudnick.

My deepest gratitude is for the colleagues and new friends I saw everyday at work and made it a warm place. Julia Mahlke helped me with all the first (and many) German forms and phone calls that needed to be made in order to start living and working here. Stefan Bredemeyer I like to thank for sharing three different offices with me and for listening to long issues of my German misunderstandings. I am very grateful for his help with German proofreading, with small computer issues and for finding a method for me to copy a few 100.000s of text files semi-automatically in stead of all by hand, which probably saved me a few years. I warmly thank Dr. Nico Augustin for all the advice regarding maps and hydrothermalism and for his effort for the Jeddah Transect project; for tea breaks with chat, proofreading of texts, for all sort of small things and for not getting upset when I wanted to have another detail different and changed in a map. Instructions on how to prepare a cruise and what to do to finish a thesis from Dr. Tom Kwasnitschka are greatly appreciated as well as talks on all sort of practical things. Dr. Sven Petersen I thank for sharing his knowledge regarding hydrothermal circulation and for forcing me to talk German during the lunch and Frauke Rathjen for the all support with the forms and for many delicious cakes. Dr. "Izzy" Yeo I like to thank for English proof reading, funny videos and chats. All of those, as well as Dirk, Dominik, Frederik, Hanna, Kaitlyn, John, Meike, Peer, Sabine, Sebastian, Thor and everyone who was there for shorter times (or that I forgot to mention) I thank for sharing the lunch breaks and other times at Geomar and for brightening my time here.

Finally I like to express my greatest thanks to my friends and family. Nico supported me during my whole PhD and I want to thank him for encouraging me to do the big and small things and for standing by my side when I was happy as things worked, but mostly also for being there when I encountered setbacks and for making me happy again.
My family I like to thank for supporting me in my choice to go to Kiel, for all there help to make it possible to do this thesis, and for believing in me. I am very happy to got to know all the new friends I made in Germany at 'Tanzschule Gemind', the 'Kanu-Vereinigung Kiel' and 'Reitschule Stoltenberg' that made my stay in Kiel so much nicer and I am grateful for there patience with my starting German and their help to 'master' it. My friends in the Netherlands and elsewhere I thank for all their distance support in the form of many many emails and chats. At last I was glad to have my two small cats Coren and Haplo around me.

Thank you all!

Bibliography

Allen D.E., Seyfried Jr W.E. (2004) Serpentinization and heat generation: constraints from Lost City and Rainbow hydrothermal systems. *Geochim. Cosmochim. Acta* **68**, 1347-1354.

Almeev R.R., Holtz F., Koepke J., Ariskin A.A. (2007a) The effect of minor H_2O content on crystallisation in MORB: experiments, model, applications. *Goldschmidt 2007 abstracts*

Almeev R.R., Holtz F., Koepke J., Parat F., Botcharnikov R.E. (2007b) The effect of H_2O on olivine crystallization in MORB: experimental calibration at 200 MPa. *Am. Mineral.* **92**, 670-674.

Almeev R., Holtz F., Koepke J., Haase K., Devey C. (2008) Depths of partial crystallization of H_2O-bearing MORB: phase equilibria simulations of basalts at the MAR near Ascension Island (7–11 S). *J. Petrol.* **49**, 25-45.

Almeev R.R., Holtz F., Koepke J., Parat F. (2012) Experimental calibration of the effect of H_2O on plagioclase crystallization in basaltic melt at 200 MPa. *Am. Mineral.* **97**, 1234-1240.

Alt J.C., Bach W. (2006) Oxygen isotope composition of a section of lower oceanic crust, ODP Hole 735B. *Geochem. Geophys. Geosyst.* **7**, Q12008.

Alt J.C., Teagle D.A. (2003) Hydrothermal alteration of upper oceanic crust formed at a fast-spreading ridge: mineral, chemical, and isotopic evidence from ODP Site 801. *Chem. Geol.* **201**, 191-211.

Alt J.C., Honnorez J., Laverne C., Emmermann R. (1986) Hydrothermal alteration of a 1 km section through the upper oceanic crust, Deep Sea Drilling Project Hole 504B: Mineralogy, chemistry and evolution of seawater-basalt interactions. *J. Geophys. Res. Solid Earth* **91**, 10309-10335.

Altherr R., Henjes-Kunst F., Puchelt H., Baumann A. (1988) Volcanic activity in the Red Sea axial trough—evidence for a large mantle diapir? *Tectonophysics* **150**, 121-133.

Altherr R., Henjes-Kunst F., Baumann A. (1990) Asthenosphere versus lithosphere as possible sources for basaltic magmas erupted during formation of the Red Sea: constraints from Sr, Pb and Nd isotopes. *Earth Planet. Sci. Lett.* **96**, 269-286.

Anthony J.W., Bideaux R.A., Bladh K.W., C. N.M. (1997) *Handbook of Mineralogy III Halides, Hydroxides, Oxides*. Mineral Data Publishing.

Ariskin A.A., Barmina G.S. (2004) COMAGMAT: development of a magma crystallization model and its petrological applications. *Geochem. Int.* **42**, S1-S157.

Augustin N., Lackschewitz K., Kuhn T., Devey C.W. (2008) Mineralogical and chemical mass changes in mafic and ultramafic rocks from the Logatchev hydrothermal field (MAR 15 N). *Mar. Geol.* **256**, 18-29.

Augustin N., Devey C.W., van der Zwan F.M., Feldens P., Tominaga M., Bantan R.A., Kwasnitschka T. (in review) The Rifting to Spreading Transition in the Red Sea. *In review by Earth Planet. Sci. Lett.*

Bäcker H., Schoell M. (1972) New deeps with brines and metalliferous sediments in the Red Sea. *Nature Physical Science* **240**, 153-158.

Bäcker H., Richter H. (1973) Die rezente hydrothermal-sedimentäre Lagerstätte Atlantis-II-Tief im Roten Meer. *Geol. Rundsch.* **62**, 697-737.

Baker E.T., German C.R. (2004) On the global distribution of hydrothermal vent fields, in *Mid-Ocean Ridges: Hydrothermal Interactions Between the Lithosphere and Oceans, Geophys. Monogr. Ser., vol 148* (eds. C.R. German, J. Lin, L.M. Parson). AGU, Washington, D.C., 245-266.

Baker E.T., Edmonds H.N., Michael P.J., Bach W., Dick H.J.B., Snow J.E., Walker S.L., Banerjee N.R., Langmuir C.H. (2004) Hydrothermal venting in magma deserts: The ultraslow-spreading Gakkel and Southwest Indian Ridges. *Geochem. Geophys. Geosyst.* **5**, Q08002.

Baker D. (2008) The fidelity of melt inclusions as records of melt composition. *Contrib. Mineral. Petrol.* **156**, 377-395.

Barnes J.D., Cisneros M. (2012) Mineralogical control on the chlorine isotope composition of altered oceanic crust. *Chem. Geol.* **326–327**, 51-60.

Barrat J.-A., Jahn B., Joron J.-L., Auvray B., Hamdi H. (1990) Mantle heterogeneity in northeastern Africa: evidence from Nd isotopic compositions and hygromagmaphile element geochemistry of basaltic rocks from the Gulf of Tadjoura and southern Red Sea regions. *Earth Planet. Sci. Lett.* **101**, 233-247.

Bédard J.H. (1991) Cumulate recycling and crustal evolution in the Bay of Islands ophiolite. *J. Geol.*, 225-249.

Bédard J.H. (1993) Oceanic crust as a reactive filter: Synkinematic intrusion, hybridization, and assimilation in an ophiolitic magma chamber, western Newfoundland. *Geology* **21**, 77-80.

Bédard J.H., Hébert R. (1996) The lower crust of the Bay of Islands ophiolite, Canada: Petrology, mineralogy, and the importance of syntexis in magmatic differentiation in ophiolites and at ocean ridges. *J. Geophys. Res. Solid Earth* **101**, 25105-25124.

Bédard J.H., Hebert R., Berclaz A., Varfalvy V. (2000) Syntexis and the genesis of lower oceanic crust, in *Ophiolites and Oceanic crust: New insights from Field Studies and the Ocean Drilling Program* (eds. Y. Dilek). Geological Society of America, 105-120.

Bence A.E., Baylis D.M., Bender J.F., Grove T.L. (1979) Controls on the major and minor element chemistry of Mid-Ocean Ridge basalts and glasses, in *Deep Drilling Results in the Atlantic Ocean: Ocean Crust* **2,** (eds. M. Talwani, C.G. Harrison, D.E. Hayes). AGU, Washington, DC, 331-341.

Berndt M.E., Seyfried Jr W.E. (1990) Boron, bromine, and other trace elements as clues to the fate of chlorine in mid-ocean ridge vent fluids. *Geochim. Cosmochim. Acta* **54**, 2235-2245.

Bézos A. (2003) Étude des éléments lithophiles et fortement sidérophiles (Pd, Pt, Ru et Ir) dans les basaltes des dorsales océaniques. Ph.D. Thesis, l'Université de Paris.

Bischoff J.L., Rosenbauer R.J. (1987) Phase separation in seafloor geothermal systems; an experimental study of the effects on metal transport. *Am. J. Sci.* **287**, 953-978.

Blum N., Puchelt H. (1991) Sedimentary-hosted polymetallic massive sulfide deposits of the Kebrit and Shaban Deeps, Red Sea. *Mineral. Deposita* **26**, 217-227.

Bonatti E., Colantoni P., Dellavedova B., Taviani M. (1984) Geology of the red-sea transitional region (22°N-25°N). *Oceanolog. Acta* **7**, 385-398.

Bonatti E. (1985) Punctiform initiation of seafloor spreading in the Red Sea during transition from a continental to an oceanic rift. *Nature* **316**, 33-37.

Bosch D., Jamais M., Boudier F., Nicolas A., Dautria J.-M., Agrinier P. (2004) Deep and High-temperature Hydrothermal Circulation in the Oman Ophiolite—Petrological and Isotopic Evidence. *J. Petrol.* **45**, 1181-1208.

Bosworth W., Huchon P., McClay K. (2005) The Red Sea and Gulf of Aden Basins. *J. Afr. Earth Sci.* **43**, 334-378.

Botz R., Schmidt M., Wehner H., Hufnagel H., Stoffers P. (2007) Organic-rich sediments in brine-filled Shaban-and Kebrit deeps, northern Red Sea. *Chem. Geol.* **244**, 520-553.

Brewer P.G., Spencer D.W. (1969) A note on the chemical composition of the Red Sea brines, in *Hot Brines and Recent Heavy Metal Deposits in the Red Sea* (eds. E.T. Degens, D.A. Ross). Springer-Verlag, New York.

Bruguier N., Minshull T., Brozena J. (2003) Morphology and tectonics of the Mid-Atlantic Ridge, 7°–12°S. *J. Geophys. Res. Solid Earth* **108**.

Bryan W.B., Thompson G., Ludden J.N. (1981) Compositional variation in normal MORB from 22°–25°N: Mid-Atlantic Ridge and Kane Fracture Zone. *J. Geophys. Res. Solid Earth* **86**, 11815-11836.

Cannat M., Mével C., Stakes D. (1991) Stretching of the deep crust at the slow-spreading Southwest Indian Ridge. *Tectonophysics* **190**, 73-94.

Cannat M., Sauter D., Mendel V., Ruellan E., Okino K., Escartin J., Combier V., Baala M. (2006) Modes of seafloor generation at a melt-poor ultraslow-spreading ridge. *Geology* **34**, 605-608.

Cartigny P., Pineau F., Aubaud C., Javoy M. (2008) Towards a consistent mantle carbon flux estimate: Insights from volatile systematics (H_2O/Ce, δD, CO_2/Nb) in the North Atlantic mantle (14° N and 34° N). *Earth Planet. Sci. Lett.* **265**, 672-685.

Chavrit D. (2010) Cartographie globale des flux de CO_2 à l'axe des dorsales océaniques. Ph.D. thesis, University of Nantes, France.

Chavrit D., Humler E., Morizet Y., Laporte D. (2012) Influence of magma ascent rate on carbon dioxide degassing at oceanic ridges: Message in a bubble. *Earth Planet. Sci. Lett.* **357**, 376-385.

Chen Y.J. (2001) Thermal effects of gabbro accretion from a deeper second melt lens at the fast spreading East Pacific Rise. *J. Geophys. Res. Solid Earth* **106**, 8581-8588.

Cherkaoui A.S., Wilcock W.S., Dunn R.A., Toomey D.R. (2003) A numerical model of hydrothermal cooling and crustal accretion at a fast spreading mid-ocean ridge. *Geochem. Geophys. Geosyst.* **4**, 8616.

Chu D., Gordon R.G. (1998) Current plate motions across the Red Sea. *Geophys. J. Int.* **135**, 313-328.

Coakley B.J., Cochran J.R. (1998) Gravity evidence of very thin crust at the Gakkel Ridge (Arctic Ocean). *Earth Planet. Sci. Lett.* **162**, 81-95.

Cochran J.R. (1983) A model for development of Red Sea. *AAPG Bull.* **67**, 41-69.

Cochran J.R. (2005) Northern Red Sea: Nucleation of an oceanic spreading center within a continental rift. *Geochem. Geophys. Geosyst.* **6**, Q03006.

Coogan L.A. (2003) Contaminating the lower crust in the Oman ophiolite. *Geology* **31**, 1065-1068.

Coogan L.A., Saunders A.D., Kempton P.D., Norry M.J. (2000) Evidence from oceanic gabbros for porous melt migration within a crystal mush beneath the Mid-Atlantic Ridge. *Geochem. Geophys. Geosyst.* **1**, 1044.

Coogan L.A., Mitchell N.C., O'Hara M.J. (2002a) Roof assimilation at fast spreading ridges: An investigation combining geophysical, geochemical, and field evidence. *J. Geophys. Res.* **108**, 2002.

Coogan L.A., Thompson G., MacLeod C.J. (2002b) A textural and geochemical investigation of high level gabbros from the Oman ophiolite: implications for the role of the axial magma chamber at fast-spreading ridges. *Lithos* **63**, 67-82.

Coombs M.L., Sisson T.W., Kimura J.-I. (2004) Ultra-high chlorine in submarine Kīlauea glasses: evidence for direct assimilation of brine by magma. *Earth Planet. Sci. Lett.* **217**, 297-313.

Courtillot V. (1982) Propagating rifts and continental breakup. *Tectonics* **1**, 239-250.

Danyushevsky L., Sobolevz A., Dmitrievz L. (1996) Estimation of the pressure of crystallization and H_2O content of MORB and BABB glasses: calibration of an empirical technique. *Mineral. Petrol.* **57**, 185-204.

de Hoog J.C.M., Mason P.R.D., van Bergen M.J. (2001) Sulfur and chalcophile elements in subduction zones: constraints from a laser ablation ICP-MS study of melt inclusions from Galunggung Volcano, Indonesia. *Geochim. Cosmochim. Acta* **65**, 3147-3164.

Dekov V., Boycheva T., Hålenius U., Petersen S., Billström K., Stummeyer J., Kamenov G., Shanks W. (2011) Atacamite and paratacamite from the ultramafic-hosted Logatchev seafloor vent field (14°45′N, Mid-Atlantic Ridge). *Chem. Geol.* **286**, 169-184.

DeMets C., Gordon R.G., Argus D.F. (2010) Geologically current plate motions. *Geophys. J. Int.* **181**, 1-80.

Detrick R.S., Mutter J.C., Buhl P., Kim I.I. (1990) No evidence from multichannel reflection data for a crustal magma chamber in the MARK area on the Mid-Atlantic Ridge. *Nature* **347**, 61-64.

Devey C.W., Lackschewitz K.S., Baker E. (2005) Hydrothermal and volcanic activity found on the Southern Mid-Atlantic Ridge. *Eos Trans. Am. Geophys. Union* **86**, 209-212.

Devey C.W., German C., Haase K., Lackschewitz K., Melchert B., Connelly D. (2010) The Relationships Between Volcanism, Tectonism, and Hydrothermal Activity on the Southern Equatorial Mid-Atlantic Ridge, in *Diversity of Hydrothermal Systems on Slow Spreading Ocean Ridges* (eds. P.A. Rona, C.W. Devey, J. Dyment, B.J. Murton), 133-152.

Dick H.J.B., Natland J.H., Alt J.C., Bach W., Bideau D., Gee J.S., Haggas S., Hertogen J.G.H., Hirth G., Holm P.M., Ildefonse B., Iturrino G.J., John B.E., Kelley D.S., Kikawa E., Kingdon A., LeRoux P.J., Maeda J., Meyer P.S., Miller D.J., Naslund H.R., Niu Y.-L., Robinson P.T., Snow J., Stephen R.A., Trimby P.W., Worm H.-U., Yoshinobu A. (2000) A long in situ section of the lower ocean crust: results of ODP Leg 176 drilling at the Southwest Indian Ridge. *Earth Planet. Sci. Lett.* **179**, 31-51.

Dick H., Ozawa K., Meyer P., Niu Y., Robinson P., Constantin M., Hebert R., Maeda J., Natland J., Hirth G. (2002) Primary silicate mineral chemistry of a 1.5-km section of very slow spreading lower ocean crust: ODP Hole 735B, Southwest Indian Ridge. *Proc. Ocean Drill. Program Sci. Results* **176,** 1-61.

Dick H.J.B., Lin J., Schouten H. (2003) An ultraslow-spreading class of ocean ridge. *Nature* **426**, 405-412.

Donnelly K. (2002) The genesis of E-MORB: extensions and limitations of the hot spot model. PhD Thesis, Columbia University.

Dungan M., Rhodes J.M. (1978) Residual glasses and melt inclusions in basalts from DSDP Legs 45 and 46: Evidence for magma mixing. *Contrib. Mineral. Petrol.* **67**, 417-431.

Dunn R.A., Toomey D.R., Solomon S.C. (2000) Three-dimensional seismic structure and physical properties of the crust and shallow mantle beneath the East Pacific Rise at 9°30'N. *J. Geophys. Res. Solid Earth* **105**, 23537-23555.

Eder W., Schmidt M., Koch M., Garbe-Schönberg D., Huber R. (2002) Prokaryotic phylogenetic diversity and corresponding geochemical data of the brine–seawater interface of the Shaban Deep, Red Sea. *Environ. Microbiol.* **4**, 758-763.

Edmonds H.N., Michael P.J., Baker E.T., Connelly D.P., Snow J.E., Langmuir C.H., Dick H.J.B., Muhe R., German C.R., Graham D.W. (2003) Discovery of abundant hydrothermal venting on the ultraslow-spreading Gakkel ridge in the Arctic Ocean. *Nature* **421**, 252-256.

Elburg M.A., Kamenetsky V.S., Foden J.D., Sobolev A. (2007) The origin of medium-K ankaramitic arc magmas from Lombok (Sunda arc, Indonesia): Mineral and melt inclusion evidence. *Chem. Geol.* **240**, 260-279.

Elkins L., Sims K., Prytulak J., Blichert-Toft J., Elliott T., Blusztajn J., Fretzdorff S., Reagan M., Haase K., Humphris S. (2014) Melt generation beneath Arctic Ridges: Implications from U decay series disequilibria in the Mohns, Knipovich, and Gakkel Ridges. *Geochim. Cosmochim. Acta* **127**, 140-170.

Engdahl E.R., van der Hilst R., Buland R. (1998) Global teleseismic earthquake relocation with improved travel times and procedures for depth determination. *Bull. Seismol. Soc. Am.* **88**, 722-743.

Expedition Scientific Party (2005) Oceanic core complex formation, Atlantis Massif, Mid-Atlantic Ridge: drilling into the footwall and hanging wall of a tectonic exposure of deep, young oceanic lithosphere to study deformation, alteration, and melt generation. *IODP Preliminairy Reports* **305**.

Féraud G., Zumbo V., Sebai A., Bertrand H. (1991) $^{40}Ar/^{39}Ar$ age and duration of tholeiitic magmatism related to the early opening of the Red Sea rift. *Geophys. Res. Lett.* **18**, 195-198.

Fietzke J., Frische M., Hansteen T.H., Eisenhauer A. (2008) A simplified procedure for the determination of stable chlorine isotope ratios ($\delta^{37}Cl$) using LA-MC-ICP-MS. *J. Anal. At. Spectrom.* **23**.

Forsyth D.W. (1992) *Geophysical constraints on mantle flow and melt generation beneath mid-ocean ridges. Geophys. Monogr. Ser.* **71** (eds. J.P. Morgan, D.K. Blackman, J.M. Sinton). American Geophysical Union, Washington D. C.

Fouquet Y. (1997) Where are the large hydrothermal sulphide deposits in the oceans? *Phil. Trans. Roy. Soc. Math. Phys. Eng. Sci.* **355**, 427-441.

Fournier R. (1987) Conceptual models of brine evolution in magmatic-hydrothermal systems. *US Geol. Surv. Prof. Pap* **1350**, 1487-1506.

France L., Ildefonse B., Koepke J. (2009) Interactions between magma and hydrothermal system in Oman ophiolite and in IODP Hole 1256D: Fossilization of a dynamic melt lens at fast spreading ridges. *Geochem. Geophys. Geosyst.* **10**.

France L., Koepke J., Ildefonse B., Cichy S.B., Deschamps F. (2010) Hydrous partial melting in the sheeted dike complex at fast spreading ridges: experimental and natural observations. *Contrib. Mineral. Petrol.* **160**, 683-704.

Francis D. (1986) The pyroxene paradox in MORB glasses - a signature of picritic parental magmas? *Nature* **319**, 586-589.

GeoReM database: *http://georem.mpch-mainz.gwdg.de*. Application version 14; 04/01/2012.

German C., Connelly D., Evans A., Parson L. (2002) Hydrothermal activity on the southern Mid-Atlantic Ridge. *AGU Fall Meeting Abstracts* **1,** 1361.

Ghebreab W. (1998) Tectonics of the Red Sea region reassessed. *Earth Sci. Rev.* **45**, 1-44.

Gillis K.M., Thompson G., Kelley D.S. (1993) A view of the lower crustal component of hydrothermal systems at the Mid-Atlantic Ridge. *J. Geophys. Res. Solid Earth* **98**, 19597-19619.

Gillis K.M., Coogan L.A., Chaussidon M. (2003) Volatile element (B, Cl, F) behaviour in the roof of an axial magma chamber from the East Pacific Rise. *Earth Planet. Sci. Lett.* **213**, 447-462.

Girdler R.W. (1991) The Afro-Arabian rift system—an overview. *Tectonophysics* **197**, 139-153.

Goldstein S.L., Soffer G., Langmuir C.H., Lehnert K.A., Graham D.W., Michael P.J. (2008) Origin of a Southern Hemisphere' geochemical signature in the Arctic upper mantle. *Nature* **453**, 89-93.

Gregory R.T., Taylor H.P. (1981) An oxygen isotope profile in a section of Cretaceous oceanic crust, Samail Ophiolite, Oman: Evidence for $\delta^{18}O$ buffering of the oceans by deep (> 5 km) seawater-hydrothermal circulation at mid-ocean ridges. *J. Geophys. Res. Solid Earth* **86**, 2737-2755.

Grevemeyer I., Reston T.J., Moeller S. (2013) Microseismicity of the Mid-Atlantic Ridge at 7°S–8°15′S and at the Logatchev Massif oceanic core complex at 14°40′N–14°50′N. *Geochem. Geophys. Geosyst.* **14**, 3532-3554.

Guennoc P., Pautot G., Coutelle A. (1988) Surficial structures of the northern Red Sea axial valley from 23 N to 28 N: Time and space evolution of neo-oceanic structures. *Tectonophysics* **153**, 1-23.

Gurvich E.G. (2006) Metalliferous sediments of the Red Sea, in *Metalliferous Sediments of the World Ocean: Fundamental Theory of Deep-Sea Hydrothermal Sedimentation* (eds. Springer Berlin Heidelberg, 127-210.

Haase K.M., Mühe R., Stoffers P. (2000) Magmatism during extension of the lithosphere: geochemical constraints from lavas of the Shaban Deep, northern Red Sea. *Chem. Geol.* **166**, 225-239.

Haase K., Koschinsky A., Petersen S., Devey C.W., German C., Lackschewitz K., Melchert B., Seifert R., Borowski C., Giere O. (2009) Diking, young volcanism and diffuse hydrothermal activity on the southern Mid-Atlantic Ridge: The Lilliput field at 9 33′S. *Mar. Geol.* **266**, 52-64.

Hannington M., Jamieson J., Monecke T., Petersen S., Beaulieu S. (2011) The abundance of seafloor massive sulfide deposits. *Geology* **39**, 1155-1158.

Hansteen T.H., Klügel A. (2008) Fluid inclusion thermobarometry as a tracer for magmatic processes. *Rev. Mineral. Geochem.* **69**, 143-177.

Harper G.D. (1985) Tectonics of slow spreading mid-ocean ridges and consequences of a variable depth to the brittle/ductile transition. *Tectonics* **4**, 395-409.

Hart S., Erlank A., Kable E. (1974) Sea floor basalt alteration: some chemical and Sr isotopic effects. *Contrib. Mineral. Petrol.* **44**, 219-230.

Hartmann M. (1985) Atlantis-II Deep geothermal brine system. Chemical processes between hydrothermal brines and Red Sea deep water. *Mar. Geol.* **64**, 157-177.

Hasenclever J., Theissen-Krah S., Rüpke L.H., Morgan J.P., Iyer K., Petersen S., Devey C.W. (2014) Hybrid on-axis plus ridge-perpendicular circulation reconciles hydrothermal flow observations at fast spreading ridges. *Nature*, in press.

Henstock T.J., Woods A.W., White R.S. (1993) The accretion of oceanic crust by episodic sill intrusion. *J. Geophys. Res. Solid Earth* **98**, 4143-4161.

Herzberg C. (2004) Partial crystallization of mid-ocean ridge basalts in the crust and mantle. *J. Petrol.* **45**, 2389-2405.

Hoernle K., Hauff F., Kokfelt T.F., Haase K., Garbe-Schönberg D., Werner R. (2011) On- and off-axis chemical heterogeneities along the South Atlantic Mid-Ocean-Ridge (5–11°S): Shallow or deep recycling of ocean crust and/or intraplate volcanism? *Earth Planet. Sci. Lett.* **306**, 86-97.

Hofmann A.W. (1988) Chemical differentiation of the Earth: the relationship between mantle, continental crust, and oceanic crust. *Earth Planet. Sci. Lett.* **90**, 297-314.

Hofmann A.W., Jochum K.P., Seufert M., White W.M. (1986) Nb and Pb in oceanic basalts: new constraints on mantle evolution. *Earth Planet. Sci. Lett.* **79**, 33-45.

International Seismological Centre (2011) *On-line Bulletin*: http://www.isc.ac.uk, Thatcham, United Kingdom.

Izzeldin A.Y. (1987) Seismic, gravity and magnetic surveys in the central part of the Red Sea: their interpretation and implications for the structure and evolution of the Red Sea. *Tectonophysics* **143**, 269-306.

Izzeldin A.Y. (1989) Transverse structures in the central part of the Red Sea and implications on early stages of oceanic accretion. *Geophys. J. Oxf.* **96**, 117-129.

Jambon A., Déruelle B., Dreibus G., Pineau F. (1995) Chlorine and bromine abundance in MORB: the contrasting behaviour of the Mid-Atlantic Ridge and East Pacific Rise and implications for chlorine geodynamic cycle. *Chem. Geol.* **126**, 101-117.

Jarosewich E., Nelen J.A., Norberg J.A. (1980) Reference Samples for Electron Microprobe Analysis. *Geostand. Newslett.* **4**, 43-47.

Jochum K.P., Stoll B., Herwig K., Willbold M., Hofmann A.W., Amini M., Aarburg S., Abouchami W., Hellebrand E., Mocek B., Raczek I., Stracke A., Alard O., Bouman C., Becker S., Dücking M., Brätz H., Klemd R., de Bruin D., Canil D., Cornell D., de Hoog C.-J., Dalpé C., Danyushevsky L., Eisenhauer A., Gao Y., Snow J.E., Groschopf N., Günther D., Latkoczy C., Guillong M., Hauri E.H., Höfer H.E., Lahaye Y., Horz K., Jacob D.E., Kasemann S.A., Kent A.J.R., Ludwig T., Zack T., Mason P.R.D., Meixner A., Rosner M., Misawa K., Nash B.P., Pfänder J., Premo W.R., Sun W.D., Tiepolo M., Vannucci R., Vennemann T., Wayne D., Woodhead J.D. (2006) MPI-DING reference glasses for in situ microanalysis: New reference values for element concentrations and isotope ratios. *Geochem. Geophys. Geosyst.* **7**, Q02008.

Jochum K.P., Weis U., Stoll B., Kuzmin D., Yang Q., Raczek I., Jacob D.E., Stracke A., Birbaum K., Frick D.A. (2011) Determination of reference values for NIST SRM 610–617 glasses following ISO guidelines. *Geostand. Geoanal. Res.* **35**, 397-429.

Jokat W., Ritzmann O., Schmidt-Aursch M.C., Drachev S., Gauger S., Snow J. (2003) Geophysical evidence for reduced melt production on the Arctic ultraslow Gakkel mid-ocean ridge. *Nature* **423**, 962-965.

Kamenetsky V., Gurenko A. (2007) Cryptic crustal contamination of MORB primitive melts recorded in olivine-hosted glass and mineral inclusions. *Contrib. Mineral. Petrol.* **153**, 465-481.

Kawahata H., Nohara M., Ishizuka H., Hasebe S., Chiba H. (2001) Sr isotope geochemistry and hydrothermal alteration of the Oman ophiolite. *J. Geophys. Res. Solid Earth* **106**, 11083-11099.

Kelemen P.B., Aharonov E. (1998) Periodic Formation of Magma Fractures and Generation of Layered Gabbros in the Lower Crust Beneath Oceanic Spreading Ridges, in *Faulting and Magmatism at Mid-Ocean Ridges* (eds. W.R. Buck, P.T. Delaney, J.A. Karson, Y. Lagabrielle). American Geophysical Union, 267-289.

Kelemen P.B., Shimizu N., Salters V.J.M. (1995) Extraction of mid-ocean-ridge basalt from the upwelling mantle by focused flow of melt in dunite channels. *Nature* **375**, 747-753.

Kelemen P.B., Koga K., Shimizu N. (1997) Geochemistry of gabbro sills in the crust-mantle transition zone of the Oman ophiolite: implications for the origin of the oceanic lower crust. *Earth Planet. Sci. Lett.* **146**, 475-488.

Kelley D.S., Delaney J.R. (1987) Two-phase separation and fracturing in mid-ocean ridge gabbros at temperatures greater than 700°C. *Earth Planet. Sci. Lett.* **83**, 53-66.

Kendrick M.A., Arculus R., Burnard P., Honda M. (2013) Quantifying brine assimilation by submarine magmas: Examples from the Galápagos Spreading Centre and Lau Basin. *Geochim. Cosmochim. Acta* **123**, 150-165.

Kent A.J.R., Norman M.D., Hutcheon I.D., Stolper E.M. (1999a) Assimilation of seawater-derived components in an oceanic volcano: evidence from matrix glasses and glass inclusions from Loihi seamount, Hawaii. *Chem. Geol.* **156**, 299-319.

Kent A.J.R., Clague D.A., Honda M., Stolper E.M., Hutcheon I.D., Norman M.D. (1999b) Widespread assimilation of a seawater-derived component at Loihi Seamount, Hawaii. *Geochim. Cosmochim. Acta* **63**, 2749-2761.

Kent A.J.R., Peate D.W., Newman S., Stolper E.M., Pearce J.A. (2002) Chlorine in submarine glasses from the Lau Basin: seawater contamination and constraints on the composition of slab-derived fluids. *Earth Planet. Sci. Lett.* **202**, 361-377.

Klauke S. (2000) Seltene Erden in heißen Salzlösungen aus dem Atlantis II-Tief, Rotes Meer. Diplom Thesis, Christian-Albrechts-Universität Kiel.

Klügel A. (1998) Reactions between mantle xenoliths and host magma beneath La Palma (Canary Islands): constraints on magma ascent rates and crustal reservoirs. *Contrib. Mineral. Petrol.* **131**, 237-257.

Koepke J., Feig S., Snow J. (2005) Late stage magmatic evolution of oceanic gabbros as a result of hydrous partial melting: Evidence from the Ocean Drilling Program (ODP) Leg 153 drilling at the Mid-Atlantic Ridge. *Geochem. Geophys. Geosyst.* **6**, Q02001.

Koepke J., France L., Müller T., Faure F., Goetze N., Dziony W., Ildefonse B. (2011) Gabbros from IODP Site 1256, equatorial Pacific: Insight into axial magma chamber processes at fast spreading ocean ridges. *Geochem. Geophys. Geosyst.* **12**.

Korenaga J., Kelemen P.B. (1997) Origin of gabbro sills in the Moho transition zone of the Oman ophiolite: Implications for magma transport in the oceanic lower crust. *J. Geophys. Res. Solid Earth* **102**, 27729-27749.

Kovalenko V.I., Naumov V.B., Girnis A.V., Dorofeeva V.A., Yarmolyuk V.V. (2006) Estimation of the average contents of H_2O, Cl, F, and S in the depleted mantle on the basis of the compositions of melt inclusions and quenched glasses of mid-ocean ridge basalts. *Geochem. Int.* **44**, 209-231.

Kvassnes A.S., Grove T. (2008) How partial melts of mafic lower crust affect ascending magmas at oceanic ridges. *Contrib. Mineral. Petrol.* **156**, 49-71.

Langmuir C.H., Klein E.M., Plank T. (1992) Petrological systematics of mid-ocean ridge basalts: Constraints on melt generation beneath ocean ridges, in *Mantle Flow and Melt Generation at Mid-Ocean Ridges. Geophys. Monogr. Ser.* **71,** (eds. J. Phipps Morgan, D.K. Blackman, J.M. Sinton), 183-280.

Laubier M., Schiano P., Doucelance R., Ottolini L., Laporte D. (2007) Olivine-hosted melt inclusions and melting processes beneath the FAMOUS zone (Mid-Atlantic Ridge). *Chem. Geol.* **240**, 129-150.

Laughton A. (1970) A new bathymetric chart of the Red Sea. *Phil. Trans. R. Soc. London, Ser. A*, 21-22.

Laurila T.E., Hannington M.D., Petersen S., Garbe-Schönberg D. (2014) Early Depositional History of Metalliferous Sediments in the Atlantis II Deep of the Red Sea: Evidence from Rare Earth Element Geochemistry. *Geochim. Cosmochim. Acta* **126**, 146-168.

le Roux P.J., Shirey S.B., Hauri E.H., Perfit M.R., Bender J.F. (2006) The effects of variable sources, processes and contaminants on the composition of northern EPR MORB (8–10°N and 12–14°N): Evidence from volatiles (H_2O, CO_2, S) and halogens (F, Cl). *Earth Planet. Sci. Lett.* **251**, 209-231.

Lecuyer C., Reynard B. (1996) High-temperature alteration of oceanic gabbros by seawater (Hess Deep, Ocean Drilling Program Leg 147): Evidence from oxygen isotopes and elemental fluxes. *J. Geophys. Res. Solid Earth* **101**, 15883-15897.

Lee C.-T., Rudnick R.L. (1999) Compositionally stratified cratonic lithosphere: petrology and geochemistry of peridotite xenoliths from the Labait tuff cone, Tanzania. *Proceedings of the 7th International Kimberlite Conference* (eds. J. Gurney, S.R. Richardson) 503-521.

Lehnert K., Su Y., Langmuir C., Sarbas B., Nohl U. (2000) A global geochemical database structure for rocks. *Geochem. Geophys. Geosyst.* **1**, 1012.

Ligi M., Bonatti E., Bortoluzzi G., Cipriani A., Cocchi L., Caratori Tontini F., Carminati E., Ottolini L., Schettino A. (2012) Birth of an ocean in the Red Sea: Initial pangs. *Geochem. Geophys. Geosyst.* **13**, Q08009.

Lissenberg C.J., Dick H.J.B. (2008) Melt–rock reaction in the lower oceanic crust and its implications for the genesis of mid-ocean ridge basalt. *Earth Planet. Sci. Lett.* **271**, 311-325.

Lissenberg C.J., Bédard J.H., van Staal C.R. (2004) The structure and geochemistry of the gabbro zone of the Annieopsquotch ophiolite, Newfoundland: implications for lower crustal accretion at spreading ridges. *Earth Planet. Sci. Lett.* **229**, 105-123.

Lister C.R.B. (1974) On the Penetration of Water into Hot Rock. *Geophys. J. Int.* **39**, 465-509.

Maclennan J., Hulme T., Singh S.C. (2005) Cooling of the lower oceanic crust. *Geology* **33**, 357-366.

Magenheim A.J., Spivack A.J., Michael P.J., Gieskes J.M. (1995) Chlorine stable isotope composition of the oceanic crust: Implications for Earth's distribution of chlorine. *Earth Planet. Sci. Lett.* **131**, 427-432.

Maicher D., White J. (2001) The formation of deep-sea Limu o Pele. *Bull. Volcanol.* **63**, 482-496.

Makris J., Henke C.H., Egloff F., Akamaluk T. (1991) The gravity field of the Red Sea and East Africa. *Tectonophysics* **198**, 369-381.

Manheim F. (1974) Red Sea geochemistry. *Init. Repts. Deep Sea Drill. Proj.* **23**, 975-998.

Manning C.E., MacLeod C.J., Weston P.E. (2000) Lower-crustal cracking front at fast-spreading ridges: Evidence from the East Pacific Rise and the Oman ophiolite. *Spec. Pap. Geol. Soc. Am.* **349**, 261-272.

McCulloch M.T., Gregory R.T., Wasserburg G.J., Taylor H.P. (1981) Sm-Nd, Rb-Sr, and $^{18}O/^{16}O$ isotopic systematics in an oceanic crustal section: Evidence from the Samail Ophiolite. *J. Geophys. Res. Solid Earth* **86**, 2721-2735.

McDonough W.F., Sun S.s. (1995) The composition of the Earth. *Chem. Geol.* **120**, 223-253.

Melchert B., Devey C.W., German C., Lackschewitz K., Seifert R., Walter M., Mertens C., Yoerger D., Baker E., Paulick H. (2008) First evidence for high-temperature off-axis venting of deep crustal/mantle heat: The Nibelungen hydrothermal field, southern Mid-Atlantic Ridge. *Earth Planet. Sci. Lett.* **275**, 61-69.

Mével C. (1981) Occurrence of pumpellyite in hydrothermally altered basalts from the Vema fracture zone (Mid-Atlantic Ridge). *Contrib. Mineral. Petrol.* **76**, 386-393.

Mével C., Cannat M. (1991) Lithospheric stretching and hydrothermal processes in oceanic gabbros from slow-spreading ridges, in *Ophiolite genesis and evolution of the oceanic lithosphere* (eds. T.J. Peters, A. Nicolas, R. Coleman). Springer, 293-312.

Meyer P., Dick H.B., Thompson G. (1989) Cumulate gabbros from the Southwest Indian Ridge, 54°S-7°16′E: implications for magmatic processes at a slow spreading ridge. *Contrib. Mineral. Petrol.* **103**, 44-63.

Michael P. (1995) Regionally distinctive sources of depleted MORB: Evidence from trace elements and H2O. *Earth Planet. Sci. Lett.* **131**, 301-320.

Michael P.J., Schilling J.-G. (1989) Chlorine in mid-ocean ridge magmas: Evidence for assimilation of seawater-influenced components. *Geochim. Cosmochim. Acta* **53**, 3131-3143.

Michael P.J., Cornell W.C. (1998) Influence of spreading rate and magma supply on crystallization and assimilation beneath mid-ocean ridges: Evidence from chlorine and major element chemistry of mid-ocean ridge basalts. *J. Geophys. Res.* **103**, 18325-18356.

Michael P., Langmuir C., Dick H., Snow J., Goldstein S., Graham D., Lehnert K., Kurras G., Jokat W., Mühe R. (2003) Magmatic and amagmatic seafloor generation at the ultraslow-spreading Gakkel ridge, Arctic Ocean. *Nature* **423**, 956-961.

Miller D.M., Goldstein S.L., Langmuir C.H. (1994) Cerium/lead and lead isotope ratios in arc magmas and the enrichment of lead in the continents. *Nature* **368**, 514-520.

Minshull T., Bruguier N., Brozena J. (1998) Ridge-plume interactions or mantle heterogeneity near Ascension Island? *Geology* **26**, 115-118.

Mitchell N.C., Ligi M., Ferrante V., Bonatti E., Rutter E. (2010) Submarine salt flows in the central Red Sea. *Geol. Soc. Am. Bull.* **122**, 701-713.

Möller H. (2002) Magma Genesis and Mantle Source at the Mid-Atlantic Ridge East of Ascension Island. PhD, Dissertation at Christian-Albrechts-Univeristät zu Kiel.

Monin A., Plakhin E., Podrazhansky A., Sagalevich A., Sorokhtin O. (1981) Visual observations of the Red Sea hot brines. *Nature* **291**, 222-225.

Montési L.G., Behn M.D. (2007) Mantle flow and melting underneath oblique and ultraslow mid-ocean ridges. *Geophys. Res. Lett.* **34**.

Moreira M., Valbracht P., Staudacher T., Allègre C. (1996) Rare gas systematics in Red Sea ridge basalts. *Geophys. Res. Lett.* **23**, 2453-2456.

Morgan J.P., Chen Y.J. (1993) The genesis of oceanic crust: Magma injection, hydrothermal circulation, and crustal flow. *J. Geophys. Res. Solid Earth* **98**, 6283-6297.

Mottl M. (2003) Partitioning of energy and mass fluxes between mid-ocean ridge axes and flanks at high and low temperature, in *Energy and mass transfer in marine hydrothermal systems* (eds. P. Halbach, V. Tunnicliffe, J.R. Hein). Dahlem University Press, Berlin Germany, 271-286.

Moune S., Sigmarsson O., Thordarson T., Gauthier P.-J. (2007) Recent volatile evolution in the magmatic system of Hekla volcano, Iceland. *Earth Planet. Sci. Lett.* **255**, 373-389.

Natland J.H., Dick H.J. (1996) Melt migration through high-level gabbroic cumulates of the East Pacific Rise at Hess Deep: the origin of magma lenses and the deep crustal structure of fast-spreading ridges. *Proc. Ocean Drill. Program Sci. Results, Initial Reports* 21-58.

Nehlig P., Juteau T. (1988) Flow porosities, permeabilities and preliminary data on fluid inclusions and fossil thermal gradients in the crustal sequence of the Sumail ophiolite (Oman). *Tectonophysics* **151**, 199-221.

Nehlig P., Juteau T., Bendel V., Cotten J. (1994) The root zones of oceanic hydrothermal systems: Constraints from the Samail ophiolite (Oman). *J. Geophys. Res. Solid Earth* **99**, 4703-4713.

Nicolas A., Reuber I., Benn K. (1988) A new magma chamber model based on structural studies in the Oman ophiolite. *Tectonophysics* **151**, 87-105.

Nicolas A., Mainprice D., Boudier F. (2003) High-temperature seawater circulation throughout crust of oceanic ridges: A model derived from the Oman ophiolites. *J. Geophys. Res. Solid Earth* **108**, 2371.

Niu Y., Hekinian R. (1997) Spreading-rate dependence of the extent of mantle melting beneath ocean ridges. *Nature* **385**, 326-329.

Omar G.I., Steckler M.S. (1995) Fission Track Evidence on the Initial Rifting of the Red Sea: Two Pulses, No Propagation. *Science* **270**, 1341-1344.

Palme H., O'Neill H.S.C. (2003) Cosmochemical Estimates of Mantle Composition, in *Treatise on Geochemistry* **2,** (eds. D.H. Heinrich, K.T. Karl). Pergamon, Oxford, 1-38.

Paulick H., Münker C., Schuth S. (2010) The influence of small-scale mantle heterogeneities on Mid-Ocean Ridge volcanism: Evidence from the southern Mid-Atlantic Ridge (7°30′S to 11°30′S) and Ascension Island. *Earth Planet. Sci. Lett.* **296**, 299-310.

Pautot G. (1983) Les fosses de la Mer Rouge: approche géomorphologique d'un stade initial d'ouverture océanique réalisée à l'aide du Seabeam. *Oceanolog. Acta* **6**, 235-244.

Pautot G., Guennoc P., Coutelle A., Lyberis N. (1984) Discovery of a large brine deep in the northern Red Sea. *Nature* **310**, 133-136.

Perfit M.R., Cann J.R., Fornari D.J., Engels J., Smith D.K., Ian Ridley W., Edwards M.H. (2003) Interaction of sea water and lava during submarine eruptions at mid-ocean ridges. *Nature* **426**, 62-65.

Pierret M.C., Clauer N., Bosch D., Blanc G., France-Lanord C. (2001) Chemical and isotopic ($^{87}Sr/^{86}Sr$, $\delta^{18}O$, δD) constraints to the formation processes of Red-Sea brines. *Geochim. Cosmochim. Acta* **65**, 1259-1275.

Pierret M., Clauer N., Bosch D., Blanc G. (2010) Formation of Thetis Deep metal-rich sediments in the absence of brines, Red Sea. *J. Geochem. Explor.* **104**, 12-26.

Plank T., Langmuir C.H. (1992) Effects of the melting regime on the composition of the oceanic crust. *J. Geophys. Res. Solid Earth* **97**, 19749-19770.

Pontbriand C.W., Soule S.A., Sohn R.A., Humphris S.E., Kunz C., Singh H., Nakamura K.i., Jakobsson M., Shank T. (2012) Effusive and explosive volcanism on the ultraslow-spreading Gakkel Ridge, 85°E. *Geochem. Geophys. Geosyst.* **13**.

Portnyagin M., Almeev R., Matveev S., Holtz F. (2008) Experimental evidence for rapid water exchange between melt inclusions in olivine and host magma. *Earth Planet. Sci. Lett.* **272**, 541-552.

Putirka K.D. (2008) Thermometers and barometers for volcanic systems. *Rev. Mineral. Geochem.* **69**, 61-120.

Putirka K., Johnson M., Kinzler R., Longhi J., Walker D. (1996) Thermobarometry of mafic igneous rocks based on clinopyroxene-liquid equilibria, 0–30 kbar. *Contrib. Mineral. Petrol.* **123**, 92-108.

Quick J.E., Denlinger R.P. (1993) Ductile deformation and the origin of layered gabbro in ophiolites. *J. Geophys. Res. Solid Earth* **98**, 14015-14027.

Reid I., Jackson H. (1981) Oceanic spreading rate and crustal thickness. *Mar. Geophys. Res.* **5**, 165-172.

Rhodes J.M., Dungan M.A., Blanchard D.P., Long P.E. (1979) Magma mixing at mid-ocean ridges: Evidence from basalts drilled near 22° N on the Mid-Atlantic Ridge. *Tectonophysics* **55**, 35-61.

Ridley W.I., Perfit M.R., Smith M.C., Fornari D.J. (2006) Magmatic processes in developing oceanic crust revealed in a cumulate xenolith collected at the East Pacific Rise, 9°50′N. *Geochem. Geophys. Geosyst.* **7**, Q12O04.

Roeder P., Emslie R. (1970) Olivine-liquid equilibrium. *Contrib. Mineral. Petrol.* **29**, 275-289.

Roeser H.A. (1975) A detailed magnetic survey of the southern Red Sea. *Geol. Jahrb.* **13**, 131-153.

Rona P.A. (1982) Evaporites at passive margins, in *Dynamics of Passive Margins* **6,** (eds. R.A. Scrutton). American Geophysical Union, Washington D.C., 116-132.

Rudnick R.L., McDonough W.F., Chappell B.W. (1993) Carbonatite metasomatism in the northern Tanzanian mantle: Petrographic and geochemical characteristics. *Earth Planet. Sci. Lett.* **114**, 463-475.

Rudnick R.L., McDonough W.F., Orpin A. (1994) Northern Tanzanian Peridotite Xenoliths: a comparison with Kaapvaal Peridotites and inferences on metasomatic interactions. *Proceedings of the 5th International Kimberlite Conference: Kimberlites, Related Rocks and Mantle Xenoliths* (eds. H.O.A. Meyer, O.H. Leonardos) 336 - 353.

Rutherford M.J. (2008) Magma ascent rates. *Rev. Mineral. Geochem.* **69**, 241-271.

Ryabchikov I.D. (2001) Deep Geopheres and Ore Genesis. *Geol. Rudn. Mestorozhd.* **43**, 195-207.

Saal A.E., Hauri E.H., Langmuir C.H., Perfit M.R. (2002) Vapour undersaturation in primitive mid-ocean-ridge basalt and the volatile content of Earth's upper mantle. *Nature* **419**, 451-455.

Salters V.J.M., Stracke A. (2004) Composition of the depleted mantle. *Geochem. Geophys. Geosyst.* **5**, Q05B07.

Schilling J.-G., Bergeron M.B., Evans R., Smith J.V. (1980) Halogens in the Mantle Beneath the North Atlantic [and Discussion]. *Phil. Trans. R. Soc. London, Ser. A* **297**, 147-178.

Schoell M., Hartmann M. (1973) Detailed temperature structure of the hot brines in the Atlantis II Deep area (Red Sea). *Mar. Geol.* **14**, 1-14.

Schramm B., Devey C.W., Gillis K.M., Lackschewitz K. (2005) Quantitative assessment of chemical and mineralogical changes due to progressive low-temperature alteration of East Pacific Rise basalts from 0 to 9 Ma. *Chem. Geol.* **218**, 281-313.

Searle R.C., Ross D.A. (1975) A Geophysical Study of the Red Sea Axial Trough between 20· 5° and 22° N. *Geophys. J. Int.* **43**, 555-572.

Searle R., Escartin J. (2004) The rheology and morphology of oceanic lithosphere and mid-ocean ridges, in *Mid-Ocean Ridges. Geophys. Monogr. Ser.* **148,** (eds. C.R. German, J. Lin, L.M. Parson), 63-93.

Shanks W., Bischoff J. (1980) Geochemistry, sulfur isotope composition, and accumulation rates of Red Sea geothermal deposits. *Econ. Geol.* **75**, 445-459.

Shaw C., Klügel A. (2002) The pressure and temperature conditions and timing of glass formation in mantle-derived xenoliths from Baarley, West Eifel, Germany: the case for amphibole breakdown, lava infiltration and mineral–melt reaction. *Mineral. Petrol.* **74**, 163-187.

Shaw A.M., Behn M.D., Humphris S.E., Sohn R.A., Gregg P.M. (2010) Deep pooling of low degree melts and volatile fluxes at the 85 E segment of the Gakkel Ridge: Evidence from olivine-hosted melt inclusions and glasses. *Earth Planet. Sci. Lett.* **289**, 311-322.

Shishkina T., Botcharnikov R., Holtz F., Almeev R., Portnyagin M.V. (2010) Solubility of H_2O-and CO_2-bearing fluids in tholeiitic basalts at pressures up to 500MPa. *Chem. Geol.* **277**, 115-125.

Sobolev A.V., Nikogosian I.K. (1994) Petrology of long-lived mantle plume magmatism: Hawaii (Pacific) and Reunion Island (Indian Ocean). *Petroloy* **2**, 111-144.

Soule S.A., Fornari D.J., Perfit M.R., Ridley W.I., Reed M.H., Cann J.R. (2006) Incorporation of seawater into mid-ocean ridge lava flows during emplacement. *Earth Planet. Sci. Lett.* **252**, 289-307.

Stakes D., Vanko D.A. (1986) Multistage hydrothermal alteration of gabbroic rocks from the failed Mathematician Ridge. *Earth Planet. Sci. Lett.* **79**, 75-92.

Stakes D., Mével C., Cannat M., Chaput T. (1991) Metamorphic stratigraphy of Hole 735B. *Proc. Ocean Drill. Program Sci. Results* **118,** 153-180.

Stolper E. (1982) The speciation of water in silicate melts. *Geochim. Cosmochim. Acta* **46**, 2609-2620.

Streck M.J., Wacaster S. (2006) Plagioclase and pyroxene hosted melt inclusions in basaltic andesites of the current eruption of Arenal volcano, Costa Rica. *J. Volcanol. Geotherm. Res.* **157**, 236-253.

Stroncik N.A., Haase K.M. (2004) Chlorine in oceanic intraplate basalts: Constraints on mantle sources and recycling processes. *Geology* **32**, 945-948.

Sultan M., Becker R., Arvidson R.E., Shore P., Stern R.J., El Alfy Z., Attia R.I. (1993) New constraints on Red Sea rifting from correlations of Arabian and Nubian Neoproterozoic outcrops. *Tectonics* **12**, 1303-1319.

Sun W.D., Binns R.A., Fan A.C., Kamenetsky V.S., Wysoczanski R., Wei G.J., Hu Y.H., Arculus R.J. (2007) Chlorine in submarine volcanic glasses from the eastern manus basin. *Geochim. Cosmochim. Acta* **71**, 1542-1552.

Swift S.A., Bower A.S., Schmitt R.W. (2012) Vertical, horizontal, and temporal changes in temperature in the Atlantis II and Discovery hot brine pools, Red Sea. *Deep Sea Res. Part I* **64**, 118-128.

Tracy R.J. (1980) Petrology and genetic significance of an ultramafic xenolith suite from Tahiti. *Earth Planet. Sci. Lett.* **48**, 80-96.

Tramontini C., Davies D. (1969) A seismic refraction survey in the Red Sea. *Geophys. J. Int.* **17**, 225-241.

Unni C., Schilling J.-G. (1978) Cl and Br degassing by volcanism along the Reykjanes Ridge and Iceland. *Nature* **272**, 19-23.

van der Zwan F.M., Fietzke J., Devey C.W. (2012) Precise measurement of low (< 100 ppm) chlorine concentrations in submarine basaltic glass by electron microprobe. *J. Anal. At. Spectrom.* **27**, 1966-1974.

van der Zwan F.M., Devey C.W., Augustin N., Almeev R.R., Bantan R.A., Basaham A. (in review) Hydrothermal activity at the slow-spreading Red Sea Rift traced by chlorine in basalt. *In review by Geochim. Cosmochim. Act.*

VanTongeren J.A., Kelemen P.B., Hanghøj K. (2008) Cooling rates in the lower crust of the Oman ophiolite: Ca in olivine, revisited. *Earth Planet. Sci. Lett.* **267**, 69-82.

Villiger S., Müntener O., Ulmer P. (2007) Crystallization pressures of mid-ocean ridge basalts derived from major element variations of glasses from equilibrium and fractional crystallization experiments. *J. Geophys. Res. Solid Earth* **112**.

Volker F., McCulloch M.T., Altherr R. (1993) Submarine basalts from the Red Sea: new Pb, Sr, and Nd isotopic data. *Geophys. Res. Lett.* **20**, 927-930.

Von Damm K., Lilley M., Shanks III W., Brockington M., Bray A., O'Grady K., Olson E., Graham A., Proskurowski G. (2003) Extraordinary phase separation and segregation in vent fluids from the southern East Pacific Rise. *Earth Planet. Sci. Lett.* **206**, 365-378.

Wasch L.J., van der Zwan F.M., Nebel O., Morel M.L.A., Hellebrand E.W.G., Pearson D.G., Davies G.R. (2009) An alternative model for silica enrichment in the Kaapvaal subcontinental lithospheric mantle. *Geochim. Cosmochim. Acta* **73**, 6894-6917.

Weaver S.J., Langmuir C.H. (1990) Calculation of phase equilibrium in mineral-melt systems. *Comput. Geosci.* **16**, 1-19.

Whitmarsh R., Weser O., Ross D. (1974) Initial reports of the deep sea drilling project. *Washington, DC: US Government Printing Office* **23**, 35-56.

Winckler G., Kipfer R., Aeschbach–Hertig W., Botz R., Schmidt M., Schuler S., Bayer R. (2000) Sub sea floor boiling of Red Sea Brines: New indication from noble gas data. *Geochim. Cosmochim. Acta* **64**, 1567-1575.

Yamashita S., Kitamura T., Kusakabe M. (1997) Infrared spectroscopy of hydrous glasses of arc magma compositions. *Geochem. J. Jap.* **31**, 169-174.

Yang H.-J., Kinzler R.J., Grove T. (1996) Experiments and models of anhydrous, basaltic olivine-plagioclase-augite saturated melts from 0.001 to 10 kbar. *Contrib. Mineral. Petrol.* **124**, 1-18.

Zhao M., Canales J.P., Sohn R.A. (2012) Three-dimensional seismic structure of a Mid-Atlantic Ridge segment characterized by active detachment faulting (Trans-Atlantic Geotraverse, 25°55′N-26°20′N). *Geochem. Geophys. Geosyst.* **13**.

Zierenberg R.A., Shanks III W.C. (1988) Isotopic studies of epigenetic features in metalliferous sediment, Atlantis II Deep, Red Sea. *Can. Mineral.* **26**, 737-753.

Publications related to this thesis

Peer-review publications

van der Zwan F.M., Devey C.W., Hansteen T.H., Almeev R.R., Augustin N., Frische M., Bantan R.A. – (in prep.) Lower crustal hydrothermal circulation at slow-spreading ridges – evidence from chlorine in Arctic and South Atlantic basalt glasses and melt inclusions. *In preparation for submission by Contributions to Mineralogy and Petrology.*

van der Zwan F.M., Devey C.W., Augustin N., Almeev R.R., Bantan R.A., Basaham A. (in review) Hydrothermal activity at the slow-spreading Red Sea Rift traced by chlorine in basalt. *In review by Geochim. Cosmochim. Act.*

Augustin N., Devey C.W., van der Zwan F.M., Feldens P., Tominaga M., Bantan R.A., Kwasnitschka T. (2014) The Rifting to Spreading Transition in the Red Sea. *Earth Planet. Sci. Lett.* **395**, 217-230.

van der Zwan F.M., Fietzke J., Devey C.W. (2012) Precise measurement of low (< 100 ppm) chlorine concentrations in submarine basaltic glass by electron microprobe. *J. Anal. At. Spectrom.* **27**, 1966-1974.

Conference Abstracts

van der Zwan F.M., Devey C.W. (2014) The depth of hydrothermal circulation at slow-spreading ridges traced by chlorine in basalt. [Invited Talk] *IPGP PhD Student Meeting, 24.-28.03.2014 Paris.*

van der Zwan F.M., Devey C.W., Augustin N., Basaham A., Bantan R.A., Fietzke J., Almeev R.R. (2013) Assimilation of hydrothermally altered crust at slow spreading ridges. [Poster] In: *Goldschmidt Conference 2013, 25.-30.08.2013, Florence, Italy, Mineralogical Magazine* **77** (5), 2393.

van der Zwan F.M., Augustin N., Devey C.W., Bantan R., Kwasnitschka T. (2013) New insights into volcanism and tectonics in the Red Sea Rift. [PICO] *Geophysical Research Abstracts*, **15**, EGU2013-7188

Metz D., Augustin N., van der Zwan F.M., Bantan R., Al-Aidaroos A.M. (2013) Mabahiss Mons, 25.5°N Red Sea Rift: Tectonics and Volcanism of a Large Submarine Dome Volcano. [PICO] *Geophysical Research Abstracts*, **15**, EGU2013-10487

Augustin N., Devey C.W., Feldens P., van der Zwan F.M., Bantan R., Kwasnitschka T. (2012) The transition from rifting to spreading in the Red Sea: No sign of discrete spreading nodes? [Talk] In: *AGU Fall Meeting 2012, 03.-07.12.2012, San Francisco, USA*, 11E-07

van der Zwan F.M., Devey C.W., Augustin N., Basaham A., Bantan R., Fietzke J., Almeev R.R. (2012) Hydrothermal circulation in the slow spreading Red Sea traced by chlorine. [Talk] In: *AGU Fall Meeting 2012, 03.-07.12.2012, San Francisco, USA*, 12A-08

Augustin N., Devey C.W., Bantan R., van der Zwan F.M., Feldens P. and Kwasnitschka T. (2012) Hatiba to Port Sudan Deep (Red Sea) Imaging a growing Ocean. [Talk] In: *Goldschmidt Conference 2012, 24.-29.06.2012, Montreal, Canada*

van der Zwan F.M., Fietzke J., Devey C.W., Almeev R.R., Haase K.M. (2012) Tracing seawater-rock interaction in slow spreading oceanic crust: precise chlorine measurements in MORB by microprobe. [Talk] In: *Goldschmidt Conference 2012, 24.-29.06.2012, Montreal, Canada*